Fast Magneto-Coriolis Modes and Pressure Torques arising from Torsional Alfvén Modes in Planetary Cores

Felix Gerick

To cite this version:

Felix Gerick. Fast Magneto-Coriolis Modes and Pressure Torques arising from Torsional Alfvén Modes in Planetary Cores. Earth Sciences. Université Grenoble Alpes [2020-..], 2020. English. NNT : 2020GRALU027 . tel-03506924

HAL Id: tel-03506924
https://theses.hal.science/tel-03506924

Submitted on 3 Jan 2022

THÈSE

Pour obtenir le grade de

DOCTEUR DE L'UNIVERSITÉ GRENOBLE ALPES

Spécialité : Sciences de la Terre et de l'Univers et de l'Environnement

Arrêté ministériel : 25 mai 2016

Présentée par

Felix GERICK

Thèse dirigée par **Dominique JAULT**, Directeur de Recherche
et codirigée par **Jérome NOIR**

préparée au sein du **Laboratoire Institut des Sciences de la Terre**
dans **l'École Doctorale Terre, Univers, Environnement**

Modes magnéto-Coriolis rapides et couples de pression résultant des modes de torsion d'Alfvén dans les noyaux planétaires

Fast Magneto-Coriolis Modes and Pressure Torques arising from Torsional Alfvén Modes in Planetary Cores

Thèse soutenue publiquement le **4 décembre 2020**,
devant le jury composé de :

Monsieur DOMINIQUE JAULT
DIRECTEUR DE RECHERCHE, CNRS DELEGATION ALPES, Directeur de thèse
Monsieur JEROME NOIR
DOCTEUR EN SCIENCES, ETH ZURICH - SUISSE, Co-directeur de thèse
Madame CHANTAL STAQUET
PROFESSEUR DES UNIVERSITES, UNIVERSITE GRENOBLE ALPES, Présidente
Monsieur CHRISTOPHER FINLAY
PROFESSEUR, UNIVERSITE TECHNIQUE DU DANEMARK, Rapporteur
Monsieur YVES ROGISTER
MAITRE DE CONFERENCES HDR, UNIVERSITE DE STRASBOURG, Rapporteur
Monsieur MICHEL RIEUTORD
PROFESSEUR DES UNIVERSITES, UNIVERSITE TOULOUSE-III-PAUL- SABATIER, Examinateur

Abstract

Earth's magnetic field and rotation rate change on periods of several years. In this thesis it is investigated if and how such changes can be caused by modes (standing waves) in the liquid and conducting core. To do so, a model for a rapidly rotating and electrically conducting planetary core is developed that is able to handle non-idealized magnetic fields and a non-spherical boundary. We exploit the rapid rotation of the fluid to simplify our model, using the so-called quasi-geostrophic assumption, where the horizontal components of the velocity become invariant along the axis of rotation. By deriving such a model in a non-axisymmetric geometry, we are able to investigate the pressure torque exerted onto the core-mantle boundary by modes, which are linear solutions to the model. So-called torsional Alfvén modes are of particular interest, as they consist of differentially rotating geostrophic cylinders, potentially carrying axial angular momentum. These cylinders act against the tension of sheared radial magnetic field lines, showing their Alfvénic nature. In Earth's core they are assumed to have periods of a few years, and they have been correlated to changes in the length of day on periods of about six years.

Our results suggest that the pressure torque associated with such torsional Alfvén modes is inefficient to explain the observed changes in Earth's length of day. It is found that the amplitude of the pressure associated with these modes should be independent of the rotation rate, if the volume does not allow for non-closed geostrophic contours. It needs to be investigated if the pressure torque can be increased by considering more complex geometries than the ellipsoid, investigated here. Otherwise, torsional Alfvén modes in the core must be coupled to an electrically conducting layer in the lowermost mantle or by a gravitational torque to explain the observed changes in the length of day.

In a second part we investigated Magneto-Coriolis modes in a homogeneous spherical core model, where we can describe the magnetic field in such a way that magnetic field changes on the core surface do not vanish. Geomagnetic observations reveal changes of Earth's magnetic field on various time scales, ranging from several millions of years to inter-annual changes. Projecting the observations through the mantle, inter-annual changes of the magnetic field on the core surface are accounted for by flows in the liquid outer core.

In our model we calculate Magneto-Coriolis modes of periods of several years. These fast Magneto-Coriolis modes show strong focusing of their kinetic and magnetic energy in the equatorial region, while maintaining a relatively large spatial structure along the azimuthal direction. Their properties agree with some observations and inferred core flows. We find additionally, in contrast to what has been assumed previously, that these modes are not affected significantly by magnetic diffusion. The new model opens a new way of inverting geomagnetic observations to the flow and magnetic field deep within the Earth's outer core.

Résumé

Le champ magnétique terrestre et le taux de rotation de la Terre varient sur des périodes de plusieurs années. Cette thèse a pour but de comprendre si et comment de tels changements peuvent être causés par des modes (ondes stationnaires) dans le noyau liquide et conducteur. Pour ce faire, un modèle de noyau planétaire en rotation rapide et électriquement conducteur est développé, capable de gérer des champs magnétiques complexes et une frontière non sphérique. Nous exploitons la rotation rapide pour simplifier notre modèle, en utilisant l'hypothèse dite quasi-géostrophique, où les composantes horizontales de la vitesse deviennent invariantes le long de l'axe de rotation. En dérivant un tel modèle dans une géométrie non axisymétrique, nous sommes en mesure d'étudier le couple de pression exercé sur la limite noyau-manteau par des modes, qui sont des solutions linéaires au modèle. Les modes d'Alfvén dits de torsion sont particulièrement intéressants, car ils consistent en des cylindres géostrophiques en rotation différentielle les uns par rapport aux autres, potentiellement porteurs d'un moment angulaire axial. Ces cylindres agissent contre la tension des lignes de champ magnétique radiales cisaillées, ce qui montre leur nature Alfvénique. Dans le noyau terrestre, on suppose qu'ils ont des périodes de quelques années et on les a corrélés aux changements de la longueur du jour.

Nos résultats suggèrent que le couple de pression associé à de tels modes de torsion Alfvén est inefficace pour expliquer les changements observés dans la longueur du jour terrestre sur des périodes d'environ 6 ans. Il s'avère que l'amplitude de la pression associée à ces modes devrait être indépendante de la vitesse de rotation, si le volume ne permet pas de prendre en compte les contours géostrophiques non fermés. Il convient d'étudier si le couple de pression peut être augmenté en considérant des géométries plus complexes que l'ellipsoïde, considéré ici. Sinon, les modes de torsion Alfvén dans le noyau doivent être couplés à une couche électriquement conductrice dans le manteau inférieur ou par couplage gravitationnel pour expliquer les changements observés dans la longueur du jour.

Dans une deuxième partie, nous avons étudié les modes de Magneto-Coriolis dans un modèle de noyau sphérique et homogène, où nous pouvons exprimer le champ magnétique de manière à pouvoir calculer les changements de champ magnétique à la surface du noyau. Sur Terre, les observations du champ géomagnétique à la surface révèlent des changements du champ magnétique à différentes échelles de temps, allant de plusieurs millions d'années à des changements interannuels. En projetant les observations à travers le manteau, les changements interannuels du champ magnétique à la surface du noyau sont interprétés comme le résultat d'une magnétohydrodynamique simple dans le noyau externe liquide.

Dans notre modèle, nous calculons les modes de Magneto-Coriolis de périodes de plusieurs années. Ces modes de Magneto-Coriolis rapides montrent une forte focalisation de leur énergie cinétique et magnétique dans la région équatoriale, tout en maintenant une structure spatiale relativement importante le long de la direction azimutale. Leurs propriétés concordent avec certaines propriétés des observations magnétiques et des mouvements à la surface du noyau récemment proposés. De plus, contrairement à ce qui a été supposé précédemment, nous constatons que ces modes ne sont pas affectés de manière significative par la diffusion magnétique. Le nouveau modèle ouvre une nouvelle façon d'inverser les observations géomagnétiques pour en déduire les mouvements et le champ magnétique dans les profondeurs du noyau externe de la Terre.

Acknowledgments

This thesis would not have been possible without the support I received the last three years.

First and foremost, I want to thank my supervisors Dominique Jault and Jérôme Noir, who carried me with their experience into the field of core fluid dynamics and had to endure uncountable questions. You always found time for discussions and helped me in times of inevitable despair, which has been greatly appreciated.

A big thanks to the members of my jury, Chris Finlay, Michel Rieutord, Yves Rogister and Chantal Staquet for evaluating, commenting on and discussing over my work. Especially Chris Finlay and Yves Rogister are to thank, being the main examiners (rapporteurs) of the thesis. I deeply regret that the circumstances at the time did not allow me to welcome everyone for the defense and thank you in person.

I would also like to thank all the members of the Geodynamo work group at ISTerre in Grenoble for welcoming me and including me into several, sometimes heated, discussions, coffee breaks and barbecues. It has been a pleasure to work among you.

For my stay at the Earth and Planetary Magnetism group at ETH in Zürich I would like to thank all the members for the good times, especially during the ski trips! Thanks to Andy Jackson for hosting me and the support I received, even past the end when I was unable to return to Grenoble due to the ongoing pandemic.

Thanks also to all the friends that I have made over the last years, who filled these years with good memories at the universities, in the bars and restaurants of the cities, and on top of rocks and mountains. It is not possible to list everyone, but I would like to mention Amber, Camille, Eirik, Isabelle, Jacques, Jeremie, Johannes, Jonathan, Line, Margot, Michael, Nathan and Sylvie from Grenoble. Adriaan, Andrea, Ben, Daria, Emily, Fabian, Jesper, Jiawen, Julien, Lars, Leo, Nele, Nicolo, Nienke, Paul, Patrick, Theo and Ziga from Zürich.

My deepest gratitude to my family and Nolwenn for your love and support.

Contents

List of Figures

Chapter 1

Introduction

1.1 Overview

Understanding the liquid flow within Earth's core remains one of the biggest challenges of geophysics. The dynamics that occur in planetary core flows are rich, small scale turbulence that connects to large scale vortices, plumes caused by convection, zonal jets, stratified layers and waves, just to name a few. How these dynamics connect to observations is most evident for the generation of a magnetic field within the Earth's core, often referred to as the geodynamo problem. It is known now that Earth's magnetic field (and that of many other celestial bodies) is generated within the convecting liquid core, linking geomagnetic field observations at the Earth's surface to the flows in the core. A detailed view into the evolution of Earth's magnetic field has been made possible through a drastic increase of coverage, in both spatial and temporal space, by recent satellite observations (Olsen and Stolle, 2012). From these observations time dependent global geomagnetic field models are produced (e.g. a recent model by Finlay et al., 2020). Then, assuming that the mantle is almost insulating, these magnetic field models can be projected to the core-mantle boundary (CMB) by potential field theory (e.g. Courtillot et al., 1978; Whaler and Gubbins, 1981), resulting in time dependent maps of the radial magnetic field at the CMB. These changes in the radial magnetic field are assumed to be caused by motions in the liquid core. No unique flow is able to explain the observations and prior assumptions on the flow in the core are needed, when inferring flows from the magnetic field observations (Backus, 1968). This non-uniqueness is reduced by prior kinematic assumptions. For example, when the flow is dominated by a balance between the rotational and pressure forces, known as a geostrophic balance, it aligns in columns invariant along the rotation axis (Proudman, 1916; Taylor, 1917). Assuming this balance is satisfied in a region close to the CMB has allowed the inference of surface flow fields from the geomagnetic field maps (Le Mouël et al., 1985; Gire and Le Mouël, 1990). Numerical simulations and laboratory experiments of fluids under rapid rotation also revealed that this invariance along the rotation axis is largely present throughout the bulk of a liquid planetary core model, even when permeated by a magnetic field (Nataf et al., 2008; Gillet et al., 2011; Schaeffer et al., 2017; Guervilly et al., 2019).

Therefore, simplifying the problem at hand by assuming a dominant geostrophic balance seems reasonable. Models that consider perturbations to this balance are called quasi-geostrophic models. They have been successful in capturing convective and turbulent motions (Guervilly et al., 2019; Gastine, 2019), as well as linear dynamics (Labbé et al., 2015; Maffei et al., 2017), within a planetary core.

In this thesis we focus on such linear dynamics, more specifically on modes, in the fluid core. Modes are standing waves bounded by a finite domain, here the finite volume of the liquid core. A toy example of a mode, often presented to physics students, is the guitar string that oscillates as a standing wave when played. It is fixed at both ends of the string, and oscillates against the restoring force of the tension of the string. Similarly, wave motions in a fluid occur when a fluid parcel is perturbed from an equilibrium state and a restoring force acts, resulting in an oscillatory motion. Depending on the relevant parameters, e.g. the rotation rate or magnetic field strength, different forces can act as a restoring force for fluid modes in a planetary core. Examples of modes include: (i) hydrodynamic inertial modes, that result from a balance of inertia and Coriolis forces (e.g Greenspan, 1968); (ii) Magneto-Coriolis modes, dominated by a balance between Coriolis and Lorentz forces counteracting inertia (Lehnert, 1954; Malkus, 1967); (iii) torsional Alfvén modes, where inertia is balanced by the Lorentz force with differentially rotating cylinders shearing a radial magnetic field (Braginsky, 1970). Particular emphasis is given to quasi-geostrophic Magneto-Coriolis modes and torsional Alfvén modes. Magneto-Coriolis modes have long been proposed as a possible source of geomagnetic field changes on periods of a few centuries to a few decades (Hide, 1966). The retrograde (westward in the Earth's context) phase velocity of the largest scale Magneto-Coriolis modes seems to be in good agreement with some of the westward motion of the changes in Earth's magnetic field (e.g. Finlay and Jackson, 2003). It has been suggested that geophysically relevant modes with smaller periods, i.e. a few years, can only exist within a stratified layer at the top of the core (Buffett, 2014; Buffett and Matsui, 2019) or for strong toroidal background magnetic fields (Hori et al., 2015). Another possible explanation for inter-annual geomagnetic field changes are quasi-geostrophic Alfvén waves observed in numerical simulations, that travel along an uprising plume within the convecting outer core (Aubert and Finlay, 2019). To understand if quasi-geostrophic modes at these periods are able to explain inter-annual geomagnetic field changes is one of the objectives of this thesis.

Another connection between the flow in the core and observations on the Earth's surface are the changes of Earth's rotational parameters. These include changes in the length-of-day (LOD) and changes of the orientation of the rotation axis (Dehant et al., 2017). Although most changes in the LOD of Earth are accounted for by the effects of tidal forces, atmospheric and ocean dynamics, some variations on periods of a few years to decades remain unexplained and have long been attributed to dynamics in the core (Munk and MacDonald, 1960; Hide, 1966; Jault et al., 1988). As such, torsional Alfvén waves with periods similar to the 6 yr oscillation in the LOD have been proposed as a possible source of these LOD changes (Gillet et al., 2010). Having identified torsional Alfvén waves as a possible flow feature that evolves on periods of a few years, the key challenge remains to explain the transfer of angular momentum between the core and the solid mantle. Several coupling mechanisms, namely viscous, gravitational, electromagnetic and topographic coupling, have been conjectured and besides the viscous coupling no conclusive evidence exists to reject either of these mechanisms (e.g. Bullard et al., 1950; Hide, 1969; Hide and Weightman, 1977; Jault and Mouël, 1991; Roberts and Aurnou, 2012). In this work, emphasis is given to the mechanism of topographic coupling through a deformed CMB. In case the core is not a perfect sphere, a hypothesis justified by geodynamic and seismic evidence (see details in Section 1.2.4), a pressure torque from the flow in the liquid core can be exerted onto the solid mantle, changing its angular momentum (Hide, 1969). This non-axisymmetric boundary has to be incorporated into a model to investigate topographic coupling of modes in the core with the mantle. So far, the study of torsional Alfvén modes has been limited to axisymmetric volumes (with the exception of some idealized cases Vidal et al., 2016). The major objective of this thesis is the modeling of torsional Alfvén modes in a non-axisymmetric domain to study the pressure torque exerted onto the CMB.

The thesis is structured as follows. The basic properties of Earth's core and the equations governing the flow within are laid out in the following sections. Different approaches to the derivation of quasi-geostrophic models are given in Chapter 2. Modes within a planetary core are introduced in Chapter 3. These chapters give the background and methods applied in Chapter 4 and 5. In Chapter 4 we investigate torsional Alfvén modes in a rotating ellipsoid and the associated pressure torque exerted onto the CMB. Quasi-geostrophic Magneto-Coriolis modes on periods of a few years and their magnetic field perturbations are studied in Chapter 5. The last chapter gives a summary of the findings and a discussion of open questions.

1.2 Earth's core

1.2.1 Earth's interior structure

The Earth interior structure is mostly determined through seismological observations. The first quantitative model of the Earth's interior was proposed by Wiechert (1897) leading to a large interest in seismological modeling of Earth's deep interior. From these seismological models a layered structure of Earth's interior can be inferred, with a thin crust at the surface that lies above a silicate mantle. The presence of an iron core below the mantle was first shown by Oldham (1906) and 30 years later Lehmann (1936) was the first to separate the iron core into a liquid outer core and a solid inner core. A schematic of the Earth interior, displaying the crust, mantle, outer core and inner core is shown in Figure 1.1 (left), where the layer depths are shown to

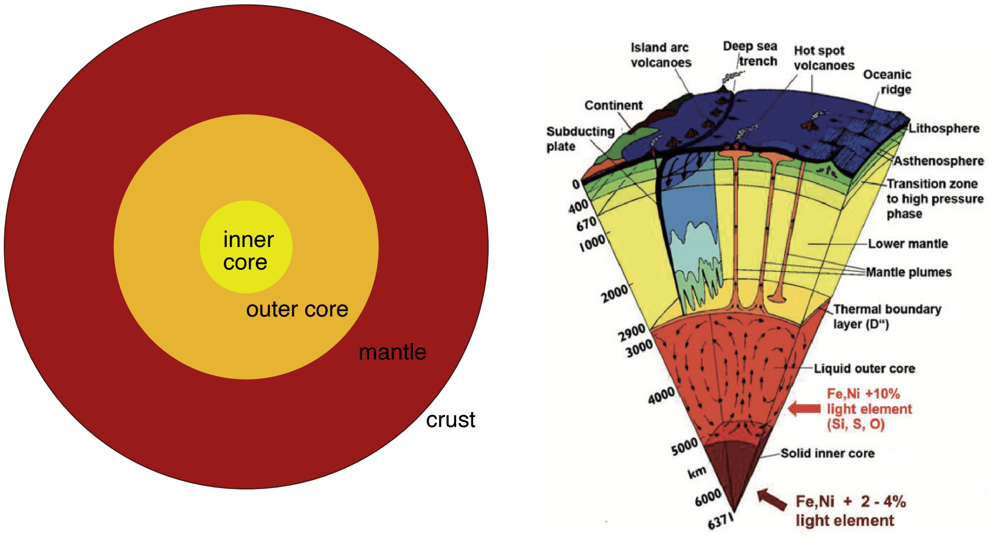

Figure 1.1: Schematic of Earth's interior structure to scale, with a very thin crust surrounding the mantle, a liquid outer core and a solid inner core (left). Sketch of dynamics within the mantle and core not to scale (right), from Davidson (2013). Reproduced with permission of Cambridge University Press.

scale and correspond to the values of the Preliminary Earth Model (Dziewonski and Anderson, 1981). This interior model is idealized, assuming radial symmetry and homogeneous layers. Some of the dynamics that occur are illustrated in Figure 1.1 (right). The mean radius of the Earth is $R_\oplus = 6370\,\mathrm{km}$. At the surface the relatively small crust extends to a depth of up to only around 70 km. The largest volume and mass is taken by the silicate mantle, extending down to a depth of 2890 km. The mantle encloses the core of radius $R_c = 3480\,\mathrm{km}$, with the solid inner core of radius $R_i = 1220\,\mathrm{km}$ within.

1.2.2 Properties of the liquid outer core

The liquid outer core predominantly consists of an iron-nickel alloy, with about 10% of lighter elements like oxygen, sulfur and silicon (e.g McDonough, 2003). The density of the outer core is about 1.09×10^4 kg m^{-2} (e.g. Olson, 2015), making it about twice as dense as the overlaying mantle. This gives it a total moment of inertia of $I_c = 9.14 \times 10^{36}\,\mathrm{kg\,m^2}$ (Gross, 2015). Since Earth rotates around its axis at rate of $7.27 \times 10^{-5}\,\mathrm{rad\,s^{-1}}$, the core's angular momentum is $L_c = 6.64 \times 10^{32}\,\mathrm{kg\,m^2\,s^{-1}}$. The pressure in the outer core is $\mathcal{O}\left(10^{11}\right)$ Pa and temperatures reach up to $4700 \pm 500\,\mathrm{K}$ (Olson, 2015). The kinematic viscosity of the fluid outer core is estimated to be $\mathcal{O}\left(10^{-6}\right)\,\mathrm{m^2\,s^{-1}}$ (Wijs et al., 1998). Since the core mostly consists of iron its electrical conductivity is large, even at the given pressure and temperature conditions. It has a value of approximately $1.55 \times 10^6\,\mathrm{Sm^{-1}}$ inferred from density functional theory calculations (Pozzo et al., 2014).

Below the CMB and just above the inner core it has been suggested that stably stratified layers could be present, possibly having a large influence on waves within the core (e.g. Braginsky, 1993). However, these layers remain a challenge to be resolved by seismological observations (see Hardy and Wong, 2019, and references therein).

1.2.3 Geodynamo and convection in the outer core

The effects in a conducting fluid to constructively generate magnetic energy, leading to a self-sustained magnetic field, is known as dynamo theory. Originally put forward by Larmor (1919) and Elsasser (1946), dynamo theory now encompasses a large literature (e.g. textbooks by Moffatt, 1978; Roberts, 2015). Through the constructive twisting and shearing of magnetic field lines by fluid motions, a large scale magnetic field can be generated. Going into the details of dynamo theory is beyond the scope of this thesis and we refer the interested reader to a recent textbook by Moffatt and Dormy (2019) which gives an adequate introduction and review of the topic.

Without explaining the theory of dynamo action we can discuss a source of energy input that is needed to drive it. Due to a slow overturning of the mantle, heat can be transported efficiently out from the core (Schubert et al., 2001). This cooling is essential for thermal convection in the liquid outer core (convective motion in the core illustrated in Figure 1.1, right). However, thermal convection alone is insufficient to drive dynamo action in Earth's core (Fearn and Loper, 1981; Pozzo et al., 2012). Compositional convection, through the release of light elements by inner core nucleation (Verhoogen, 1961), is today the widely accepted driver of the current Earth's magnetic field generation (see Jones, 2015, for a detailed review). High resolution convective geodynamo simulations have shown remarkable resemblance to Earth's magnetic field, despite operating at physical parameters different to those relevant for the Earth (Glatzmaiers and Roberts, 1995; Jones, 2000; Schaeffer et al., 2017).

Compositional convection relies on the presence of an inner core. However, the age of the solid inner core is still very much under debate, with estimates ranging between 700 Myr to 1.5 Gyr (Pozzo et al., 2012; Biggin et al., 2015; Labrosse, 2015). Evidence from palaeomagnetic samples suggests that the magnetic field has been operating for about 3.4 Gyr (Tarduno et al., 2010). More recent work has even suggested that the geodynamo has been operating for as long as 4.2 Gyr, only a few hundred million years after Earth's formation and the moon forming giant impact (Tarduno et al., 2020). Another source of driving convection or turbulent motion in the liquid core prior to inner core nucleation is thus needed. Chemical convection through precipitation of light elements (especially Magnesium) from the mantle into the outer core has been suggested as a possible driver of convection (O'Rourke and Stevenson, 2016; Badro et al., 2018). Another proposed driver of dynamo action are turbulent motions triggered by orbital forcing (Malkus, 1968; Kerswell, 1996; Reddy et al., 2018), although it is unclear if it could have been efficient enough for the early geodynamo.

1.2.4 Core-mantle boundary topography

The CMB is likely not a perfect sphere. The overturning of the mantle causes uprising of lighter and hot material and downwelling of heavier and colder material near the CMB (see Bercovici, 2015, for a broad introduction to mantle dynamics). These uprising plumes and downwellings are assumed to pull and push on the CMB, leading to its deformation (Hager et al., 1985; Forte and Peltier, 1989; Forte et al., 1995). Seismic tomography maps of the CMB are able to resolve deflections of the CMB on lateral spatial scales of thousands of kilometers. These studies suggest that a peak-to-peak amplitude of the CMB topography can reach up to 3 km (Sze and van der Hilst, 2003; Koper et al., 2003). These figures of the topography amplitude seem to agree with recent geodynamic simulations of smaller length scale topography (Heyn et al., 2020). Whether these smaller length scales can be observed seismologically is an open question (Mancinelli and Shearer, 2016).

The large scale polar flattening of the CMB, caused by the rotation and tidal torques, has been estimated in terms of an ellipticity of 2.65×10^{-3}, corresponding to a difference of about 9 km between polar and equatorial radius (Mathews et al., 2002). It is constrained by the influence of the so-called free core nutation (FCN) mode on the solid Earth's nutation, a latitudinal wobble of the rotation axis (see also Dehant and Mathews, 2013). This polar flattening is certainly relevant for the nutation of Earth, but has no relevant influence on the axial topographic torque that is of interest here.

1.3 The equations governing flows in planetary cores

In this section a synopsis of the basic equations of a rotating, incompressible and conducting fluid is given. Most of the hydrodynamic equations are found in textbooks (e.g Greenspan, 1968). For more detailed derivations of the hydrodynamic equations we refer the reader to Zhang and Liao (2017). The basics on the magneto-hydrodynamic (MHD) equations can be found in Roberts (1967) and Backus et al. (1996).

1.3.1 Fluid description in the rotating frame

The evolution of a fluid at a position $\mathbf{r}$ with a velocity $\mathbf{u} = \partial\mathbf{r}/\partial t$ and density ρ is described by the conservation of momentum $\rho\mathbf{u}$ through the momentum equation and the conservation of mass through the continuity equation. For an incompressible fluid the continuity equation reduces to

$$\boldsymbol{\nabla} \cdot \mathbf{u} = 0. \tag{1.1}$$

In the non-rotating frame the momentum equation is

$$\frac{d\mathbf{u}}{dt} = -\frac{1}{\rho}\nabla P + \nu \boldsymbol{\nabla}^2 \mathbf{u} + \mathbf{F}, \tag{1.2}$$

with $d\mathbf{u}/dt = \partial\mathbf{u}/\partial t + (\mathbf{u}\cdot\boldsymbol{\nabla})\,\mathbf{u}$ the material derivative, P the hydrodynamic pressure, ν the kinematic viscosity and $\mathbf{F}$ a body force, e.g. the Lorentz force $\mathbf{F}_L$ or buoyancy force $\mathbf{F}_B$. In the frame rotating constantly around an axis $\boldsymbol{\Omega}$ the material derivative is

$$\left(\frac{d\mathbf{u}}{dt}\right)_{\Omega} = \frac{\partial\mathbf{u}}{\partial t} + (\mathbf{u}\cdot\boldsymbol{\nabla})\,\mathbf{u} + \boldsymbol{\Omega}\times(\boldsymbol{\Omega}\times\mathbf{r}) + 2\boldsymbol{\Omega}\times\mathbf{u}, \tag{1.3}$$

where the last two terms are the apparent forces arising from the change of reference frame. They correspond to the centrifugal acceleration and the Coriolis force, respectively. The centrifugal acceleration is a conservative force and can be combined with the hydrodynamic pressure into the so-called reduced pressure

$$p = P - \frac{\rho}{2}(\boldsymbol{\Omega}\times\mathbf{r})\cdot(\boldsymbol{\Omega}\times\mathbf{r}), \tag{1.4}$$

so that the momentum equation in the rotating frame of reference is given by

$$\frac{\partial\mathbf{u}}{\partial t} + (\mathbf{u}\cdot\boldsymbol{\nabla})\,\mathbf{u} + 2\boldsymbol{\Omega}\times\mathbf{u} = -\frac{1}{\rho}\nabla p + \nu\,\boldsymbol{\nabla}^2\mathbf{u} + \mathbf{F}. \tag{1.5}$$

To include buoyancy in the incompressible limit the Boussinesq approximation can be applied, where density anomalies are due to thermal fluctuations and only significant if they are multiplied by the gravitational acceleration (Spiegel and Veronis, 1960). This approximation is almost universally used in modern convective geodynamo simulations (Jones, 2015). The governing equations are then supplemented by the heat equation. Since it is not the goal of this work to investigate topics related to convection or stratification, buoyancy is not considered in our models.

Geostrophic motions

Consider a very large rotation frequency, a very small viscosity and time scales that are much larger than the rotation period. When no additional forces $\mathbf{F}$ in (1.5) are taken into account, the flow reduces to a balance between Coriolis force and pressure force

$$2\rho\,\boldsymbol{\Omega}\times\mathbf{u} = -\nabla p, \tag{1.6}$$

known as the geostrophic balance. By taking the curl of this balance, we find the well-known Proudman-Taylor theorem (Proudman, 1916; Taylor, 1917)

$$(\boldsymbol{\Omega}\cdot\boldsymbol{\nabla})\,\mathbf{u} = \frac{\partial\mathbf{u}}{\partial z} = \mathbf{0}. \tag{1.7}$$

In a finite fluid volume the motion is columnar along the rotation axis, and if the volume is additionally symmetric about an equatorial plane, the motion is purely horizontal. This balance is often assumed to be dominant in atmospheres and planetary core fluids, allowing for significant simplification of the system. Slight perturbations to such a geostrophic balance are called quasi-geostrophic motions. The theory of models for such quasi-geostrophic motions in planetary cores is discussed in Chapter 2.

1.3.2 Magnetohydrodynamic equations

When considering a conducting liquid it is necessary to take electromagnetic effects into account. The force on a charge moving in the divergence-free magnetic field **B** is known as the Lorentz force

$$\mathbf{F}_L = \mu_0^{-1}(\boldsymbol{\nabla} \times \mathbf{B}) \times \mathbf{B}, \tag{1.8}$$

with μ_0 the magnetic permeability in vacuum. It is included in the momentum equation (1.5).
In a moving conductor Ohm's law reads

$$\mathbf{j} = \sigma\left(\mathbf{E} + \mathbf{u} \times \mathbf{B}\right), \tag{1.9}$$

with $\mathbf{j} = \mu_0^{-1}\boldsymbol{\nabla} \times \mathbf{B}$ the current density and σ the electrical conductivity. Combined with Faraday's law of induction

$$\frac{\partial \mathbf{B}}{\partial t} = -\boldsymbol{\nabla} \times \mathbf{E}, \tag{1.10}$$

gives the well-known induction equation

$$\frac{\partial \mathbf{B}}{\partial t} = \boldsymbol{\nabla} \times (\mathbf{u} \times \mathbf{B}) + \eta\, \boldsymbol{\nabla}^2 \mathbf{B}, \tag{1.11}$$

with $\eta = (\mu_0 \sigma)^{-1}$ the magnetic diffusivity.
The equations to describe the fluid and magnetic field evolution in a rotating planetary core are thus

$$\frac{\partial \mathbf{u}}{\partial t} + (\mathbf{u} \cdot \boldsymbol{\nabla})\, \mathbf{u} + 2\,\boldsymbol{\Omega} \times \mathbf{u} = -\frac{1}{\rho}\nabla p + \nu\, \boldsymbol{\nabla}^2 \mathbf{u} + \frac{1}{\mu_0 \rho}\left(\boldsymbol{\nabla} \times \mathbf{B}\right) \times \mathbf{B}, \tag{1.12a}$$

$$\frac{\partial \mathbf{B}}{\partial t} = \boldsymbol{\nabla} \times (\mathbf{u} \times \mathbf{B}) + \eta\, \boldsymbol{\nabla}^2 \mathbf{B} \tag{1.12b}$$

$$\boldsymbol{\nabla} \cdot \mathbf{u} = \boldsymbol{\nabla} \cdot \mathbf{B} = 0. \tag{1.12c}$$

Since the fluid is bounded to a volume $\mathcal{V}$ of finite size, boundary conditions are needed. For the velocity these boundary conditions depend on whether or not the viscous or inviscid case is considered. In the latter case the fluid is subject to the non-penetrating boundary condition

$$\mathbf{u} \cdot \mathbf{n} = 0 \quad \text{at}\, \partial\mathcal{V}, \tag{1.13}$$

where $\mathbf{n}$ is the vector normal to the boundary $\partial\mathcal{V}$. In the viscous case, the fluid must move with the boundary, i.e. it can not slip, so that $\mathbf{u}\times\mathbf{n} = \mathbf{0}$. Together with (1.13), which also must be satisfied, it follows that $\mathbf{u} = \mathbf{0}$ at $\partial\mathcal{V}$.
For the magnetic field, generally, the boundary conditions are (Jones, 2008)

$$[\mathbf{B}\cdot\mathbf{n}] = 0, \tag{1.14a}$$
$$[\mathbf{B}\times\mathbf{n}] = \mu_0\mathbf{j}_S, \tag{1.14b}$$

where $[\cdot]$ denotes a jump across the boundary, and $\mathbf{j}_S$ are surface currents. If the outside region is a perfect conductor, the electrical currents are expelled from the conductor and are located at its surface only. Then, the boundary condition reduces to

$$\mathbf{B}\cdot\mathbf{n} = 0 \quad \text{at } \partial\mathcal{V}. \tag{1.15}$$

In case the outside region is not a perfect conductor, the boundary condition simplifies to

$$[\mathbf{B}] = 0. \tag{1.16a}$$

This is further restricted if the outside region is perfectly insulating. Then the magnetic field in the exterior must take the form

$$\mathbf{B} = \nabla\Phi, \tag{1.17}$$

with Φ a scalar potential that vanishes at a distance infinitely far away from the boundary.

1.3.3 Dimensional analysis

A powerful tool used in many fluid mechanics problem is the non-dimensionalization of the governing equations. Dimensional analysis aims to give insight in the dominant forces of the equations by estimating their relative importance. The idea is that all physical quantities in the system, scalar and vectorial, can be divided into their mean characteristic amplitude, that is constant in time and space, and a variable part. Usually, one defines a characteristic time T and a characteristic length scale L. In the context of Earth's core these could be for example the rotation period and radius of Earth's core, respectively. As a consequence the time derivative and differential operator are $\partial_t = T^{-1}\hat{\partial}_t$ and $\nabla = L^{-1}\hat{\nabla}$, respectively. For example, the acceleration is written as $\partial_t\mathbf{u} = UT^{-1}\hat{\partial}_t\hat{\mathbf{u}}$, with $U = LT^{-1}$ the scalar characteristic velocity and $\hat{\mathbf{u}}$ the non-dimensional velocity. For readability the hat annotation is omitted in the remainder of this document and whether or not the quantity is dimensional or non-dimensional should be identifiable in the respective context.
In this way the characteristic amplitude ratio between different forces or time scales can be calculated. These ratios are non-dimensional by definition and usually named

after their discoverers. The ratio of the non-linear term to the Coriolis force defines the Rossby number

$$\mathrm{Ro} = \frac{U}{L\Omega}, \tag{1.18}$$

with $\Omega = |\boldsymbol{\Omega}| = T_\Omega^{-1}$ the angular frequency. In Earth's core, it is estimated to be $\mathcal{O}\left(10^{-6}\right)$, with $L = R_c$ and the convective velocity $U = 5 \times 10^{-4}$ ms^{-1} (Jones, 2015). Another ratio is the Ekman number

$$\mathrm{Ek} = \frac{\nu}{\Omega L^2}, \tag{1.19}$$

comparing viscous diffusion to Coriolis force (Ekman, 1905). It is estimated to be as low as $\mathcal{O}\left(10^{-15}\right)$ for for Earth's core parameters (see Section 1.2.2).

In the MHD case the velocity of an Alfvén wave, $U_A = B_0(\mu_0\rho)^{-1/2}$, with B_0 the characteristic magnetic field strength, can be considered. Alfvén waves are solutions to the linearized and non-rotating MHD equations (Alfvén, 1942). Their periods, referred to as Alfvén time, is thus $T_A = LU_A^{-1}$. The Lehnert number compares the rotation time to the Alfvén time

$$\mathrm{Le} = \frac{B_0}{\sqrt{\rho\mu_0}L\Omega}, \tag{1.20}$$

to estimate the relative importance of Coriolis force to the non-rotating linear MHD system (Lehnert, 1954). It is estimated to be $\mathcal{O}\left(10^{-4}\right)$ in Earth's core with $B_0 = 3\,\mathrm{mT}$ in the core (Gillet et al., 2010). Although Le is not as popularly used in the geodynamo literature, it has been shown to be the appropriate estimate for comparing the strength of Coriolis and Lorentz forces at time scales much shorter than the magnetic diffusion time (Jault, 2008).

The magnetic Prandtl number

$$\mathrm{Pm} = \frac{\nu}{\eta}, \tag{1.21}$$

compares the magnetic diffusion time to the viscous diffusion time. Its value is $\mathcal{O}\left(10^{-6}\right)$ in Earth's core, for the before-mentioned parameter estimates.

The Lundquist number

$$\mathrm{Lu} = \frac{B_0 L}{\eta\sqrt{\mu_0\rho}}, \tag{1.22}$$

compares the magnetic diffusion time to the Alfvén time (Lundquist, 1949). It is estimated to be $\mathcal{O}\left(10^{5}\right)$ in Earth's core, meaning that magnetic diffusion occurs on much longer periods than the time scales associated with Alfvén waves.

We can express the MHD equations in their non-dimensional form. There are several ways, but since we are interested in analyzing dynamics that occur on times much slower than the rotation period and faster than the magnetic diffusion time, we choose our characteristic time to be the Alfvén time. The characteristic length scale is the core radius R_c, so that the characteristic velocity is given by the Alfvén velocity $u_A = R_c T_A^{-1}$. The non-dimensionalized form of (1.12) is then

$$\frac{\partial \mathbf{u}}{\partial t} + (\mathbf{u} \cdot \boldsymbol{\nabla})\, \mathbf{u} + \frac{2}{\mathrm{Le}}\, \mathbf{1}_\Omega \times \mathbf{u} = -\, \nabla p + \frac{\mathrm{Pm}}{\mathrm{Lu}}\, \boldsymbol{\nabla}^2 \mathbf{u} + (\boldsymbol{\nabla} \times \mathbf{B}) \times \mathbf{B}, \tag{1.23a}$$

$$\frac{\partial \mathbf{B}}{\partial t} = \boldsymbol{\nabla} \times (\mathbf{u} \times \mathbf{B}) + \frac{1}{\mathrm{Lu}}\, \boldsymbol{\nabla}^2 \mathbf{B}, \tag{1.23b}$$

$$\boldsymbol{\nabla} \cdot \mathbf{u} = 0. \tag{1.23c}$$

With $\mathrm{Pm}/\mathrm{Lu} = 10^{-11}$ and $\mathrm{Lu}^{-1} = 10^{-5}$ viscous dissipation and magnetic diffusion can be neglected in the bulk of Earth's core at time scales close to T_A. We use this assumption in most of the subsequent discussions and results. The influence of diffusion on modes at periods close to the Alfvén time is discussed in Section 5.2.

1.3.4 Reduced models in planetary fluid dynamics

Solving the set of non-linear partial differential equations (1.12) is challenging, both from a mathematical and computational view. For Earth's core parameters the direct numerical simulation (DNS) is not possible even on the most powerful supercomputers to date. As a consequence, several different strategies have been applied.

An obvious step is a change of parameters to make numerical calculations feasible. It has been suggested (e.g. by Christensen et al., 2010) that one can extrapolate results at the computationally feasible parameter regime to Earth-like parameters, but this is still under debate (e.g. Cheng and Aurnou, 2016).

Many DNS are combined with the introduction of hyperdiffusivity, where an artificial damping is applied. A variation of this are so-called large eddy simulations (LES), that uses hyperdiffusivity at the smallest scales to suppress small scale turbulence (Nataf and Schaeffer, 2015), which is costly to resolve. They have shown some promising results in capturing fast dynamics in a planetary core (Aubert et al., 2017; Aubert and Finlay, 2019). Most notably, hyperdiffusive models or LES do not simplify the mathematical problem at hand.

Through scale analysis, so-called asymptotic models try to approximate the full model up to a certain degree of a small parameter expansion (Calkins et al., 2015; Calkins, 2018). At leading order of the small parameter, that is the ratio of convective length-scale to the container height, these models find a geostrophic balance and therefore carry the name quasi-geostrophic (QG) models. The columnar structure that follows by this balance is exploited to reduce the model to two dimensions. First results seem promising, but so far these asymptotic models are limited to Cartesian periodic boxes and the way to a spherical domain is unclear (Plumley et al., 2018).

QG models have initially developed in the atmospheric community for the study of thin layers under rapid rotation (Charney, 1948), their fundamental assumption is a geostrophic balance at leading order. QG models, that assume this balance a-priori, unlike the asymptotic models, have been previously embraced by many other studies of planetary core dynamics (e.g. Busse, 1970; Pais and Jault, 2008; Canet et al.,

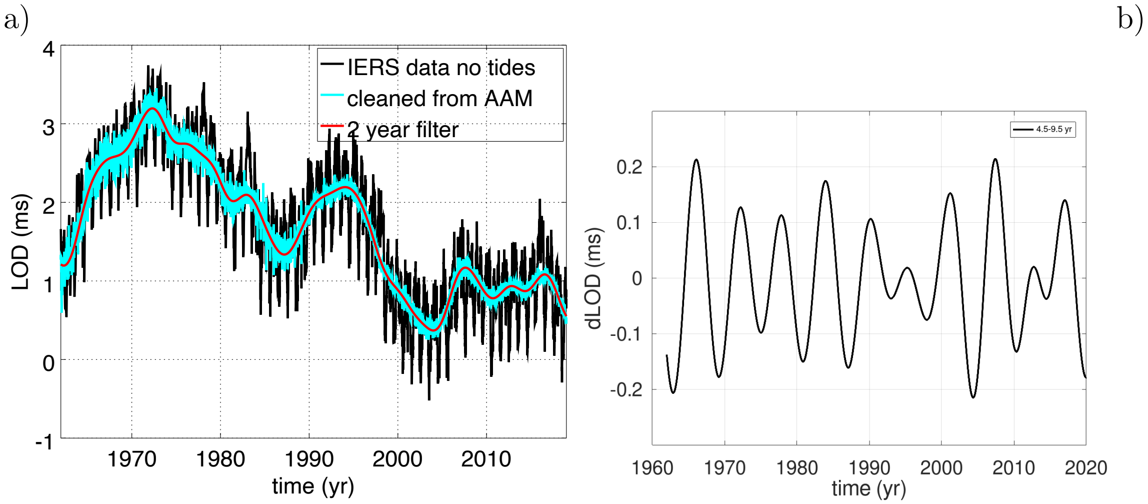

Figure 1.2: a) Observed LOD variations, the signal cleaned from variations by ocean dynamics (AAM) and the cleaned signal with a 2 year low pass filter. b) LOD variations filtered between 4.5 and 9.5 years. Courtesy of Nicolas Gillet.

2014). Chapter 2 gives a detailed introduction to the derivation of QG models from various approaches.

1.4 Length-of-day variations and core-mantle interactions

1.4.1 Observed length-of-day variations

The length-of-day (LOD) on Earth is approximately 86400 s long and variations to it are on the order of a few milliseconds (Stephenson et al., 1995). Earth's rotation measurements in the past mostly consisted of lunar occultations (Stephenson et al., 2016). Today it is measured by continuous observations of the night sky through Very-Long-Baseline-Interferometry and other advanced methods (see Gross, 2015, for a review on measurements). The observed variations show millennial trends at the longest periods, but also decadal, annual and even sub-diurnal periods (Stephenson et al., 2016). The millennial linear trend corresponds to tidal friction (or tidal dissipation) of the Earth-moon system, gradually slowing Earth's rotation, and a relatively small contribution is thought to be accounted to the post-glacial rebound of Earth, loosing its oblateness and thus accelerating its rotation (Stephenson et al., 2016). Other variations of periods around 1500 yr are accounted to coupling between the core and the mantle, but the relevant core dynamics are speculative (Stephenson et al., 1995; Dumberry and Bloxham, 2006).
At shorter time scales annual and seasonal variations are superimposed with interannual trends, as shown as the black line in Figure 1.2a. In this Figure the inter-

annual trend is obtained by subtracting the modeled LOD variations of an oceanic and atmospheric loading model from the observed LOD variations (e.g. Gross et al., 2003; Holme and de Viron, 2005). Furthermore, an oscillation with a period around 6 yr and amplitude of 0.1–0.2 ms is found when analyzing the corrected signal (Vondrak, 1977; Abarca del Rio et al., 2000; Holme and de Viron, 2013; Gillet et al., 2015). An example of the 6 yr oscillation in the LOD variation time series is shown in Figure 1.2b. Such a change in the rotation rate corresponds to a change in angular momentum $\mathcal{O}\left(10^{16}\right)$ Nm. Although atmospheric contributions to inter-annual frequencies are possible and not fully understood (e.g. Yu et al., 2020), it is generally assumed that the 6 yr oscillation originates from dynamics in the core that are coupled to the mantle. Some studies have proposed that these changes in the LOD are correlated with geomagnetic jerks, fast changes in the variations of the magnetic field (Holme and de Viron, 2005, 2013; Duan and Huang, 2020a). This suggests that both the geomagnetic field observations and the changes in LOD are caused by dynamics in the fluid outer core. Gillet et al. (2010) showed that torsional Alfvén modes in the outer core could be responsible for the angular momentum transport. How these dynamics may couple to the solid mantle is reviewed in the following subsections.

1.4.2 Torque balance

Without influences from the exterior, the angular momentum of the core-mantle system $\mathbf{L}_{\text{tot}}$ must be conserved, so that

$$\frac{d\mathbf{L}_{\text{tot}}}{dt} = \frac{d\mathbf{L}}{dt} + \frac{d\mathbf{L}_m}{dt} = \mathbf{0}, \tag{1.24}$$

with $\mathbf{L}$ and $\mathbf{L}_m$ the angular momentum of the core and the rigid mantle, respectively. The core angular momentum may be further divided into that of the inner core and the outer core, but since the moment of inertia of the inner core is less than 1% that of the outer core, we neglect this separation. Assuming a rigid mantle and no variation in the orientation of the rotation axis, changes in $\mathbf{L}_m$ are tied directly to the net torque balance in the outer core

$$\frac{\partial \mathbf{L}}{\partial t} = -\mathbf{\Gamma}_{\text{c}} - \mathbf{\Gamma}_{\Omega} + \mathbf{\Gamma}_{\text{p}} + \mathbf{\Gamma}_{\nu} + \mathbf{\Gamma}_{\text{L}} + \mathbf{\Gamma}_{\text{g}}, \tag{1.25}$$

with

$$\frac{\partial \mathbf{L}}{\partial t} = \rho \int_{\mathcal{V}} \mathbf{r} \times \frac{\partial \mathbf{u}}{\partial t} \, \mathrm{d}V, \tag{1.26a}$$

$$\mathbf{\Gamma}_{\mathrm{c}} = 2\rho \int_{\mathcal{V}} \mathbf{r} \times (\mathbf{\Omega} \times \mathbf{u}) \, \mathrm{d}V, \tag{1.26b}$$

$$\mathbf{\Gamma}_{\Omega} = \rho \int_{\mathcal{V}} \mathbf{r} \times \left(\frac{\partial \Omega}{\partial t} \mathbf{1}_{\Omega} \times \mathbf{r} \right) \, \mathrm{d}V, \tag{1.26c}$$

$$\mathbf{\Gamma}_{\mathrm{p}} = -\int_{\mathcal{V}} \mathbf{r} \times \nabla p \, \mathrm{d}V = -\int_{\partial \mathcal{V}} p \, (\mathbf{r} \times \mathbf{n}) \, \mathrm{d}S, \tag{1.26d}$$

$$\mathbf{\Gamma}_{\nu} = \nu\rho \int_{\mathcal{V}} \mathbf{r} \times \boldsymbol{\nabla}^2 \mathbf{u} \, \mathrm{d}V, \tag{1.26e}$$

$$\mathbf{\Gamma}_{\mathrm{L}} = \frac{1}{\mu_0} \int_{\mathcal{V}} \mathbf{r} \times ((\boldsymbol{\nabla} \times \mathbf{B}) \times \mathbf{B}) \, \mathrm{d}V, \tag{1.26f}$$

$$\mathbf{\Gamma}_{\mathrm{g}} = \int_{\mathcal{V}} \mathbf{r} \times \mathbf{F}_B \, \mathrm{d}V. \tag{1.26g}$$

The individual contributions correspond to the Coriolis torque $\mathbf{\Gamma}_{\mathrm{c}}$, the Poincaré torque $\mathbf{\Gamma}_{\Omega}$, the hydrodynamic pressure torque $\mathbf{\Gamma}_{\mathrm{p}}$, the viscous torque $\mathbf{\Gamma}_{\nu}$, the Lorentz torque $\mathbf{\Gamma}_{\mathrm{L}}$ and the gravitational torque $\mathbf{\Gamma}_{\mathrm{g}}$. The latter arises from a possible buoyancy force $\mathbf{F}_B$. In (1.25) we have neglected the contribution of the non-linear term in the momentum equation, as it vanishes exactly for the non-penetrating boundary. The Lorentz torque can be split into the magnetic pressure torque $\mathbf{\Gamma}_{\mathrm{pm}}$ and a magnetic tension torque $\mathbf{\Gamma}_{\mathrm{b}}$, so that

$$\mathbf{\Gamma}_{\mathrm{L}} = \mathbf{\Gamma}_{\mathrm{pm}} + \mathbf{\Gamma}_{\mathrm{b}}, \tag{1.27}$$

with

$$\mathbf{\Gamma}_{\mathrm{pm}} = -\frac{1}{2\mu_0\rho} \int_{\mathcal{V}} \mathbf{r} \times \nabla \left(\mathbf{B}^2 \right) \, \mathrm{d}V = -\frac{1}{2\mu_0\rho} \int_{\partial \mathcal{V}} \mathbf{B}^2 \, (\mathbf{r} \times \mathbf{n}) \, \mathrm{d}S, \tag{1.28a}$$

$$\mathbf{\Gamma}_{\mathrm{b}} = \frac{1}{\mu_0\rho} \int_{\mathcal{V}} \mathbf{r} \times ((\mathbf{B} \cdot \boldsymbol{\nabla}) \, \mathbf{B}) \, \mathrm{d}V. \tag{1.28b}$$

$$\tag{1.28c}$$

It is seen that, similar to the non-linear term, for the conducting boundary condition (1.15) the magnetic tension torque $\mathbf{\Gamma}_{\mathrm{b}}$ vanishes. For an insulating mantle, the Lorentz torque $\mathbf{\Gamma}_{\mathrm{L}}$ vanishes entirely.

Along the rotation axis, usually assumed to be along $\mathbf{1}_z$ (unless specified, we have

$\mathbf{1}_\Omega = \mathbf{1}_z$ in the remainder of this work), the Coriolis torque is zero

$$\begin{aligned}
\Gamma_{c,z} &= 2\rho \mathbf{1}_z \cdot \int_{\mathcal{V}} \mathbf{r} \times (\mathbf{\Omega} \times \mathbf{u}) \, \mathrm{d}V \\
&= 2\Omega\rho \mathbf{1}_z \cdot \int_{\mathcal{V}} (s\mathbf{1}_s + z\mathbf{1}_z) \times (\mathbf{1}_z \times \mathbf{u}) \, \mathrm{d}V \\
&= 2\Omega\rho \mathbf{1}_z \cdot \int_{\mathcal{V}} (s\mathbf{1}_s \cdot \mathbf{u} + z\mathbf{1}_z \cdot \mathbf{u})\mathbf{1}_z - z\mathbf{u} \, \mathrm{d}V \\
&= 2\Omega\rho \int_{\mathcal{V}} s\mathbf{1}_s \cdot \mathbf{u} + z\mathbf{1}_z \cdot \mathbf{u} - z\mathbf{1}_z \cdot \mathbf{u} \, \mathrm{d}V \\
&= \Omega\rho \int_{\mathcal{V}} \boldsymbol{\nabla} \cdot \left(s^2\mathbf{u}\right) \mathrm{d}V \\
&= \Omega\rho \int_{\partial\mathcal{V}} s^2\mathbf{u} \cdot \mathbf{n} \, \mathrm{d}A \\
&= 0.
\end{aligned} \tag{1.29}$$

Also shown in Davidson (2016, eq. 14.98). The rotation is assumed to be constant, $\partial_t\Omega = 0$, so that $\mathbf{\Gamma}_\Omega = \mathbf{0}$ and the axial torque balance reduces to

$$\frac{\partial L_z}{\partial t} = \Gamma_{\mathrm{p},z} + \Gamma_{\nu,z} + \Gamma_{\mathrm{pm},z} + \Gamma_{\mathrm{b},z} + \Gamma_{\mathrm{g},z}. \tag{1.30}$$

The estimated strength of these torques in Earth's core is discussed in the following section. In Chapter 4 we investigate the torque balance of torsional Alfvén modes in a rotating ellipsoid assuming that viscosity is negligible, the mantle is perfectly conducting and no buoyancy is present. Then, the axial angular momentum must be balanced by the hydrodynamic and magnetic pressure torque.

1.4.3 Core-mantle coupling mechanisms

The mechanical coupling, i.e. the mechanism to exchange angular momentum, could also be referred to as torquing (Hide, 1989). This paraphrasing emphasizes the direct correspondence of these coupling mechanisms to a torque exerted on the boundary. A short summary of the proposed mechanisms and their estimates in the Earth's core as proposed by the literature is given. For a more thorough discussion of the topic the reader is referred to the review by Roberts and Aurnou (2012). As the axial torque balance (1.30) suggests, the change in angular momentum in the core may be caused by a viscous, gravitational, electromagnetic or topographic torque. The torque estimates are compared to the 10^{16} Nm change in angular momentum associated with the variations in the LOD at a 6 yr period.

Viscous

Viscous stresses between the viscous fluid outer core and a rigid mantle contribute to the torque balance. However, the viscous torque $\mathbf{\Gamma}_\nu$ is generally assumed to be negligible as a coupling mechanism (Bullard et al., 1950; Rochester et al., 1984). It can be estimated to be $\Gamma_{\nu,z} \sim \frac{8}{5}\pi\rho R_c^4\sqrt{\mathrm{Ek}}\Omega U \sim 10^{14}$ Nm (by considering eq. (5) in Jault, 1995, without magnetic part) for a velocity $U = 5 \times 10^{-6}$ m/s (Gillet et al., 2015). The amplitude of $\mathbf{\Gamma}_\nu$, unsurprisingly, depends strongly on the hard to estimate viscosity in the core (Wijs et al., 1998), but even for the highest plausible values the torque is still too small. Even in the case that turbulent viscosity is the relevant value to be taken into account, it is still an order of magnitude below the torque associated with changes of the LOD at inter-annual periods (Roberts and Aurnou, 2012).

Gravitational

To couple the inner core and the mantle gravitationally the so-called Mantle-Inner-Core-Gravitational (MICG) coupling has been proposed (Buffett, 1996a,b). In this scenario a deformed inner core exerts a torque on a deformed CMB. The mechanism is usually illustrated by considering an equatorial ellipticity of the inner core and the CMB with the semi-major axes out of phase. The phase lag between the two bulges can then lead to a gravitational force restoring to an equilibrium state. It is under debate if the deformations of the inner core are sustained long enough to make such a scenario effective, as it strongly depends on the viscosity of the inner core (Orman, 2004; Mound and Buffett, 2006; Deguen, 2012). The coupling of the flow in the liquid core to the conducting inner core is likely strong and the correct treatment of it in the proposed MICG models is important. Mound and Buffett (2003) consider the tangent cylinder, that is the cylinder drawn by the radius of the inner core and the height of the outer core, rigidly coupled to the inner core rotation, whereas Duan and Huang (2020b) propose that the inner and outer core are decoupled through a thin diffusive layer. Recent studies claim to have found a corresponding signal at a 5.8 yr period in GPS gravity signals (Ding and Chao, 2018). Other studies at a similar time have suggested that measurement errors are still too large to infer relevant gravitational signals from the core (Watkins et al., 2018).

Electromagnetic

If the lower mantle is not perfectly insulating it is possible that it is coupled electromagnetically to flows in the outer core. The conductivity of the lowermost mantle is not well constrained today and depends strongly on the mineral physics at CMB conditions. There is some evidence for thin iron enriched, and thus conducting, layers near the CMB from seismological observations and experimental chemical partitioning studies (Wicks et al., 2010; Otsuka and Karato, 2012), while other experiments suggest the opposite (Ozawa et al., 2009).

Initially introduced by Bullard et al. (1950) and put forward by Rochester and Bullard (1960), electromagnetic (EM) coupling of core flows with such a potential layer of high conductance has been discussed widely in the literature (e.g. Stix and

Roberts, 1984; Holme, 1998; Jault, 2003; Dumberry and Mound, 2008). A conductance of the lowermost mantle $\mathcal{O}\left(10^8\right)$ S was found to suffice to account for the LOD changes for optimized flows at the core surface (Holme, 1998). Similarly, Gillet et al. (2010) used a conductance on the same order of magnitude to explain the changes in the LOD by torsional Alfvén modes in the core. However, for example Ohta et al. (2010) give an upper limit $\mathcal{O}\left(10^7\right)$ S, an order of magnitude below what is needed to have a sufficient EM coupling. Jault (2015) linked the damping influence of a conducting mantle to the spectrum geomagnetic field changes, showing that the ratio between conductances of the upper and lower mantle is the key factor. The complicated relationship of Earth's nutation and the FCN might also be strongly influenced by a conducting lowermost mantle (Buffett, 1992; Buffett and Christensen, 2007; Kuang et al., 2019). Dumberry and More (2020) have recently suggested that weak energy in the secular variations in the south pacific region point towards a strongly conducting area in the lowermost mantle. A lot of uncertainties remain, but if other coupling mechanisms can be ruled out a layer with enhanced conductivity at the bottom of the mantle is needed to transfer angular momentum to the mantle.

Topographic

The idea of a pressure torque exerted from the flow onto a deformed mantle reaches back to Munk and MacDonald (1960), who extends the concept of inertial coupling developed in the framework of nutation and precession theories of Poincaré (1910) to changes in the rotation speed. In an axisymmetric domain, the axial pressure torque is exactly zero and cannot contribute to the torque balance, as seen in (1.26d). A departure from axisymmetry is referred to as topography and this departure can be on the very largest scales, e.g. ellipticity of the CMB. Then, a pressure torque, or topographic torque, can act on the deformed boundary. Hide (1969) and Hide and Weightman (1977) estimated that such a torque could be very effective in Earth's core. By considering a typical height of the topography ϵ (named h in the article), it was proposed that the pressure acting on the boundary should scale as $\Omega\rho U\epsilon$, with U the characteristic velocity. Values of U have been inferred from tangential geostrophic (TG) flows, leading to a pressure as large as 10^3 Pa (Jault and Mouël, 1990). Tangential geostrophy relies on the assumption that the flow field close to the surface is in a geostrophic balance and the associated pressure is easily obtained (Le Mouël et al., 1985; Jault and Mouël, 1989). Most flows, including QG flows, are however not exactly represented by TG flows and the assumption breaks down at the equator. The estimate of a pressure of a generic flow from the TG pressure is not necessarily correct.

Some studies have considered a local domain with a deformed boundary to investigate stresses at at the CMB (Braginsky, 1998; Glane and Buffett, 2018; Jault, 2020). A strong amplification of the topographic coupling through stratification was suggested by Glane and Buffett (2018). Then, all stresses are through small scale topography within a stratified layer. A key issue remains to explain transfer of momentum from the boundary to the bulk of the fluid (Jault, 2020), underlining the importance of a global study.

1.5 Geomagnetic field changes and core flow inversions

The most prominent changes of Earth's magnetic field are so-called reversals, where the dominant dipole component exchanges polarity over a time of a few thousands of years, occurring sporadically over time scales of hundreds of thousands to millions of years (Glatzmaier and Coe, 2015). These are the very longest term evolutions of the geomagnetic field. On time scales of several years up to several hundreds of years, changes in Earth's magnetic field are referred to as secular variations. Due to their long time evolution they may only be explained by changes in the interior of Earth. Changes on the order of seconds to several months are dominated by currents in the magnetosphere and ionosphere that are mostly induced by solar wind interactions (Baumjohann and Nakamura, 2007; Olsen and Stolle, 2012). Since these changes are not of interior origin, they are not of interest here.

The earliest observed change in the geomagnetic field is a dominant westward drift, detected by Halley (1692), and first quantified by Bullard et al. (1950), to be 0.18°/yr. The explanation of this feature has puzzled many scientists and is still under active debate (e.g. Yukutake, 1981; Jault et al., 1988; Bardsley, 2018).

In the last century observations have been mostly based on ground observatory magnetometers (Turner et al., 2015). Before the first observatories were founded observations of the magnetic field mostly stem from exploration and trading ships that twenty years ago were compiled together with the ground observatory data into a long term temporally varying magnetic field model known as *gufm1* (Jackson et al., 2000). In more recent years, the satellite era has improved observations substantially, both in spatial and temporal resolution. A global coverage by different missions over the last decades allows for increasing resolution of the internal magnetic field changes at periods of a few years (Hulot et al., 2015).

The magnetic field observations on Earth's surface can be projected down to the CMB, assuming that the overlying mantle is electrically insulating (e.g. Courtillot et al., 1978; Whaler and Gubbins, 1981). If the mantle is not a perfect insulator it acts as a filter on the magnetic field changes that originate from the core and are observed on the surface (Runcorn, 1955; Backus, 1983; Jault, 2015). From the downward projection a time dependent map of the radial magnetic field component at the CMB is obtained (e.g. Gillet et al., 2013). In these maps recent geomagnetic field models show strong equatorial focusing of the energy in the inter-annual secular variations near the equatorial region (Chulliat et al., 2015; Gillet et al., 2019; Kloss and Finlay, 2019). There does not seem to be a preferred direction of propagation along the azimuthal direction, with both westward and eastward propagating secular variations being observed (see also Chi-Durán et al., 2020). Some of these magnetic field changes can be associated with wave motions (see Section 3.5).

In a further step, the maps of the radial magnetic field component at the CMB have been used to infer the flow in the core, presumably causing the changes of the magnetic field, but several assumptions have to be made. It has been assumed that, at periods of a few years to decades, changes of the magnetic field result from advection by core flows and magnetic diffusion can be neglected, known as the frozen flux assumption (Roberts and Scott, 1965). There is debate on the accuracy of this assumption, with some models that include diffusion showing that it can have a large influence on the inversion (Amit and Christensen, 2008; Jackson and Finlay, 2015). Regardless of the effect of diffusion, the problem remains that many flows are theoretically able to explain the observed magnetic field changes (Backus, 1968). This ill-posedness of the inverse problem may never be solved, but physically motivated constraints can be imposed to lower the subset of possible flow solutions. First mentioned by Hills (1979) and put forward by Le Mouël (1984); Le Mouël et al. (1985) the idea of the tangential geostrophic assumption is that flows close to the surface are in a geostrophic balance. The first numerical inversion of geomagnetic data using this assumption was done by Gire and Le Mouël (1990), but it fails near the equatorial region (Backus and Le Mouël, 1986). Another kinematic constraint was put forward by Lloyd and Gubbins (1990), assuming that the flow is purely toroidal close to the CMB. However, at the CMB the magnetic field must match a potential field, requiring a strong shear of the toroidal component close to the CMB and inference of induced toroidal core flows is difficult (Jault and Le Mouël, 1991). In both approaches, the flow on small scales, i.e. not over the whole core size, are dominantly toroidal.

The flows obtained through these assumptions couple only mechanically to the secular variations and the inversion of the flow field is not constrained by the magnitude of the magnetic field changes, i.e. the flow field remains the same for any amplitude of the magnetic field. Also, these inversions only solve for the flow field close to the surface, not within the bulk of the core.

Other, more recent approaches to invert for core flows are based on data assimilation through statistics obtained from numerical geodynamo simulations (e.g. Fournier et al., 2010; Aubert, 2013, 2014; Barrois et al., 2017, 2018). Information from DNS of the MHD equations and the resulting radial magnetic field component at the surface are used to invert geomagnetic observations. In these models, information about the flows and the magnetic field within the deep interior of the core, as well as the effects of diffusion can be investigated. However, these inversions heavily depend on the prior, i.e. the numerical simulation, which is calculated on physical parameters different to those relevant to Earth's core.

Chapter 2

Quasi-geostrophic models

The term quasi-geostrophic (QG) motion has been coined by Sutcliffe (1939) to describe a small departure to the geostrophic balance. In the same year Rossby (1939) used slight perturbations to the geostrophic balance to derive QG inertial waves, that today carry his name. The first QG model with explicit equations was given by atmospheric scientist Charney (1948). The formulation of QG models was a game changer in meteorological modeling and forecasting, reducing mathematical complexity and allowing numerical solvability.

In the context of Earth's core Hide (1966) first discussed the quasi-geostrophic approximation for the investigation of hydromagnetic waves. A formulation of QG equations for the application to planetary cores was given by Busse (1970) using also a small slope approximation. A short introduction into his derivation is presented in Section 2.1. Besides the small slope approximation, we present three other ways to derive sets of QG equations. This includes the z-averaged vorticity equation, a Galerkin approach and a Lagrangian approach.

Usually, QG models in the core assume a dominant geostrophic balance a priori (Canet et al., 2009, 2014), or impose a constraint on the horizontal velocity (Schaeffer and Cardin, 2005), based on the columnar flow structures observed, e.g. in numerical observations (Gillet et al., 2011; Schaeffer et al., 2017).

Many adaptations of QG models exist (e.g. including buoyancy, Aubert et al., 2003; Gastine, 2019), and we cannot possibly discuss all of them here. Instead we focus on the basic assumptions and approaches to derive the essential parts of a reduced momentum equation.

2.1 Small slope approximation

The first formulation of QG equations in the context of planetary cores was given by Busse (1970), expanding the velocity in terms of the steepness of the slope of the enclosing boundary ϵ, assumed to be small. This parameter may be small in the annulus considered by Busse (1970) and illustrated in Figure 2.1. However, for a full

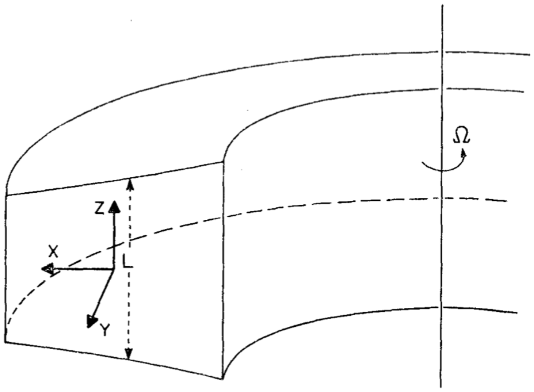

Figure 2.1: Cylindrical annulus with sloping top and bottom boundaries. In this illustration the column height is notated $L = 2h$. Reprint of Figure 3 of Busse (1975) with permission from Oxford University Press.

sphere an expansion in ϵ is only valid near the rotation axis and diverges near the equator.

An alternative version of the work by previous authors is presented here (Busse, 1970, 1975; Jault and Finlay, 2015). It has to be noted that all of these derivations, including the one presented here, have either not considered or are incapable of handling correctly the magnetic field. The characteristic time scale is chosen to be the rotation period and the characteristic length scale is the core radius. Thus, the Rossby number (1.18), Lehnert number (1.20), Ekman number (1.19) and magnetic Prandtl number (1.21) are used to write the non-dimensionalized set of equations

$$\frac{\partial \mathbf{u}}{\partial t} + \mathrm{Ro}\left(\mathbf{u}\cdot\boldsymbol{\nabla}\right)\mathbf{u} + 2\,\mathbf{1}_\Omega \times \mathbf{u} = -\nabla p + \mathrm{Ek}\,\boldsymbol{\nabla}^2\mathbf{u} + \frac{\mathrm{Le}^2}{\mathrm{Ro}}\left(\boldsymbol{\nabla}\times\mathbf{B}\right)\times\mathbf{B}, \tag{2.1a}$$

$$\frac{\partial \mathbf{B}}{\partial t} = \mathrm{Ro}\,\boldsymbol{\nabla}\times\left(\mathbf{u}\times\mathbf{B}\right) + \frac{\mathrm{Ek}}{\mathrm{Pm}}\boldsymbol{\nabla}^2\mathbf{B}, \tag{2.1b}$$

We have $\epsilon = |\nabla h|$ with h the geostrophic column height as our small parameter. To be specific, h is the column half height, but for simplicity we do not differentiate between the two. The velocity, pressure and frequency are expanded as

$$\mathbf{u} = \mathbf{u}_0 + \epsilon\mathbf{u}_1 + \epsilon^2\mathbf{u}_2 + ..., \tag{2.2}$$

$$p = p_0 + \epsilon p_1 + \epsilon^2 p_2 + ..., \tag{2.3}$$

$$\omega = \epsilon\omega_1 + \epsilon^2\omega_2 + ..., \tag{2.4}$$

respectively. The leading order momentum equations is

$$\mathrm{Ro}\left(\mathbf{u}_0\cdot\boldsymbol{\nabla}\right)\mathbf{u}_0 + 2\,\mathbf{1}_\Omega \times \mathbf{u}_0 = -\nabla p_0 + \mathrm{Ek}\,\boldsymbol{\nabla}^2\mathbf{u}_0 + \frac{\mathrm{Le}^2}{\mathrm{Ro}}\left(\boldsymbol{\nabla}\times\mathbf{B}\right)\times\mathbf{B}, \tag{2.5a}$$

Considering the values of $\mathrm{Ek} = 10^{-15}$, $\mathrm{Le} = 10^{-4}$, and $\mathrm{Ro} = 10^{-6}$, relevant for Earth, the leading order is given by the geostrophic balance

$$2\,\mathbf{1}_\Omega \times \mathbf{u}_0 = -\nabla p_0. \tag{2.6}$$

The boundary condition reduces to the non-penetration condition, $\mathbf{u} \cdot \mathbf{n} = \mathbf{u} \cdot (\mathbf{1}_z \pm \nabla h) = 0$. It is expanded the same way in terms of ϵ and reads $\mathbf{u}_0 \cdot \mathbf{1}_z = 0$ at $z = \pm h$ at leading order. Solutions to (2.6) are then given by

$$\mathbf{u}_0 = \frac{1}{2}\mathbf{1}_z \times \nabla p_0, \tag{2.7}$$

with $u_{0,z} = 0$ to satisfy the boundary condition.

At the next order of the boundary condition, we get $\mathbf{u}_1 \cdot \mathbf{1}_z \pm \mathbf{u}_0 \cdot \nabla h = 0$, so that

$$u_{1,z} = \mp \mathbf{u}_0 \cdot \nabla h \quad \text{at}\, z = \pm h. \tag{2.8}$$

Including the next order of ϵ in the momentum equation, but subtracting (2.6), the set of equations is given by

$$\frac{\partial \mathbf{u}_0}{\partial t} + \mathrm{Ro}^*\left(\mathbf{u}_0 \cdot \boldsymbol{\nabla}\right)\mathbf{u}_0 + 2\,\mathbf{1}_\Omega \times \mathbf{u}_1 = -\nabla p_1 + \mathrm{Ek}^*\,\boldsymbol{\nabla}^2\mathbf{u}_0 + \frac{(\mathrm{Le}^*)^2}{\mathrm{Ro}^*}\left(\boldsymbol{\nabla} \times \mathbf{B}\right) \times \mathbf{B}, \tag{2.9}$$

where $\mathrm{Ro}^* = \mathrm{Ro}/\epsilon$ (and analogous for Le^*, Ek^* and Pm^*). In this step we have omitted the non-linear, viscous and Lorentz term of the next order, as they appear with the factors $\epsilon\mathrm{Ro}$, $\epsilon\mathrm{Ek}$ and $\epsilon\mathrm{Le}^2\mathrm{Ro}^{-1}$, respectively. This allows us to neglect these terms. This equation is suitable in the case that $1 \gg \epsilon \gg [\mathrm{Ro}, \mathrm{Ek}, \mathrm{Le}^2\mathrm{Ro}^{-1}]$.

So far the system is not closed, as we have only one equation for the unknowns $\mathbf{u}_0$, $\mathbf{u}_1$ and p_1. We may eliminate the pressure by taking the curl of (2.9). The 3-D equation that arises describes the evolution of the vorticity $\boldsymbol{\omega} = \boldsymbol{\nabla} \times \mathbf{u}$, and can be divided into the horizontal and vertical components. At leading order the structure is columnar, so that the horizontal vorticity components are small compared to the vertical/axial vorticity component ω_z. Most of the flow dynamics are then described by the axial vorticity component, which varies weakly along z. We can obtain an evolution equation of the axial vorticity by taking the z-component of the curl of the momentum equation (2.9) and find

$$\frac{\partial \omega_{z,0}}{\partial t} + \mathrm{Ro}^*(\mathbf{u}_0 \cdot \boldsymbol{\nabla})\,\omega_{z,0} - 2\frac{\partial u_{1,z}}{\partial z} = \mathrm{Ek}^*\,\nabla^2\omega_{z,0} + \frac{(\mathrm{Le}^*)^2}{\mathrm{Ro}^*}\,\mathbf{1}_z \cdot \boldsymbol{\nabla} \times ((\boldsymbol{\nabla} \times \mathbf{B}) \times \mathbf{B}), \tag{2.10}$$

with the axial vorticity of $\mathbf{u}_0$ given by

$$\omega_{z,0} = \mathbf{1}_z \cdot (\boldsymbol{\nabla} \times \mathbf{u}_0) = -\nabla^2 p_0. \tag{2.11}$$

Then, the crucial step is to average (2.10) along the z-component. For the Coriolis term, by using the boundary condition (2.8), this results in

$$\frac{1}{2h}\int_{-h}^{h} 2\frac{\partial u_{1,z}}{\partial z}\,\mathrm{d}z = \frac{1}{h}u_{1,z}\Big|_{z=\pm h} = -\frac{1}{h}\nabla h \cdot \mathbf{u}_0. \tag{2.12}$$

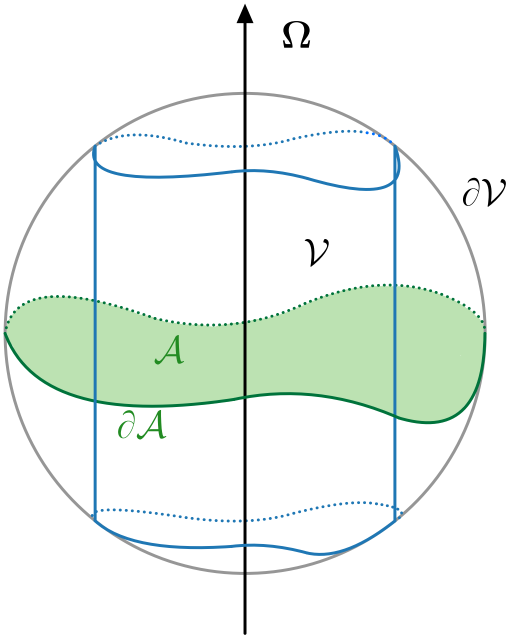

Figure 2.2: Schematic of a geostrophic column (blue) in an equatorially symmetric but non-axisymmetric volume $\mathcal{V}$. The area of the equatorial plane $\mathcal{A}$ is shaded in green.

We have eliminated $\mathbf{u}_1$ from the z-averaged momentum equation, that now reads

$$\frac{\partial \omega_{z,0}}{\partial t} + \mathrm{Ro}^* (\mathbf{u}_0 \cdot \boldsymbol{\nabla})\, \omega_{z,0} + \frac{2}{h} \nabla h \cdot \mathbf{u}_0 = \mathrm{Ek}^*\, \nabla^2 \omega_{z,0} + \frac{(\mathrm{Le}^*)^2}{2h\mathrm{Ro}^*} \int_{-h}^{h} \mathbf{1}_z \cdot \boldsymbol{\nabla} \times ((\boldsymbol{\nabla} \times \mathbf{B}) \times \mathbf{B})\, \mathrm{d}z. \tag{2.13}$$

It is complemented by the unaltered three dimensional induction equation. This approach can also be carried out without the assumption of incompressibility (Pais and Jault, 2008), that we have used to write our initial momentum equation (2.1). In either way, the derivation of this set of QG MHD equations does not handle correctly an expansion of the magnetic field. It is assumed to be small enough to not contribute to the leading geostrophic balance. An expansion of the magnetic field by the boundary slope could only be justified when considering the local boundary condition of a perfectly conducting CMB, which reduces to $\mathbf{B} \cdot \mathbf{n} = 0$ similar to the velocity. The lack of rigor in handling the Lorentz force in the derivation and the inapplicability near the equatorial region render the small slope approach obsolete.

2.2 Quasi-geostrophic approximation

Schaeffer and Cardin (2005) introduced a QG model without assuming a small slope of the boundary $\partial\mathcal{V}$. The approach was originally given in a sphere, but can be extended to a more general volume $\mathcal{V}$. Here, we consider $\mathcal{V}$ to be equatorially symmetric, but not axisymmetric, as illustrated in Figure 2.2. No non-closed geostrophic contours exist and the volume is not punctured, i.e. no inner core is considered. Each contour of constant column height $2h$ (shown in Figure 2.2 in blue), can be mapped bijectively to a contour in the sphere.

In the approach by Schaeffer and Cardin (2005) the a priori assumption is made that the horizontal velocity $\mathbf{u}_\perp$ depends only on the horizontal coordinates $\mathbf{r}_\perp$ and not on the coordinate along the rotation axis, so that $\mathbf{u}_\perp = \mathbf{u}_\perp(\mathbf{r}_\perp)$. By the conservation of mass in the incompressible case, we find that

$$\frac{\partial u_z}{\partial z} = -\boldsymbol{\nabla}_\perp \cdot \mathbf{u}_\perp. \tag{2.14}$$

Within the equatorially symmetric volume, this gives

$$u_z = -z\boldsymbol{\nabla}_\perp \cdot \mathbf{u}_\perp. \tag{2.15}$$

At the boundaries $z = \pm h$, the $\mathbf{u}\cdot\mathbf{n} = 0$ condition gives

$$u_z = \pm\nabla h \cdot \mathbf{u}_\perp, \tag{2.16}$$

so that we may write

$$\boldsymbol{\nabla}\cdot(\mathbf{u}_\perp h) = 0. \tag{2.17}$$

Then, the horizontal velocity can be written as

$$\mathbf{u}_\perp = \frac{1}{h}\boldsymbol{\nabla}\times\psi(\mathbf{r}_\perp)\mathbf{1}_z, \tag{2.18}$$

with $\psi(\mathbf{r}_\perp)$ the scalar stream function. The full QG velocity takes the form (Bardsley, 2018)

$$\mathbf{u} = \nabla\psi\times\nabla\left(\frac{z}{h}\right). \tag{2.19}$$

If additionally the volume is axisymmetric, the column height is a function of the cylindrical radius only, $h = h(s)$, and cylindrical coordinates apply. Then, (2.19) is written as (Labbé et al., 2015)

$$\mathbf{u} = \frac{1}{sh}\frac{\partial\psi}{\partial\phi}\mathbf{1}_s - \frac{1}{h}\frac{\partial\psi}{\partial s}\mathbf{1}_\phi + \frac{z}{sh^2}\frac{\partial h}{\partial s}\frac{\partial\psi}{\partial\phi}\mathbf{1}_z, \tag{2.20}$$

which is equivalent to the expression initially given by Schaeffer and Cardin (2005), who considered a stream function $\Psi = \psi/h$ and $h = \sqrt{1-s^2}$ in the sphere.

In case equatorial symmetry is not present, we can denote z_t and z_b the top and bottom boundary height. The column height is then given as $h = (z_t - z_b)/2$ and we can also define a midpoint $z_0 = (z_t + z_b)/2$. The QG velocity is then written as

$$\mathbf{u} = \nabla\psi\times\nabla\left(\frac{z-z_0}{h}\right). \tag{2.21}$$

In this work only equatorially symmetric domains are considered and, when mentioned, QG velocity usually refers to a velocity of the form (2.19).
This expression is the basis to derive the QG equations from a vorticity equation, presented in the next section. It is also used as a basis in the Galerkin approach and in the Lagrangian approach the same expression is found, imposing equivalent assumptions on the movement of individual fluid particles.

2.3 Vorticity equation

As already introduced in the derivation in 2.1, a frequently applied approach to reduce the 3-D momentum equation to 2-D scalar equation has been the z-averaged axial vorticity equation (Aubert et al., 2003; Schaeffer and Cardin, 2005; Pais and Jault, 2008; Canet et al., 2014). This is motivated by the fact that the horizontal components of the vorticity are small compared to the axial component, when assuming that the velocity takes a predominantly columnar structure. The velocity is assumed in the form (2.19), as introduced in the previous section. Then, considering the z-averaged axial vorticity equation allows us to describe a large part of the flow by a single scalar stream function that is independent of the vertical coordinate. Taking the z-averaged axial curl translates into the operator

$$\boldsymbol{\mathcal{W}}(\mathbf{f}) = -\frac{1}{h}\left\langle \mathbf{1}_z \cdot \boldsymbol{\nabla} \times \mathbf{f} \right\rangle = \frac{1}{h}\left\langle \boldsymbol{\nabla} \cdot \left(\mathbf{1}_z \times \mathbf{f}\right) \right\rangle, \tag{2.22}$$

where $\langle\cdot\rangle = \int_{-h}^{h} \cdot \, \mathrm{d}z$ is the integral along the rotation axis. We consider the Alfvén period T_A as the characteristic time scale. Then, we apply (2.22) to the terms in the governing momentum equation (1.23a),

$$\mathbf{f}(\mathbf{u}) = \frac{\partial \mathbf{u}}{\partial t} + (\mathbf{u} \cdot \boldsymbol{\nabla})\,\mathbf{u} + \frac{2}{\mathrm{Le}}\,\mathbf{1}_\Omega \times \mathbf{u} + \nabla p - \frac{\mathrm{Pm}}{\mathrm{Lu}}\,\boldsymbol{\nabla}^2\mathbf{u} - (\boldsymbol{\nabla} \times \mathbf{B}) \times \mathbf{B}, \tag{2.23}$$

with $\mathbf{u}$ of the form (2.19).
For the inertial force we get,

$$\begin{aligned}
\boldsymbol{\mathcal{W}}\left(\frac{\partial \mathbf{u}}{\partial t}\right) &= \frac{1}{h}\left\langle \boldsymbol{\nabla} \cdot \left(\mathbf{1}_z \times \left(\nabla \frac{\partial \psi}{\partial t} \times \nabla\left(\frac{z}{h}\right)\right)\right)\right\rangle && \text{(2.24a)}\\
&= 2\boldsymbol{\nabla} \cdot \left(\frac{1}{h}\nabla \frac{\partial \psi}{\partial t}\right), && \text{(2.24b)}\\
&= 2\mathcal{D}_\omega \frac{\partial \psi}{\partial t}, && \text{(2.24c)}
\end{aligned}$$

with

$$\mathcal{D}_\omega \psi = \boldsymbol{\nabla} \cdot \left(\frac{1}{h}\nabla \psi\right) = -\omega_z. \tag{2.25}$$

The pressure force vanishes, as $\boldsymbol{\nabla} \times \nabla p \equiv \mathbf{0}$. The Coriolis force is simply

$$\begin{aligned}
\boldsymbol{\mathcal{W}}\left(\frac{2}{\mathrm{Le}}\mathbf{1}_z \times \mathbf{u}\right) &= \frac{2}{h\mathrm{Le}}\left\langle \boldsymbol{\nabla} \cdot (\mathbf{1}_z \times (\mathbf{1}_z \times \mathbf{u}))\right\rangle && (2.26)\\
&= \frac{2}{h\mathrm{Le}}\left\langle \boldsymbol{\nabla} \cdot (u_z \mathbf{1}_z)\right\rangle && (2.27)\\
&= \frac{4}{\mathrm{Le}}\nabla\psi \times \nabla\left(\frac{1}{h}\right) \cdot \mathbf{1}_z && (2.28)\\
&= \frac{4}{\mathrm{Le}}\left\{\psi, \frac{1}{h}\right\} && (2.29)
\end{aligned}$$

with

$$\{X, Y\} = (\nabla X \times \nabla Y) \cdot \mathbf{1}_z. \tag{2.30}$$

We rewrite $\mathbf{u} \cdot \nabla\mathbf{u} = (\boldsymbol{\nabla} \times \mathbf{u}) \times \mathbf{u} + \nabla\mathbf{u}^2/2$. Since the gradient term vanishes when applying the curl, the non-linear term can be written as $\boldsymbol{\omega} \times \mathbf{u}$. Then, we find that the non-linear term is given by

$$\begin{aligned}
\boldsymbol{\mathcal{W}}(\boldsymbol{\omega} \times \mathbf{u}) &= \frac{1}{h}\left\langle \boldsymbol{\nabla} \cdot (\mathbf{1}_z \times (\boldsymbol{\omega} \times \mathbf{u}))\right\rangle\\
&= \frac{1}{h}\left\langle \boldsymbol{\nabla} \cdot (u_z \boldsymbol{\omega} - \omega_z \mathbf{u})\right\rangle\\
&= -\frac{1}{h}\left\langle \nabla\omega_z \cdot \mathbf{u} - \nabla u_z \cdot \boldsymbol{\omega}\right\rangle\\
&= 2\left(\frac{1}{h}\nabla(\mathcal{D}_\omega\psi) \cdot (\nabla\psi \times \mathbf{1}_z) - \nabla\psi \times \nabla\left(\frac{1}{h}\right) \cdot \mathbf{1}_z\mathcal{D}_\omega\psi\right)\\
&= 2\left\{\frac{1}{h}\mathcal{D}_\omega\psi, \psi\right\}.
\end{aligned} \tag{2.31}$$

Here, we used (2.25), and $\nabla u_z = \partial_z\mathbf{u} + \mathbf{1}_z \times \boldsymbol{\omega}$.
The viscous term is simply

$$\boldsymbol{\mathcal{W}}\left(\frac{\mathrm{Pm}}{\mathrm{Lu}}\boldsymbol{\nabla}^2\mathbf{u}\right) = 2\frac{\mathrm{Pm}}{\mathrm{Lu}}\mathcal{D}_\omega\nabla^2\psi. \tag{2.32}$$

It remains the Lorentz force, which we leave as an implicit term, so that the scalar momentum equation is given by

$$\mathcal{D}_\omega\frac{\partial\psi}{\partial t} + \left\{\frac{1}{h}\mathcal{D}_\omega\psi, \psi\right\} - \frac{2}{\mathrm{Le}}\left\{\frac{1}{h}, \psi\right\} = \frac{\mathrm{Pm}}{\mathrm{Lu}}\mathcal{D}_\omega\nabla^2\psi + \frac{1}{2}\boldsymbol{\mathcal{W}}((\boldsymbol{\nabla} \times \mathbf{B}) \times \mathbf{B}). \tag{2.33}$$

This equation has often been shown in terms of the axial vorticity $\omega_z = -\mathcal{D}_\omega\psi$ (e.g. Schaeffer and Cardin, 2005).

Although, there are reasons to consider the axial vorticity equation instead of the equatorial components of the vorticity equation, this choice remains somehow arbitrary. In this work, I will rely on the projection of the momentum equation on the sub-space of the QG motions, what is essentially a Galerkin method. This is similar to considering the energy equation (see Green and Naghdi, 1976), and it turns out that this approach is not equivalent to the axial vorticity equation.

2.4 Galerkin approach

Galerkin methods are used to to find approximate solutions to partial differential equations (PDE), and are today the preferred method for solving elliptical PDEs. As an example, to solve Poisson's equation $-\nabla^2\Phi = f$ the so-called weak form is found by projecting the equation onto a set of test functions Φ', so that

$$-\int_{\mathcal{V}} \Phi'\nabla^2\Phi \,\mathrm{d}V = \int_{\mathcal{V}} \Phi' f \,\mathrm{d}V. \tag{2.34}$$

Then, by Green's first identity and assuming that $\Phi' = 0$ at $\partial\mathcal{V}$, the weak form is given as

$$\int_{\mathcal{V}} \nabla\Phi' \cdot \nabla\Phi \,\mathrm{d}V = \int_{\mathcal{V}} \Phi' f \,\mathrm{d}V. \tag{2.35}$$

The solutions are limited to lie within the set of test functions Φ'. So far this is a continuous problem. In the Galerkin method we seek the most appropriate basis Φ'_i that describe a solution Φ_k to (2.35) in a discrete and finite dimensional subset of the actual solution, so that $\Phi_k = \sum_i \alpha_{k,i}\Phi'_i$. Solutions to the weak form are orthogonal to the residuals of the full solution, i.e. $\int_{\mathcal{V}} \nabla\Phi'_i \cdot \nabla\Phi_k \,\mathrm{d}V - \int_{\mathcal{V}} \nabla\Phi'_i \cdot \nabla\Phi \,\mathrm{d}V = 0$. Galerkin methods are also applied successfully in rotating fluid dynamics (e.g Lebovitz, 1989; Li et al., 2010). By choosing an appropriate basis, we can seek solutions that satisfy a weak form of the governing 3-D equations. In the context of quasi-geostrophic models we choose velocities of the form (2.19) as our test functions. Instead of using the operator (2.22) we project the momentum equation (1.23a) onto the QG velocities $\mathbf{u}'$, as first presented in Labbé et al. (2015) in the sphere. The weak form of the momentum equation is written as

$$\int_{\mathcal{V}} \mathbf{u}' \cdot \mathbf{f}(\mathbf{u}) \,\mathrm{d}V = 0, \qquad \forall \mathbf{u}', \tag{2.36}$$

with

$$\mathbf{f}(\mathbf{u}) = \frac{\partial \mathbf{u}}{\partial t} + (\mathbf{u}\cdot\boldsymbol{\nabla})\mathbf{u} + \frac{2}{\mathrm{Le}}\mathbf{1}_\Omega \times \mathbf{u} + \nabla p - \frac{\mathrm{Pm}}{\mathrm{Lu}}\boldsymbol{\nabla}^2\mathbf{u} - (\boldsymbol{\nabla}\times\mathbf{B})\times\mathbf{B}. \tag{2.37}$$

Substituting (2.19) into (2.36) yields

$$
\begin{aligned}
\int_{\mathcal{V}} \mathbf{u}' \cdot \mathbf{f}\,\mathrm{d}V &= \int_{\mathcal{V}} \nabla\psi' \times \nabla\left(\frac{z}{h}\right) \cdot \mathbf{f}\,\mathrm{d}V,\\
&= \int_{\mathcal{V}} \nabla\psi' \cdot \left(\nabla\left(\frac{z}{h}\right) \times \mathbf{f}\right)\,\mathrm{d}V,\\
&= -\int_{\mathcal{V}} \psi' \boldsymbol{\nabla} \cdot \left(\nabla\left(\frac{z}{h}\right) \times \mathbf{f}\right)\,\mathrm{d}V,\\
&= -\int_{\mathcal{A}} \psi' \left\langle \boldsymbol{\nabla} \cdot \left(\nabla\left(\frac{z}{h}\right) \times \mathbf{f}\right)\right\rangle \mathrm{d}A,\\
&= -\int_{\mathcal{A}} \psi' \boldsymbol{\mathcal{Q}}(\mathbf{f})\,\mathrm{d}A,
\end{aligned}
\tag{2.38}
$$

with $\int_{\mathcal{A}} \cdot\,\mathrm{d}A$ the integral over the equatorial surface plane $\mathcal{A}$ (see green area in Figure 2.2). We have transformed the weak form into a scalar form, where now the stream functions ψ' are the scalar test functions. The projection operator $\boldsymbol{\mathcal{Q}}$ is defined as

$$
\boldsymbol{\mathcal{Q}}(\mathbf{f}) = \left\langle \boldsymbol{\nabla} \cdot \left(\nabla\left(\frac{z}{h}\right) \times \mathbf{f}\right)\right\rangle. \tag{2.39}
$$

Note, that this is the correct way of writing this operator, compared to Gerick et al. (2020), who exchanged the order of z-averaging and divergence operation. For most of the forces within the QG assumption this is equivalent and the derived equations are identical, but when considering a general force this might not be true. Comparing this projection operator to the operator $\boldsymbol{\mathcal{W}}$, we find that

$$
\boldsymbol{\mathcal{Q}}(\mathbf{f}) = \boldsymbol{\mathcal{W}}(\mathbf{f}) + \left\langle z\nabla\left(\frac{1}{h}\right) \cdot (\boldsymbol{\nabla} \times \mathbf{f})\right\rangle. \tag{2.40}
$$

A term that scales with the slope of the boundary is additionally taken into account. For expression (2.38) to be zero for any test function ψ', the QG velocity $\mathbf{u}$ must satisfy

$$
\boldsymbol{\mathcal{Q}}\left(\frac{\partial \mathbf{u}}{\partial t} + \mathbf{u} \cdot \boldsymbol{\nabla}\mathbf{u} + \frac{2}{\mathrm{Le}}\mathbf{1}_{\Omega} \times \mathbf{u} - \frac{\mathrm{Pm}}{\mathrm{Lu}}\boldsymbol{\nabla}^2\mathbf{u} - (\boldsymbol{\nabla} \times \mathbf{B}) \times \mathbf{B}\right) = 0, \tag{2.41}
$$

where the pressure gradient is omitted, as it vanishes in the projection.
As in the vorticity approach the application of the projection operator to the individual forces is given. The inertial force is written as

$$
\boldsymbol{\mathcal{Q}}\left(\frac{\partial \mathbf{u}}{\partial t}\right) = \left\langle \boldsymbol{\nabla} \cdot \left(\nabla\left(\frac{z}{h}\right) \times \left(\nabla\frac{\partial \psi}{\partial t} \times \nabla\left(\frac{z}{h}\right)\right)\right)\right\rangle = 2\mathcal{D}\frac{\partial \psi}{\partial t}. \tag{2.42}
$$

Here, the linear operator $\mathcal{D}$ is given by

$$
\begin{aligned}
\mathcal{D}\Psi &= \boldsymbol{\nabla} \cdot \left(\frac{1}{h}\nabla\Psi + \frac{1}{3h}\nabla h \times (\nabla\Psi \times \nabla h)\right), && \text{(2.43a)}\\
&= \boldsymbol{\nabla} \cdot \mathbf{G}(\psi), && \text{(2.43b)}\\
&= \mathcal{D}_{\omega} + \frac{1}{3h}\nabla h \times (\nabla\Psi \times \nabla h), && \text{(2.43c)}
\end{aligned}
$$

with $\mathbf{G}(\psi) = \frac{1}{h}\nabla\Psi + \frac{1}{3h}\nabla h \times (\nabla\Psi \times \nabla h)$. It is seen that that an additional term is included compared to the operator $\mathcal{D}_\omega$ obtained by $\boldsymbol{\mathcal{W}}(\mathbf{u})$. This term is especially important when ∇h is large. For a comparison between linear solutions of both models see Labbé et al. (2015) or Maffei et al. (2017).

To project the Coriolis force and non-linear term, we find the projection of the general force of the form $\boldsymbol{\xi} \times \mathbf{u}$, which gives

$$\boldsymbol{\mathcal{Q}}\left(\boldsymbol{\xi} \times \mathbf{u}\right) = \left\langle \boldsymbol{\nabla} \cdot \left(- \left(\nabla \left(\frac{z}{h}\right) \cdot \boldsymbol{\xi} \right) \mathbf{u} \right) \right\rangle, \tag{2.44}$$

which holds for any $\mathbf{u}$ satisfying the boundary condition $\mathbf{u} \cdot \mathbf{n} = 0$ on $\partial\mathcal{V}$. This is further simplified to

$$\langle \boldsymbol{\nabla} \cdot \Phi\mathbf{u} \rangle = \left\{ \frac{\langle \Phi \rangle}{h}, \psi \right\}, \tag{2.45}$$

with $\Phi = -\nabla\left(\frac{z}{h}\right) \cdot \boldsymbol{\xi}$ and $\{X, Y\} = (\nabla X \times \nabla Y) \cdot \mathbf{1}_z$.

For the non-linear term $\boldsymbol{\xi} = \boldsymbol{\nabla} \times \mathbf{u}$ and we can write

$$\begin{aligned}
\langle \Phi \rangle &= \left\langle -\nabla \left(\frac{z}{h}\right) \cdot (\boldsymbol{\nabla} \times \mathbf{u}) \right\rangle && \text{(2.46a)}\\
&= \left\langle -\nabla \left(\frac{z}{h}\right) \cdot \left(\boldsymbol{\nabla} \times \left(\nabla\psi \times \nabla \left(\frac{z}{h}\right)\right)\right) \right\rangle && \text{(2.46b)}\\
&= \left\langle \boldsymbol{\nabla} \cdot \left(\nabla \left(\frac{z}{h}\right) \times \left(\nabla\psi \times \nabla \left(\frac{z}{h}\right)\right)\right) \right\rangle && \text{(2.46c)}\\
&= 2\mathcal{D}\psi, && \text{(2.46d)}
\end{aligned}$$

The non-linear term is then given by

$$\boldsymbol{\mathcal{Q}}\left((\boldsymbol{\nabla} \times \mathbf{u}) \times \mathbf{u}\right) = 2\left\{ \frac{1}{h}\mathcal{D}\psi, \psi \right\}. \tag{2.47}$$

For the Coriolis force $\boldsymbol{\xi} = 2/\mathrm{Le}\,\mathbf{1}_\Omega$ and thus $\langle \Phi \rangle = -4/\mathrm{Le}$, so that the Coriolis force reduces to

$$\boldsymbol{\mathcal{Q}}\left(\frac{2}{\mathrm{Le}}\mathbf{1}_\Omega \times \mathbf{u}\right) = -\frac{4}{\mathrm{Le}}\left\{ \frac{1}{h}, \psi \right\}. \tag{2.48}$$

Since the Laplace operator is linear also, the viscous term is simply

$$\boldsymbol{\mathcal{Q}}\left(\frac{\mathrm{Pm}}{\mathrm{Lu}}\boldsymbol{\nabla}^2\mathbf{u}\right) = 2\frac{\mathrm{Pm}}{\mathrm{Lu}}\mathcal{D}\nabla^2\psi. \tag{2.49}$$

The QG scalar momentum equation is then, analogous to (2.33), given by

$$\mathcal{D}\frac{\partial\psi}{\partial t} + \left\{ \frac{1}{h}\mathcal{D}\psi, \psi \right\} - \frac{2}{\mathrm{Le}}\left\{ \frac{1}{h}, \psi \right\} = \frac{\mathrm{Pm}}{\mathrm{Lu}}\mathcal{D}\nabla^2\psi + \frac{1}{2}\boldsymbol{\mathcal{Q}}\left((\boldsymbol{\nabla} \times \mathbf{B}) \times \mathbf{B}\right). \tag{2.50}$$

By identifying the projection operator that arises in the weak form of the momentum equation it is apparent how we can include additional forces, as long as the boundary conditions on $\mathbf{u}$ remain the same. We recall that the non-penetration boundary condition is strictly speaking insufficient for the viscous case, where the no-slip condition should be satisfied. However, when considering a very small viscosity, the boundary layer is so thin that one may neglect it to describe the fluid dynamics in the bulk. The influence of the viscous boundary layer is then parameterized by an additional forcing term, called Ekman pumping (e.g. Schaeffer and Cardin, 2005; Gastine, 2019).

2.5 Lagrangian formalism

In this section an alternative approach to the derivation of a QG model is given, starting from the Lagrangian density of an ideal MHD system. A complete introduction to the variational principle is beyond the scope of this section and the reader is referred to the book by Lanczos (1986) for a historical and conceptual approach, as well as a complete mathematical description. Deriving reduced equations through the variational approach is already established in atmospheric sciences (e.g. Salmon, 1983; Tort and Dubos, 2014), and approaches for shallow layer MHD have been made (Dellar, 2003, 2004). Here, this approach is applied to rapidly rotating MHD in a planetary core. Dynamically consistent z-averaged equations are derived, leading to a set of scalar QG equations similar to those derived previously.
The principle of stationary action S says that the variation of the action vanishes

$$\delta S = \delta \int L \, \mathrm{d}t = \delta \iint \mathcal{L} \, \mathrm{d}V \, \mathrm{d}t = 0, \tag{2.51}$$

with the Lagrangian L being the volume integral of the Lagrangian density $\mathcal{L}$. The Lagrangian density can be seen physically as the energy density of the system and thus the Lagrangian is the energy of the whole system at one point in time. Classically, the Lagrangian is written as

$$L = T - V, \tag{2.52}$$

with V the potential energy and T the kinetic energy

$$T = \int_{\mathcal{V}} \frac{1}{2} \rho \mathbf{u}^2 \, \mathrm{d}V. \tag{2.53}$$

The potential energy depends on the considered system and can be for example the gravitational potential or the magnetic energy.
The Lagrangian density $\mathcal{L}$ of an ideal, incompressible and constantly rotating MHD system, depending on position $\mathbf{r}$, velocity $\mathbf{u}$ and time t is written as

$$\mathcal{L}(\mathbf{r}, \mathbf{u}, t) = \rho \left(\frac{1}{2} \mathbf{u}^2 + \boldsymbol{\Omega} \times \mathbf{r} \cdot \mathbf{u} - \frac{1}{2\mu_0 \rho} \mathbf{B}^2 - \Pi \boldsymbol{\nabla} \cdot \mathbf{u} \right), \tag{2.54}$$

with the so-called Lagrange multiplier Π used to enforce mass conservation $\boldsymbol{\nabla} \cdot \mathbf{u} = 0$, and the term $\boldsymbol{\Omega} \times \mathbf{r} \cdot \mathbf{u}$ that has to be considered in the rotating reference frame.

The velocity is given as $\mathbf{u} = d_t\mathbf{r} = \partial_t\mathbf{r} + (\mathbf{u}\cdot\boldsymbol{\nabla})\,\mathbf{r}$. Because the fluid is ideal, the conservation of magnetic flux is given by the ideal induction equation

$$\frac{\partial\mathbf{B}}{\partial t} = \boldsymbol{\nabla}\times(\mathbf{u}\times\mathbf{B})\,. \tag{2.55}$$

A particle is identified by the Lagrangian labels $\mathbf{r}_0 = (x_0, y_0, z_0)$, for which the fluid is at equilibrium at some time $t = 0$. It's path $\mathbf{r}(\mathbf{r}_0, t)$ is given by

$$\mathbf{r} = \mathbf{r}(\mathbf{r}_0, t). \tag{2.56}$$

This mapping is taken to be volume preserving, so that the volume element is unit,

$$F = \frac{\partial(x,y,z)}{\partial(x_0,y_0,z_0)} = \begin{vmatrix} \frac{\partial x}{\partial x_0} & \frac{\partial y}{\partial x_0} & \frac{\partial z}{\partial x_0} \\ \frac{\partial x}{\partial y_0} & \frac{\partial y}{\partial y_0} & \frac{\partial z}{\partial y_0} \\ \frac{\partial x}{\partial z_0} & \frac{\partial y}{\partial z_0} & \frac{\partial z}{\partial z_0} \end{vmatrix} = 1. \tag{2.57}$$

Since the goal is to establish dynamically consistent depth-averaged equations, a fluid element is restricted to move in columns (Salmon, 1983; Dellar and Salmon, 2005; Dellar, 2011). We assume, without loss of generality, $\boldsymbol{\Omega} = \Omega\mathbf{1}_z$. The columnar motion hypothesis consists in two assumptions. First, the independence of a particle's horizontal coordinates on the particle's initial position z_0 along $\mathbf{1}_z$, so that

$$x = x(x_0, y_0, t), \tag{2.58}$$

$$y = y(x_0, y_0, t). \tag{2.59}$$

Second, a particle initially on the boundary stays on it. For an equatorially symmetric domain of column height $2h(x,y)$ this translates to

$$z = \pm h(x,y) \quad \text{at} \quad z_0 = \pm h_0(x_0,y_0), \tag{2.60}$$

where $h_0(x_0, y_0) = h_0(x_0, y_0, t = 0)$ is the column half height of the particle at $t = 0$. This can be generalized to equatorially asymmetric domains, but is not considered here for simplicity.

Following Miles and Salmon (1985), the volume element reduces to

$$F = \frac{\partial(x,y)}{\partial(x_0,y_0)}\frac{\partial z}{\partial z_0} = 1. \tag{2.61}$$

Integrating over z_0 and using (2.60) we find that

$$\frac{z}{h(x,y)} = \frac{z_0}{h_0(x_0,y_0)}, \tag{2.62}$$

and, if the column height does not explicitly depend on time, the vertical velocity u_z is given by

$$u_z = \frac{dz}{dt} = \frac{z_0}{h_0}\frac{dh}{dt} = \frac{z_0}{h_0}\left(\mathbf{u}_\perp\cdot\nabla_\perp h\right) = \frac{z}{h}\left(\mathbf{u}_\perp\cdot\nabla_\perp h\right). \tag{2.63}$$

Together with the incompressibility of the flow it follows that $\boldsymbol{\nabla} \cdot (\mathbf{u}_\perp h) = 0$ and the horizontal velocity can again be written as (2.18). Once more we discover the expression (2.19)

$$\mathbf{u} = \mathbf{u}_\perp + u_z \mathbf{1}_z = \nabla\psi \times \nabla \left(\frac{z}{h}\right), \tag{2.64}$$

for the velocity. This might be unsurprising, realizing that we have made the same assumptions from a different perspective.

We can rewrite the magnetic energy by relating the variation of magnetic field to a variation of the position through the ideal induction equation

$$\boldsymbol{\delta}\mathbf{B} = \boldsymbol{\nabla} \times (\boldsymbol{\delta}\mathbf{r} \times \mathbf{B}). \tag{2.65}$$

Using the identity $(\boldsymbol{\nabla} \times \mathbf{A}) \cdot \mathbf{B} = \boldsymbol{\nabla} \cdot (\mathbf{A} \times \mathbf{B}) + \mathbf{A} \cdot (\boldsymbol{\nabla} \times \mathbf{B})$ the variation of the magnetic energy is rewritten as

$$-\frac{1}{\mu_0} \iint \boldsymbol{\delta}\mathbf{B} \cdot \mathbf{B} \, \mathrm{d}V \, \mathrm{d}t = -\frac{1}{\mu_0} \iint \boldsymbol{\nabla} \cdot ((\boldsymbol{\delta}\mathbf{r} \times \mathbf{B}) \times \mathbf{B}) + \boldsymbol{\delta}\mathbf{r} \cdot ((\boldsymbol{\nabla} \times \mathbf{B}) \times \mathbf{B}) \, \mathrm{d}V \, \mathrm{d}t \tag{2.66}$$

$$= -\frac{1}{\mu_0} \iint \boldsymbol{\nabla} \cdot ((\mathbf{B} \cdot \boldsymbol{\delta}\mathbf{r})\mathbf{B} - \mathbf{B}^2 \boldsymbol{\delta}\mathbf{r}) + \boldsymbol{\delta}\mathbf{r} \cdot ((\boldsymbol{\nabla} \times \mathbf{B}) \times \mathbf{B}) \, \mathrm{d}V \, \mathrm{d}t \tag{2.67}$$

The first term on the right hand side vanishes, when the boundary conditions on $\mathbf{u}$ and $\mathbf{B}$ are $\boldsymbol{\delta}\mathbf{r} \cdot \mathbf{n} = 0$ (non-penetration condition) and $\mathbf{B} \cdot \mathbf{n} = 0$ (perfectly conducting boundary condition), respectively. For $\mathbf{B} \cdot \mathbf{n} \neq 0$ the treatment of the boundary term is more complicated. The volume of the energy density encompasses all of $\mathbb{R}^3$, and we can subdivide it into the finite volume of the fluid interior and an infinitely extending exterior. Two surface terms arise, with two normal vectors of opposing sign. If the outside of the fluid volume is not a perfect conductor, $\mathbf{B}$ is continuous across the boundary. Then, if we additionally assume that $\boldsymbol{\delta}\mathbf{r}$ on the surface is the same for both sides of the surface integrals, the two surface integrals cancel out. In doing so we have neglected the discontinuity of $\boldsymbol{\delta}\mathbf{r}$ across the boundary. A proper mathematical description of the variation of $\boldsymbol{\delta}\mathbf{B}$ in the exterior is missing here, which should solely depend on $\boldsymbol{\delta}\mathbf{r}$ just below the surface of the fluid interior. The exterior part of the second term on the right hand side vanishes for a perfectly conducting or insulating exterior, with $\mathbf{B} = \mathbf{0}$ or $\mathbf{j} = \mathbf{0}$, respectively. In the following, we consider the surface term to vanish.

The remaining term is rewritten

$$-\iint \boldsymbol{\delta}\mathbf{r} \cdot (\mathbf{j} \times \mathbf{B}) \, \mathrm{d}V \, \mathrm{d}t = -\iint \left(\boldsymbol{\delta}\mathbf{r}_\perp + \frac{z}{h}(\boldsymbol{\delta}\mathbf{r}_\perp \cdot \nabla h)\mathbf{1}_z\right) \cdot (\mathbf{j} \times \mathbf{B}) \, \mathrm{d}V \, \mathrm{d}t \tag{2.68}$$

with $\mathbf{j} = \mu_0^{-1} \boldsymbol{\nabla} \times \mathbf{B}$ and the displacement of the form (2.64). Since the incompressibility constraint is independent of z, with $\boldsymbol{\nabla} \cdot \mathbf{u} = h^{-1} \boldsymbol{\nabla} \cdot (h\mathbf{u}_\perp) = 0$, the Lagrange multiplier is also a function of the horizontal coordinates only, $\Pi = \Pi(\mathbf{r}_\perp)$, so that

$$\int \Pi \cdot \nabla \mathbf{u} \mathrm{d}V = -\int_{\mathcal{V}} \mathbf{u} \cdot \nabla \Pi \, \mathrm{d}V = -\int_{\mathcal{V}} \mathbf{u}_\perp \cdot \nabla \Pi \, \mathrm{d}V. \tag{2.69}$$

The variation of the action now only consists of the variation of the horizontal velocity and horizontal displacement

$$\begin{aligned} \delta \iint \rho \Bigg(\frac{1}{2} \left(\mathbf{u}_\perp^2 + \frac{z^2}{h^2} \left(\mathbf{u}_\perp \cdot \nabla h \right)^2 \right) + \boldsymbol{\Omega} \times \mathbf{r}_\perp \cdot \mathbf{u}_\perp - \mathbf{u}_\perp \cdot \nabla \Pi \\ - \frac{1}{\rho} \left(\boldsymbol{\delta} \mathbf{r}_\perp + \frac{z}{h} (\boldsymbol{\delta} \mathbf{r}_\perp \cdot \nabla h) \mathbf{1}_z \right) \cdot (\mathbf{j} \times \mathbf{B}) \Bigg) \, \mathrm{d}V \, \mathrm{d}t. \end{aligned} \tag{2.70}$$

Following Salmon (1983) we obtain a z-averaged Lagrangian density

$$\begin{aligned} \hat{\mathcal{L}} = \int_{-h}^{h} \mathcal{L} \, \mathrm{d}z = & 2h\rho \left(\frac{1}{2} \left(\mathbf{u}_\perp^2 + \frac{1}{3} \left(\mathbf{u}_\perp \cdot \nabla h \right)^2 \right) + \boldsymbol{\Omega} \times \mathbf{r}_\perp \cdot \mathbf{u}_\perp - \mathbf{u}_\perp \cdot \nabla \Pi \right) \\ & - \left\langle \left(\mathbf{r}_\perp + \frac{z}{h} (\mathbf{r}_\perp \cdot \nabla h) \mathbf{1}_z \right) \cdot (\mathbf{j} \times \mathbf{B}) \right\rangle . \end{aligned} \tag{2.71}$$

This Lagrangian density is related to the variation of the action as

$$\delta S = \delta \int \int_{\mathcal{A}} \hat{\mathcal{L}} \, \mathrm{d}S \, \mathrm{d}t = 0, \tag{2.72}$$

with $\mathcal{A}$ the equatorial surface plane.
After partial integration this is equivalent to applying the Euler-Lagrange equation

$$\frac{d}{dt} \frac{\partial \hat{\mathcal{L}}}{\partial \mathbf{u}_\perp} - \frac{\partial \hat{\mathcal{L}}}{\partial \mathbf{r}_\perp} = 0, \tag{2.73}$$

to obtain the z-averaged vector momentum equation

$$\rho \frac{d}{dt} \left(\mathbf{u}_\perp + \frac{1}{3} \left(\mathbf{u}_\perp \cdot \nabla h \right) \nabla h \right) + 2\rho \, \boldsymbol{\Omega} \times \mathbf{u}_\perp = -\nabla \Pi + \frac{1}{2h} \left\langle \mathbf{j} \times \mathbf{B} + \frac{z}{h} \nabla h \mathbf{1}_z \cdot (\mathbf{j} \times \mathbf{B}) \right\rangle . \tag{2.74}$$

Unlike in the approaches presented before, we find a vector equation that carries a 2-D pressure-like term.
Let us define

$$\mathbf{v} = \mathbf{u}_\perp + \frac{1}{3} (\mathbf{u}_\perp \cdot \nabla h) \nabla h, \tag{2.75}$$

to rewrite the material derivative as

$$\frac{d\mathbf{v}}{dt} = \frac{\partial \mathbf{v}}{\partial t} + (\mathbf{u}_\perp \cdot \boldsymbol{\nabla}) \mathbf{v} \tag{2.76}$$

The scalar equations are obtained by replacing $\mathbf{u}_\perp = h^{-1}\boldsymbol{\nabla} \times \psi\mathbf{1}_z$ into (2.74) and taking the z-component of the curl of (2.74).
By applying the curl and taking the z-component on $\mathbf{v}$, we get

$$\begin{aligned}
\mathbf{1}_z \cdot \boldsymbol{\nabla} \times \mathbf{v} &= \mathbf{1}_z \cdot \boldsymbol{\nabla} \times \left(\mathbf{u}_\perp + \frac{1}{3}\left(\mathbf{u}_\perp \cdot \nabla h\right)\nabla h\right), \\
&= \mathbf{1}_z \cdot \boldsymbol{\nabla} \times \left(\frac{1}{h}\nabla\psi \times \mathbf{1}_z + \frac{1}{3h}\nabla\psi \times \mathbf{1}_z \cdot \nabla h \nabla h\right), \\
&= -\nabla \cdot \left(\frac{1}{h}\nabla\psi + \frac{1}{3h}\nabla h \times \left(\nabla\psi \times \nabla h\right)\right), \\
&= -\boldsymbol{\nabla} \cdot \mathbf{G}(\psi), \\
&= -\mathcal{D}\psi.
\end{aligned} \tag{2.77}$$

We find the same operator (2.43) that is derived in the Galerkin approach.
For the non-linear term we find

$$\mathbf{1}_z \cdot \boldsymbol{\nabla} \times ((\mathbf{u}_\perp \cdot \boldsymbol{\nabla})\mathbf{v}) = \boldsymbol{\nabla} \cdot \left((\mathbf{u}_\perp \cdot \boldsymbol{\nabla})\left(\mathbf{u}_\perp \times \mathbf{1}_z + \frac{1}{3}(\mathbf{u}_\perp \cdot \nabla h)\nabla h \times \mathbf{1}_z\right)\right), \tag{2.78}$$

$$= -\boldsymbol{\nabla} \cdot \left((\mathbf{u}_\perp \cdot \boldsymbol{\nabla})\left(\frac{1}{h}\nabla\psi + \frac{1}{3h}\nabla h \times (\nabla\psi \times \nabla h)\right)\right), \tag{2.79}$$

$$= -\boldsymbol{\nabla} \cdot ((\mathbf{u}_\perp \cdot \boldsymbol{\nabla})\mathbf{G}). \tag{2.80}$$

At this stage further simplifications were not made. We remark that this form of the non-linear term is likely not equivalent to the one found in the Galerkin approach.
The Coriolis force is again

$$\mathbf{1}_z \cdot \boldsymbol{\nabla} \times (2\boldsymbol{\Omega} \times \mathbf{u}_\perp) = 2\Omega\left\{\frac{1}{h}, \psi\right\}. \tag{2.81}$$

The pressure term vanishes naturally and the Lorentz force term is kept in an implicit form. The scalar momentum equation is given by

$$\mathcal{D}\frac{\partial\psi}{\partial t} + \boldsymbol{\nabla} \cdot \left(\left(\mathbf{u}_\perp \cdot \boldsymbol{\nabla}\right)\mathbf{G}\right) = 2\Omega\left\{\frac{1}{h}, \psi\right\} + \frac{1}{2\rho}\boldsymbol{\mathcal{X}}(\mathbf{j} \times \mathbf{B}), \tag{2.82}$$

with the operator

$$\boldsymbol{\mathcal{X}}(\mathbf{f}) = \mathbf{1}_z \cdot \boldsymbol{\nabla} \times \frac{1}{h}\left\langle \mathbf{f} + \frac{z}{h}\nabla h \mathbf{1}_z \cdot \mathbf{f}\right\rangle. \tag{2.83}$$

For the case of a columnar magnetic field (see the next section) it can be shown that $\boldsymbol{\mathcal{X}}(\mathbf{j} \times \mathbf{B}) = \boldsymbol{\mathcal{Q}}(\mathbf{j} \times \mathbf{B})$, but this does not necessarily hold in the general case. It is unclear why the inviscid part of the two scalar momentum equations (2.82) and (2.50) is not equivalent. Only the linear hydrodynamic part is exactly equivalent. Further investigations into the derivation of the scalar QG momentum equation seems to be necessary.

We have shown here how a depth-averaged momentum equation is obtained from the energy density of the system, without the need of first deriving a fully 3-D vector equation. As a side product from deriving the scalar momentum equation (2.82), the vector equation in the equatorial plane (2.74) is given. This equation can give us access to the quantity Π of the reduced system, that could be associated with a pressure. How Π relates to the 3-D pressure is unclear, as Π is only a function of the horizontal coordinates. Having access to the pressure of the QG equations is essential to investigate dynamic deformations at the CMB, that have been neglected here.

Another benefit of the Lagrangian approach is the natural adaptation to arbitrary coordinate systems through the Lagrangian labels. The relation of Lagrangian labels to Eulerian coordinates in space can be interpreted as a coordinate mapping. Through this, time dependent boundaries could be treated by a mapping of the Lagrangian labels that also depends on time. This is relevant to investigating the influence on core flows from a tidally deformed CMB (Sasao et al., 1980; Yoder et al., 1981).

A limitation of the Lagrangian approach to the reduced equations is the restriction to ideal fluids. The concept of the microscopically acting dissipation of energy inherently disagrees with the principle of least action (Lanczos, 1986).

2.6 Columnar magnetic field

To fully reduce our system to two dimensions an alternative representation of the magnetic field is needed. Approaches have been made using so-called squared products (Canet et al., 2009; Maffei and Jackson, 2017), which are z-averaged quantities arising in the reduced Lorentz force $\boldsymbol{\mathcal{W}}(\mathbf{j}\times\mathbf{B})$. So far, the system that arises had to be closed by neglecting boundary terms without proper physical justification. Only recently, Jackson and Maffei (2020) have proposed a new theoretical model that is able to close this system, by exploiting non-symmetric axial integrals in a spherical core. Here, we choose to represent the magnetic field similar to the velocity by a potential A, so that

$$\mathbf{B} = \mathbf{B}_\perp + B_z\mathbf{1}_z = \nabla A \times \nabla\left(\frac{z}{h}\right). \tag{2.84}$$

There are obvious limitations to this assumption and it is not supported by observations or theory. However, it has been used successfully to study magnetic modes in a 2-D MHD system (Canet et al., 2014; Labbé et al., 2015), and allows for significant computational simplification. Following Gerick et al. (2020) we apply the projection operator (2.39) to the Lorentz term to get

$$\boldsymbol{\mathcal{Q}}\left((\boldsymbol{\nabla}\times\mathbf{B})\times\mathbf{B}\right) = 2\left\{\frac{1}{h}\mathcal{D}A, A\right\}, \tag{2.85}$$

analogous to the non-linear term (2.47). The scalar momentum equation (2.50) is then written

$$\mathcal{D}\frac{\partial\psi}{\partial t} + \left\{\frac{1}{h}\mathcal{D}\psi, \psi\right\} = 2\Omega\left\{\frac{1}{h}, \psi\right\} + \left\{\frac{1}{h}\mathcal{D}A, A\right\}. \tag{2.86}$$

It remains to find a reduced induction equation. By considering

$$\mathbf{u}\times\mathbf{B} = \frac{1}{h^2}\nabla\psi\times\nabla A - \frac{z}{h^3}\left\{\psi, A\right\}\nabla h, \tag{2.87}$$

$$= \frac{C}{h}\mathbf{1}_z - \frac{Cz}{h^2}\nabla h, \tag{2.88}$$

with $C = \frac{1}{h}\left\{\psi, A\right\}$, and taking the curl

$$\boldsymbol{\nabla}\times(\mathbf{u}\times\mathbf{B}) = \frac{1}{h}\nabla C\times\mathbf{1}_z - \frac{z}{h^2}\nabla C\times\nabla h \tag{2.89a}$$

$$= \nabla C\times\nabla\left(\frac{z}{h}\right), \tag{2.89b}$$

we find an expression for the right hand side of the ideal induction equation. Since the left hand side is simply

$$\frac{\partial\mathbf{B}}{\partial t} = \nabla\left(\frac{\partial A}{\partial t}\right)\times\nabla\left(\frac{z}{h}\right), \tag{2.90}$$

the induction equation reduces to

$$\frac{\partial A}{\partial t} = \frac{1}{h}\left\{\psi, A\right\}. \tag{2.91}$$

This fully 2-D model has been used in the sphere to solve for MHD modes (Labbé et al., 2015), and has been used as well in our study of torques in the ellipsoid.

2.7 Non-axisymmetric core volume

To estimate the efficiency of topographic coupling to transfer axial angular momentum from the core to the mantle one has to consider a non-axisymmetric core. Previously, most QG models for core modeling have been tailored to axisymmetric volumes (or Cartesian periodic boxes), with the exception of the models by Bell and Soward (1996) and Herrmann and Busse (1998) who investigated convection in an annulus of sinusoidally modulated column height. More recently Calkins et al. (2012) studied the effect of a meridional ridge that perturbs the otherwise cylindrically symmetric annulus subject to thermal convection. The torque exerted onto the CMB was not investigated in these studies. To study the torque in a full volume that is topologically equivalent to a sphere we considered the ellipsoid. Unfortunately, the simple geometry does not imply a simple treatment of the mathematical problem. We have also laid out the building blocks to study more complex geometries, by considering non-orthogonal coordinates. The approaches followed here have the necessary condition that there exist no non-closed geostrophic contours. This is important when investigating the torque of flows (or modes, more specifically), as discussed in Chapter 4 and 6. Some technical aspects on how to discretize such a non-axisymmetric model are presented.

The simplest non-axisymmetric geometry that deviates from the sphere is an ellipsoid of semi axes a, b and c, defined by

$$\frac{x^2}{a^2} + \frac{y^2}{b^2} + \frac{z^2}{c^2} = 1. \tag{2.92}$$

For simplicity, we consider the semi axis c aligned with the rotation axis $\mathbf{1}_\Omega = \mathbf{1}_z$, so that x and y are the horizontal coordinates in the equatorial plane. The semi axis c may be the same as one of a or b, technically making the volume a spheroid, as for the study of axial torques the important parameter is the equatorial ellipticity

$$\epsilon = \frac{a^2 - b^2}{a^2 + b^2}. \tag{2.93}$$

The influence of polar flattening on QG inertial modes has been previously investigated elsewhere (Maffei et al., 2017) and is not discussed here, although a study of the influence on MHD modes is necessary.

To investigate flows in an ellipsoid one obvious consideration is the so-called Poincaré-transform, that scales the Cartesian coordinates by the semi-axes. Spatial derivatives are also scaled by the semi axes and one can derive an equation that maps the ellipsoidal problem to a spherical problem. This equation has many difficulties that arise and an easy removal of the pressure term, as for the non-transformed equations, is not possible. We do not follow this approach and instead consider a basis of polynomial flows in the ellipsoid, following what has been put forward by Lebovitz (1989). In the second part of this section I outline how non-orthogonal coordinates can be used for a description with elliptic-cylindrical coordinates in the ellipsoid and general coordinates in arbitrary geometries.

2.7.1 Cartesian basis in the ellipsoid

The Galerkin approach is also commonly known as the finite element method. It has not been very popular in incompressible fluid dynamics applications, as implicit terms arise when considering a time stepped integrator where a linear system has to be solved at each time step (Durran, 2013). For the linear system considered here, that does not explicitly depend on time, these issues are not present and the linear system is constructed only once. Lebovitz (1989) has shown that an inviscid and incompressible hydrodynamic flow in the ellipsoid is representable by an infinite sum of basis vectors that are constructed through Cartesian monomials. This has been shown to hold for any inviscid and incompressible flow, including the magnetic case (Backus and Rieutord, 2017; Ivers, 2017). This realization gives great power to the Galerkin approach introduced in section 2.4, as Cartesian monomials are easily integrated over the volume of the ellipsoid. If one is able to create a Cartesian velocity basis in the ellipsoid, we can project the 3-D equations, that are valid in any geometry, onto the subset of velocities in the ellipsoid to find equations that govern flows in this geometry.

Lebovitz (1989) has proposed a method to construct a basis of vectors from Cartesian monomials for the set of polynomial flows $\boldsymbol{\mathcal{P}}_N(\mathcal{V})$ of degree N in the volume $\mathcal{V}$. These Cartesian monomials can be divided into the monomials independent of z and all others, so that

$$p_i = \begin{cases} 1, x, y, xy, ..., x^{N-1}, y^{N-1} & \text{for} \quad i = 1, ..., N_2 \\ z, xz, yz, ..., z^{N-1} & \text{for} \quad i = N_2 + 1, ..., N_4 \end{cases} \tag{2.94}$$

with $N_2 = N(N+1)/2$ and $N_4 = N(N+1)(N+2)/6$. The $N_3 = 2N_3 + N_2$ basis vectors $\mathbf{u}_i$ are then constructed as

$$\begin{aligned} \mathbf{u}_i &= \boldsymbol{\nabla} \times (p_i F \mathbf{1}_x) && \text{for} \quad i = 1, ..., N_4, && (2.95a) \\ \mathbf{u}_{N_2+i} &= \boldsymbol{\nabla} \times (p_i F \mathbf{1}_y) && \text{for} \quad i = 1, ..., N_4, && (2.95b) \\ \mathbf{u}_{2N_2+i} &= \boldsymbol{\nabla} \times (p_i F \mathbf{1}_z) && \text{for} \quad i = 1, ..., N_2, && (2.95c) \end{aligned}$$

with $F = 1 - x^2/a^2 - y^2/b^2 - z^2/c^2$, which ensures that $\mathbf{u} \cdot \mathbf{n} = 0$ on the boundary. This basis can also be used for the 3-D magnetic field satisfying the perfectly conducting boundary condition (Vidal et al., 2016, 2019). It has been used in the literature to calculate inviscid inertial modes the ellipsoid (e.g. Vidal and Cébron, 2017). In fact, all inertial modes are completely described by polynomials in the ellipsoid, and in return inertial modes form a complete basis for any inviscid and incompressible polynomial flow in the ellipsoid (Backus and Rieutord, 2017; Ivers, 2017, more details in chapter 3). An alternative basis for $\boldsymbol{\mathcal{P}}_N(\mathcal{V})$ in the ellipsoid has been proposed by Ivers (2017), based on spherical harmonics in a poloidal-toroidal decomposition. If these spherical harmonics are written in Cartesian coordinates, we may equivalently use this basis (see appendix in Gerick et al., 2021).

As outlined by Gerick et al. (2020), a 2-D polynomial decomposition in the Cartesian coordinates can be obtained for QG velocities of the form (2.19) in an ellipsoid, similar to the 3-D case. To satisfy the polynomial form of the velocity components, the stream function must satisfy (Maffei et al., 2017)

$$\psi = h^3 \, p(x, y) = h^3 \sum_i \hat{\alpha}_i p_i, \tag{2.96}$$

with the complex-valued coefficients $\hat{\alpha}_i$ and the monomials (2.94) with $i \in [0, N_2]$. At any position in the equatorial plane (x, y) we have

$$\frac{h^2}{c^2} = 1 - \frac{x^2}{a^2} - \frac{y^2}{b^2}. \tag{2.97}$$

Thus, if we additionally define $G = h^2/2$, the gradient of the column height is related to the gradient of G, which is polynomial, by

$$h\nabla h = \nabla G = -c^2 \begin{pmatrix} x/a^2 \\ y/b^2 \\ 0 \end{pmatrix}. \tag{2.98}$$

Substituting $\psi_i = h^3 p_i$ into (2.19) and using (2.98), the QG basis vectors $\mathbf{u}_i$ can be written as

$$\mathbf{u}_i = h^2 \nabla p_i \times \mathbf{1}_z + 3p_i \nabla G \times \mathbf{1}_z - z\nabla p_i \times \nabla G. \tag{2.99}$$

We may use this basis to project our linearized 3-D equation to directly obtain a linear system that is solvable for QG modes in the ellipsoid. Each forcing $\mathbf{f}(\mathbf{u}_j|\mathbf{B}_j)$ in the momentum equation (inertial, Coriolis, pressure, and Lorentz force) is projected onto $\mathbf{u}'_i$. Depending on the model, $\mathbf{u}'_i$ is either QG (2.99) or 3-D (2.95). Analogously the induction equation is projected onto the basis vectors $\mathbf{B}'_i$. In a discrete form, each term in (2.36) can be written as

$$f_{ij} = \int_{\mathcal{V}} \mathbf{u}'_i \cdot \mathbf{f}(\mathbf{u}_j|\mathbf{B}_j)\,\mathrm{d}V, \tag{2.100}$$

with $\mathbf{f}(\mathbf{u}_j|\mathbf{B}_j)$ the inertial, Coriolis, pressure or Lorentz force. Because the integrand of (2.100) is a Cartesian polynomial, we can integrate it exactly over the volume by using (Lebovitz, 1989)

$$\int_{\mathcal{V}} x^i y^j z^k\,\mathrm{d}V = \begin{cases} abc\frac{a^i b^j c^k \Gamma((1+i)/2)\Gamma((1+j)/2)\Gamma((1+k)/2)}{\Gamma((5+i+j+k)/2)} & \text{for } i,j,k \text{ even} \\ 0 & \text{else} \end{cases}, \tag{2.101}$$

with $\Gamma(n) = (n-1)!$. This may be written in terms of factorials, by rewriting $\Gamma(n+1/2) = \sqrt{\pi}(2n)!(4^n n!)^{-1}$. In this way we create coefficient matrices U_{ij}, C_{ij} and L_{ij} for the inertial, Coriolis and Lorentz force, respectively. The pressure force vanishes in this step. Analogously, the induction equation is projected onto the basis $\mathbf{B}'_i$ and the resulting coefficient matrices of the temporal change of the magnetic field and magnetic advection are B_{ij} and V_{ij}, respectively. Due to the properties of the inner product, U_{ij} and B_{ij} are identical and Hermitian. In case the bases are orthonormal, U_{ij} and B_{ij} are identity matrices. The resulting generalized eigen problem is

$$\mathrm{i}\omega\mathbf{M}\mathbf{x} = \mathbf{D}\mathbf{x}. \tag{2.102}$$

with

$$\mathbf{M} = \begin{pmatrix} U_{ij} & 0 \\ 0 & B_{ij} \end{pmatrix}, \qquad \mathbf{D} = \begin{pmatrix} C_{ij} & L_{ij} \\ V_{ij} & 0 \end{pmatrix}, \tag{2.103}$$

and $\mathbf{x} = (\alpha_j, \zeta_j)$, so that $\mathbf{u} = \sum_j \alpha_j \mathbf{u}_j$ and $\mathbf{B} = \sum_j \zeta_j \mathbf{B}_j$. The dimensions of each sub-matrix depends on the bases chosen for the velocity and the magnetic field.

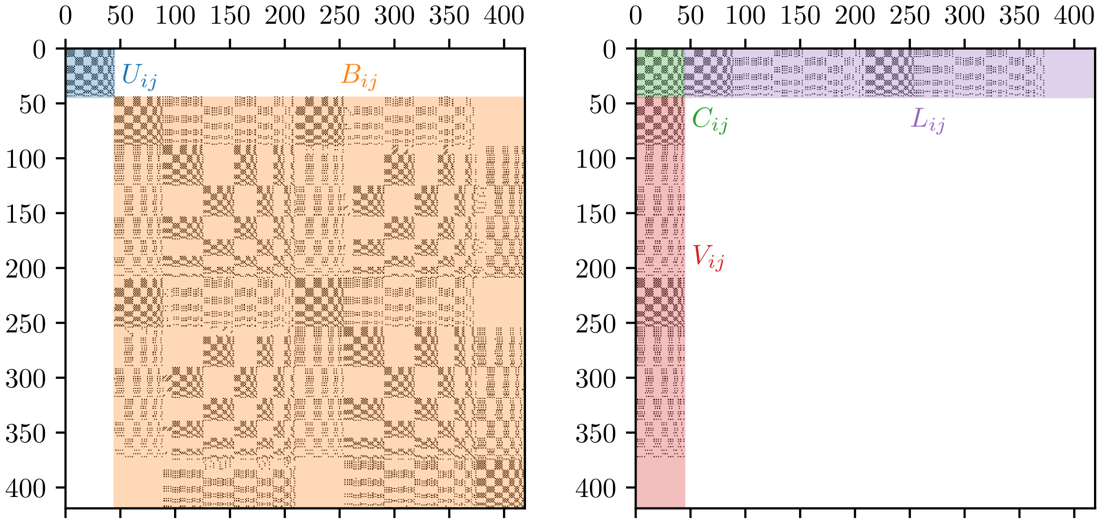

Figure 2.3: Sparse entries of the matrices **M** (left) and **D** (right) for the ellipsoidal MHD hybrid model using a Galerkin approach at $N = 9$. The individual sub-matrices have been colored and labelled, to aid understanding the structure and dimensions of the total matrices.

As presented in Gerick et al. (2020), in case of the QG model we may use the stream function ψ' of the form (2.96) as a test function and project the scalar momentum equation (2.86) on this basis, so that (2.100) reduces to

$$f_{ij} = \int_{\mathcal{A}} \tilde{\psi}_i f(\tilde{\psi}_j|\tilde{A}_j)\,\mathrm{d}A, \tag{2.104}$$

where now $f(\tilde{\psi}|\tilde{A})$ corresponds to a force in the scalar momentum equation (2.86). We have verified that it is exactly equivalent to project the 3-D momentum equation (2.100) onto the QG velocity basis (2.99) and to project the scalar momentum equation (2.86) onto the basis for the stream function (2.96).

For details on the implementation, see Section 3.6.2. The matrices **M** and **B** that arise in the case of a hybrid model in the ellipsoid, with a QG velocity and a 3-D magnetic field are shown in Figure 2.3.

2.7.2 Non-orthogonal coordinate systems

In an ellipsoid the geostrophic contours are ellipses of equal aspect ratio. Thus, even in the simple geometry of the ellipsoid, to have one coordinate constant along a geostrophic contour requires a non-orthogonal coordinate system (if the contours were confocal ellipses the orthogonal ellipsoidal coordinates could be used). Basics of tensor calculus that are used in this Section are summarized in Appendix A. The issue of non-orthogonal coordinates has been avoided by considering the transformed

Cartesian coordinates for the ellipsoid, where such a transformation is straightforward when considering a Galerkin approach. For more complex geometries, but where geostrophic contours are still closed, it is appropriate to define a coordinate system that follows such contours of constant column height h with

$$\mathbf{q} = (h, \varphi, z), \tag{2.105}$$

with $\varphi \in [0, 2\pi]$ the pseudo-azimuth, so that $\mathbf{r}(h, \varphi = 0, z) = \mathbf{r}(h, \varphi = 2\pi, z)$. The geostrophic part of the velocity can be regarded as the average over a geostrophic column. This is equivalent to considering a stream function

$$\tilde{\psi}(h) = \frac{\oint \psi(h, \varphi)\,\mathrm{d}\varphi}{\oint \mathrm{d}\varphi}, \tag{2.106}$$

depending only on the geostrophic column half height h. In this coordinate system we can thus describe geostrophic motions by

$$\mathbf{u}_G = \nabla\tilde{\psi}(h) \times \nabla\left(\frac{z}{h}\right) = u_G(h, \varphi)\mathbf{g}_2, \tag{2.107a}$$

with $u_G(h, \varphi) = (Jh)^{-1}\frac{\partial\tilde{\psi}}{\partial h}$ and the covariant basis vector in φ-direction $\mathbf{g}_2$. The Jacobian of the coordinate mapping is $J(h, \varphi, z) = \det(g_{ij})$. The metric elements are given as $g_{ij} = \mathbf{g}_i \cdot \mathbf{g}_j$. If $J = J(h)$, e.g. in the case of the sphere or the ellipsoid, the geostrophic pressure p_G is well defined and depends on h only

$$2\rho\mathbf{u}_G \times \mathbf{\Omega} = -\nabla p_G \tag{2.108a}$$

$$\Leftrightarrow \frac{2\rho\Omega}{h}\frac{\partial\tilde{\psi}}{\partial h} = \frac{\partial p_G}{\partial h}. \tag{2.108b}$$

This could lead us to the conclusion that, as long as the Jacobian J is just a function of h, no motions that follow geostrophic contours can exert a pressure torque on the enclosing boundary. Gerick et al. (2020) have shown that this conclusion is wrong and the pressure associated with any non-steady flow cannot be fully described by a geostrophic pressure (see Chapter 4 for more details).

In the ellipsoid, mapping from the Cartesian coordinates to $\mathbf{q}$ is defined as

$$x = a\sqrt{1-h^2}\cos\varphi, \tag{2.109a}$$

$$y = b\sqrt{1-h^2}\sin\varphi, \tag{2.109b}$$

$$z = cz, \tag{2.109c}$$

with the volume element $J = abch$. The metric tensor is given by

$$\mathbf{G} = \begin{pmatrix} a^2\cos^2(\varphi) + b^2\sin^2(\varphi) & \frac{h\left(-a^2+b^2\right)\sin(2\varphi)}{2} & 0 \\ \frac{H\left(-a^2+b^2\right)\sin(2\varphi)}{2} & h^2\left(a^2\sin^2(\varphi) + b^2\cos^2(\varphi)\right) & 0 \\ 0 & 0 & c^2 \end{pmatrix}. \tag{2.110}$$

Unlike for the orthogonal cylindrical coordinates, this metric tensor is not diagonal and its elements depend on φ. Thus, the vector calculus operators couple the equation in φ. Handling the reduced equations in a classical discretization, i.e. a Fourier decomposition in φ and a polynomial or discrete grid description in h, is challenging. In more complex geometries, this approach is inevitable, but requires even more complex mappings, metric tensors and Christoffel symbols. These challenges require the use of computer algebra systems (CAS). A package in the Julia programming language that is able to calculate any coordinate mapping and all associated tensor calculus operators has been developed[1]. It is based on the *SymPy* CAS (Meurer et al., 2017) and is solely limited by computational efficiency of this toolbox to compute arbitrary complex systems. Technically, this should allow us to transform the scalar QG equations to an arbitrary geometry, as long as a mapping $\mathbf{r} \to \mathbf{q}$ exists.

Approaches to discretize the non-orthogonal system

A classical way of discretizing a partial differential equation (PDE) and the differential operators within them, is finite differencing. The idea comes from a Taylor expansion of a function $f(x)$ around a discrete point x_0, so that

$$f(x+x_0) = f(x_0) + \left.\frac{\partial f(x)}{\partial x}\right|_{x=x_0}(x-x_0) + \left.\frac{\partial^2 f(x)}{\partial x^2}\right|_{x=x_0}(x-x_0)^2 + \ldots \tag{2.111}$$

Each derivative of f can then be obtained by neglecting all terms of higher order and equating to the derivative, e.g. the first derivative is given by

$$\left.\frac{\partial f}{\partial x}\right|_{x=x_0} \approx \frac{f(x+x_0)-f(x_0)}{x-x_0}. \tag{2.112}$$

To obtain a discrete expression of these finite differences, the spatial domain is separated into a grid of discrete sampling points $x_i = x_1, \ldots, x_N$. The higher our resolution the more small scale dynamics can be captured, at the obvious cost of more computational complexity for higher resolutions. The accuracy of this approximation clearly depends on the number and distance of grid points, that may be regularly or irregularly spaced. Different degrees of approximation exist, that take more neighboring points in the grid into account as the degree is increased (Fornberg, 1988). Boundary conditions are not as straight forward as the differencing within the domain, but for example by using so-called ghost points (points outside the domain that are not solved for) we can include the boundary condition appropriately. An easy example are the periodic boundary conditions for a discrete grid $x_i = x_1, \ldots, x_N$. Then the boundaries are simply linked by the ghost points to the end $x_0 = x_N$ and beginning $x_{N+1} = x_1$ of the grid. The ease of implementation of finite differencing has lead to its popularity as a tool to numerically solve partial differential equations.

---

[1] The package is available at `https://github.com/fgerick/CurvilinearCalculus.jl`.

However, finite differencing comes at a cost of accuracy and convergence of the solution (Durran, 2013). An implementation that is able to handle irregular spaced grids and complex boundary conditions at arbitrary approximation order is under development in the Julia programming language[2].

As is common in numerical calculations, symmetries of the problem at hand allow for faster and more accurate calculation of solutions. Especially periodicity in one or more of the spatial direction can be exploited for significant computational reductions. The discrete Fourier transform is now widely used in many scientific computations and is available through the *FFTW* package, famous for its high performance (Frigo and Johnson, 2005). When they are suitable, the convergence of spectral methods for solving PDEs is usually much better than, e.g., finite differences (Durran, 2013). In cylindrical coordinates the azimuthal coordinate ϕ is periodic and we can represent a function $f(s,\phi)$ along this coordinate by its Fourier components $\hat{f}_m(s)$, so that (Fourier, 1822)

$$f(s,\phi) = \int_{-\infty}^{\infty} \hat{f}_m(s) \exp(\mathrm{i}m\phi)\,\mathrm{d}m. \tag{2.113}$$

This Fourier transform (2.113) can be carried out analytically in simple cases, where the equations do not explicitly depend on ϕ. The derivatives of f with respect to ϕ are then simply

$$\frac{\partial^k f}{\partial \phi^k} = \int_{-\infty}^{\infty} (\mathrm{i}m)^k \hat{f}_m \exp(\mathrm{i}m\phi)\,\mathrm{d}m. \tag{2.114}$$

When the PDE has no explicit dependency in ϕ, the individual Fourier components m are decoupled and one can solve the equations for each m independently. This is for example the case in the hydrodynamic linear QG problem (e.g. equation 3.6 in Maffei et al., 2017).

If an explicit dependency on ϕ is introduced, either through a non-axisymmetric background magnetic field $\mathbf{B}_0$ or non-orthogonal coordinates, the Fourier components are no longer decoupled and the system is not closed. A sufficiently large truncation M of the Fourier decomposition is then needed to ensure that dynamics occurring on wave numbers $m \ll M$ are well resolved.

Consider the following toy PDE

$$g(\phi)\frac{\partial f(\phi)}{\partial \phi} = f(\phi), \tag{2.115}$$

where an explicit ϕ dependence is introduced through a function $g(\phi)$. By using the convolution theorem, Fourier transforming gives us

$$\int_{-\infty}^{\infty} \hat{g}_k \mathrm{i}m \hat{f}_m \exp(\mathrm{i}(m-k)\phi)\,\mathrm{d}m = \int_{-\infty}^{\infty} \hat{f}_m \exp(\mathrm{i}m\phi)\,\mathrm{d}m, \tag{2.116}$$

---

[2] Available at `https://github.com/SciML/DiffEqOperators.jl`

with $\hat{g}_k$ the k-th Fourier component of $g(\phi)$. Then, a comparison of coefficients leads to a system of equations

$$\sum_{|k+m|\leqslant M} \mathrm{i}m\hat{g}_k\hat{f}_m\delta_{m-k,m} = \sum_{|k+m|\leqslant M} \hat{f}_m. \tag{2.117}$$

Analogous to the toy example we can write the stream function and magnetic potential as

$$\psi(s_i,\phi_j,t) = \sum_{m=-M}^{M} \alpha_{im}\hat{\psi}_m(s_i)\exp(\mathrm{i}(m\phi_j+\omega t)), \tag{2.118a}$$

$$A(s_i,\phi_j,t) = \sum_{m=-M}^{M} \zeta_{im}\hat{A}_m(s_i)\exp(\mathrm{i}(m\phi_j+\omega t)). \tag{2.118b}$$

Such a discretization has been used for example by Labbé et al. (2015), where the convolution is done analytically. This is feasible in their case, where only a $\cos(n\phi)$ dependency is introduced by the background magnetic field. For more complex cases this has to be done numerically. The combination of Fourier decomposition in azimuth and finite differencing in cylindrical radius allows for the full discretization of the scalar momentum equations for the fully 2-D QG models. Choosing a cylindrical radial grid resolution N and a truncation in azimuth M, the resulting linear system is given by the two matrices $\mathbf{M},\mathbf{D} \in \mathbb{C}^{N(2M+1)\times N(2M+1)}$ and the coefficient vector $\mathbf{x} \in \mathbb{C}^{N(2M+1)}$, that contains all coefficients α_{im}, ζ_{im}.

As an example for the sparsity of these matrices, $\mathbf{M}$ and $\mathbf{D}$ are shown in Figure 2.4, for the Malkus problem, where $\mathbf{B}_0 = s\mathbf{1}_\varphi$ in the ellipsoidal cylindrical coordinates, with $M = 8$ and $N = 32$. Here, (2.86) is discretized using the CAS toolbox to symbolically calculates the generalized equation for the coordinates in the ellipsoid. Then, the azimuthal direction is decomposed by its Fourier components and handles the products of explicit φ dependencies in front of the azimuthal derivatives accordingly. The cylindrical radial dependency is discretized by a suitable finite differencing order with Dirichlet boundary conditions ($\psi = 0$ at $s = 0, 1$). All this happens in code and we only have to define the coordinate transform and the operators $\mathcal{D}$ and $\{\cdot,\cdot\}$ that appear in the equations. The sparsity of the matrices is apparent and we can take full advantage of this by storing them in a sparse matrix format.

An alternative for discretizing the cylindrical radius is a polynomial decomposition. Maffei et al. (2017) showed that the stream function $\psi(s,\phi)$ of QG inertial modes are exactly described by Jacobi polynomials in s. A decomposition in Jacobi polynomials thus seems appropriate. An advantage of such a representation is obvious when the modes are exactly described by Jacobi polynomials. For other modes it is not trivial that the representation is really advantageous compared to finite differences, although it might well be. A disadvantage of the polynomial decomposition is that derivative operators are not local. That means technically, that the matrix representation of these derivative operators is dense, not sparse, as in the finite differencing case. This

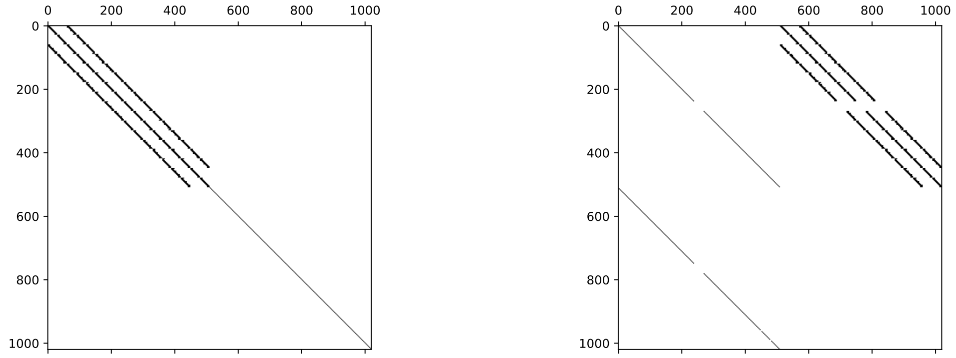

Figure 2.4: Sparse entries of the matrices **M** (left) and **B** (right) for the ellipsoidal QG Malkus model, discretized by Fourier and finite differences.

is not a constraint for small enough degrees. However, at large enough polynomial degree this becomes a memory constraint even on modern computers.

Chapter 3

Modes in a planetary core

Waves are present in most scenarios where a fluid description is suitable (Lighthill, 1978). It is therefore reasonable to assume that waves are also present in the liquid outer core. Waves are usually illustrated as perturbations oscillating periodically around an equilibrium state by a balance of inertia and a restoring force. For a planetary core, which is generally described as an incompressible, rapidly rotating and electrically conducting fluid, the restoring force can be for example the Coriolis or Lorentz force. Many waves have been derived theoretically from the governing equations already a long time ago. Examples, that are discussed here, include inertial waves (Thomson, 1880; Bryan and Darwin, 1889), Magneto-Coriolis waves (Lehnert, 1954; Hide, 1966; Malkus, 1967) and torsional Alfvén waves (Braginsky, 1970). In the following decades to their theoretical discovery many experiments have confirmed the existence of some of these waves (e.g. Oser, 1958; Fultz, 1959; Schmitt et al., 2008; Nornberg et al., 2010; Schmitt et al., 2013), and in the more recent years there has been some evidences for their existence also in Earth's core (see Section 3.5).
When oscillatory motions are considered in the entirety of the volume, i.e. including the influence of the enclosing boundary, one speaks of modes instead of waves. Here, we focus on inviscid MHD modes without considering buoyancy, with emphasis on the equatorially symmetric modes. For more detailed introductions into the theory of modes, also in the presence of buoyancy, it is referred to Roberts and Soward (1972) and Finlay (2008). In general, to obtain modes as a solution to the governing equation two assumptions have to be made. First, the velocity can be separated into a steady background $\mathbf{u}_0(\mathbf{r})$ and a fluctuating part $\tilde{\mathbf{u}}(\mathbf{r}, t)$, so that $\mathbf{u} = \mathbf{u}_0 + \tilde{\mathbf{u}}$. Second, the time dependency of the fluctuating part is assumed periodic, so that $\tilde{\mathbf{u}} = \tilde{\mathbf{u}}'(\mathbf{r}) \exp(\mathrm{i}\omega t)$. The same is done for the magnetic field, when included, so that $\mathbf{B} = \mathbf{B}_0 + \tilde{\mathbf{B}}' \exp(\mathrm{i}\omega t)$. In the remainder, unless specified, the fluctuating part is simply written as $\mathbf{u}$ and $\mathbf{B}$.

3.1 Inertial modes

First investigated by Thomson (1880) in a cylinder and calculated in the sphere by (Bryan and Darwin, 1889), inertial oscillations in a rotating fluid have been known for a long time. Inertial oscillations arise in rotating fluid when a fluid mass is moved perpendicular to the axis of rotation away from the equilibrium mean zonal motion. Then, the acting Coriolis acceleration deflects the motion of the fluid mass and forces it to move in a circular-like motion around the mean flow. Unless damped by viscosity, this motion is kept indefinitely.

Inviscid inertial modes can be sought as solutions to the linear hydrodynamic problem

$$\mathrm{i}\omega\mathbf{u} + 2\boldsymbol{\Omega}\times\mathbf{u} + \nabla p = 0, \tag{3.1}$$

accompanied by the inviscid boundary condition $\mathbf{u}\cdot\mathbf{n} = 0$. If an infinitely extending volume is considered, this boundary condition can be omitted. The solutions to (3.1) are then found by considering a plane-wave ansatz and are called inertial waves. We focus on the boundary value problem here. When eliminating the velocity the so-called Poincaré-equation

$$\nabla^2 p - \frac{4}{\omega^2}\left(\boldsymbol{\Omega}\cdot\nabla\right)^2 p = 0, \tag{3.2}$$

is obtained. It can be shown (Greenspan, 1968), that infinitely many solutions $(\omega_k, \mathbf{u}_k)$ exist which satisfy $|\omega_k| \leqslant 2\Omega$. These solutions are called inertial modes and are orthogonal, if not degenerate

$$(\omega_i - \omega_j)\int_{\mathcal{V}} \mathbf{u}_i^\dagger\cdot\mathbf{u}_j\,\mathrm{d}V = 0, \tag{3.3}$$

where $\mathbf{u}_i^\dagger$ denotes the complex conjugate of $\mathbf{u}_i$. When the frequencies are equal, $\omega_i = \omega_j$, the solutions are called degenerate. In this case the spatial solutions $\mathbf{u}_i$ and $\mathbf{u}_j$ need not to be orthogonal. A well known example of such a degeneracy is the so-called geostrophic mode, with $\omega = 0$. From (3.1) we see that in this case the geostrophic balance (1.6) is recovered and the linear combination of all spatial solutions to the geostrophic balance make up the geostrophic mode (e.g. Liao and Zhang, 2010)

$$\mathbf{u}_G(\mathbf{r}_\perp) = \sum_i \gamma_i\mathbf{u}_{G,i}(\mathbf{r}_\perp), \tag{3.4}$$

with $\gamma_i \in \mathbb{C}$. Due to the columnar structure it is only a function of $\mathbf{r}_\perp$, as $\frac{\partial\mathbf{u}}{\partial z} = \mathbf{0}$. Sometimes in the literature it is differentiated between inertial modes and the geostrophic mode, and the set of both is referred to as Coriolis modes (Ivers et al., 2015; Ivers, 2017). The name Coriolis modes could be seen also as more accurate, since the restoring force is the Coriolis force, not inertia.

One example of an inertial mode as a solution to the inertial mode equation (3.1) is presented in Figure 3.1. To highlight the non-columnar form that inertial modes can have in general, an equatorially non-symmetric mode is chosen. This is illustrated

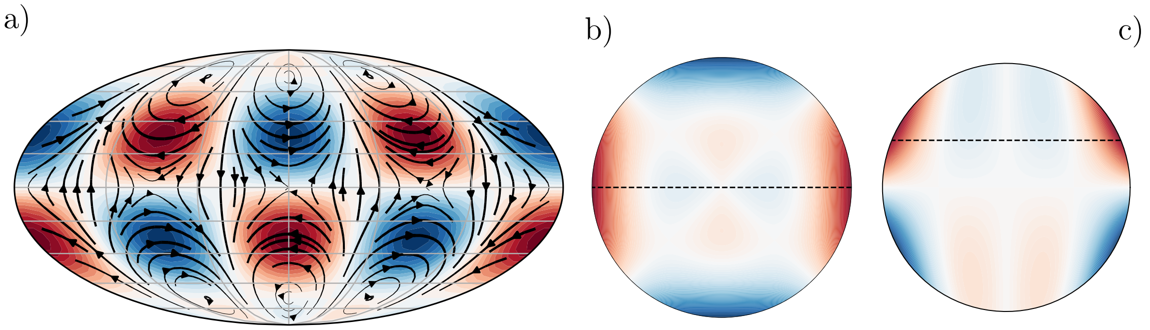

Figure 3.1: Equatorially asymmetric inertial mode with a frequency of $\omega = 0.76\,[\Omega]$, calculated from a Galerkin model solving (3.1). Displayed are a) surface velocity with colors indicating u_ϕ, b) horizontal section of u_ϕ and c) meridional section of u_ϕ. The meridional section is indicated as a dashed line in the horizontal section and vice versa. A horizontal section off the equatorial plane is chosen, as the velocity in the equatorial plane is zero for this mode.

well in the meridional section in Figure 3.1 c). Such large scale and non-symmetric inertial modes are characteristic of high frequencies close to the rotation frequency Ω.

Inertial modes and waves play an important role in rotating fluid dynamics (Greenspan, 1968; Zhang and Liao, 2017), being associated with transport of energy and mixing through inertial wave turbulence (e.g. Galtier, 2003; Le Reun et al., 2017). More recent work has also made inertial wave turbulence responsible for the two-dimensionalization, i.e. the build up of geostrophic structures through wave interactions including the geostrophic mode (Burmann and Noir, 2018; Le Reun et al., 2019; Brons et al., 2020).

Analytical solutions to the inertial modes have been given in the sphere (Zhang et al., 2001) and the spheroid (Zhang et al., 2004), with the frequency being the roots of a univariate polynomial. In an ellipsoid Vantieghem (2014) was the first to give an analytical solution to the largest scale modes. For modes of smaller scale the solutions are also only numerical, as the complexity of the polynomials quickly diminishes any analytical efforts.

It has been shown in the sphere (Ivers et al., 2015) and ellipsoids (Backus and Rieutord, 2017; Ivers, 2017), and in rotating cylindrical channels (Cui et al., 2014) that any incompressible and inviscid flow, which includes also flows in the presence of a Lorentz force, can be fully described by a linear combination of Coriolis modes. This property has been demonstrated only for the sphere, the spheroid and the ellipsoid. It is unclear if this property holds in volumes where geostrophic contours cannot be mapped bijectively to those in the sphere, e.g. a spherical shell or a cylinder (Backus and Rieutord, 2017). In the case of the spherical shell some inviscid inertial modes are irregular and take the form of attractors (Rieutord and Valdettaro, 1997). In the presence of viscosity axially invariant modes can, however, remain regular (e.g. Vidal and Schaeffer, 2015). From the completeness and orthogonality of the Coriolis modes, Ivers (2017) has shown, that only linear Coriolis modes carry angular momentum in the ellipsoid. This property is fairly easily demonstrated, once the difficult part of proving the completeness and orthogonality of the modes is done. From the completeness it follows that any inviscid flow in the ellipsoid can be written as $\mathbf{u} = \alpha_k \mathbf{u}_k$ (summing over k), with $\mathbf{u}_k$ the spatial solutions to (3.1) in the ellipsoid. Any flow, linear in the spatial coordinates can, be written as $\mathbf{u}^l = \mathbf{c} \times \mathbf{r} + \nabla\Phi$, with $\mathbf{c}$ a constant vector and Φ a potential that is at most quadratic in the spatial coordinates. We can also completely describe $\mathbf{u}^l$ by a linear combination the Coriolis modes $\mathbf{u}_i$ linear in the spatial coordinates, so that $\mathbf{u}^l = \beta_i \mathbf{u}_i$. With these relations we can rewrite the angular momentum of any flow $\mathbf{u}$ along the arbitrary axis $\mathbf{c}$, so that

$$\begin{aligned}
\mathbf{c} \cdot \mathbf{L} &= \mathbf{c} \cdot \int_{\mathcal{V}} \mathbf{r} \times \mathbf{u} \, \mathrm{d}V && (3.5)\\
&= \int_{\mathcal{V}} \mathbf{c} \times \mathbf{r} \cdot \mathbf{u} \, \mathrm{d}V && (3.6)\\
&= \int_{\mathcal{V}} (\mathbf{u}^l - \nabla\Phi) \cdot \mathbf{u} \, \mathrm{d}V && (3.7)\\
&= \alpha_k \beta_i \int_{\mathcal{V}} \mathbf{u}_i \cdot \mathbf{u}_k \, \mathrm{d}V - \underbrace{\int_{\mathcal{V}} \nabla\Phi \cdot \mathbf{u} \, \mathrm{d}V}_{=0} && (3.8)\\
&= \alpha_k \beta_i \delta_{ik}. && (3.9)
\end{aligned}$$

In the last step we have used the orthogonality condition of the Coriolis modes. It is seen, that the angular momentum projects only onto the linear components of the flow. Thus, only these components of any flow $\mathbf{u}$ can contribute to the angular momentum. Put differently, angular momentum is carried only by

$$\hat{\mathbf{u}}_1 = \begin{pmatrix} 0 \\ -z/c^2 \\ y/b^2 \end{pmatrix}, \; \hat{\mathbf{u}}_2 = \begin{pmatrix} -z/c^2 \\ 0 \\ x/a^2 \end{pmatrix}, \; \hat{\mathbf{u}}_3 = \begin{pmatrix} -y/b^2 \\ x/a^2 \\ 0 \end{pmatrix}, \qquad (3.10)$$

with a spatially uniform vorticity in the x, y and z directions, respectively. The fact that all angular momentum is carried by the uniform vorticity is not in contradiction with previous studies, that associated the angular momentum to the t_1^0 and t_3^0 toroidal scalars of surface flows (Jault and Mouël, 1991), as the axial uniform vorticity component projects on these two scalars on the core surface.

3.2 Quasi-geostrophic inertial modes

Within all analytical solutions Zhang et al. (2001) identified a class of inertial modes that are symmetric about the equatorial axis with frequencies given approximately by

$$\lambda_{N,m} \approx -\frac{2}{m+2}\left(\left(1+\frac{m(m+2)}{N(2N+2m+1)}\right)^{1/2}-1\right), \tag{3.11}$$

with N the latitudinal complexity and m the azimuthal wave number of the mode. These modes travel prograde, i.e. eastward on Earth, and can be regarded as nearly geostrophic inertial modes.

Such nearly geostrophic inertial modes are captured by QG models. A numerical comparison between QG inertial modes from the vorticity equation QG model and (3.11) was first given by Canet et al. (2014). Maffei et al. (2017) compared (3.11) to analytical solutions of the hydrodynamic QG models derived from the vorticity equation and the Galerkin approach (introduced in Chapter 2). For the Galerkin approach, the frequencies of the QG inertial modes in a spheroid are given by

$$\omega_N^m = -\frac{m}{N(2N+2m+1)+m/2+m^2b^2/6}, \tag{3.12}$$

with b the vertical semi axis of the spheroid ($b=1$ corresponds to the sphere). The corresponding stream function of the modes is given by

$$\psi_N^m = s^m h^3 P_{N-1}^{(3/2,m)}(2s^2-1), \tag{3.13}$$

with $P_N^{(\alpha,\beta)}(x)$ a Jacobi polynomial. A similar analytical expression is derived for the Rossby mode equation from a vorticity approach. In this case the frequencies are altered, so that the last term in the denominator of (3.12) vanishes, i.e. for $b=0$. A comparison of the analytical solutions is shown in Figure 3.2. In general, the models agree well, with the Galerkin approach having better agreement with the 3-D solutions. The largest difference between the QG approximation and the 3-D solutions are for the fundamental modes ($N=1$) and large m. From this figure it is also apparent that, unless $m \gg 20$, the slowest QG inertial modes are those of smallest azimuthal wavenumber m.

In a local β-plane analysis, a linearization of the variation of the Coriolis force, Rossby (1939) discovered waves in a thin layer that are eastward, i.e. prograde, traveling perturbations to a mean zonal flow, which today carry his name. They are essentially QG inertial waves and thus QG inertial modes are also often referred to as Rossby modes (RM).

The RM with a frequency $\lambda_{2,1} \approx 0.68\,[\Omega]$ is visualized in Figure 3.3. It illustrates how the azimuthal wavenumber m and latitudinal complexity N is counted. The columnar structure is easily seen in the meridional slice. Also, the meridional and equatorial slice show that RM focus their kinetic energy near the equatorial region. This focusing of energy has been associated with the slope of the spherical boundary, acting as a wave guide (e.g. Zhang, 1993).

The studies of RM in planetary core have been limited to axisymmetric cases. Bardsley (2018) has written out the general expression of the RM equation, but investigated Rossby waves in the spherical case.

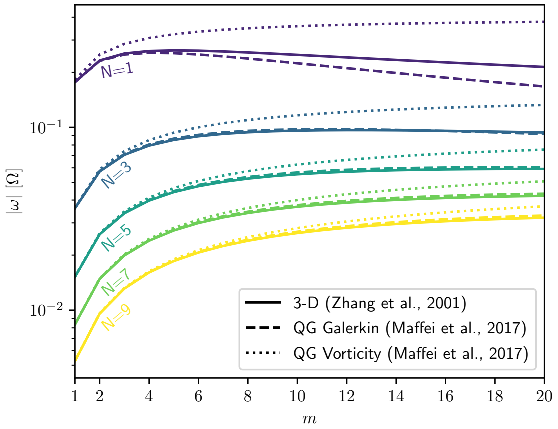

Figure 3.2: Comparison between analytical expressions (3.12) and (3.11) as well as (3.12) for $b = 0$ (corresponding to the vorticity equation approach) of QG and equatorially symmetric 3-D inertial modes, respectively (Zhang et al., 2001; Maffei et al., 2017).

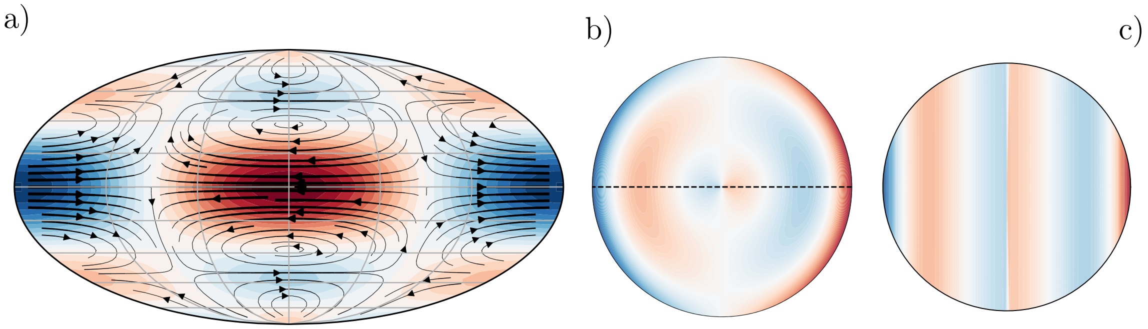

Figure 3.3: QG inertial mode with a frequency of $\omega = 0.068\,[\Omega]$, calculated from the QG model of the Galerkin approach. This mode corresponds to the $m = 1$, $N = 2$ QG inertial mode. Displayed are a) surface velocity with colors indicating u_ϕ, b) equatorial section of u_ϕ and c) meridional section of u_ϕ. The meridional section is indicated as a dashed line in the equatorial section.

3.3 Magneto-Coriolis modes

Initially discovered by Lehnert (1954) as plane waves in a uniform magnetic field parallel to the rotation axis, Magneto-Coriolis (MC) waves take their name by dominant magnetic and rotational forces that counteract inertia. When magnetic and rotational forces almost balance each other the inertial force can be small, i.e. the modes evolve on long time scales. Hide (1966) introduced, in analogy to Rossby (1939), the small slope approximation to study the influence of a spherical boundary on such MC waves. However, still considering a local β-plane approximation, the waves do not fully account for the spherical boundary. For a purely zonal mean magnetic field $\mathbf{B}_M = s\mathbf{1}_\phi$ Malkus (1967) was the first to show analytical solutions for MC modes (MCM) in a sphere. The magnetic field considered has a uniform current along the axis of rotation and satisfies $\mathbf{B}\cdot\mathbf{n} = 0$ at the boundary. For this field the advection term in the induction equation and the Lorentz force simplify significantly and the governing equations can be related to the Poincaré equation for the pressure (3.2). Then, the solutions to the MHD problem are directly linked to the inertial modes. In his study, Malkus (1967) gave the frequency of the modes as a function of the inertial mode frequency $\lambda_{N,m}$, so that

$$\omega^{\pm}_{N,m} = \frac{1}{2\mathrm{Le}}\lambda_{N,m}\left(1 \pm \left(1+\frac{4\mathrm{Le}^2 m(m{-}\lambda_{N,m})}{\lambda^2_{N,m}}\right)^{1/2}\right), \tag{3.14}$$

here given in dimensions of the Alfvén wave frequency u_A/R_0 (Labbé et al., 2015). Two mode families of frequencies ω^+ and ω^- arise, which are slightly modified inertial modes and Magneto-Coriolis modes, respectively.

It is apparent that for a small Le and for m and N not much greater than $\mathcal{O}(10)$, the frequencies of inertial modes are not strongly modified by the presence of the magnetic field. This is seen when comparing the slightly modified QG inertial modes to the QG inertial modes in the purely hydrodynamic case. Besides the scaling of Le^{-1} of the frequency, no difference can be observed visually between Figure 3.6 (left) and 3.2. The relative difference of the frequencies is only $\mathcal{O}(10^{-6})$, when scaled in the same way. In Figure 3.4 the $m = 1$ and $N = 2$ QG inertial mode in the Malkus field is shown. The difference between the Malkus field and the hydrodynamic mode (Figure 3.3) is not visible, when inspecting the velocity structure. The only characteristic is that this mode is now complemented by a small amplitude magnetic field perturbation. As the magnetic field in the Malkus model has to satisfy $\mathbf{B}\cdot\mathbf{n} = 0$ at $\partial\mathcal{V}$, the radial magnetic field perturbation vanishes towards the boundary and is strongest in the interior. For this mode the magnetic field perturbation is small, with a ratio of the kinetic to the magnetic energy $\mathcal{O}(10^5)$. At smaller spatial scales or other Le this ratio can change significantly. The ratio of kinetic to magnetic energy of plane MC waves is given analytically by (Acheson and Hide, 1973)

$$\frac{E_{\mathrm{kin}}}{E_{\mathrm{mag}}} = \frac{\omega^2}{(\mathbf{u}\cdot\mathbf{k})^2}, \tag{3.15}$$

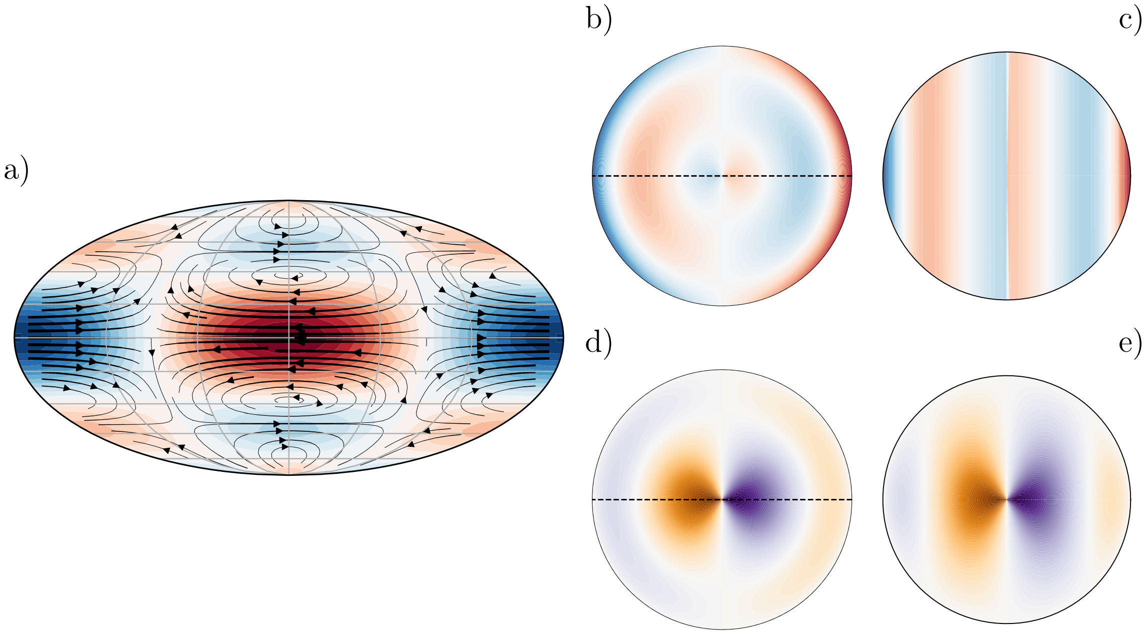

Figure 3.4: Slightly modified QG inertial mode for the Malkus field, at $\mathrm{Le} = 10^{-4}$, with a frequency of $\omega = 6.79 \times 10^2$, calculated from the QG model of the Galerkin approach. This mode corresponds to the $m = 1$, $N = 2$ slightly modified QG inertial mode and may be compared to the RM in Figure 3.3. Displayed are a) surface velocity with colors indicating u_ϕ, b) equatorial section of u_ϕ, c) meridional section of u_ϕ, d) equatorial section of B_r and e) meridional section of B_r. The meridional sections are indicated as dashed lines in the equatorial sections.

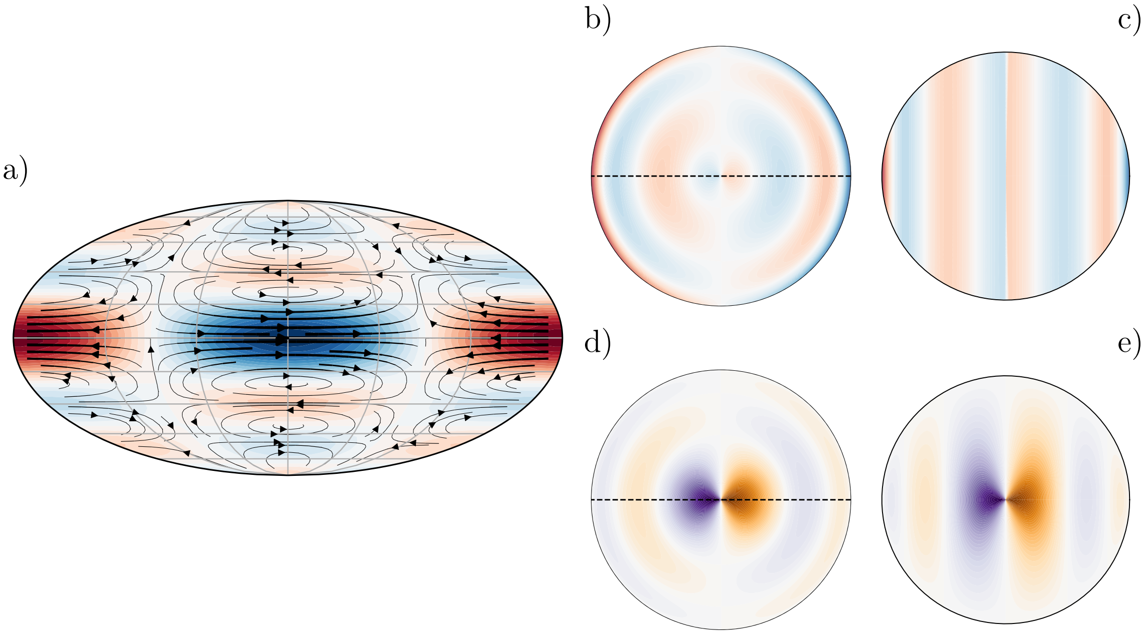

Figure 3.5: Magneto-Coriolis mode for the Malkus field, at $\mathrm{Le} = 10^{-4}$, with a frequency of $\omega = 2.87 \times 10^{-3}$, calculated from the QG model of the Galerkin approach. This mode corresponds to the $m = 1$, $N = 3$ Magneto-Coriolis mode. Displayed are the surface velocity with colors indicating u_ϕ a), equatorial section of u_ϕ b), meridional section of u_ϕ c), equatorial section of B_r d) and meridional section of B_r. The meridional sections are indicated as dashed lines in the equatorial sections.

where $\mathbf{k}$ is the wave vector and ω is scaled by the Alfvén wave frequency. For Alfvén waves this energy ratio is unity, as $\omega^2 = (\mathbf{u}\cdot\mathbf{k})^2$. It has been found numerically that for the Malkus modes this ratio is exactly

$$\frac{E_{\mathrm{kin}}}{E_{\mathrm{mag}}} = \frac{8}{15}\frac{\left(\omega^{\pm}_{N,m}\right)^2}{m^2}, \tag{3.16}$$

with m the azimuthal wave number. A small Le corresponds to a regime where the rotational forces dominate over the magnetic forces. Accordingly, if the magnetic field is stronger while the rotation rate is the same, Le increases and the influence of the magnetic field on the inertial mode frequencies is larger. Likewise, this is achieved by having a slower rotation rate and the same magnetic field strength.

The other family of modes of frequencies $\omega^{-}_{N,m}$, of interest here, evolves on periods much longer than the inertial modes. They are strongly influenced by the magnetic field and are mostly in balance between Coriolis and Lorentz force. Their frequencies are much lower than unity, when considering the largest scale modes and $\mathrm{Le} \lesssim 10^{-3}$. Similarly, their kinetic to magnetic energy ratio is much smaller than unity. For the mode presented in Figure 3.5, $E_{\mathrm{kin}}/E_{\mathrm{mag}} = \mathcal{O}\left(10^{-6}\right)$. The spatial structure is very similar to that of RM, with a change in the amplitude of the magnetic field that

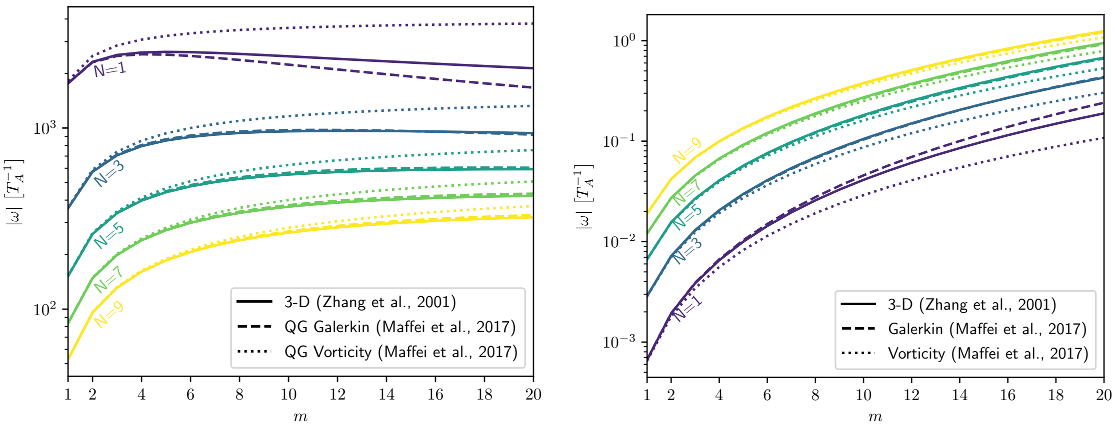

Figure 3.6: Comparison between equatorially symmetric 3-D and QG Malkus modes using the analytical expression (3.14) combined with (3.12) and (3.11) as well as (3.12) for $b = 0$ (corresponding to the vorticity equation approach) for the inertial mode frequencies, respectively. Slightly modified QG inertial modes (left) and Magneto-Coriolis modes (right) at $\mathrm{Le} = 10^{-4}$.

now dominates the velocity. Another important characteristic is the phase velocity $v_p = \omega/m$. Whereas RM travel prograde ($v_p > 0$), MCM travel retrograde ($v_p < 0$). When scaled by the angular frequency, Magneto-Coriolis mode frequencies are proportional to the square of the background magnetic field strength, B_0^2, as can be seen from (3.14) or by dimensional analysis of the induction equation and the balance between Coriolis and Lorentz force. This is presented in Figure 3.8 (right), in the case of a non-axisymmetric magnetic field.

In case thermal buoyancy is added to the system, MCM are complemented by an Archimedes force and carry the name Magneto-Archimedes-Coriolis (MAC) modes (Braginsky, 1964, 1967; Finlay, 2007).

Within a geodynamo simulation, slowly evolving MC waves were identified by Hori et al. (2015) and proposed to be sensitive to strong toroidal magnetic fields.

The study of MCM in the literature has been limited to idealized background magnetic fields and axisymmetric domains, so that the system of equations is simplified significantly and modes of different azimuthal wavenumber can be treated independently.

3.4 Taylor's constraint and torsional Alfvén modes

When considering the very slowest evolutions of a rotating MHD system (1.12), inertial and viscous forces are negligible and the flow is assumed to be in the so-called magnetostrophic balance

$$2\rho\mathbf{\Omega} \times \mathbf{u} = -\nabla p + \mathbf{F}, \tag{3.17}$$

with $\mathbf{F} = \mathbf{j} \times \mathbf{B} + \mathbf{F}_B$. The homogeneous part of this balance is again the geostrophic balance. The geostrophic motions are also solutions to the adjoint problem (Jault and Finlay, 2015) and thus the constraint named after Taylor (1963) is given by

$$\int_{\mathcal{V}} \mathbf{u}_G \cdot (\mathbf{j} \times \mathbf{B}) \, \mathrm{d}V = 0. \tag{3.18}$$

In writing this, either buoyancy is neglected or the volume is assumed axisymmetric. This constraint says that the Lorentz force on any geostrophic fluid column, drawn by the line of constant column height, vanishes. In the spherical case this constraint can be written as

$$\iint\limits_{\Sigma(s)} (\mathbf{j} \times \mathbf{B}) \cdot \mathbf{1}_\phi s \, \mathrm{d}\phi \mathrm{d}z, \tag{3.19}$$

the integral over the surface $\Sigma(s)$ of a geostrophic cylinder of radius s.
It has been suggested that in Earth's core the magnetostrophic balance is satisfied, being in a so-called Taylor-state, and many studies have worked on the construction of such states (e.g. Livermore et al., 2008; Wu and Roberts, 2015; Hardy et al., 2018). Here, we are interested in time dependent perturbations to such a Taylor-state.
One way to consider time dependent perturbations to the Taylor state are so-called pseudo-geostrophic motions (Gans, 1971), that may be written as

$$\mathbf{u}_{PG}(\mathbf{r}_\perp, t) = \sum_i \gamma_i(t) \mathbf{u}_{G,i}(\mathbf{r}_\perp). \tag{3.20}$$

This form of flow is equivalent to the geostrophic mode (3.4) with time dependent coefficients $\gamma_i(t)$.
We reintroduce inertia into the system and, in analogy to the derivation of the QG model by the Galerkin approach, we can project the momentum equation onto the pseudo-geostrophic velocities as test velocities. The pressure gradient term vanishes due to the non-penetration condition and the Coriolis term does not project onto the pseudo-geostrophic velocities. The weak form is thus given by

$$\int_{\mathcal{V}} \mathbf{u}'_{PG} \cdot \frac{\partial \mathbf{u}}{\partial t} \, \mathrm{d}V = \int_{\mathcal{V}} \mathbf{u}'_{PG} \cdot (\mathbf{j} \times \mathbf{B}) \, \mathrm{d}V. \tag{3.21}$$

It is apparent, that pseudo-geostrophic motions act as a perturbation to a Taylor-state (3.18). The pseudo-geostrophic motions are balanced solely by the Lorentz force acting on the fluid column. A balance between inertia and magnetic forces is characteristic of Alfvén waves. Here, the motions are differentially moving geostrophic columns that stretch the magnetic field that permeates them (see an illustration in the sphere in Figure 3.7). We will find that these motions are of oscillatory nature and are known as torsional Alfvén waves or torsional Alfvén modes (TM), initially discovered by Braginsky (1970).

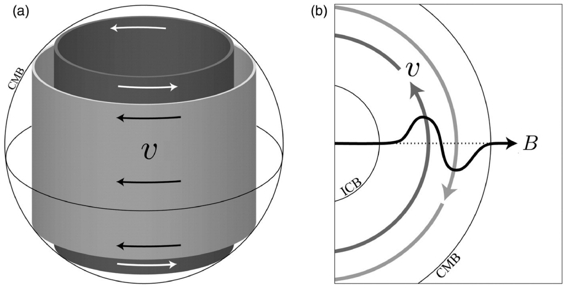

Figure 3.7: Schematic of a torsional Alfvén mode in a sphere, illustrating the differentially rotating geostrophic cylinders (a) and the stretching of the cylindrical radial magnetic field lines by such differential rotation (b). Reproduction of Figure 4 from Roberts and Aurnou (2012) with permission from Taylor & Francis.

To derive a governing wave equation, let us further simplify (3.21) by considering the spherical case. Then, $\mathbf{u}_{PG} = u_{PG}(s,t)\mathbf{1}_\phi$ and similar to Taylor's constraint (3.19) in the sphere, (3.21) is written as

$$\int_0^1 u_{PG}(s,t)s \iint\limits_{\Sigma(s)} \mathbf{1}_\phi \cdot \frac{\partial \mathbf{u}}{\partial t}\, \mathrm{d}\phi \mathrm{d}z\, \mathrm{d}s = \int_0^1 u_{PG}(s,t)s \iint\limits_{\Sigma(s)} \mathbf{1}_\phi \cdot (\mathbf{j} \times \mathbf{B})\, \mathrm{d}\phi \mathrm{d}z\, \mathrm{d}s. \quad (3.22)$$

The left hand side can be integrated explicitly

$$\iint\limits_{\Sigma(s)} \frac{\partial \mathbf{u}}{\partial t} \cdot \mathbf{1}_\phi s\, \mathrm{d}\phi \mathrm{d}z = 4\pi h s \frac{\partial u_{PG}(s,t)}{\partial t}. \quad (3.23)$$

This is true, as the cylindrical average of any azimuthal velocity $\mathbf{u} \cdot \mathbf{1}_\phi$ is exactly represented by a pseudo-geostrophic velocity. Thus, we can write

$$4\pi h s \frac{\partial u_{PG}(s,t)}{\partial t} = \iint\limits_{\Sigma(s)} (\mathbf{j} \times \mathbf{B}) \cdot \mathbf{1}_\phi s\, \mathrm{d}\phi \mathrm{d}z. \quad (3.24)$$

In the next step, it is assumed that the magnetic field is only advected by exactly these pseudo-geostrophic motions, so that

$$\frac{\partial \mathbf{B}}{\partial t} = \boldsymbol{\nabla} \times (\mathbf{u}_{PG} \times \mathbf{B}). \quad (3.25)$$

We have neglected here also the magnetic diffusion. For a more complete derivation including magnetic diffusion we refer to Braginsky (1970) or Jault (2003).
Then, upon taking the time derivative of (3.24) and substituting the emerging time derivatives of the magnetic field by (3.25), the one-dimensional torsional mode equation can be derived as

$$4\pi\rho h \frac{\partial^2 u_{PG}(s,t)}{\partial t^2} = \frac{1}{\mu_0 s^2} \frac{\partial}{\partial s} \left(s^2 \frac{\partial}{\partial s} \left(\frac{u_{PG}(s,t)}{s} \right) \oint \int (\mathbf{B} \cdot \mathbf{1}_s)^2\, \mathrm{d}z \mathrm{d}\phi \right). \quad (3.26)$$

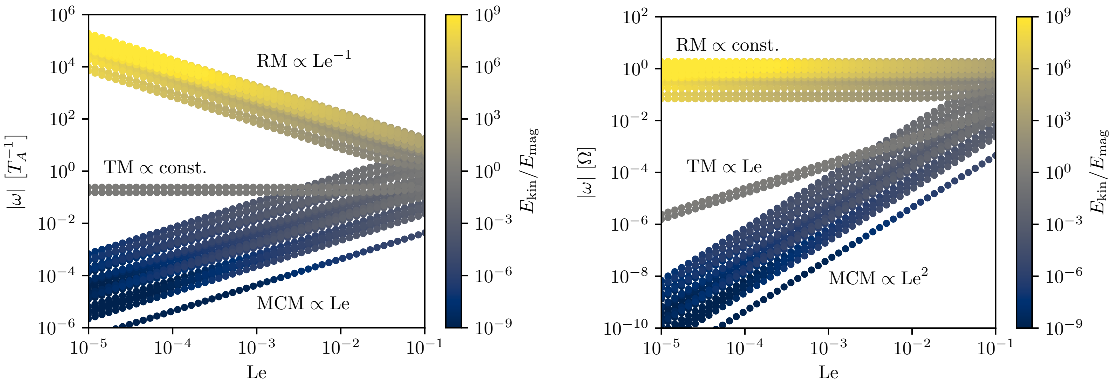

Figure 3.8: Frequency spectra of modes in the sphere as a function of Lehnert number, scaled by the Alfvén frequency (left) and the rotation frequency (right). Reproduction of Vidal et al. (2019, Figure B.1) and Gerick et al. (2020, Figure 1), for a magnetic field $\mathbf{B}_0 = (-y, x - z/10, x/10)^{\mathsf{T}}$. Colors indicate the ratio of kinetic to magnetic energy.

From this TM equation it is apparent that the differential rotation of geostrophic cylinders counteracts the magnetic tension by the stretched radial magnetic field lines, as illustrated in 3.7.

In the literature (3.26) is often written in terms of $\xi(s,t) = u_{PG}(s,t)/s$ and the mean-squared radial Alfvén velocity

$$v_A^2(s) = \frac{1}{4\pi s h \mu_0 \rho} \oint \int (\mathbf{B} \cdot \mathbf{1}_s)^2 s \, \mathrm{d}z \mathrm{d}\phi, \tag{3.27}$$

so that

$$s^3 h \frac{\partial^2 \xi}{\partial t^2} = \frac{\partial}{\partial s}\left(h s^3 \frac{\partial \xi}{\partial s} v_A^2 \right) \tag{3.28}$$

The solvability of (3.28) depends on $v_A^2(s)$, in case the radial magnetic field vanishes at the equator, so that $v_A^2 = 0$ at $s = 1$. Then, it is required that the magnetic field strength does not decay too quickly, namely it has to satisfy $v_A^2(s) \sim h^\nu$ with $\nu < 2$ (Maffei and Jackson, 2016).

By dimensional analysis we can see that the frequency of TM must scale as $\omega \sim B_0$, when scaled by the rotation frequency, and to be constant for different values of B_0, when scaled by the Alfvén period. To illustrate this, the spectra of a 3-D model in the sphere (Vidal et al., 2019) are shown in Figure 3.8. Here, a magnetic field linear in the spatial coordinates has been used, which has $v_A^2 \neq 0$, in contrast to the Malkus field. This is the necessary criterion to introduce TM in the system. When the Alfvén period is used as a characteristic time scale (Figure 3.8, left), the frequencies of TM are constant as a function of Le. In contrast, frequencies of RM are proportional to Le^{-1} and those of MCM to Le. Also shown is the ratio of kinetic to magnetic energy as colors. For the TM this ratio is almost exactly unity, as anticipated from the dispersion relation of Alfvén waves and (3.15).

When the frequencies are in turn scaled by the angular frequencies (Figure 3.8, right), the TM frequencies are proportional to Le. RM are then independent of Le, showing that they are not affected by the background magnetic field strength, when rotation is dominant. The frequencies of MCM on the other side are strongly dependent on the background magnetic field strength within the bulk, as they are proportional to Le^2.

Torsional waves have been found in multiple high resolution geodynamo simulations in the recent years, hinting that they might be abundant in Earth's core conditions (e.g. Teed et al., 2015; Schaeffer et al., 2017).

The numerical modeling of TM has been limited to axisymmetric domain (with the exception of Vidal et al., 2016, that showed TM in the ellipsoid, but did not investigate them further). It is unclear if one can write a 1-D TM equation (3.28) without axisymmetry. QG models are capable of solving for TM and an extension to non-axisymmetric domains is presented in section 2.7.

3.5 Excitation and presence of hydromagnetic modes in Earth's core

For the excitation of hydromagnetic waves and modes in Earth's core a few mechanisms have been proposed, that are shortly listed here. A forcing through the topography at the CMB has been suggested by Hide (1966). Also, tidal forcing could lead to the excitation of modes in the fluid core (Kerswell, 1994; Le Bars et al., 2015). In another scenario, a non-axisymmetric magnetic field component could lead to magnetic instabilities that drive slow MC wave motions (Acheson, 1972). More recently, Gillet et al. (2017) have shown that TM may be excited through stochastic forcing, without the need of an exterior periodical forcing. Another proposed excitation mechanism for TM are jets forming at the inner core boundary, as observed in a convective DNS of the core flow (Teed et al., 2019). There is no consensus on a specific excitation mechanism as of today and more research is needed.

If modes are excited in the Earth's liquid core, it has been proposed to have impacts on Earth's rotation and magnetic field (Hide and Roberts, 1961; Hide, 1966; Braginsky, 1970). Zatman and Bloxham (1997) and Buffett et al. (2009) inverted inferred core-flow models to TM in the core, assuming their period should lie close to 60 yr (as also proposed initially by Braginsky, 1970). By this they followed a characteristic cylindrical radial magnetic field strength in the core of about ~ 0.3 mT. More recently, Gillet et al. (2010) identified TM in the zonal component of inferred surface core flows with periods of only a few years, leading to a magnetic field strength of $\sim 2-4$ mT. The same authors linked the transport of angular momentum by these modes to the variations of the LOD and found a strong correlation for the time period considered. MC modes/waves are non-zonal and typically evolve on very long periods, i.e. $\mathcal{O}\left(10^2-10^4\right)$ yr for Earth, at the largest scales (e.g. Finlay et al., 2010). In a stably stratified layer below the CMB Buffett (2014) suggested the presence of

MAC waves with periods of 60 yr, in agreement with changes in the geomagnetic field. Finlay and Jackson (2003) also associated such MAC waves to westward propagating secular variations at a phase velocity of 17 km/yr near the equator. Chulliat et al. (2015) find eastward and westward traveling waves of phase velocities between 550–1700 yr and compare the observed wave speeds to MAC waves.

3.6 Numerical calculation of modes

Unless only the hydrodynamic case for the very smallest polynomial degrees is considered (Vantieghem, 2014), modes in the ellipsoid or with a non idealized background magnetic field need to be obtained by numerical approximation. To numerically calculate modes two steps are required in general.

1. Discretize the momentum equation (and induction equation) and its derivatives and find a Matrix representation $\mathbf{M}$, $\mathbf{D}$ of the discretized linear equation.
2. Solve the arising generalized eigen problem $\omega\mathbf{M}\mathbf{x} = \mathbf{D}\mathbf{x}$ numerically.

For the discretization multiple approaches can be made and some of them are introduced in Section 2.7.2. For a more detailed summary on finite differences and spectral methods the interested reader is referred to the textbook by Durran (2013). Once discretized and transformed into a form of linear operators, or matrices, the steps to solve for linear modes are the same. For very high resolutions or high polynomial degrees these matrices can be very large, and possibly cannot be stored in a dense form. Algorithms to solve for eigen solutions then become increasingly costly. Some approaches that still allow us to find a few modes, when direct methods are not feasible, are introduced here.

3.6.1 Solving the generalized eigen problem

Solving for eigenvalues may be straightforward for simple, small examples with matrices that are not larger than 3×3. The eigenvalues of a matrix $\mathbf{A}$ can be obtained as solutions to the characteristic polynomial $\det(\lambda\mathbf{I} - \mathbf{A})) = 0$, with $\mathbf{I}$ the identity matrix. Depending on $\mathbf{A}$, this can already be challenging for the smallest matrices. For the matrices that are typically encountered in the context of modes of rotating fluids, the matrix dimensions are $\mathcal{O}\left(10^2 - 10^4\right)$, and any analytical efforts are fruitless. One has to rely on numerical methods. The detailed discussion on all the linear algebra for these algorithms goes beyond the scope of this work and just a few methods that allow us to solve the generalized eigen problem are introduced here (2.102). When the matrices are small enough, a direct solver can be used. One way is implemented in the Fortran *LAPACK* routines (Anderson et al., 1999), which are generally accessible from different languages, and is based on the generalized Schur factorization.

For matrices with dimension larger than 10^3 these direct methods start to be very costly also, as all possible eigenvalues have to be calculated in these methods. To only solve for a subset of eigenvalues multiple algorithms have been developed. The implicitly restarted Arnoldi method is based on the QR algorithm and is implemented in the *ARPACK* library (Lehoucq et al., 1998). A nice illustration of the algorithm is given in Hernández et al. (2007). Another method is called Krylov-Schur method (Stewart, 2001). It shares many similarities with the implicitly restarted Arnoldi method, but claims to be numerically more stable (Stewart, 2001). I refer to Hernandez et al. (2015) for a more detailed introduction to the Krylov-Schur method.

In general it is easier to solve a standard eigen value problem than the generalized eigen value problem. To transform (2.102) into a standard eigenvalue problem we can invert $\mathbf{M}$, so that

$$\lambda\mathbf{x} = \mathbf{A}\mathbf{x}, \tag{3.29}$$

where $\lambda = \mathrm{i}\omega$ and $\mathbf{A} = \mathbf{M}^{-1}\mathbf{D}$. In practice this inverse is not calculated explicitly, as $\mathbf{M}^{-1}$ is not necessarily sparse and it is expensive to calculate. Instead, we can factorize $\mathbf{M}$, so that $\mathbf{PM} = \mathbf{LU}$, with $\mathbf{P}$ a pivoting matrix and $\mathbf{L}$ and $\mathbf{U}$ a lower and upper triangular matrix, respectively. This is more commonly known as the LU-factorization and a sparse implementation is available through the *UMFPACK* library (Davis, 2004). Then, we are able to solve the linear problem $\mathbf{Ax} = \mathbf{b}$ for $\mathbf{x}$, without the need of Gaussian elimination. This factorization can be seen as a preconditioner and we have made use of the explicit matrix representation (even though it is a sparse matrix representation). If $\mathbf{M}$ is only a linear operator (without an explicit matrix representation), this preconditioning is very difficult and convergence of the iterative methods is poor. After finding the LU-factorization, the standard eigenvalue problem (3.29) can be solved iteratively for the largest eigen pairs $(\lambda_k, \mathbf{x}_k)$. The sparse solvers can also be applied to follow an eigen solution through the parameter space by targeting an eigen value that is fed a-priori into the algorithm. An example of this tracking is given in Gerick et al. (2020). To do so, we apply a targeted shift-and-invert method

$$(\mathbf{D} - \sigma\mathbf{M})^{-1}\mathbf{D}\mathbf{x} = \lambda\mathbf{x} \tag{3.30}$$

around a target $\sigma \in \mathbb{C}$, with the new eigenvalue $\lambda = (\mathrm{i}\omega - \sigma)^{-1}$. This strategy is efficient to compute the eigenvalues close to the target σ (which is chosen close to the desired eigenvalue $\mathrm{i}\omega$). This is due to the fact that the convergence of iterative algorithms is best for the largest eigen values. This approach has previously been used successfully in the context of rotating fluid modes (e.g. Rieutord and Valdettaro, 1997; Vidal and Schaeffer, 2015).

For the largest scale problems one might have to consider distributed memory algorithms. For the algorithms introduced here, one can use the *SLEPc* library (Hernandez et al., 2005), which uses Message-Passing-Interface (MPI) to distribute the workload.

Another inevitable difficulty is that the MHD mode problem is very ill-conditioned. The geostrophic solutions are of zero frequency, in contrast to the inertial modes at the fastest end. Together with the magnetic modes of intermediate frequencies the spectrum spans multiple orders of magnitudes that is challenging from a numerical perspective. In our study we have encountered many issues with numerical convergence of the eigen solvers, when considering high polynomial degrees. A solution has been the increase in numerical accuracy by using quadruple precision floating point numbers. The standard libraries are based on 64-bit floating point numbers, although *SLEPc* can be compiled against quadruple precision arithmetics. In our work we relied on recent implementations of linear algebra packages in the Julia programming language.

3.6.2 Code examples

Since the Julia programming language (simply Julia hereafter) is new in the scientific community, a few words on the language and some implementation details are given. Julia has been developed with the target of scientific computing. It tries to solve the problem of two languages, that is prototyping in a typically slow high-level language and reimplementing the code in a low level language when performance is critical (Bezanson et al., 2017). The syntax and basics of the language are not discussed here, for the interested reader I refer to `https://julialang.org`, where instructions on installation, first steps, package management and advanced usage are much more clearly and correctly introduced than could be done here. For those using the Python programming language or MATLAB ® the high-level syntax of Julia should feel fairly familiar, even at first glance.

The implementation of the QG model from a Galerkin approach requires almost only a polynomial toolbox that is able to do basic arithmetic and calculus operations on multivariate polynomials. In Julia this functionality is given through two packages named *TypedPolynomials.jl* and *MultivariatePolynomials.jl*[1]. As the name of the package indicates, it allows for different types of the coefficients, ranging from integers, rationals, symbolic variables to arbitrary precision floating point numbers, thanks to Julia's multiple dispatch paradigm. On top of the basic functionality, we can define the vector calculus operators. The vector algebra is already in the standard library of the Julia programming language.

To demonstrate just how simple the Galerkin approach with a basis from Cartesian monomials is in Julia, one can implement a fully functional Rossby mode solver in the ellipsoid in just 40 lines of code.

---

[1] Available at `https://github.com/JuliaAlgebra/TypedPolynomials.jl` and `https://github.com/JuliaAlgebra/MultivariatePolynomials.jl` or simply by installing them by running `]add TypedPolynomials MultivariatePolynomials` within the Julia REPL.

```
using LinearAlgebra, TypedPolynomials, MultivariatePolynomials

@polyvar x y z
N,a,b,c = 7, 1.25, 1.1, 0.9
const ez = [0,0,1]
∇(ψ) = [differentiate.(ψ,(x,y,z))...]

function u(n,m,a,b,c)
  h2 = c^2*(1-x^2/a^2-y^2/b^2)
  ∇G = [-c^2*x/a^2,-c^2*y/b^2,0]
  return h2*∇(x^n*y^m) × ez + 3x^n*y^m*∇G × ez - z*∇(x^n*y^m) × ∇G
end
v(N,a,b,c) = [u(ci...,a,b,c) for ci in [[i,j] for i=0:N for j=0:N if (i+j<N)]]

inertial(u) = u
coriolis(u,Ω)  = -2*Ω×u

facnp1(n) = factorial(big(2n))//(big(4)^n*factorial(big(n)))

function intVm(i, j, k, a::Ta, b::Tb, c::Tc) where {Ta,Tb,Tc}
  coeff = Ta(facnp1(big(i÷2))*facnp1(big(j÷2))*
            facnp1(big(k÷2))//(8*facnp1(big((4+i+j+k)÷2))) )
  return (1 + (-1)^i)*(1 + (-1)^j)*(a^(1 + i))*(b^(1 + j))*c*((-c)^k +
c^k) *coeff
end

intVm(p,a,b,c) =  intVm(exponents(p)..., a,b,c)

function intVp(p, a,b,c)
  return sum(coefficients(p).*intVm.(monomial.(terms(p)), a,b,c))
end

inner_product(u,v,a,b,c) = intVp(dot(u,v), a,b,c)

vs = v(N, a, b, c)
M = [inner_product(vi, inertial(vj),    a,b,c) for vi in vs, vj in vs]
B = [inner_product(vi, coriolis(vj,ez), a,b,c) for vi in vs, vj in vs]


esol = eigen(B, M)
ω = esol.values
```

Let us go through the code in a few steps. First, the needed packages are loaded, with `LinearAlgebra` being the standard library. Then, we define our polynomial Cartesian variables and the maximum polynomial degree and the semi axes. The next part is to introduce the basis. For this we define the gradient. The inertial force and coriolis force are defined as one would write them naturally. Then we need to define the volume integral, which actually makes up most of the code. Two helper functions, `intVm` and `intVp`, are defined to finally define the inner product. The function `intVm` is being defined twice. This is an example of Julia's multiple dispatch paradigm, that dispatches the call of a function according to its input, once with four input parameters and once with five input parameters. This multiple dispatch is of course more powerful than this, but this goes beyond this section. At the end we define our basis vectors `vs` and then construct our two matrices **M** and **B** accordingly. Then we can use the `eigen` function to compute eigenvalues and vectors. As an example the eigen values are extracted, which give us the frequencies of the Rossby modes up to a polynomial degree $N = 7$ in an ellipsoid of semi-axes $a, b, c = 1.25, 1.1, 0.9$.

Of course, in this example some performance penalties have been accepted, and this implementation will be fairly slow for much larger polynomial degrees. It demonstrates, however, that Julia gives us the right tools and lets us express most of the mathematics in a very intuitive way. It also demonstrates how easy the Galerkin approach with Cartesian polynomials is implemented and extended. To include other forces in this, all that has to be done is define it in the same way it is written mathematically, as long as the boundary conditions remain the same. When including the induction equation some more adaptions have to be done, namely the assembly of the matrices is more complicated, but the general idea remains the same.

In the actual implementation more optimizations have been done. A costly part of the matrix assembly is the inner product and for large polynomial degrees this is the bottleneck of the calculation, but many allocations can be avoided. Some force matrices are symmetric and thus only half of the computations are necessary. Also the matrices are usually sparse, i.e. most entries are zero, which do not have to be stored entirely. Many other optimizations are possible, but go beyond this section. An optimized and more general version of this is implemented in the package *Mire.jl*[2]. The usage of this package is documented online.

---

[2] Available at `https://github.com/fgerick/Mire.jl`

Chapter 4

Torsional Alfvén modes in a non-axisymmetric domain

For the first time the topographic torque of TM is investigated in a non-axisymmetric core model without the need of an idealized, axisymmetric magnetic field. To this end, a QG model has been adapted to an ellipsoidal core volume, capable of capturing TM, RM and MCM for different background magnetic fields. The method based on Cartesian polynomials has proven to be the most accurate and easiest approach to achieve this, giving large flexibility of the model to be adapted to different bases of the velocity and the magnetic field and background magnetic fields. The exact integration of Cartesian polynomials over the ellipsoidal volume is desirable also for the accurate estimate of the net torque balance. The results have been published in Geophysical Journal International (Gerick et al., 2020) and are presented in Section 4.1. In addition, another approach with possible further extension, based on non-orthogonal coordinates, is shortly mentioned in 4.3. A short discussion on how to access the pressure associated with QG flows is given in Section 4.2.

4.1 Pressure torque of torsional Alfvén modes acting on an ellipsoidal mantle

Geophysical Journal International

Geophys. J. Int. (2020) **222,** 338–351
Advance Access publication 2020 April 15
GJI Geomagnetism, Rock Magnetism and Palaeomagnetism

doi: 10.1093/gji/ggaa166

Pressure torque of torsional Alfvén modes acting on an ellipsoidal mantle

F. Gerick,[1,2] D. Jault,[1] J. Noir[2] and J. Vidal[3]

[1] *Univ. Grenoble Alpes, Univ. Savoie Mont Blanc, CNRS, IRD, IFSTTAR, ISTerre, 38000 Grenoble, France*
[2] *Institute of Geophysics, ETH Zurich, Zurich, Switzerland. E-mail: felix.gerick@univ-grenoble-alpes.fr*
[3] *Department of Applied Mathematics, School of Mathematics, University of Leeds, Leeds, LS29JT, United Kingdom*

Accepted 2020 April 2. Received 2020 April 2; in original form 2020 February 7

SUMMARY

We investigate the pressure torque between the fluid core and the solid mantle arising from magnetohydrodynamic modes in a rapidly rotating planetary core. A 2-D reduced model of the core fluid dynamics is developed to account for the non-spherical core–mantle boundary. The simplification of such a quasi-geostrophic model rests on the assumption of invariance of the equatorial components of the fluid velocity along the rotation axis. We use this model to investigate and quantify the axial torques of linear modes, focusing on the torsional Alfvén modes (TM) in an ellipsoid. We verify that the periods of these modes do not depend on the rotation frequency. Furthermore, they possess angular momentum resulting in a net pressure torque acting on the mantle. This torque scales linearly with the equatorial ellipticity. We estimate that for the TM calculated here topographic coupling to the mantle is too weak to account for the variations in the Earth's length-of-day.

Key words: Core; Earth rotation variations; Numerical modelling.

1 INTRODUCTION

Decadal variations in the Earth's length-of-day (LOD) have long been associated with dynamics in the liquid outer core (Munk & MacDonald 1960; Hide 1966; Jault *et al.* 1988; Gross 2015). More specifically, a pronounced variation on a period of roughly six years cannot be explained by atmospheric, oceanic and tidal forces, which are responsible for LOD variations on shorter timescales (Abarca del Rio *et al.* 2000; Holme & de Viron 2013). Torsional Alfvén modes (TM) in the outer core, first studied by Braginsky (1970), have been proposed later as the origin of the 6-yr variation in the LOD (Gillet *et al.* 2010). In the sphere, these oscillations consist of differentially rotating nested geostrophic cylinders, stretching and shearing the magnetic field lines. Recent advances in magnetic field observations and inverse modelling of the outer core flow at the core–mantle boundary (CMB) have revealed recurring TM with 4-yr traveltime through the Earth's outer core (Gillet *et al.* 2010, 2015). Gillet *et al.* (2017) investigated the LOD variations that result from the TM propagation, assuming that the only stresses between the core and the mantle are electromagnetic. Relying on the study of Schaeffer & Jault (2016), they inferred constraints on the electrical conductivity of the lowermost mantle. To account for the observed LOD variations, a conductance of the lowermost mantle of $3 \times 10^7 - 10^8$ S is needed (Gillet *et al.* 2017). Another mechanism of coupling outer core dynamics to the solid mantle is through gravitational coupling between a deformed inner core and a non-spherical CMB (Buffett 1996a,b; Mound & Buffett 2006). A phase lag between the deformations leads to a torque on the mantle. Even though recent advances in atmospheric and oceanic tide modelling have improved the isolation of gravitational signals from core dynamics, the measurements are still inconclusive (Davies *et al.* 2014; Watkins *et al.* 2018).

The third mechanism, investigated here, that may account for exchange of angular momentum between core and mantle is topographic coupling. It has long been proposed that, for a non-spherical CMB, there could be a significant pressure torque exerted by flows in the outer core (Hide 1969). The fluid pressure should scale as $\rho\Omega U R_0$, where ρ is the core density, Ω the angular speed of the Earth's rotation, U a typical horizontal velocity and R_0 the core radius. A typical amplitude of $\mathcal{O}(10^3)$ Pa has been obtained from core surface velocity models, assuming a local balance of force (tangential geostrophy) at the core surface (Jault & Le Mouël 1990). These models have now been superseded by quasi-geostrophic (QG) models that rely on a global assumption, for which it is assumed that the equatorial components of the fluid velocity are invariant along the rotation axis, as observed at leading order in numerical simulations (e.g. Gillet *et al.* 2011; Schaeffer *et al.* 2017). QG models have been shown to capture the fundamental features of rapidly rotating hydrodynamics by comparing with 3-D numerical simulations (Gastine 2019; Guervilly *et al.* 2019). Furthermore, QG models incorporating the magnetic field have been used to investigate spherical TM (Canet *et al.* 2014; Labbé *et al.* 2015). In this framework, the surface pressure cannot be inferred from the velocity. In the most general case, the pressure is a 3-D quantity given by the Lagrange multiplier associated to incompressibility. For QG models we can introduce a Lagrange multiplier associated to incompressibility, but it is only a 2-D function of the coordinates in the equatorial plane. Therefore, we cannot infer the 3-D pressure at the CMB from the velocity field only.

For an axisymmetric core, the axial pressure torque vanishes exactly for any flow. To investigate the influence of non-axisymmetric CMBs, the ellipsoidal geometry can be considered as a first step. From seismological observations a peak-to-peak amplitude of CMB topography of about 3 km has been inferred (Koper *et al.* 2003; Sze & van der Hilst 2003), corresponding to an equatorial ellipticity $\mathcal{O}(10^{-3})$.

Here, we derive a generic QG model that does not assume axisymmetry, which is then compared to a hybrid model using QG velocities and 3-D magnetic fields in the case of an ellipsoid. We present the linear modes and their axial angular momentum, as well as the hydrodynamic pressure torque that the fluid exerts on the solid container. Finally, we discuss the possible implications of this study for Earth-like liquid cores.

2 PROBLEM SETUP

2.1 Magnetohydrodynamic equations

We consider a fluid of homogeneous density ρ, uniform kinematic viscosity ν and magnetic diffusivity η, which is enclosed in a rigid container of volume $\mathcal{V}$ and boundary $\partial\mathcal{V}$. The time evolution of the velocity field $\mathbf{u}$ and the magnetic field $\mathbf{B}$ is given by the incompressible magnetohydrodynamics (MHD) equations. In the reference frame rotating with the angular velocity Ω, they read

$$\frac{\partial \mathbf{u}}{\partial t} + (\mathbf{u}\cdot\nabla)\,\mathbf{u} = -2\,\Omega\times\mathbf{u} - \frac{1}{\rho}\nabla p + \nu\,\nabla^2\mathbf{u} + \frac{1}{\mu_0\rho}(\nabla\times\mathbf{B})\times\mathbf{B}, \tag{1a}$$

$$\frac{\partial \mathbf{B}}{\partial t} = \nabla\times(\mathbf{u}\times\mathbf{B}) + \eta\,\nabla^2\mathbf{B}, \tag{1b}$$

with p the reduced pressure and μ_0 the magnetic permeability in vacuum. MHD eq. (1) are completed by the solenoidal conditions $\nabla\cdot\mathbf{B} = \nabla\cdot\mathbf{u} = 0$. The characteristic length scale R_0 is determined by the container size, which is taken as its mean radius. In ellipsoids, R_0 is the geometric mean $R_0 = (abc)^{1/3}$ of the three semi-major axes $[a, b, c]$. The angular velocity is given by $\Omega = \Omega\mathbf{1}_\Omega$ and the characteristic background magnetic field strength is B_0. We define the characteristic time $t_0 = R_0/u_A$, where $u_A = B_0/\sqrt{\rho\mu_0}$ is the characteristic Alfvén wave velocity. The characteristic pressure is then given by ρu_A^2. The dimensionless equations read

$$\frac{\partial \mathbf{u}}{\partial t} + (\mathbf{u}\cdot\nabla)\,\mathbf{u} = -\frac{2}{\mathrm{Le}}\mathbf{1}_\Omega\times\mathbf{u} - \nabla p + \frac{\mathrm{Pm}}{\mathrm{Lu}}\nabla^2\mathbf{u} + (\nabla\times\mathbf{B})\times\mathbf{B}, \tag{2a}$$

$$\frac{\partial \mathbf{B}}{\partial t} = \nabla\times(\mathbf{u}\times\mathbf{B}) + \frac{1}{\mathrm{Lu}}\nabla^2\mathbf{B}, \tag{2b}$$

where we introduce the Lehnert number Le (measuring the strength of the Lorentz force relative to the Coriolis force), the Lundquist number Lu (comparing magnetic induction to magnetic diffusion) and the magnetic Prandtl number Pm (comparing kinematic viscosity to magnetic diffusion). They are given by

$$\mathrm{Le} = \frac{B_0}{\Omega R_0\sqrt{\mu_0\rho}}, \quad \mathrm{Lu} = \frac{R_0 B_0}{\eta\sqrt{\mu_0\rho}}, \quad \mathrm{Pm} = \frac{\nu}{\eta}. \tag{3}$$

Typical values for the Earth's outer core, with radius $R_0 \approx 3478$ km, kinematic viscosity $\nu \approx 10^{-6}\ \mathrm{m^2 s^{-1}}$ (Wijs *et al.* 1998), mean radial magnetic field strength $B_0 \approx 3$ mT (Gillet *et al.* 2010) and electrical conductivity $\sigma \approx 1.55\times10^6\ \mathrm{Sm^{-1}}$ (Pozzo *et al.* 2014), are $\mathrm{Le} = \mathcal{O}(10^{-4})$, $\mathrm{Lu} = \mathcal{O}(10^5)$ and $\mathrm{Pm} = \mathcal{O}(10^{-6})$. The dynamics we will be considering operate on timescales shorter than magnetic diffusion and viscous spin-up times. Hence, we will neglect viscous and Ohmic dissipations. The governing equations are

$$\frac{\partial \mathbf{u}}{\partial t} + (\mathbf{u}\cdot\nabla)\,\mathbf{u} = -\frac{2}{\mathrm{Le}}\mathbf{1}_\Omega\times\mathbf{u} - \nabla p + (\nabla\times\mathbf{B})\times\mathbf{B}, \tag{4a}$$

$$\frac{\partial \mathbf{B}}{\partial t} = \nabla\times(\mathbf{u}\times\mathbf{B}). \tag{4b}$$

Eq. (4) are supplemented with appropriate boundary conditions. In the diffusionless approximation, the velocity needs to satisfy only the non-penetration condition $\mathbf{u}\cdot\mathbf{n} = 0$ on ∂V. If $\mathbf{B}\cdot\mathbf{n} = 0$ at an initial time $t = 0$, the normal component of the induction equation ensures that the normal component of $\mathbf{B}$ is zero at all later times (see Backus *et al.* 1996).

2.2 Torque balance

The net torque balance of the system is given by

$$\frac{\partial \mathbf{L}}{\partial t} + \Gamma_\mathrm{c} = \Gamma_\mathrm{p} + \Gamma_\mathrm{L}, \tag{5}$$

with the angular momentum $\mathbf{L}$, the hydrodynamic pressure torque Γ_p, the Coriolis torque Γ_c and the Lorentz torque Γ_L given by

$$\mathbf{L} = \int_\mathcal{V} \mathbf{r}\times\mathbf{u}\,\mathrm{d}V, \tag{6a}$$

$$\Gamma_\mathrm{p} = -\int_\mathcal{V} \mathbf{r}\times\nabla p\,\mathrm{d}V = -\int_{\partial\mathcal{V}} p\,(\mathbf{r}\times\mathbf{n})\,\mathrm{d}S, \tag{6b}$$

$$\Gamma_\mathrm{c} = 2\int_\mathcal{V} \mathbf{r}\times(\Omega\times\mathbf{u})\,\mathrm{d}V, \tag{6c}$$

$$\Gamma_\mathrm{L} = \int_\mathcal{V} \mathbf{r}\times((\nabla\times\mathbf{B})\times\mathbf{B})\,\mathrm{d}V. \tag{6d}$$

We can further split up the Lorentz torque into magnetic pressure torque Γ_pm and a magnetic tension torque Γ_b as

$$\Gamma_\mathrm{L} = \Gamma_\mathrm{b} + \Gamma_\mathrm{pm}, \tag{7}$$

with

$$\Gamma_\mathrm{pm} = -\frac{1}{2}\int_\mathcal{V} \mathbf{r}\times\nabla\left(\mathbf{B}^2\right)\,\mathrm{d}V = -\frac{1}{2}\int_{\partial\mathcal{V}} \mathbf{B}^2(\mathbf{r}\times\mathbf{n})\,\mathrm{d}S, \tag{8a}$$

$$\Gamma_\mathrm{b} = \int_\mathcal{V} \mathbf{r}\times((\mathbf{B}\cdot\nabla)\,\mathbf{B})\,\mathrm{d}V. \tag{8b}$$

For a perfectly conducting boundary (with $\mathbf{B}\cdot\mathbf{n} = 0$ on $\partial\mathcal{V}$), Γ_b vanishes exactly [see eq. (45) in Roberts & Aurnou 2012] and only the magnetic pressure torque Γ_pm contributes to the torque balance (5).

The axial component of the Coriolis torque Γ_c also vanishes (see equation 14.98 in Davidson 2016). In the axial direction, the torque balance reduces to

$$\frac{\partial L_z}{\partial t} = \Gamma_{\mathrm{p},z} + \Gamma_{\mathrm{pm},z}. \tag{9}$$

Hence, any changes of the axial angular momentum of the fluid can only result from the unbalance between the magnetic and hydrodynamic pressure torques. For the sphere, the transformation of the volume integral into a surface integral shows that the pressure torques (6b) and (8a) vanish, so that no change in angular momentum is possible.

2.3 Geostrophic motions and torsional Alfvén modes

In a container of volume $\mathcal{V}$ that can be continuously deformed into a sphere, such that the height of the fluid column h along the rotation axis is a homeomorphism between the volume $\mathcal{V}$ and the sphere, all contours of constant h (geostrophic contours) are closed. Examples of such containers include the full sphere (not a spherical shell) or ellipsoids. It is often postulated that incompressible flows in such a container can be expanded as (e.g. Greenspan 1968)

$$\mathbf{u} = \sum_j^{\infty} \gamma_j(t)\,\mathbf{u}_{G,j}(\mathbf{r}_\perp) + \sum_i^{\infty} \alpha_i(t)\,\mathbf{u}_i(\mathbf{r}), \tag{10}$$

where $\mathbf{u}_{G,j}(\mathbf{r}_\perp)$ are the (degenerate) geostrophic solutions (e.g. Liao & Zhang 2010, in spheres) that only depend on the position perpendicular to the rotation axis $\mathbf{r}_\perp$. They are given by the geostrophic equilibrium

$$2\,\Omega \times \mathbf{u}_{G,j} = -\nabla p_{G,j}, \tag{11}$$

and their superposition is commonly referred to as the geostrophic mode $\mathbf{u}_G = \sum_j \mathbf{u}_{G,j}$ (e.g. Greenspan 1968). Additionally, $\mathbf{u}_i(\mathbf{r})$ are the spatial eigensolutions of the inertial wave equation (e.g. Vantieghem 2014, in ellipsoids)

$$\frac{\partial \mathbf{u}_i}{\partial t} + 2\,\Omega \times \mathbf{u}_i = -\nabla p_i. \tag{12}$$

Expansion (10) has proven to be exact for the ellipsoid (Backus & Rieutord 2017; Ivers 2017).

From balance (11) it is clear that the axial geostrophic pressure torque vanishes, as the axial Coriolis torque vanishes for any flow $\mathbf{u}$. However, this is no longer the case when the flow is time dependent, even if it remains mainly geostrophic (or 'pseudo-geostrophic', Gans 1971), such that $\mathbf{u}_{PG}(\mathbf{r}_\perp, t) \simeq \sum_j \gamma_j(t)\,\mathbf{u}_{G,j}$ (i.e. with $|\gamma_j| \gg |\alpha_i|$). In the presence of a Lorentz force the pseudo-geostrophic flow is governed by

$$\frac{\partial \mathbf{u}_{PG}}{\partial t} = -\frac{2}{\mathrm{Le}}\,\mathbf{1}_\Omega \times \mathbf{u}_{PG} - \nabla p + (\nabla \times \mathbf{B}) \times \mathbf{B}. \tag{13}$$

Using the geostrophic equilibrium (11) we substitute the Coriolis acceleration for its pressure gradient. Additionally, rewriting the Lorentz force in terms of the magnetic pressure gradient and the Maxwell term, (13) takes the form

$$\frac{\partial \mathbf{u}_{PG}}{\partial t} = -\nabla(p_A + p_m) + (\mathbf{B} \cdot \nabla)\mathbf{B}, \tag{14}$$

with $p_A = p - \sum_j \gamma_j p_{G,j}$ and $p_m = \mathbf{B}^2/2$. Besides the magnetic pressure p_m, an ageostrophic component p_A remains in the pressure. They may both exert a torque on the container if it is not spherical.

TM, also called 'torsional oscillations' (Braginsky 1970), are examples of such pseudo-geostrophic flows. They are solutions of the linearized eq. (4) for $\mathrm{Le} \ll 1$, and reduce to the ordinary geostrophic mode in the limit $\mathrm{Le} \to 0$. When scaled by the reciprocal of the Alfvén time scale T_A, the TM frequencies are constant (see Fig. 1). Their Alfvén wave nature is also evident in the ratio of kinetic energy to magnetic energy, which is $\mathcal{O}(1)$ as indicated by the grey colour in Fig. 1. We define TM to have a frequency independent of Le when $\mathrm{Le} \ll 1$ (if scaled by T_A^{-1}) and of approximately unit ratio between kinetic and magnetic energy. These two features clearly differentiate them from other modes present, namely the so-called fast modes and slow modes. The fast modes are slightly modified inertial modes, with frequencies on the order of the angular frequency, and their energy is mostly kinetic (see Fig. 1, yellow dots). The slow modes (or Magneto–Coriolis modes) have a frequency much lower than the angular frequency and a small kinetic energy compared to the magnetic energy (see Fig. 1, dark blue dots).

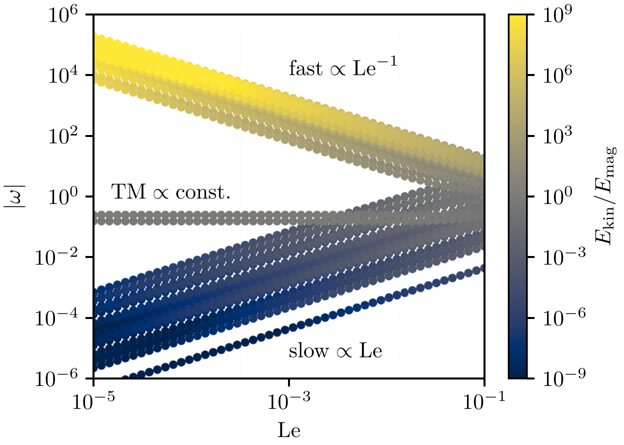

Figure 1. Mode frequencies as a function of Lehnert number in the sphere. The imposed magnetic field is $\mathbf{B}_0 = (-y, x - z/10, x/10)^T$, following Vidal *et al.* (2019). The colours indicate the ratio of kinetic energy to magnetic energy, where yellow indicates a larger kinetic energy and blue a larger magnetic energy. The modes are separated into slow modes, fast modes and TM for $\mathrm{Le} \ll 1$.

In the axisymmetric case, the geostrophic mode can be written as $\mathbf{u}_G = u_G(s)\mathbf{1}_\phi$ and a pseudo-geostrophic flow is simply $\mathbf{u}_{PG} \simeq u_{PG}(s,t)\mathbf{1}_\phi$ (with s the cylindrical radius and ϕ the azimuthal angle). The projection of the linearized momentum eq. (4a) onto the geostrophic mode reduces to the 1-D equation

$$\rho h \frac{\partial^2 u_{PG}(s,t)}{\partial t^2} = \frac{1}{s^2}\frac{\partial}{\partial s}\left(h s^3 \frac{\partial}{\partial s}\left(\frac{u_{PG}(s,t)}{s}\right) \int B_s^2 \mathrm{d}z \right), \tag{15}$$

only depending on the radial distance s to the rotation axis. Roberts & Aurnou (2012) referred to this equation as the canonical torsional wave equation. We refer the reader to Roberts (1972) and Jault (2003) for details on the derivation. In the case of the ellipsoid, we shall consider TM within the framework of a QG model retaining ageostrophic components of the flow.

2.4 Quasi-geostrophic equation with generic geostrophic contours

We assume that the horizontal velocity components are independent of the coordinate z along the rotation axis, $\mathbf{u}_\perp = \mathbf{u}_\perp(\mathbf{r}_\perp, t)$. Together with the non-penetration boundary condition, $\mathbf{u} \cdot \mathbf{n} = 0$ on $\partial\mathcal{V}$, the mass continuity equation $\nabla \cdot \mathbf{u} = 0$ and the assumption of an equatorially symmetric volume $\mathcal{V}$ the QG velocity takes the form (e.g. Bardsley 2018)

$$\mathbf{u} = \mathbf{u}_\perp(\mathbf{r}_\perp, t) + u_z \mathbf{1}_z = \nabla\psi \times \nabla\left(\frac{z}{h}\right), \tag{16}$$

with $h = h(\mathbf{r}_\perp)$ the height of the fluid column, $\mathbf{u}_\perp(\mathbf{r}_\perp, t) = \frac{1}{h}\nabla\psi \times \mathbf{1}_z$, $u_z = \frac{z}{h}\mathbf{u}_\perp \cdot \nabla h$ and $\psi = \psi(\mathbf{r}_\perp, t)$ a scalar stream function. By construction, ψ is constant at the equator $\partial\mathcal{A}$ for the volume $\mathcal{V}$ considered here. Following the boundary condition arising naturally when $h \to 0$ at $\partial\mathcal{A}$ (Maffei *et al.* 2017), we choose $\psi = 0$ on $\partial\mathcal{A}$. Note that, if ψ is constant along geostrophic contours (i.e. it is a function of h only), we recover the geostrophic velocity (see Appendix A).

To derive an evolution equation for this scalar stream function, we project the momentum eq. (4a) onto the subset $\mathbf{u}'$ of QG velocities (16) following Labbé *et al.* (2015) and Bardsley (2018).

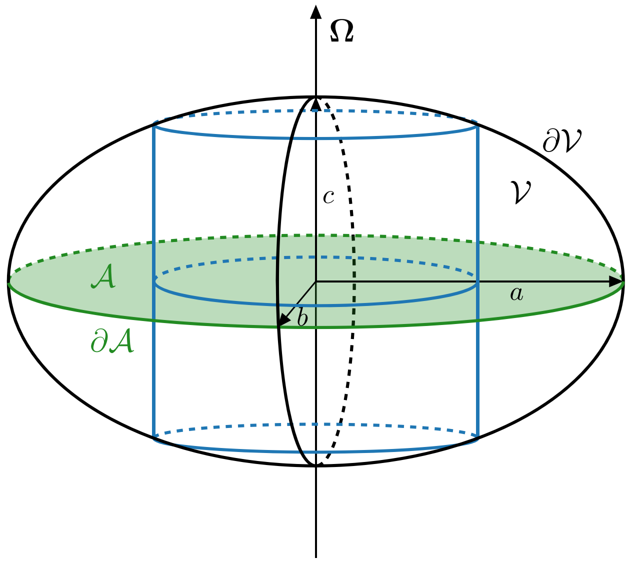

Figure 2. Schematic of a geostrophic column (blue) in an ellipsoid of volume $\mathcal{V}$ where one of the principal axes is aligned with the rotation axis Ω. The area of the equatorial plane $\mathcal{A}$ is shaded in green.

This method is essentially a variational approach, which consists in finding solutions $\mathbf{u}$ satisfying

$$\int_{\mathcal{V}} \mathbf{u}'\cdot\mathbf{f}(\mathbf{u})\,\mathrm{d}V = 0, \qquad \forall\mathbf{u}', \tag{17}$$

where

$$\mathbf{f}(\mathbf{u}) = \frac{\partial\mathbf{u}}{\partial t} + (\mathbf{u}\cdot\nabla)\mathbf{u} + \frac{2}{\mathrm{Le}}\mathbf{1}_\Omega\times\mathbf{u} + \nabla p - (\nabla\times\mathbf{B})\times\mathbf{B}, \tag{18}$$

with $\mathbf{u}'$ and $\mathbf{u}$ of the form (16). Substituting (16) into (17) yields

$$\int_{\mathcal{V}} \mathbf{u}'\cdot\mathbf{f}\,\mathrm{d}V = \int_{\mathcal{V}} \nabla\psi'\times\nabla\left(\frac{z}{h}\right)\cdot\mathbf{f}\,\mathrm{d}V, \tag{19a}$$

$$= \int_{\mathcal{A}} \nabla\psi'\cdot\left\langle\nabla\left(\frac{z}{h}\right)\times\mathbf{f}\right\rangle\mathrm{d}S, \tag{19b}$$

$$= -\int_{\mathcal{A}} \psi'\nabla\cdot\left\langle\nabla\left(\frac{z}{h}\right)\times\mathbf{f}\right\rangle\mathrm{d}S, \tag{19c}$$

$$= -\int_{\mathcal{A}} \psi'\mathcal{Q}(\mathbf{f})\,\mathrm{d}S, \tag{19d}$$

with the projection operator $\mathcal{Q}$ defined as

$$\mathcal{Q}(\mathbf{f}) = \nabla\cdot\left\langle\nabla\left(\frac{z}{h}\right)\times\mathbf{f}\right\rangle, \tag{20}$$

where $\langle\cdot\rangle = \int_{-h}^{h}\cdot\,\mathrm{d}z$ is the integral along the rotation axis and $\int_{\mathcal{A}}\cdot\,\mathrm{d}S$ the integral over the equatorial surface plane $\mathcal{A}$ (shown in Fig. 2 for the ellipsoid). In this step, we made use of the boundary condition $\psi = 0$ at the equator $\partial\mathcal{A}$. For expression (19d) to be zero for any test function ψ', the QG velocity $\mathbf{u}$ must satisfy

$$\mathcal{Q}\left(\frac{\partial\mathbf{u}}{\partial t} + \mathbf{u}\cdot\nabla\mathbf{u} + \frac{2}{\mathrm{Le}}\mathbf{1}_\Omega\times\mathbf{u} - (\nabla\times\mathbf{B})\times\mathbf{B}\right) = 0, \tag{21}$$

where the pressure gradient is omitted, as it vanishes in the projection.

First, we consider the inertial term, which simplifies as

$$\mathcal{Q}\left(\frac{\partial\mathbf{u}}{\partial t}\right) = \nabla\cdot\left\langle\nabla\left(\frac{z}{h}\right)\times\left(\nabla\frac{\partial\psi}{\partial t}\times\nabla\left(\frac{z}{h}\right)\right)\right\rangle, \tag{22a}$$

$$= 2\mathcal{D}\frac{\partial\psi}{\partial t}, \tag{22b}$$

with

$$\mathcal{D}\Psi = \nabla\cdot\left(\tfrac{1}{h}\nabla\Psi + \tfrac{1}{3h}\nabla h\times(\nabla\Psi\times\nabla h)\right). \tag{23}$$

We can derive the projection for a force in the form of $\boldsymbol{\xi}\times\mathbf{u}$ as follows:

$$\mathcal{Q}(\boldsymbol{\xi}\times\mathbf{u}) = \nabla\cdot\left\langle-\left(\nabla\left(\frac{z}{h}\right)\cdot\boldsymbol{\xi}\right)\mathbf{u}\right\rangle, \tag{24}$$

which holds for any $\mathbf{u}$ satisfying the boundary condition $\mathbf{u}\cdot\mathbf{n} = 0$ on $\partial\mathcal{V}$. We may further simplify this by considering $\Phi = -\nabla\left(\frac{z}{h}\right)\cdot\boldsymbol{\xi}$

$$\nabla\cdot\langle\Phi\mathbf{u}\rangle = \nabla\cdot\left\langle\frac{\Phi}{h}\nabla\times\mathbf{1}_z + \Phi z\nabla\psi\times\nabla\left(\frac{1}{h}\right)\right\rangle, \tag{25a}$$

$$= \nabla\cdot\left(\frac{\langle\Phi\rangle}{h}\nabla\psi\times\mathbf{1}_z + \langle z\Phi\rangle\nabla\psi\times\nabla\left(\frac{1}{h}\right)\right), \tag{25b}$$

$$= \left\{\frac{\langle\Phi\rangle}{h},\psi\right\}, \tag{25c}$$

with

$$\{X, Y\} = (\nabla X\times\nabla Y)\cdot\mathbf{1}_z. \tag{26}$$

Let us write $\mathbf{u}\cdot\nabla\mathbf{u} = (\nabla\times\mathbf{u})\times\mathbf{u} + \nabla\mathbf{u}^2/2$. Since the gradient term vanishes exactly in the projection, the non-linear term can be written in the generic form $\boldsymbol{\xi}\times\mathbf{u}$, with $\boldsymbol{\xi} = \nabla\times\mathbf{u}$. For the non-linear term we thus have

$$\langle\Phi\rangle = \left\langle-\nabla\left(\frac{z}{h}\right)\cdot(\nabla\times\mathbf{u})\right\rangle, \tag{27a}$$

$$= \left\langle\nabla\cdot\left(\nabla\left(\frac{z}{h}\right)\times\left(\nabla\psi\times\nabla\left(\frac{z}{h}\right)\right)\right)\right\rangle, \tag{27b}$$

$$= 2\mathcal{D}\psi. \tag{27c}$$

We have used here $\langle\nabla\cdot\mathbf{x}\rangle = \nabla\cdot\langle\mathbf{x}\rangle$, which can be demonstrated to hold for $\mathbf{x} = \nabla\left(\frac{z}{h}\right)\times\left(\nabla\psi\times\nabla\left(\frac{z}{h}\right)\right)$. The non-linear term is then given by

$$\mathcal{Q}((\nabla\times\mathbf{u})\times\mathbf{u}) = 2\left\{\frac{1}{h}\mathcal{D}\psi,\psi\right\}. \tag{28}$$

For the Coriolis force $\boldsymbol{\xi} = 2/\mathrm{Le}\,\mathbf{1}_\Omega$ and thus $\langle\Phi\rangle = \left\langle-\nabla\left(\frac{z}{h}\right)\cdot\Omega\right\rangle = -4/\mathrm{Le}$, so that the Coriolis force reduces to

$$\mathcal{Q}\left(\frac{2}{\mathrm{Le}}\mathbf{1}_\Omega\times\mathbf{u}\right) = -\frac{4}{\mathrm{Le}}\left\{\frac{1}{h},\psi\right\}. \tag{29}$$

The QG scalar momentum equation is then given by

$$\mathcal{D}\frac{\partial\psi}{\partial t} + \left\{\frac{1}{h}\mathcal{D}\psi,\psi\right\} = \frac{2}{\mathrm{Le}}\left\{\frac{1}{h},\psi\right\} + \frac{1}{2}\mathcal{Q}((\nabla\times\mathbf{B})\times\mathbf{B}). \tag{30}$$

We can close the system by assuming that the 3-D magnetic field in (30) is advected only by the QG velocity. This is, to the authors' knowledge, the first presentation of a hybrid model with QG velocities and 3-D magnetic field. Such a model is desirable especially in geodynamo modelling, where it is found that a strong columnar motion is accompanied by a magnetic field of 3-D structure (e.g. Schaeffer *et al.* 2017).

To derive a fully 2-D model we assume the same form for the magnetic field, as for the velocity

$$\mathbf{B} = \nabla A\times\nabla\left(\frac{z}{h}\right), \tag{31}$$

with $A = A(\mathbf{r}_\perp, t)$ a scalar potential. By construction, such a magnetic field satisfies the perfectly conducting boundary condition $\mathbf{B}\cdot\mathbf{n} = 0$. This approximation has been used previously to investigate TM in QG models (Canet *et al.* 2014; Labbé *et al.* 2015). Under this assumption, the Lorentz term simplifies analogous to

(28), such that

$$\mathcal{Q}\left((\nabla \times \mathbf{B}) \times \mathbf{B}\right) = 2\left\{\frac{1}{h}\mathcal{D}A,\, A\right\}. \tag{32}$$

The scalar momentum equation is then written in terms of ψ and A only

$$\mathcal{D}\frac{\partial \psi}{\partial t} + \left\{\frac{1}{h}\mathcal{D}\psi,\, \psi\right\} = 2\Omega\left\{\frac{1}{h},\, \psi\right\} + \left\{\frac{1}{h}\mathcal{D}A,\, A\right\}. \tag{33}$$

The ideal induction eq. (4b) can be simplified as follows:

$$\mathbf{u} \times \mathbf{B} = \frac{1}{h^2}\nabla\psi \times \nabla A - \frac{z}{h^3}\{\psi, A\}\nabla h, \tag{34}$$

$$= \frac{C}{h}\mathbf{1}_z - \frac{Cz}{h^2}\nabla h, \tag{35}$$

with $C = \frac{1}{h}\{\psi, A\}$. Taking the curl then gives

$$\nabla \times (\mathbf{u} \times \mathbf{B}) = \frac{1}{h}\nabla C \times \mathbf{1}_z - \frac{z}{h^2}\nabla C \times \nabla h \tag{36a}$$

$$= \nabla C \times \nabla\left(\frac{z}{h}\right). \tag{36b}$$

Thus, the induction equation is given by

$$\frac{\partial A}{\partial t} = \frac{1}{h}\{\psi, A\}. \tag{37}$$

In the sphere, where cylindrical coordinates apply, the eqs (33) and (37) are exactly equivalent to the equations obtained by Labbé *et al.* (2015).

3 METHODS FOR THE ELLIPSOID

We now consider the case of an ellipsoid with semi axes a, b and c defined by

$$\frac{x^2}{a^2} + \frac{y^2}{b^2} + \frac{z^2}{c^2} = 1. \tag{38}$$

To keep equatorial symmetry, we also consider that the rotation axis is aligned with the c-axis, $\mathbf{1}_\Omega = \mathbf{1}_z$ (Fig. 2).

3.1 Cartesian monomial basis in the ellipsoid

Since the ellipsoid is a quadratic surface, smooth-enough solutions can be sought by using an infinite sequence of Cartesian polynomials (Lebovitz 1989). This approach has proven accurate to describe 3-D inviscid flows in ellipsoids (e.g. Vantieghem *et al.* 2015; Vidal & Cébron 2017; Vidal *et al.* 2020). The 3-D inertial modes are exactly described by polynomials in the ellipsoid (Backus & Rieutord 2017; Ivers 2017), and also the QG and 3-D inertial modes in the spheroid (Maffei *et al.* 2017; Zhang & Liao 2017). Additionally, the MHD modes upon idealized background magnetic fields (e.g. Malkus 1967) also have an exact polynomial description in the spheroid (Kerswell 1994) and the ellipsoid (Vidal *et al.* 2016).

Similarly, a 2-D polynomial decomposition in the Cartesian coordinates can be obtained for arbitrary QG vector (16) in non-axisymmetric ellipsoids as follows. To satisfy the polynomial form of the velocity components, the stream function must be given as

$$\psi = h^3\,\Pi(x, y) = h^3\sum_i \hat{\alpha}_i \Pi_i, \tag{39}$$

with the complex-valued coefficients $\hat{\alpha}_i$ and the monomials

$$\Pi_i = 1, x, y, xy, x^2, ..., x^{N-1}, y^{N-1} \tag{40}$$

with $i \in [0, N_2]$ and $N_2 = N(N+1)/2$. At any point (x, y) we have

$$\frac{h^2}{c^2} = 1 - \frac{x^2}{a^2} - \frac{y^2}{b^2}. \tag{41}$$

If additionally we define $G = h^2/2$, we can rewrite

$$h\nabla h = \nabla G. \tag{42}$$

Then, the QG basis vectors $\mathbf{u}_i$ are given by

$$\mathbf{u}_i = h^2\nabla\Pi_i \times \mathbf{1}_z + 3\Pi_i\nabla G \times \mathbf{1}_z - z\nabla\Pi_i \times \nabla G, \tag{43}$$

with the first three basis elements

$$\mathbf{u}_0 = 3c^2\begin{pmatrix} -y/b^2 \\ x/a^2 \\ 0 \end{pmatrix}, \tag{44a}$$

$$\mathbf{u}_1 = c^2\begin{pmatrix} 1 - x^2/a^2 - 4y^2/b^2 \\ 3xy/a^2 \\ -xz/a^2 \end{pmatrix}, \tag{44b}$$

$$\mathbf{u}_2 = c^2\begin{pmatrix} -3xy/b^2 \\ 4x^2/a^2 + y^2/b^2 - 1 \\ yz/b^2 \end{pmatrix}. \tag{44c}$$

The full velocity is reconstructed by

$$\mathbf{u} = \sum_{i=0}^{N_2}\hat{\alpha}_i\mathbf{u}_i. \tag{45}$$

For the linear hydrodynamic (Rossby wave) problem

$$\mathcal{D}\frac{\partial\psi}{\partial t} = 2\Omega\left\{\frac{1}{h},\, \psi\right\}, \tag{46}$$

the polynomial degree of $\psi_i = \hat{\alpha}_i h^3 \Pi_i$ is preserved, that is the QG inertia and Coriolis operators do not modify (increase) the polynomial degree, similar to the 3-D Coriolis operator in the ellipsoid (Backus & Rieutord 2017; Ivers 2017). This is no longer the case in the presence of a background magnetic field within the QG model (unless the magnetic field is only linear in the spatial coordinates, see Malkus 1967), as the Lorentz term modifies the polynomial degree. Then, the exact solutions cannot be obtained from a finite set of Π_i. Hence, we must project the governing equations onto the basis with a sufficiently large maximum polynomial degree.

3.2 Galerkin method

Since we are interested in the wave properties, we linearize equations (4) around a background state with no motion and steady magnetic field $\mathbf{B}_0$. In the Earth's core, the characteristic mean velocity field is thought to be negligible compared to the Alfvén wave velocity (Gillet *et al.* 2015; Bärenzung *et al.* 2018). Hence, the velocity and magnetic perturbations $[\tilde{\mathbf{u}}, \tilde{\mathbf{B}}]$ are given by

$$\frac{\partial\tilde{\mathbf{u}}}{\partial t} + \frac{2}{\mathrm{Le}}\mathbf{1}_\Omega \times \tilde{\mathbf{u}} = -\nabla p + (\nabla \times \mathbf{B}_0) \times \tilde{\mathbf{B}} + (\nabla \times \tilde{\mathbf{B}}) \times \mathbf{B}_0, \tag{47a}$$

$$\frac{\partial\tilde{\mathbf{B}}}{\partial t} = \nabla \times (\tilde{\mathbf{u}} \times \mathbf{B}_0). \tag{47b}$$

The linearized set of equations in the hybrid model then read

$$\mathcal{D}\frac{\partial\tilde{\psi}}{\partial t} = \frac{2}{\mathrm{Le}}\left\{\frac{1}{h},\, \tilde{\psi}\right\} + \frac{1}{2}\mathcal{Q}((\nabla \times \mathbf{B}_0) \times \tilde{\mathbf{B}} + \frac{1}{2}\mathcal{Q}((\nabla \times \tilde{\mathbf{B}}) \times \mathbf{B}_0), \tag{48a}$$

$$\frac{\partial\tilde{\mathbf{B}}}{\partial t} = \nabla \times \left(\left(\nabla\tilde{\psi} \times \nabla\left(\frac{z}{h}\right)\right) \times \mathbf{B}_0\right). \tag{48b}$$

The linearization of the magnetic field translates to $A = A_0 + \tilde{A}$ for the scalar potential and the scalar QG eqs (33) and (37) read

$$\partial_t \mathcal{D}\tilde{\psi} - \frac{2}{\mathrm{Le}}\left\{\frac{1}{h}, \tilde{\psi}\right\} = \left\{\frac{1}{h}\mathcal{D}\tilde{A}, A_0\right\} + \left\{\frac{1}{h}\mathcal{D}A_0, \tilde{A}\right\}, \tag{49a}$$

$$\frac{\partial \tilde{A}}{\partial t} = \frac{1}{h}\{\tilde{\psi}, A_0\}. \tag{49b}$$

To solve such sets of linearized equations for eigenmodes, Fourier expansions along the azimuthal direction could be used in the sphere, combined with finite differences in the radial direction (Labbé *et al.* 2015). Here, we use a Galerkin approach to project the governing equations onto the respective polynomial bases (e.g. Vidal & Cébron 2017; Vidal *et al.* 2020). This approach is suitable for the Cartesian monomial basis, as we can analytically integrate the Cartesian monomials occurring in the inner product (see formula 50 in Lebovitz 1989). For the QG model this projection is given by

$$f_{ij} = \int_{\mathcal{A}} \tilde{\psi}_i\, f(\tilde{\psi}_j, \tilde{A}_j)\,\mathrm{d}S, \tag{50}$$

where now $f(\tilde{\psi}, \tilde{A})$ corresponds to a force in the scalar momentum eq. (49a). In this way we create coefficient matrices U_{ij}, C_{ij} and L_{ij} for the inertial, Coriolis and Lorentz force, respectively. Analogously, the induction eq. (49b) is projected onto the basis $A_i = \hat{\zeta}_i h^3 \Pi_i$ and the coefficient matrices B_{ij} and V_{ij} correspond to the projections of the temporal change of the magnetic field and magnetic advection, respectively. For this model U_{ij} and B_{ij} are identical and Hermitian. Assuming that $\tilde{\psi}(\mathbf{r}_\perp, t) = \hat{\psi}(\mathbf{r}_\perp)\exp(\mathrm{i}\omega t)$ (and the same for $\tilde{A}$), so that $\partial_t\tilde{\psi} = \mathrm{i}\omega\tilde{\psi}$, the resulting matrix form is

$$\mathrm{i}\omega\mathbf{M}\mathbf{x} = \mathbf{D}\mathbf{x}, \tag{51}$$

with $\mathbf{M}, \mathbf{D} \in R^{2N_2\times 2N_2}$ of the form

$$\mathbf{M} = \begin{pmatrix} U_{ij} & 0 \\ 0 & B_{ij} \end{pmatrix}, \qquad \mathbf{D} = \begin{pmatrix} C_{ij} & L_{ij} \\ V_{ij} & 0 \end{pmatrix}, \tag{52}$$

and $\mathbf{x} = (\hat{\alpha}_j, \hat{\zeta}_j) \in C^{2N_2}$. This form is referred to as a generalized eigen problem solvable for eigen pairs $(\omega_k, \mathbf{x}_k)$.

Note that using the reduced equation and projecting onto the basis of stream functions $\tilde{\psi}_i$ is equivalent to projecting the 3-D equations onto the QG basis $\mathbf{u}_i$, apparent from (19). We use this fact for the hybrid model and project the 3-D momentum eq. (47a) onto the QG basis vectors $\mathbf{u}_i$ while keeping the full 3-D basis vectors $\mathbf{B}_i$ with coefficients ζ_i for the magnetic field. The induction eq. (47b) is projected onto the basis $\mathbf{B}_i$. The resulting matrices are $U'_{ij}, C'_{ij} \in R^{N_2\times N_2}$, $L'_{ij} \in R^{N_2\times N_3}$, $B_{ij} \in R^{N_3\times N_3}$ and $V'_{ij} \in R^{N_3\times N_2}$, so that $\mathbf{M}', \mathbf{D}' \in R^{N_2+N_3\times N_2+N_3}$ and $\mathbf{x} = (\hat{\alpha}_j, \zeta_j) \in C^{N_2+N_3}$. These matrices can be built analytically, but this becomes tedious even for a maximum polynomial degree as low as 2 and in practice this is done by computer algebra systems or numerically.

3.3 Numerical implementation

The linear problems based on Cartesian monomials are implemented in the Julia programming language (Bezanson *et al.* 2017). The QG, hybrid and 3-D models are freely available at https://github.com/fgerick/Mire.jl. The reproduction of all the results and figures from this article using these models is available through https://dx.doi.org/10.5281/zenodo.3631244.

To solve for the eigen problems, different methods have been employed. To calculate the full spectrum of eigensolutions, we use either LAPACK or recent Julia implementations for accuracy beyond standard floating point numbers (e.g. in Fig. 9). Full spectrum eigensolutions are computationally demanding, which is why we also apply targeted iterative solvers from the ARPACK library, making use of the sparsity of the matrices **M** and **D**, where approximately 13 and 30 per cent of entries are non-zero, respectively. The sparse solver is also applied to follow eigenbranches (i.e. to track a specific eigensolution through the parameter space). To do so, we apply a targeted shift-and-invert method (e.g. Rieutord & Valdettaro 1997; Vidal & Schaeffer 2015)

$$(\mathbf{D} - \sigma\mathbf{M})^{-1}\mathbf{D}\mathbf{x} = \lambda\mathbf{x} \tag{53}$$

around a target $\sigma \in C$, with the new eigenvalue $\lambda = (\mathrm{i}\omega - \sigma)^{-1}$. This strategy is efficient to compute the eigenvalues close to the target σ (which is chosen close to the desired eigenvalue $\mathrm{i}\omega$).

4 NUMERICAL RESULTS

We first validate our QG (and hybrid) model against the 3-D model for a simplified background magnetic field (Malkus 1967), and then consider a more complex background magnetic field that is able to drive TM. In this section the QG model is considered and we compare our results to a 3-D magnetic field with the hybrid model in Appendix B.

4.1 Modes in the Malkus field

An interesting first study case is the mean field introduced by Malkus (1967), originally given as a field of uniform current along the rotation axis in a sphere with $\mathbf{B}_{0,M} = s\,\mathbf{1}_\phi$ (hereafter Malkus field). In his study, the slow and the fast modes were recovered from the resulting dispersion relation (see eq. 2.28 in Malkus 1967).

In the ellipsoidal case, the Malkus field is modified to follow the elliptical geostrophic contours. This translates into the background magnetic field $\mathbf{B}_{0,z} = c^2(-y/b^2, x/a^2, 0)^T$ in Cartesian coordinates (e.g. Vidal *et al.* 2019) and a mean magnetic potential $A_0 = h^3/3$ for the QG model. Due to the lack of any magnetic field component perpendicular to the geostrophic contours, the Malkus field does not permit TM. However, that field allows us to investigate the slow and fast modes in the ellipsoid. We report, for the first time, the dependency of these modes on the equatorial ellipticity

$$\epsilon = \frac{a^2 - b^2}{a^2 + b^2}, \tag{54}$$

where $\epsilon = 0$ corresponds to the axisymmetric case. Here, we investigate the parameter range $\epsilon \in [0, 0.4]$. For all the results shown below, the semi-axis along the rotation axis is kept constant at $c = 1$. The influence of polar flattening has already been investigated previously and is not discussed here (Maffei *et al.* 2017; Zhang & Liao 2017). Throughout this study, the volume is preserved by setting $a = 1/b$ when increasing the ellipticity in the equatorial plane, so that $abc = 1$.

We compute the frequencies of two of the largest-scale fast and slow modes, and track their frequencies as a function of ϵ. The results are shown in Fig. 3. The trends of all models agree well. The fast modes decrease in frequency, whereas the slow modes increase their frequency as the ellipticity is increased. The frequency is almost independent of the ellipticity when $\epsilon \ll 1$, and the difference with respect to the spherical values scales as $|\omega(\epsilon = 0) - \omega(\epsilon)| \sim \epsilon^2$ for the fast and slow modes (see Fig. 3, bottom). This scaling may be anticipated by the relation of the fast and slow modes to the inertial modes in the ellipsoid, showing a similar scaling (compare with eq. 3.24 in Vantieghem 2014).

The Malkus field is completely determined by the geostrophic basis (as introduced in Appendix A). Hence, we do not observe

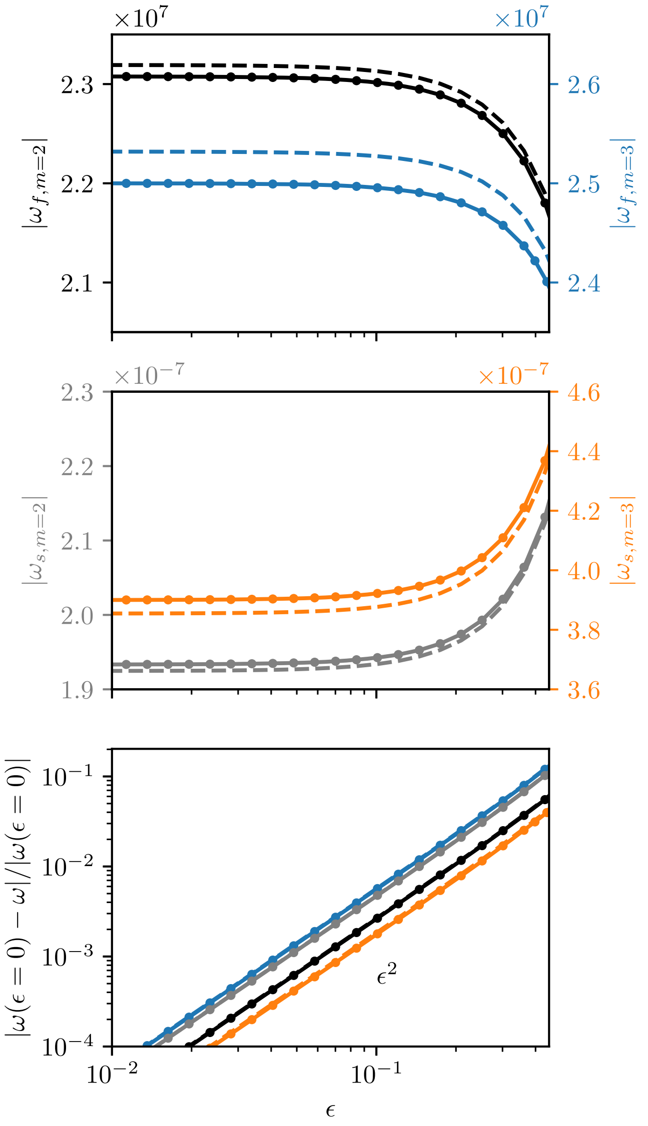

Figure 3. Frequencies $\omega_{f,\,m}$ of the fast modes (top) and $\omega_{s,\,m}$ of the slow modes (middle) as a function of ellipticity for radial complexity $l = 1$ and azimuthal wave number $m = 2, 3$. Difference between the frequency as a function of ϵ and the frequency in the sphere with $\epsilon = 0$, normalized by the frequency in the sphere, for the considered fast and slow modes (bottom). The Lehnert number is 10^{-8}. The different models are: QG (solid), hybrid (dots) and 3-D (dashed).

any differences between the QG model (solid line) and the hybrid model (dots). The differences in frequency magnitude between the 3-D model (dashed line) and the QG and hybrid model depend on the modes' complexity (see Labbé *et al.* 2015; Maffei *et al.* 2017). The discrepancies observed between the different models are similar over the entire range of ellipticities considered here ($0 \leq \epsilon \lesssim 0.4$). We are thus confident in using the QG (or hybrid) models for further analysis, as we do not observe strong 3-D effects on the modes by the equatorial ellipticity.

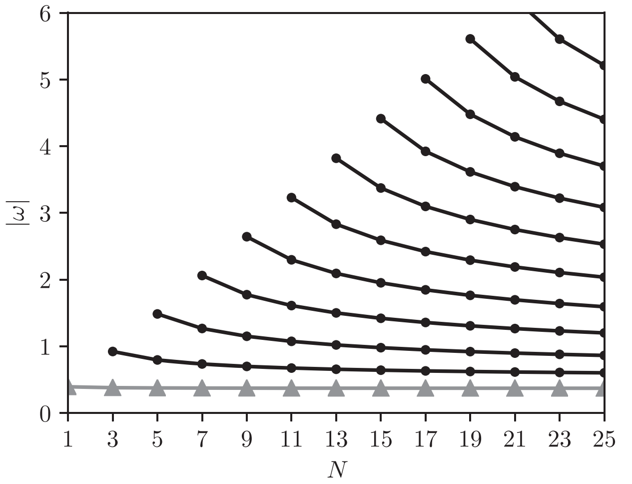

Figure 4. Convergence of frequencies as a function of truncation degree N for a background magnetic field $\mathbf{B}_{0,\mathrm{QG}}$, $\epsilon = 0.42$ and $\mathrm{Le} = 10^{-5}$. Connected lines indicate individual modes. Black lines correspond to TM and the smallest frequency mode (in grey with triangles) is the U_3-mode.

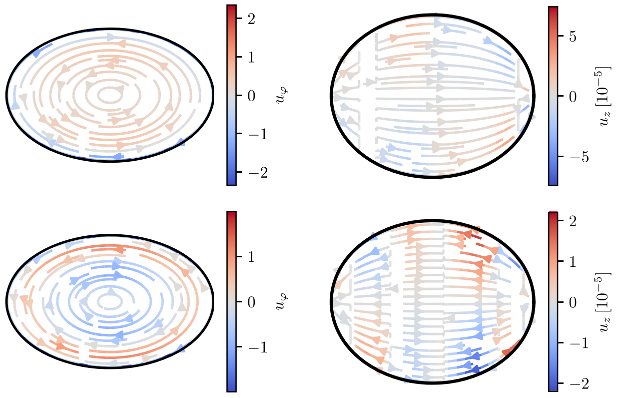

Figure 5. Equatorial sections (left) and meridional sections along the x-axis (right) of the two largest scale TM using $\mathbf{B}_{0,\mathrm{QG}}$, $\epsilon = 0.42$ and $\mathrm{Le} = 10^{-5}$. The colours indicate the velocity along the geostrophic contours u_φ and the vertical velocity u_z, respectively.

4.2 Torsional Alfvén modes

To drive TM the imposed background magnetic field must have a component perpendicular to the geostrophic contours. For the QG model, we must consider a scalar potential A_0 that is not only a function of h. We choose $A_0 = h^3(1 + x)/3$, which yields

$$\mathbf{B}_{0,\mathrm{QG}} = \frac{c^2}{3}\begin{pmatrix} -3(1+x)y/b^2 \\ (3+4x)x/a^2 + y^2/b^2 - 1 \\ yz/b^2 \end{pmatrix}. \tag{55}$$

Since the components of such a magnetic field are no longer linear in the Cartesian coordinates (contrary to the Malkus field), the convergence of the modes depends on the truncation of the maximum polynomial degree. We verify the convergence of the largest scale TM (see black lines in Fig. 4). As N is increased more TM with a larger polynomial complexity appear, with one additional TM per two polynomial degrees. This is explained by the introduction of an additional geostrophic basis vector at every second polynomial degree (see Backus & Rieutord (2017), in the sphere and Appendix A in the ellipsoid).

The equatorial and meridional sections of the two lowest frequency (and thus largest scale) TM, calculated using $\mathbf{B}_{0,\mathrm{QG}}$ at $N = 7$, are presented in Fig. 5 for a strongly deformed ellipsoid with equatorial ellipticity $\epsilon = 0.42$. As in the sphere, the velocities of TM follow the geostrophic contours that are now ellipses. The velocity structure is almost purely horizontal, seen by the ratio of the

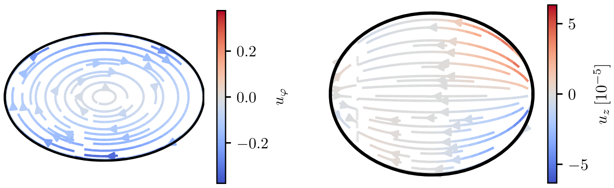

Figure 6. Equatorial section (left-hand panel) and meridional section along the x-axis (right-hand panel) of the U_3-mode using $\mathbf{B}_{0,\mathrm{QG}}$, $\epsilon = 0.42$ and Le $= 10^{-5}$. The colours indicate the velocity along the geostrophic contours u_φ and the vertical velocity u_z, respectively.

velocity amplitudes $u_\varphi/u_z \sim 10^5$, where u_φ is the velocity along an elliptical geostrophic contour and u_z is the vertical velocity.

The lowest frequency mode (highlighted in grey triangles in Fig. 4) is hereafter referred to as U_3-mode. It is already present for a truncation degree $N = 1$, where only components linear in the Cartesian coordinates are included. The equatorial and meridional section of the U_3-mode are presented in Fig. 6 for an ellipsoid with equatorial ellipticity of $\epsilon = 0.42$ and $N = 7$. Compared to other TM, it consists almost solely of a velocity with uniform vorticity along the z direction.

4.2.1 Identification of torsional Alfvén modes

When the Lehnert number is not sufficiently small to separate the branches of eigensolutions, as seen for the sphere in Fig. 1 at Le $> 10^{-3}$, a clear identification of TM in the spectrum of eigensolutions is complicated. In Fig. 7 we show the dependency of the frequency of the eigensolutions on the Lehnert number for an ellipsoid with $\epsilon = 0.42$. For the TM represented in this Figure, no dependency of the frequency on Le is observed for Le $\lesssim 10^{-3}$, as in the case of the sphere (compare Fig. 1, bottom). Similarly, the U_3-mode shows no dependency of its frequency on Le for Le $< 7 \times 10^{-4}$. For Le $\lesssim 10^{-3}$ the TM shown here and the U_3-mode do not cross any other eigensolutions (and due to their independence of Le they do not cross each other). In this region we have no difficulty in identifying individual TM or the U_3-mode. When Le is increased to values greater than 10^{-3}, more eigensolutions with frequencies close to the TM or the U_3-mode exist. Tracking these eigensolutions as a function of Le (as described in Section 3.3) reveals that they can undergo so-called avoided crossings, where two eigensolutions approach each other without ever degenerating. An example of such an avoided crossing is shown in the inset in Fig. 7, where the U_3-mode morphs into the fastest slow mode and vice versa. The two modes exchange their properties, as shown here by the ratio of kinetic to magnetic energy. Such a behaviour has been similarly observed in other geophysical wave studies (Rogister & Valette 2009), even for non-vanishing diffusivities (Triana *et al.* 2019), or in quantum systems (Rotter 2001). Labbé *et al.* (2015) chose not to show the results, obtained in the spherical case, for values of Le corresponding to avoided crossing (their figs 6, 7, 11).

We differentiate in the following the modes, characterized by their physical properties, and the eigenbranches, obtained by continuous tracking of the eigensolutions. This way, we can continue the U_3-mode and the TM out of the Le $\ll 1$ domain, where they are clearly distinguishable. We have indicated the U_3 mode and TM as well as the fastest slow mode by the coloured lines in the bottom Fig. 7.

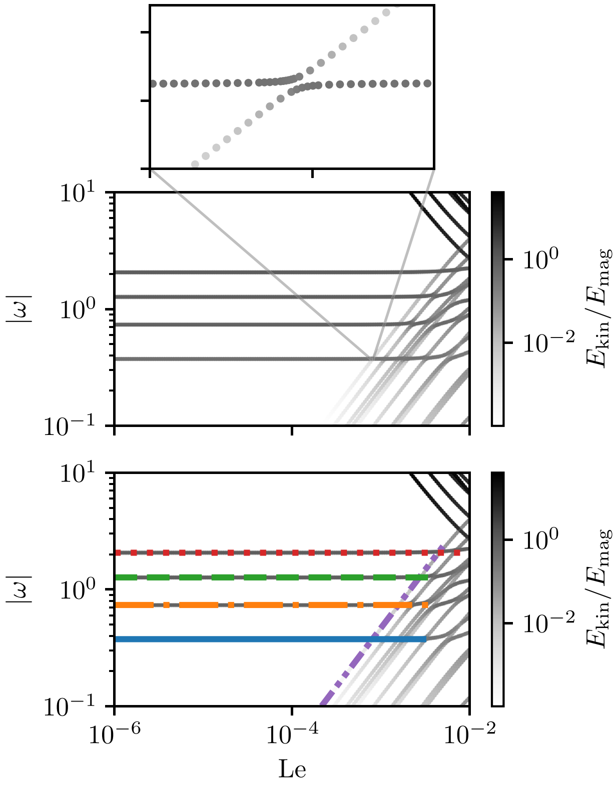

Figure 7. Frequency of eigensolutions as a function of Lehnert number for $\epsilon = 0.42$, with colours indicating the ratio of kinetic to magnetic energy (top panel). The inset shows an avoided crossing of the U_3-mode and the fastest slow mode, with dots indicating individual steps of the tracking algorithm. The frequencies of TM (orange dash–dotted, green dashed and red dotted), the U_3-mode (blue solid) and the fastest slow mode (purple dash–dot–dotted) are highlighted in the bottom panel.

4.2.2 Ellipticity effects

The dependency of the frequency on the equatorial ellipticity of TM and U_3-mode is presented in Fig. 8(top panel). It is observed that, when $\epsilon \lesssim 10^{-1}$, the change of the TM frequency is small and tends to their non-vanishing frequency in the sphere. To be more quantitative, the difference between the frequencies in the ellipsoid and the sphere scales with ϵ for the TM (see Fig. 8, bottom panel).

A very different behaviour is observed for the frequency of the U_3-mode, since the frequency itself scales with $\epsilon^{1/2}$. This means that the U_3-mode has a vanishing frequency when $\epsilon = 0$. Also, the ratio of kinetic to magnetic energy of the U_3-mode scales with ellipticity. These two properties clearly differentiate the U_3-mode from TM. The restoring force for the U_3-mode is the pressure force acting on the elliptical boundary. At small ellipticities it is only the magnetic pressure force.

4.2.3 Torque balance

The velocity and magnetic field of an eigensolution $(\tilde{\mathbf{u}}_k, \tilde{\mathbf{B}}_k, \omega_k)$ for a given $\mathbf{B}_0$ and Le are normalized as

$$\int_{\mathcal{V}} \tilde{\mathbf{u}}_k \cdot \tilde{\mathbf{u}}_k \,\mathrm{d}V + \int_{\mathcal{V}} \tilde{\mathbf{B}}_k \cdot \tilde{\mathbf{B}}_k \,\mathrm{d}V = 1, \tag{56}$$

such that they have a unit energy in dimensionless units. We can then calculate the angular momentum $\mathbf{L}_k$ by inserting $\mathbf{u}_k$ into (6a),

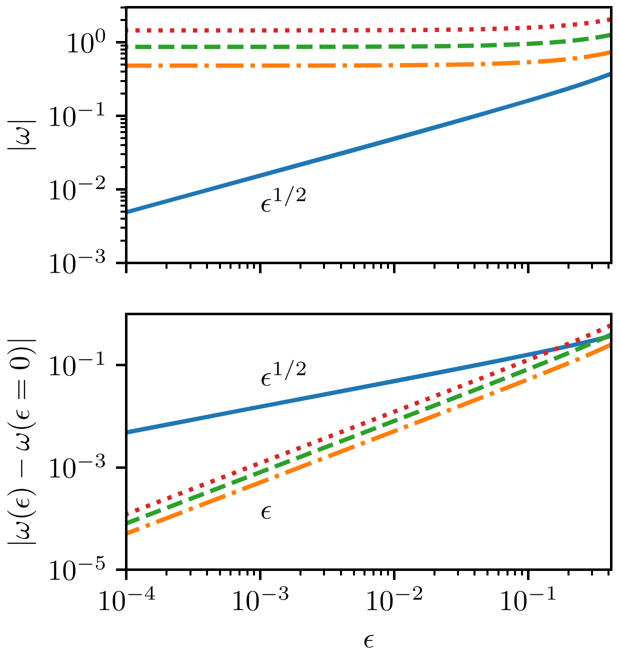

Figure 8. Frequencies of TM (orange dash–dotted, green dashed and red dotted) and the U_3-mode (blue solid) as a function of ellipticity ϵ (top panel). Difference between the frequency as a function of ϵ and the frequency in the sphere with $\epsilon = 0$ (bottom panel). The Lehnert number is $\mathrm{Le} = 10^{-5}$.

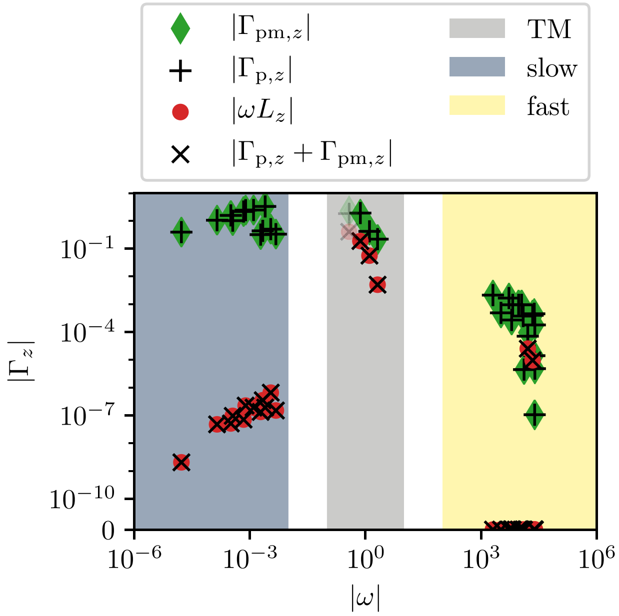

Figure 9. The z component of the torques for the background magnetic field with truncating degree $N = 7$, $\epsilon = 0.42$ and $\mathrm{Le} = 10^{-5}$. The U_3-mode is displayed slightly transparent.

and its time derivative is given by $\mathrm{i}\omega_k\mathbf{L}_k$. The linearized magnetic pressure torque is given by

$$\Gamma_{\mathrm{pm}} = -\int_{\mathcal{V}} \mathbf{r}\times\nabla\left(\tilde{\mathbf{B}}\cdot\mathbf{B}_0\right)\,\mathrm{d}V, \tag{57}$$

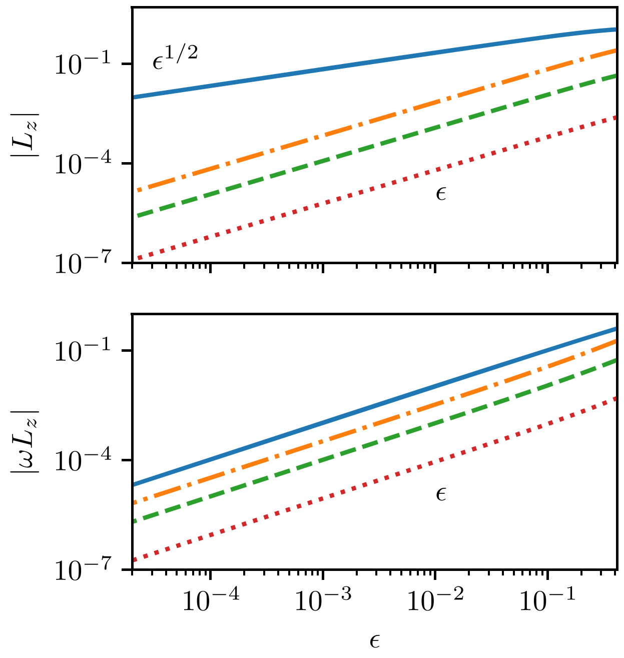

Figure 10. Axial angular momentum (top panel) and its change (bottom panel) of TM and the U_3-mode as a function of ellipticity for the background magnetic field $\mathbf{B}_{0,\mathrm{QG}}$ and $\mathrm{Le} = 10^{-5}$. The colours correspond to those in Fig. 8.

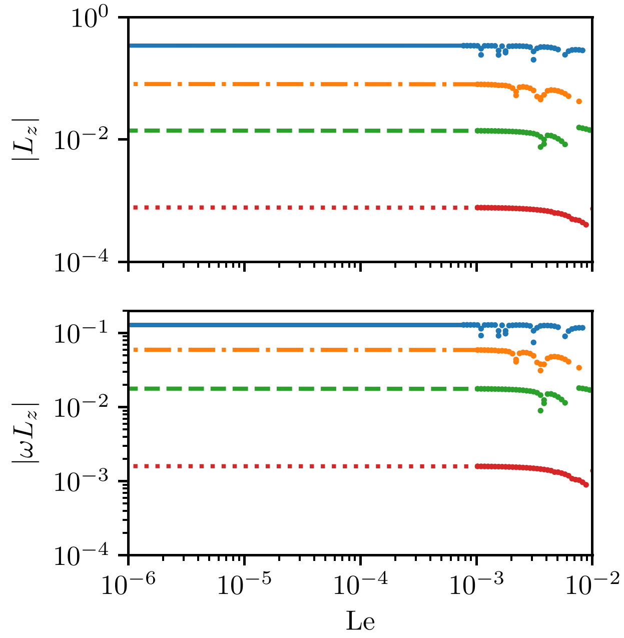

Figure 11. Axial angular momentum (top panel) and its change (bottom panel) of TM and the U_3-mode for the background magnetic field $\mathbf{B}_{0,\mathrm{QG}}$ and a, b, $c = 1.25$, 0.8, 1 ($\epsilon = 0.42$) with $N = 7$. At $\mathrm{Le} \gtrsim 10^{-3}$, where eigensolutions are influenced by avoided crossings, we have identified the modes by choosing a frequency within ±10 per cent and an angular momentum within ±50 per cent of the frequency and angular momentum at $\mathrm{Le} \ll 1$. The colours correspond to those in Fig. 8.

and $\Gamma_{\mathrm{pm},k}$ follows by inserting $\tilde{\mathbf{B}}_k$ and $\mathbf{B}_0$. The hydrodynamic pressure torque (6b) is calculated by reconstructing the pressure gradient, which cannot be done from the velocity field only. We reconstruct it instead by inserting $\tilde{\mathbf{u}}_k$, $\tilde{\mathbf{B}}_k$ and $\mathbf{B}_0$ in the momentum eq. (47a).

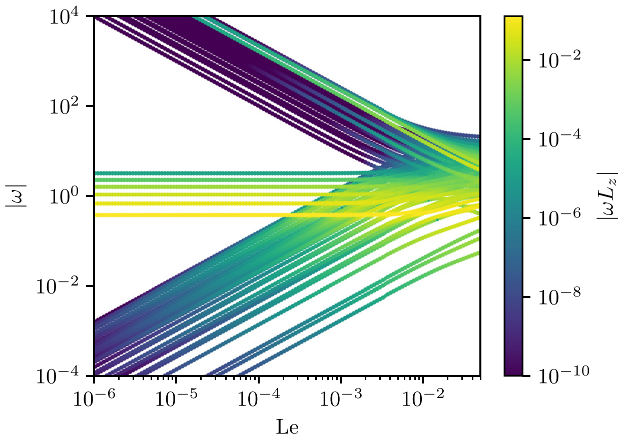

Figure 12. Change of axial angular momentum for the QG model with $\mathbf{B}_{0,\mathrm{QG}}$ and $N = 11$. The full spectrum of eigensolutions is computed at incremental steps of Le, without tracking an individual eigensolution.

Table 1. Estimation of change in angular momentum of TM for Earth's core, with $\epsilon = 10^{-3}$. The TM are normalized to have a period $T = 6$ yr. The characteristic TM velocity is set to $u_0 = 5 \times 10^{-6}$ m s^{-1}.

Model	ω	L_z	Le $[10^{-4}]$	B_0 [mT]	ωL_z [Nm]
QG	0.48	113	9.5	29.5	9.5×10^{14}
QG	0.865	18.3	5.28	16.4	1.54×10^{14}
QG	1.45	0.92	3.15	9.8	7.76×10^{12}
Hybrid	1.14	87.4	4.02	12.5	7.37×10^{14}
Hybrid	2.06	9.24	2.22	6.89	7.79×10^{13}
Hybrid	3.34	0.35	1.37	4.25	2.95×10^{12}

The axial torques in a strongly deformed ellipsoid with a, b, c = 1.25, 0.8, 1 (i.e. $\epsilon = 0.42$) are shown in Fig. 9. We find non-vanishing torques along the rotation axis for slow modes ($10^{-5} < \omega < 10^{-2}$), TM ($10^{-1} < \omega < 10$) and the fast modes ($\omega > 10^2$). For many modes the hydrodynamic, magnetic and total pressure (sum of hydrodynamic and magnetic pressure) torques do not vanish. For most fast modes $\Gamma_{\mathrm{p},z}$ balances $\Gamma_{\mathrm{pm},z}$ exactly. In case $\Gamma_{\mathrm{p},z}$ is not exactly balanced by $\Gamma_{\mathrm{pm},z}$, the total pressure torque is in balance with the non-vanishing change in angular momentum ωL_z, in agreement with eq. (9). For example, the TM with largest scale (and smallest frequency $\omega = 0.737$) has $\Gamma_{\mathrm{p},z} = -1.285 + 1.414\mathrm{i}$, $\Gamma_{\mathrm{pm},z} = 1.159 - 1.275\mathrm{i}$ and $\mathrm{i}\omega L_z = -0.126 + 0.139\mathrm{i}$. Our results show that TM yield pressure torques much larger than the slow and fast modes.

Ivers (2017) demonstrated that, in the ellipsoid, only flows of uniform vorticity carry angular momentum. They are given by

$$\hat{\mathbf{u}}_1 = \begin{pmatrix} 0 \\ -z/c^2 \\ y/b^2 \end{pmatrix}, \; \hat{\mathbf{u}}_2 = \begin{pmatrix} -z/c^2 \\ 0 \\ x/a^2 \end{pmatrix}, \; \hat{\mathbf{u}}_3 = \begin{pmatrix} -y/b^2 \\ x/a^2 \\ 0 \end{pmatrix}, \tag{58}$$

with a spatially uniform vorticity in the x-, y- and z-directions, respectively. Therefore, we determine if the modes do contain such uniform vorticity components and whether or not it accounts for the non-vanishing angular momentum. To this end, we must project the eigensolutions onto velocities (58) and the resulting angular momentum of the ith uniform vorticity component of an eigensolution with velocity $\mathbf{u}_k$ is given by

$$\hat{L}_{i,k} = \frac{1}{\sqrt{\int \hat{\mathbf{u}}_i \cdot \hat{\mathbf{u}}_i \,\mathrm{d}V}} \int_{\mathcal{V}} (\hat{\mathbf{u}}_i \cdot \tilde{\mathbf{u}}_k)(\hat{\mathbf{u}}_i \times \mathbf{r}) \cdot \mathbf{1}_i \,\mathrm{d}V. \tag{59}$$

For all modes we find (within machine precision) that $L_{z,k} = \hat{L}_{3,k}$, in agreement with the predictions by Ivers (2017).

The U_3-mode, shown slightly transparent in Fig. 9, has a velocity almost exactly equal to $\hat{\mathbf{u}}_3$ (thus the name U_3-mode). It is associated with the largest torque. However, the time scale at which this torque acts increases as the ellipticity is decreased to more geophysically relevant values, whereas it remains the same for TM.

4.2.4 *Torque variation with the ellipticity and Lehnert number*

We show in Fig. 10 the dependency on the ellipticity of the angular momentum in z (top panel), and the associated changes (bottom panel). The angular momentum scales with ϵ for the TM, and with $\epsilon^{1/2}$ for the U_3-mode. Since the frequency is almost independent of ϵ for the TM, and scales with $\epsilon^{1/2}$ for the U_3-mode, the change in angular momentum scales with ϵ for all modes. A vanishing change in angular momentum is necessary to satisfy the torque balance in the sphere, where the pressure torque vanishes exactly. Departures from the aforementioned scalings are only observed for strongly deformed ellipsoids (i.e. $\epsilon > 0.1$). For TM with higher frequencies, the spatial complexity of the modes increases and their angular momentum and the change in angular momentum decreases.

In Fig. 11 we show the evolution of the angular momentum and change in angular momentum of TM and the U_3-mode as a function of the Lehnert number. For Le $\lesssim 10^{-3}$ we observe no dependency on Le for the angular momentum. Thus, because the frequency is also independent of Le (see Fig. 7), there is no dependency of the change in angular momentum on Le and the total pressure torque must scale in the same way.

The frequencies of the eigenbranches are close-by when Le $> 10^{-3}$, and they undergo the previously discussed avoided crossings. However, we are still able to identify the TM and U_3-mode by their frequency and angular momentum when Le $\ll 1$ (see Fig. 11). To check the influence of truncation on the results, we have computed the change in angular momentum of all the eigensolutions as a function of Le for the truncation degree $N = 11$. The U_3 mode and the TM can be well characterized by their angular momentum (see Fig. 12). Comparison between our results for $N = 7$ and $N = 11$ makes us confident that our angular momentum calculations for U_3 and the largest scale TM are converged at $N = 7$.

To check the generality of these results, we have considered a 3-D magnetic field in the hybrid model. The results are presented in Appendix B. No qualitative differences with the results of the QG model are found, even if the background magnetic field has a different topology. We follow from this that our results extend to more complex background magnetic field geometries. Further verification was done using a fully 3-D model, where no QG assumption is made on the velocity (not shown).

5 DISCUSSION AND CONCLUSIONS

5.1 Pressure torque and angular momentum of torsional Alfvén modes in ellipsoids

We have found that TM in the ellipsoid can have a non-vanishing angular momentum. Their angular momentum is fully accounted for by their uniform vorticity flow component along the rotation axis. This fully agrees with Ivers (2017), who proved that only uniform vorticity flows have non-zero angular momentum. In the hydrodynamic case (without magnetic field), only the geostrophic mode can have a non-vanishing axial angular momentum. Since its frequency is zero, the change in axial angular momentum vanishes. All other inertial modes in a non-conductive fluid enclosed in an ellipsoid are orthogonal to the geostrophic mode and no inertial mode can produce a net axial torque acting on the boundary. In MHD, the modes have a magnetic component and we lose the orthogonality properties between the velocity components. It is well known that TM exist, whose frequency is non-zero, with a dominant velocity component along the geostrophic contours. We have shown that these TM keep following the geostrophic contours for an ellipsoidal domain, and carry angular momentum through their uniform vorticity component when non-axisymmetry is present. This change in angular momentum must be balanced by the total pressure torque, as the Coriolis torque is exactly zero along the rotation axis and in our model the magnetic tension torque Γ_b also vanishes. Our results confirm this balance, and there are modes for which the hydrodynamic pressure torque is larger than the magnetic pressure torque. It is worth discussing whether our results extend to the case of a perfectly insulating boundary, where the magnetic tension torque Γ_b exactly balances the magnetic pressure torque Γ_{pm}. Then, only the hydrodynamic pressure torque can balance changes in angular momentum. Investigating perfectly insulating boundaries remains a future problem as it is inherently impossible by our methodology and out of the scope of this work.

We have shown that the frequency of TM remains independent of the Lehnert number, as is the case in the sphere. The angular momentum is also independent of the Lehnert number, and thus is the change of angular momentum and the associated pressure torque. The frequency of TM is also almost unaffected by small ellipticities. The angular momentum (and its change) of TM scales as ϵ, so that it vanishes in the sphere (as it should).

In addition to the TM, we observed the particular U_3-mode, mainly of uniform vorticity in the axial direction, carrying angular momentum. For a strongly deformed ellipsoid with $\epsilon = \mathcal{O}(10^{-1})$ the frequency of the U_3-mode happens to be in the range of TM. As for TM the frequency and the angular momentum of the U_3-mode does not depend on Le for small enough Le. However, in contrast to TM its frequency scales with $\epsilon^{1/2}$, a mode behaviour so far unknown to the authors. The U_3-mode is thus geostrophic in the sphere, with a vanishing frequency. Its frequency also vanishes for the hydrodynamic case, regardless of the ellipticity. A magnetic field with a component perpendicular to the geostrophic contours is needed in addition to non-axisymmetry to drive this mode.

Another interesting application of our model is the extension to more complex geometries (as long as closed geostrophic contours exist). The derived equations are indeed independent of the (possibly non-orthogonal) coordinate system. The ellipsoidal case presented here can be used as a benchmark for follow up work in this direction. We have additionally presented the first hybrid model, with the velocity in the QG assumption and a 3-D magnetic field. A property highly desirable in core flow dynamics, where a columnar flow model seems appropriate, but the magnetic field is clearly three dimensional (e.g. Schaeffer *et al.* 2017).

5.2 Geophysical implications

Our results suggest that TM in the Earth's core, which have periods on the scale of a few years, exert a pressure torque onto the solid mantle, provided the CMB is non-axisymmetric. The observed variations in the LOD are $\mathcal{O}(10^{-4})$ s at the 6 yr period (Gillet *et al.* 2015), which corresponds to a change in angular momentum $\mathcal{O}(10^{16})$ Nm. To compare this to the torques of TM calculated here, we redimensionalize our numerical results by assuming a characteristic velocity $u_0 = 5 \times 10^{-6}$ m s^{-1} of TM (see fig. 10 in Gillet *et al.* 2015). We match the frequencies of the calculated TM to the 6-yr period, so that a characteristic background magnetic field strength B_0 and similarly Le is defined. For an ellipticity $\epsilon = 10^{-3}$, estimated for Earth (Koper *et al.* 2003; Sze & van der Hilst 2003), the resulting values are presented in Table 1. The frequency conversion to match a 6-yr period yields a characteristic magnetic field strength of $B_0 \sim 4 - 30$ mT, hence a Lehnert number Le $= \mathcal{O}(10^{-4})$. These values are in agreement with what is expected for the Earth's outer core (Gillet *et al.* 2010). The resulting change in angular momentum, and thus the pressure torque, is at most $\mathcal{O}(10^{14})$ Nm for all modes. These values are two orders below the value needed to explain the variation of the LOD on the 6-yr period. This result can be better understood from a dimensional analysis of the pressure. First, the pressure varies linearly with the TM velocity. Secondly, the TM are independent of Ω. Therefore, the pressure associated to the velocity of TM scales with $p_0 \sim \rho u_0 u_A = \mathcal{O}(10^{-3})$ Pa. With this value, we verify that the resulting hydrodynamic pressure torque is $\mathcal{O}(10^{14})$ Nm.

In order to make the pressure torque significant, we need deviations from geostrophy so that pressure depends on Ω. This may happen in the presence of non-closed geostrophic contours. Then, 'pseudo-geostrophic' modes are replaced by Rossby modes, whose properties depend on Ω. These Rossby modes are not steady and possess the mean circulation included in the geostrophic mode otherwise (Greenspan 1968). Thus, Rossby modes driven by the magnetic field may play an important role for the pressure torque on a non-spherical boundary, where non-closed contours exist. It is easy to imagine this scenario in the presence of an inner core or at the CMB of the core, with a trough directed inwards at the equator. Stratification at the upper outer core may further increase the efficiency of the topographic torque (Braginsky 1998; Glane & Buffett 2018; Jault 2020).

Another hypothetical geophysical application is the explanation of the very long period variations in the LOD through the U_3-mode. These variations are $\mathcal{O}(10^{-3})$ s and have a period of around 1500 yr (Stephenson *et al.* 1995; Dumberry & Bloxham 2006). The U_3-mode in our model has a period of 1800 yr for Le $= 10^{-4}$ and an ellipticity of $\epsilon = 10^{-3}$. The U_3-mode could therefore be an explanation for these long period variations, but this remains a very speculative idea.

ACKNOWLEDGEMENTS

FG was partly funded by Labex OSUG@2020 (ANR10 LABX56). JN was partly funded by SNF Grant #200021_185088. JV was partly funded by STFC Grant ST/R00059X/1. This work was supported by a grant from the Swiss National Supercomputing Centre (CSCS) under project ID s872. This work has been carried out with financial support from CNES (Centre National d'Études Spatiales, France). Support is acknowledged from the European Space Agency through contract 4000127193/19/NL/IA. The authors like to thank two anonymous reviewers for their help in improving this paper.

REFERENCES

Abarca del Rio, R., Gambis, D. & Salstein, D.A., 2000. Interannual signals in length of day and atmospheric angular momentum, *Ann. Geophys.*, **18**(3), 347–364.

Aris, R., 1989. *Vectors, Tensors and the Basic Equations of Fluid Mechanics,* Dover.

Backus, G. & Rieutord, M., 2017. Completeness of inertial modes of an incompressible inviscid fluid in a corotating ellipsoid, *Phys. Rev. E,* **95**(5), 053116.

Backus, G., Parker, R. & Constable, C., 1996. *Foundations of Geomagnetism,* Cambridge Univ. Press.

Bardsley, O.P., 2018. Could hydrodynamic Rossby waves explain the westward drift? *Proc. R. Soc. A,* **474,** 20180119.

Bezanson, J., Edelman, A., Karpinski, S. & Shah, V.B., 2017. Julia: a fresh approach to numerical computing, *SIAM Rev.,* **59**(1), 65–98.

Braginsky, S.I., 1970. Torsional magnetohydrodynamics vibrations in the Earth's core and variations in day length, *Geomagn. Aeron.,* **10,** 3–12.

Braginsky, S.I., 1998. Magnetic Rossby waves in the stratified ocean of the core, and topographic core-mantle coupling, *Earth, Planets Space,* **50**(8), 641–649.

Bärenzung, J., Holschneider, M., Wicht, J., Sanchez, S. & Lesur, V., 2018. Modeling and predicting the short-term evolution of the geomagnetic field, *J. geophys. Res.,* **123**(6), 4539–4560.

Buffett, B.A., 1996a. Gravitational oscillations in the length of day, *Geophys. Res. Lett.,* **23**(17), 2279–2282.

Buffett, B.A., 1996b. A mechanism for decade fluctuations in the length of day, *Geophys. Res. Lett.,* **23**(25), 3803–3806.

Canet, E., Finlay, C.C. & Fournier, A., 2014. Hydromagnetic quasi-geostrophic modes in rapidly rotating planetary cores, *Phys. Earth planet. Inter.,* **229**(Supplement C), 1–15.

Davidson, P.A., 2016. *Introduction to Magnetohydrodynamics,* Cambridge Univ. Press, Cambridge.

Davies, C.J., Stegman, D.R. & Dumberry, M., 2014. The strength of gravitational core-mantle coupling, *Geophys. Res. Lett.,* **41**(11), 3786–3792.

Dumberry, M. & Bloxham, J., 2006. Azimuthal flows in the Earth's core and changes in length of day at millennial timescales, *Geophys. J. Int.,* **165**(1), 32–46.

Gans, R.F., 1971. On hydrodynamic oscillations in a rotating cavity, *J. Fluid Mech.,* **50,** 449–467.

Gastine, T., 2019. pizza: an open-source pseudo-spectral code for spherical quasi-geostrophic convection, *Geophys. J. Int.,* **217**(3), 1558–1576.

Gillet, N., Jault, D., Canet, E. & Fournier, A., 2010. Fast torsional waves and strong magnetic field within the Earth's core, *Nature,* **465**(7294), 74–77.

Gillet, N., Schaeffer, N. & Jault, D., 2011. Rationale and geophysical evidence for quasi-geostrophic rapid dynamics within the Earth's outer core, *Phys. Earth planet. Inter.,* **187**(3), 380–390.

Gillet, N., Jault, D. & Finlay, C.C., 2015. Planetary gyre, time-dependent eddies, torsional waves, and equatorial jets at the Earth's core surface, *J. geophys. Res.,* **120**(6), 3991–4013.

Gillet, N., Jault, D. & Canet, E., 2017. Excitation of travelling torsional normal modes in an Earth's core model, *Geophys. J. Int.,* **210**(3), 1503–1516.

Glane, S. & Buffett, B., 2018. Enhanced core-mantle coupling due to stratification at the top of the core, *Front. Earth Sci.,* **6,** doi:10.3389/feart.2018.00171.

Greenspan, H.P., 1968. *The Theory of Rotating Fluids,* Cambridge Univ. Press.

Gross, R.S., 2015. 3.09 - earth rotation variations core-long period, in *Treatise on Geophysics (Second Edition),* pp. 215–261, ed. Schubert, G., Elsevier.

Guervilly, C., Cardin, P. & Schaeffer, N., 2019. Turbulent convective length scale in planetary cores, *Nature,* **570**(7761), 368.

Hide, R., 1966. Free hydromagnetic oscillations of the Earth's core and the theory of the geomagnetic secular variation, *Phil. Trans. R. Soc., A,* **259**(1107), 615–647.

Hide, R., 1969. Interaction between the Earth's liquid core and solid mantle, *Nature,* **222**(5198), 1055–1056.

Holme, R. & de Viron, O., 2013. Characterization and implications of intradecadal variations in length of day, *Nature,* **499**(7457), 202–204.

Ivers, D., 2017. Enumeration, orthogonality and completeness of the incompressible Coriolis modes in a tri-axial ellipsoid, *Geophys. Astrophys. Fluid Dyn.,* **111**(5), 333–354.

Jault, D., 2003. Electromagnetic and topographic coupling, and LOD variations, in *Earth's Core and Lower Mantle,* pp. 56–76, eds Zhang, K., Soward, A. & Jones, C., CRC Press.

Jault, D., 2020. Tangential stress at the core-mantle interface, *Geophys. J. Int.,* **221**(2), 951–967.

Jault, D. & Le Mouël, J.-L., 1990. Core-mantle boundary shape: constraints inferred from the pressure torque acting between the core and the mantle, *Geophys. J. Int.,* **101**(1), 233–241.

Jault, D., Gire, C. & Le Mouël, J.-L., 1988. Westward drift, core motions and exchanges of angular momentum between core and mantle, *Nature,* **333,** 353–353.

Kerswell, R.R., 1994. Tidal excitation of hydromagnetic waves and their damping in the Earth, *J. Fluid Mech.,* **274,** 219–241.

Koper, K.D., Pyle, M.L. & Franks, J.M., 2003. Constraints on aspherical core structure from PKiKP-PcP differential travel times, *J. geophys. Res.,* **108**(B3), doi:10.1029/2002JB001995.

Labbé, F., Jault, D. & Gillet, N., 2015. On magnetostrophic inertia-less waves in quasi-geostrophic models of planetary cores, *Geophys. Astrophys. Fluid Dyn.,* **109**(6), 587–610.

Lebovitz, N.R., 1989. The stability equations for rotating, inviscid fluids: Galerkin methods and orthogonal bases, *Geophys. Astrophys. Fluid Dyn.,* **46**(4), 221–243.

Liao, X. & Zhang, K., 2010. A new legendre-type polynomial and its application to geostrophic flow in rotating fluid spheres, *Proc. R. Soc. A,* **466**(2120), 2203–2217.

Maffei, S., Jackson, A. & Livermore, P.W., 2017. Characterization of columnar inertial modes in rapidly rotating spheres and spheroids, *Proc. R. Soc. A,* **473**(2204), doi:10.1098/rspa.2017.0181.

Malkus, W. V.R., 1967. Hydromagnetic planetary waves, *J. Fluid Mech.,* **28**(4), 793–802.

Mound, J.E. & Buffett, B.A., 2006. Detection of a gravitational oscillation in length-of-day, *Earth planet. Sci. Lett.,* **243**(3), 383–389.

Munk, W.H. & MacDonald, G.J.F., 1960. *The Rotation of the Earth: A Geophysical Discussion,* Cambridge Univ. Press.

Pozzo, M., Davies, C., Gubbins, D. & Alfè, D., 2014. Thermal and electrical conductivity of solid iron and iron-silicon mixtures at Earth's core conditions, *Earth planet. Sci. Lett.,* **393,** 159–164.

Rieutord, M. & Valdettaro, L., 1997. Inertial waves in a rotating spherical shell, *J. Fluid Mech.,* **341,** 77–99.

Roberts, P.H., 1972. Electromagnetic core-mantle coupling, *J. Geomagn. Geoelectr.,* **24**(2), 231–259.

Roberts, P.H. & Aurnou, J.M., 2012. On the theory of core-mantle coupling, *Geophys. Astrophys. Fluid Dyn.,* **106**(2), 157–230.

Rogister, Y. & Valette, B., 2009. Influence of liquid core dynamics on rotational modes, *Geophys. J. Int.,* **176**(2), 368–388.

Rotter, I., 2001. Dynamics of quantum systems, *Phys. Rev. E,* **64**(3), 036213.

Schaeffer, N. & Jault, D., 2016. Electrical conductivity of the lowermost mantle explains absorption of core torsional waves at the equator, *Geophys. Res. Lett.,* **43**(10), 4922–4928.

Schaeffer, N., Jault, D., Nataf, H.-C. & Fournier, A., 2017. Turbulent geodynamo simulations: a leap towards Earth's core, *Geophys. J. Int.,* **211**(1), 1–29.

Stephenson, F.R., Morrison, L.V. & Smith, F.T., 1995. Long-term fluctuations in the Earth's rotation: 700 BC to AD 1990, *Phil. Trans. R. Soc. Lond., A,* **351**(1695), 165–202.

Sze, E.K.M. & van der Hilst, R.D., 2003. Core mantle boundary topography from short period PcP, PKP, and PKKP data, *Phys. Earth Planet. Inter.,* **135**(1), 27–46.

Triana, S.A., Rekier, J., Trinh, A. & Dehant, V., 2019. The coupling between inertial and rotational eigenmodes in planets with liquid cores, *Geophys. J. Int.,* **218**(2), 1071–1086.

Vantieghem, S., 2014. Inertial modes in a rotating triaxial ellipsoid, *Proc. R. Soc. A,* **470,** doi:10.1098/rspa.2014.0093.

Vantieghem, S., Cébron, D. & Noir, J., 2015. Latitudinal libration driven flows in triaxial ellipsoids, *J. Fluid Mech.,* **771,** 193–228.

Vidal, J. & Cébron, D., 2017. Inviscid instabilities in rotating ellipsoids on eccentric Kepler orbits, *J. Fluid Mech.,* **833,** 469–511.

Vidal, J. & Schaeffer, N., 2015. Quasi-geostrophic modes in the Earth's fluid core with an outer stably stratified layer, *Geophys. J. Int.,* **202**(3), 2182–2193.

Vidal, J., Cébron, D. & Schaeffer, N., 2016. Diffusionless hydromagnetic modes in rotating ellipsoids: a road to weakly nonlinear models?, in *Comptes-Rendus de la 19e Rencontre du Non-Linéaire,* Mar 2016, Paris, France.

Vidal, J., Cébron, D., ud Doula, A. & Alecian, E., 2019. Fossil field decay due to nonlinear tides in massive binaries, *Astron. Astrophys.,* **629,** A142.

Vidal, J., Su, S. & Cébron, D., 2020. Compressible fluid modes in rigid ellipsoids: towards modal acoustic velocimetry, *J. Fluid Mech.,* **885,** A39.

Watkins, A., Fu, Y. & Gross, R., 2018. Earth's subdecadal angular momentum balance from deformation and rotation data, *Scient. Rep.,* **8**(1), 13761.

Wijs,G. A.d., Kresse, G., Vočadlo, L., Dobson, D., Alfè, D., Gillan, M.J. & Price, G.D., 1998. The viscosity of liquid iron at the physical conditions of the Earth's core, *Nature,* **392**(6678), 805.

Wu, C.-C. & Roberts, P.H., 2011. High order instabilities of the Poincaré solution for precessionally driven flow, *Geophys. Astrophys. Fluid Dyn.,* **105**(2-3), 287–303.

Zhang, K. & Liao, X., 2017. *Theory and Modeling of Rotating Fluids: Convection, Inertial Waves and Precession,* Cambridge Univ. Press.

APPENDIX A: GEOSTROPHIC FLOW DESCRIBED BY A STREAM FUNCTION

The geostrophic part of the velocity can be regarded as the average over a geostrophic column. This is equivalent to considering a stream function

$$\tilde{\psi}(h) = \frac{\oint \psi(h, \varphi)\,\mathrm{d}\varphi}{\oint \mathrm{d}\varphi}, \tag{A1}$$

depending only on the geostrophic column height h. Here, we have chosen the coordinates (h, φ, z) conveniently, such that φ is the coordinated along a closed geostrophic contour of constant h and $z \in [-h, h]$ is along the rotation axis. In the axisymmetric case these coordinates are identical to the cylindrical coordinates. In the generic case, with arbitrarily shaped geostrophic contours, we have to apply curvilinear coordinates, that are not necessarily orthogonal. For non-orthogonal coordinates the dual, covariant and contravariant, bases $\mathbf{g}_i$ and $\mathbf{g}^i$ are needed. We refer the reader to Aris (1989) for more details on non-orthogonal curvilinear coordinates.

Inserting (A1) into (16) the geostrophic velocity is given by

$$\mathbf{u}_G = \nabla\tilde{\psi}(h) \times \nabla\left(\frac{z}{h}\right) \tag{A2a}$$

$$= u_G(h, \varphi)\mathbf{g}_2, \tag{A2b}$$

with $u_G(h, \varphi) = (Jh)^{-1}\frac{\partial\tilde{\psi}}{\partial h}$ and the covariant basis vector in φ-direction $\mathbf{g}_2$. Here, $J(h, \varphi, z) = \det(g_{ij})$ is the Jacobian of the coordinate mapping. The metric elements are given as $g_{ij} = \mathbf{g}_i \cdot \mathbf{g}_j$. In case of the sphere or the ellipsoid $J = J(h)$.

The geostrophic pressure p_G is well defined and depends on h only

$$2\rho\mathbf{u}_G \times \Omega = -\nabla p_G \tag{A3a}$$

$$\Leftrightarrow \frac{2\rho\Omega}{h}\frac{\partial\tilde{\psi}}{\partial h} = \frac{\partial p_G}{\partial h}. \tag{A3b}$$

To construct a basis of geostrophic velocities $\mathbf{u}_{G,i}$ being polynomial in the Cartesian coordinates the stream function $\psi_i(h)$ has to take the form

$$\tilde{\psi}_i(h) = \frac{1}{3}h^{3+2i}, \tag{A4}$$

where $h^2 = c^2(1 - x^2/a^2 - y^2/b^2)$. The basis of geostrophic velocities is given as

$$\mathbf{u}_{G,i} = \frac{1}{h}\nabla\tilde{\psi}_i \times \mathbf{1}_z = \frac{1}{3}(3 + 2i)h^{2i}\nabla g \times \mathbf{1}_z, \tag{A5}$$

with $\nabla g = -c^2(x/a^2, y/b^2, 0)^T$.

APPENDIX B: HYBRID MODEL

In the hybrid (or fully 3-D) model the background magnetic fields are less restricted, and we select an admissible field from appendix A in Wu & Roberts (2011). Namely, we consider the magnetic field

$$\mathbf{B}_{0,\mathrm{hyb}} = \begin{pmatrix} xy \\ -2b^2(x^2/a^2 + z^2/c^2) + b^2 - y^2 \\ yz \end{pmatrix}, \tag{B1}$$

named $\mathbf{v}_8$ in the quadratic basis of Wu & Roberts (2011). We choose this field, as it clearly goes beyond the magnetic field (55) while keeping the maximum polynomial degree sufficiently low to ensure convergence.

The U_3-mode and the two largest scale TM are presented in Fig. B1. Even though the background magnetic field considered here is topologically speaking very different to $\mathbf{B}_{0,\mathrm{QG}}$, the modes show a clear spatial similarity (compare Fig. 5). The axial torques are presented in Fig. B2. No qualitative difference to the QG model is observed. For modes with non-vanishing change in angular momentum the total pressure torque balances it. Again, the U_3-mode carries the largest angular momentum and for some slow modes and fast modes the change in angular momentum is also non-vanishing.

The dependency of the frequency, angular momentum and the change of angular momentum of the U_3-mode and TM on the ellipticity is shown in Fig. B3. The same scalings in ϵ are observed for the U_3-mode and the TM compared to the QG case.

Finally, we present the dependency of the angular momentum and its time derivative of the TM and the U_3-mode in Fig. B4. As in the QG case, no dependency is observed. In comparison to the QG case, the U_3-mode and the TM seem to be less influenced by avoided crossings at $\mathrm{Le} > 10^{-3}$ (compare to Fig. 11).

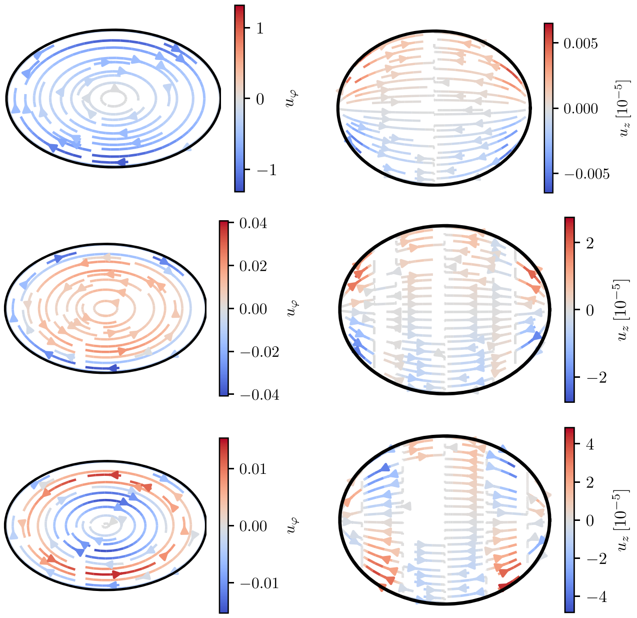

Figure B1. Equatorial sections (left-hand panel) and meridional sections along the *x*-axis (right-hand panel) of the U_3-mode (top panel) and the two largest TM (middle and bottom) using $\mathbf{B}_{0,\mathrm{hyb}}$, $\epsilon = 0.42$ and $\mathrm{Le} = 10^{-5}$. The colours indicate the velocity along the geostrophic contours u_φ and the vertical velocity u_z, respectively.

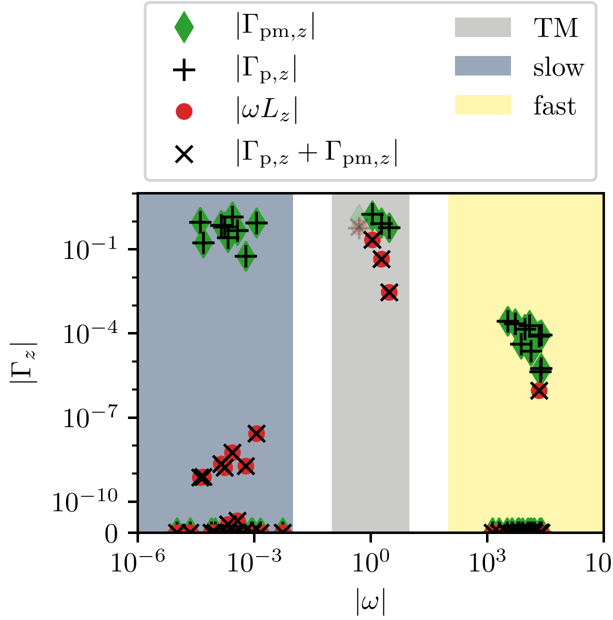

Figure B2. The *z* component of the torques using $\mathbf{B}_{0,\mathrm{hyb}}$, $\epsilon = 0.42$ and $\mathrm{Le} = 10^{-5}$ with truncating degree $N = 9$.

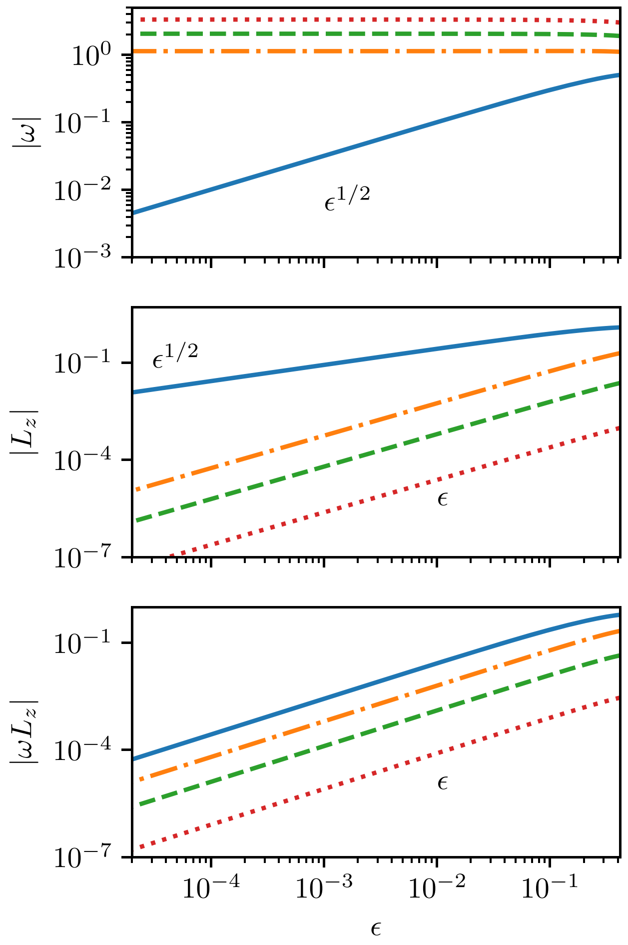

Figure B3. Frequency (top panel), axial angular momentum (middle panel) and change in axial angular momentum (bottom panel) of the three largest scale TM (orange dash-dotted, green dashed and red dotted) and the U_3-mode (blue solid) for $\mathbf{B}_{0,\mathrm{hyb}}$ and $\mathrm{Le} = 10^{-5}$ using the hybrid model.

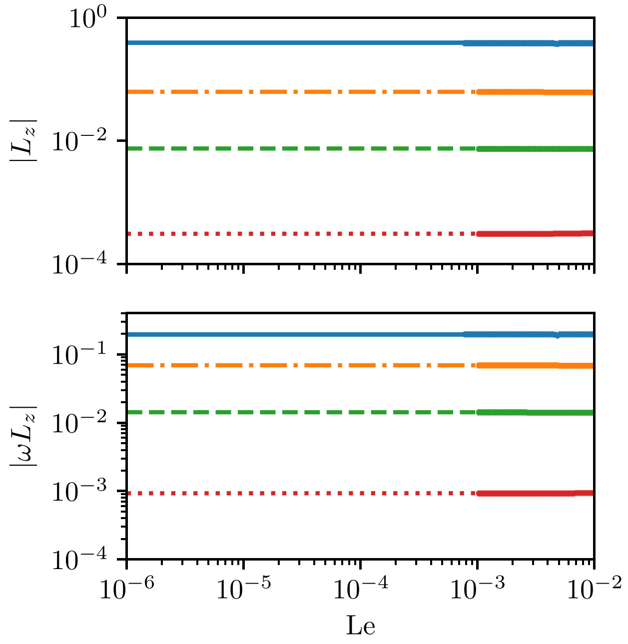

Figure B4. Axial angular momentum (top panel) and change in axial angular momentum (bottom panel) for $\mathbf{B}_{0,\mathrm{hyb}}$ and a, b, $c = 1.25, 0.8, 1$ using the hybrid model. The colours correspond to those in Fig. B3.

4.2 Pressure in a quasi-geostrophic model

In Gerick et al. (2020) we have calculated the pressure torque by assuming that the torque balance of the QG flow is reconstructed via the 3-D momentum equation. This is not strictly correct and care has to be taken. To understand why the assumption was appropriate to estimate the axial pressure torque, we compare the equatorial vector momentum equation (2.74), given by

$$\rho\frac{d}{dt}\left(\mathbf{u}_\perp + \frac{1}{3}\left(\mathbf{u}_\perp \cdot \nabla h\right)\nabla h\right) + 2\rho\,\boldsymbol{\Omega}\times\mathbf{u}_\perp = -\nabla\Pi + \frac{1}{2h}\left\langle \mathbf{j}\times\mathbf{B} + \frac{z}{h}\nabla h \mathbf{1}_z \cdot (\mathbf{j}\times\mathbf{B})\right\rangle . \tag{4.1}$$

to the inviscid 3-D momentum equation

$$\rho\frac{d\mathbf{u}}{dt} + 2\rho\,\boldsymbol{\Omega}\times\mathbf{u} = -\nabla p + \frac{1}{\mu_0}\left(\boldsymbol{\nabla}\times\mathbf{B}\right)\times\mathbf{B}. \tag{4.2}$$

The 2-D momentum equation (4.1) arises in the derivation of the QG equations from the Lagrangian approach (see Section 2.5) and carries a term, $\nabla\Pi$, that may be associated with a pressure. In the comparison of the two equations we find that the equations are alike with the exception of the Lorentz force and the inertial force. The torque of the Lorentz force reduces also to a magnetic pressure torque if $\mathbf{B}\cdot\mathbf{n} = 0$. We have then to understand only the torque of the additional term in the inertial force, given by

$$\frac{\rho}{3}\mathbf{1}_z \cdot \int_{\mathcal{V}} \mathbf{r}\times\left(\frac{d\mathbf{u}_\perp}{dt}\cdot\nabla h\right)\nabla h\,\mathrm{d}V. \tag{4.3}$$

This torque has been shown numerically to vanish for all modes shown in the article. It is possible also to show that (4.3) vanishes exactly for the axial uniform vorticity component $\mathbf{u}_\perp = (-y/b^2, x/a^2, 0)$, held accountable for the axial angular momentum (Ivers, 2017). Then, the reproduction of the pressure torque according to the 3-D torque balance is appropriate. We can not, however, calculate the actual pressure associated with the modes. There might be ways to reproduce the pressure field from the Lagrangian approach or the energy equation, but this is out of the scope of this thesis. This would be necessary to model the deformations of the core-mantle boundary.

4.3 Towards more complex geometries using non-orthogonal coordinates

For the study of torques in the ellipsoid the Cartesian polynomial basis was used. We have developed the tools necessary to investigate more complex geometries, introduced in Section 2.7.2. We can use this code to benchmark the results of the Cartesian model in the ellipsoid. The code uses symbolic computations to generate the QG equations in non-orthogonal elliptical cylindrical coordinates $\mathbf{r}\rightarrow$

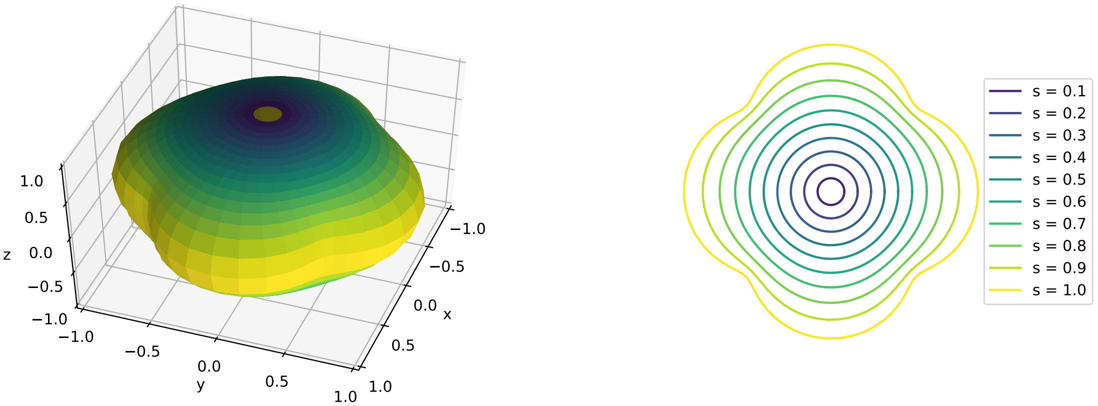

Figure 4.1: Left: Arbitrary volume described by the coordinate mapping (4.4). Right: Geostrophic contours within the volume as a function of s.

$(as\cos\varphi, bs\sin\varphi, cz)$ and then discretizes these by finite-differences in s and Fourier decomposition in φ, without having to manually combine Fourier components.

In the Malkus case that is modified to the ellipsoidal volume, using the A-formulation of the magnetic field, the eigen frequencies of the two approaches are also in quantitative agreement with relative differences $\mathcal{O}\left(10^{-9}\right)$. The estimates of the torques in this non-orthogonal coordinate model is difficult in terms of numerical accuracy. To investigate the torques we need to integrate the modes over the discrete grid used in radial direction. Such a discrete numerical integration is inaccurate compared to the Cartesian model and we have not continued our efforts for the ellipsoid. Without verifying the torques from the modes in this model, we are confident that the results of the Cartesian model are reliable as the mode frequencies of the two completely independent codes are in excellent agreement.

Besides verification of the ellipsoidal problem, the non-orthogonal coordinate model can be used to extend the study to more complex geometries, where the simple Cartesian scaling is not possible. It also allows us to easily identify properties along a line of constant column height, having adopted a coordinate system to it.

As a proof of concept for an extension to arbitrary geometries consider a volume illustrated in Figure 4.1 (left). This volume is essentially a sphere with bumps in the equatorial region (or for those familiar with spherical harmonics it can be illustrated by the sectoral spherical harmonic of degree 4). A coordinate system that is adapted to this geometry is given by

$$x = s\cos(\varphi) + s^5\cos(5\varphi)/10, \tag{4.4a}$$

$$y = s\sin(\varphi) + s^5\sin(5\varphi)/10, \tag{4.4b}$$

$$z = z. \tag{4.4c}$$

The column half height remains $h = \sqrt{1-s^2}$. The lines of constant column height, the geostrophic contours, are displayed in Figure 4.1 (right). To avoid numerical

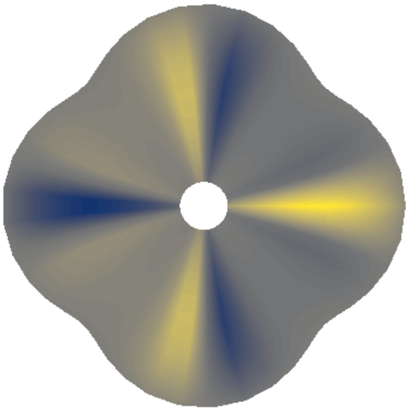

Figure 4.2: Stream function $\psi(s, \varphi)$ of the RM with the largest frequency.

issues at the origin we truncate at $s = 0.1$. The regularity at the origin needs to be investigated and ensured (compare also discussion in the sphere in Maffei et al., 2017). This is probably more complicated for coordinates such as the ones shown here.

The Rossby mode of the largest frequency, $\omega = 0.265$ is shown in Figure 4.2. These preliminary results are promising and further efforts will be devoted to this approach in the near future. When the magnetic field is described by a magnetic potential this framework should allow us to calculate torsional Alfvén modes in a complex geometry. Further investigations are needed to generalize this approach to 3-D magnetic fields. Potentially, the framework could also be extended to model the fully 3-D problems to study equatorially asymmetric modes.

Chapter 5

On quasi-geostrophic Magneto-Coriolis modes

In this chapter our work published in Geophysical Research Letters (Gerick et al., 2021) is presented. We use the model that was developed for the previous study of modes in the ellipsoid to investigate modes in the sphere. The novelty here is that the magnetic field basis is chosen so that it satisfies the insulating boundary condition. To express such a basis in Cartesian coordinates was motivated by the ellipsoidal problem, but has proven to be useful in the sphere also. In this approach we can easily study more complex background magnetic fields that are not necessarily axisymmetric. Unlike in many previous models, including the model used in the ellipsoidal case in Chapter 4, the radial magnetic field component at the CMB does not have to vanish for the insulating magnetic field basis. This allows us to investigate the radial magnetic field perturbation at the CMB associated with modes within the core. For this magnetic field basis, the extension to include magnetic diffusion is straight forward, as the boundary condition remains unaltered. This is not the case for the velocity field, when introducing viscosity. However, magnetic diffusion is more important for the dynamics in the core, as seen by the magnetic Prandtl number (1.21) that is $\mathcal{O}\left(10^{-6}\right)$ in the core. In our model, we can investigate the importance of diffusion for modes that are strongly coupled to the magnetic field and how their surface magnetic field perturbations are modified through diffusion. The introduction of diffusion comes at an additional computational cost that has to be tackled in the near future.
The article is presented in Section 5.1. In addition to the content of the article the influence of diffusion is addressed in Section 5.2. An outlook on how an insulating magnetic field basis in the ellipsoid might be achieved is given in Section 5.3.

5.1 Fast quasi-geostrophic Magneto-Coriolis modes in the Earth's core

Fast Quasi-Geostrophic Magneto-Coriolis Modes in the Earth's core

F. Gerick[1,2], D. Jault[1], J. Noir[2]

[1]CNRS, ISTerre, University of Grenoble Alpes, Grenoble, France
[2]Institute of Geophysics, ETH Zurich, Zurich, Switzerland

Key Points:

- Magneto-Coriolis modes of periods close to torsional Alfvén modes could be present in Earth's core model without stratification.
- The magnetic field changes of such modes show properties similar to geomagnetic observations, with fast changes localized near the equator.
- Our model could allow core-flow inversions from geomagnetic field data to the flow and simultaneously the magnetic field within the core.

Corresponding author: Felix Gerick, `felix.gerick@univ-grenoble-alpes.fr`

Abstract

Fast changes of Earth's magnetic field could be explained by inviscid and diffusion-less quasi-geostrophic (QG) Magneto-Coriolis modes. We present a hybrid QG model with columnar flows and three-dimensional magnetic fields and find modes with periods of a few years at parameters relevant to Earth's core. For the simple poloidal magnetic field that we consider here they show a localization of kinetic and magnetic energy in the equatorial region. This concentration of energy near the equator and the high frequency make them a plausible mechanism to explain similar features observed in recent geomagnetic field observations. Our model potentially opens a way to probe the otherwise inaccessible magnetic field structure in the Earth's outer core.

1 Introduction

Hide (1966) proposed that temporal changes of Earth's magnetic field, called secular variations (SV), could originate from linear modes present in the Earth's liquid outer core. These modes are separated into modes dominated by a balance of magnetic, Coriolis and pressure forces, known as Magneto-Coriolis modes (MCM), and modes dominated by inertial, Coriolis and pressure forces. The latter are often referred to as quasi-geostrophic (QG) inertial modes, or Rossby modes (RM). Torsional Alfvén modes (TM), consisting of geostrophic motions (Braginsky, 1970), complete the set of incompressible and diffusion-less magnetohydrodynamic (MHD) modes. They obey a balance between inertia and the magnetic force. In this study, we use a reduced model, based on the QG assumption for the velocity and a three-dimensional (3-D) magnetic field that is compatible with an insulating mantle, to investigate the SV associated with such QG modes, with a focus on MCM, in the Earth's core.

Monitoring the radial magnetic field component at the core-mantle boundary (CMB) is the main way of probing flows in the liquid outer core of Earth. A large number of studies are concerned with the inversion of the downward projected geomagnetic field to flows in the outer core, a process referred to as core-flow inversion (see Holme, 2015, for a review). The most commonly applied core-flow inversions are based on geostrophic flows tangential to the CMB (Le Mouël, 1984; Chulliat & Hulot, 2000). These inversions give the flow field local to the CMB. Several works have then inferred core dynamics from the inverted flow field at the CMB. Zatman and Bloxham (1997) and more recently Gillet et al. (2010) have inverted these surface flows to the mean radial magnetic field component within Earth's core through TM. Buffett (2014) correlated Magneto-Archimedes-Coriolis (MAC) waves in a stably-stratified layer at the top of the outer core with the inferred surface flows.

Our model potentially serves as a new forward model to invert geomagnetic field observations. In this approach a reduced set of MHD equations is solved in the bulk of the fluid. It is based on the QG assumption for the velocity, where a balance between Coriolis and pressure gradient forces is dominant, while allowing linear axial dependence of the flow field. This assumption is appropriate to investigate fluids under rapid rotation at time scales much larger than the rotation period. Different studies have shown that a large part of the inferred surface core flow is equatorially symmetric and may account for a large part of the observed secular variations (Gillet et al., 2009, 2011). Additionally, recent 3-D high resolution numerical simulations revealed a largely columnar flow structure, in agreement with the QG assumption (e.g. Schaeffer et al., 2017). To establish and maintain such a columnar flow within the Earth's core different mechanisms have been proposed, e.g. 3-D inertial-Alfvén waves that transport energy along the rotation axis (Bardsley & Davidson, 2016). Such built up of columns occurs on diurnal periods and are thus not captured in the QG model, where a columnar structure is assumed to be already established. Previously, consistently derived QG models that include a magnetic field were limited to magnetic fields that treated the CMB as a perfectly conducting boundary (Busse, 1976; Canet et al., 2014; Labbé et al., 2015; Gerick et al., 2020). For such magnetic fields the radial component at the boundary must vanish, rendering them unsuitable to associate core flows with magnetic field imprints at the CMB. There have been approaches to combine a QG model with a magnetic field that has a non-zero radial magnetic field component at the surface, but they rely on the neglect of surface terms in the induction equation that is difficult to justify (Canet et al., 2009; Maffei & Jackson, 2017). Here we present a hybrid model that combines QG velocities with a 3-D insulating magnetic field. We follow the approach presented in Gerick et al. (2020) with a new basis for the magnetic field that satisfies the insulating boundary condition at the CMB. Both the QG velocity and the magnetic field basis vectors are expressed in Cartesian polynomials. This methodology has been fruitful to model modes and instabilities in rapidly rotating ellipsoids (Vantieghem, 2014; Vidal & Cébron, 2017; Vidal et al., 2019, 2020). This Cartesian presentation of the basis vectors is particularly useful for the Galerkin approach used here, due to the easy integration of Cartesian monomials over the volume (Lebovitz, 1989). We derive a basis for the magnetic field in Cartesian polynomials, that exploits the properties of spherical harmonics.

2 A Hybrid Quasi-Geostrophic Model and Columnar Modes

2.1 Magnetohydrodynamic Equations

The equations governing the incompressible flow $\mathbf{u}$ and the magnetic field $\mathbf{B}$ in a rapidly rotating planetary core of volume $\mathcal{V}$, here assumed to be a full sphere without an inner core, are given in non-dimensionalized form by

$$\frac{\partial \mathbf{u}}{\partial t} + (\mathbf{u} \cdot \boldsymbol{\nabla})\,\mathbf{u} = -\,\frac{2}{\mathrm{Le}}\,\mathbf{1}_z \times \mathbf{u} - \nabla p + \frac{\mathrm{Pm}}{\mathrm{Lu}}\,\boldsymbol{\nabla}^2\mathbf{u} + (\boldsymbol{\nabla} \times \mathbf{B}) \times \mathbf{B}, \tag{1a}$$

$$\frac{\partial \mathbf{B}}{\partial t} = \boldsymbol{\nabla} \times (\mathbf{u} \times \mathbf{B}) + \frac{1}{\mathrm{Lu}}\,\boldsymbol{\nabla}^2\mathbf{B}. \tag{1b}$$

The non-dimensional Lehnert, Lundquist and magnetic Prandtl number are given by

$$\mathrm{Le} = \frac{B_0}{\Omega R_0 \sqrt{\mu_0 \rho}}, \quad \mathrm{Lu} = \frac{R_0 B_0}{\eta \sqrt{\mu_0 \rho}}, \quad \mathrm{Pm} = \frac{\nu}{\eta}, \tag{2}$$

with $\boldsymbol{\Omega} = \Omega \mathbf{1}_z$ the rotation vector, ρ the fluid density, p the reduced pressure, ν the kinematic viscosity, μ_0 the permeability of vacuum, η the magnetic diffusivity, R_0 the core radius and B_0 the characteristic strength of the magnetic field. The characteristic time scale is the Alfvén time scale $T_A = R_0/u_A$, where $u_A = B_0/\sqrt{\rho\mu_0}$ is the characteristic Alfvén velocity. Equations (1) are subject to the non-slip boundary condition $\mathbf{u} = \mathbf{0}$ and the continuity of the magnetic field across the boundary $[\mathbf{B}] = \mathbf{0}$, where $[\cdot]$ denotes a jump.

For parameters relevant for Earth's core, $\mathrm{Le} \sim 10^{-4}$, $\mathrm{Lu} \sim 10^{5}$ and $\mathrm{Pm} \sim 10^{-6}$ (Wijs et al., 1998; Gillet et al., 2010; Pozzo et al., 2014). Thus, if we additionally consider time scales on the order of T_A, it is appropriate to neglect viscous and diffusive effects in the bulk. In the next step, since we are interested in the linear response of the system, the velocity and magnetic field are perturbed around a background state with no motion and steady magnetic field $\mathbf{B}_0$. In the Earth's core, the characteristic mean velocity field is thought to be negligible compared to the Alfvén wave velocity (Gillet et al., 2015; Bärenzung et al., 2018). Hence, the equations describing the evolution of the velocity and magnetic perturbations $[\tilde{\mathbf{u}}, \tilde{\mathbf{B}}]$ are given by

$$\frac{\partial \tilde{\mathbf{u}}}{\partial t} + \frac{2}{\mathrm{Le}}\,\mathbf{1}_z \times \tilde{\mathbf{u}} = -\,\nabla p + (\boldsymbol{\nabla} \times \mathbf{B}_0) \times \tilde{\mathbf{B}} + (\boldsymbol{\nabla} \times \tilde{\mathbf{B}}) \times \mathbf{B}_0, \tag{3a}$$

$$\frac{\partial \tilde{\mathbf{B}}}{\partial t} = \boldsymbol{\nabla} \times (\tilde{\mathbf{u}} \times \mathbf{B}_0)\,. \tag{3b}$$

In the limit Pm $\rightarrow 0$ the boundary conditions on the velocity reduces to the non-penetration condition $\mathbf{u} \cdot \mathbf{n} = 0$, with $\mathbf{n}$ the vector normal to the boundary, and the magnetic boundary condition is not modified (Stewartson, 1957; Hide & Stewartson, 1972). Previous studies allowed for a jump in the tangential component of the magnetic field across a diffusive boundary layer (Braginsky, 1970; Jault & Finlay, 2015). Here, we assume that the motions that we are investigating are able to eliminate any current layer on the fluid surface.

2.2 Quasi-Geostrophic Velocity Basis

Assuming that the equatorial components of the velocity are independent of the coordinate z along the rotation axis; the non-penetration boundary condition, $\mathbf{u}\cdot\mathbf{n} = 0$ on the core-mantle boundary $\partial\mathcal{V}$ holds and the flow is incompressible, $\boldsymbol{\nabla} \cdot \mathbf{u} = 0$, the quasi-geostrophic (QG) velocity takes the form (Amit & Olson, 2004; Schaeffer & Cardin, 2005; Bardsley, 2018)

$$\mathbf{u} = \nabla\psi \times \nabla\left(\frac{z}{h}\right), \tag{4}$$

with h the half height of the fluid column and ψ a scalar stream function depending only on the horizontal coordinates.

In Cartesian coordinates the stream function can be expressed as (Maffei & Jackson, 2016; Gerick et al., 2020)

$$\psi_i = h^3\,\Pi_i, \tag{5}$$

with Π_i being a monomial in the equatorial Cartesian coordinates x and y of degree N, so that $i \in [0, N_2]$ with $N_2 = N(N+1)/2$. The QG basis vectors $\mathbf{u}_i$ are given by

$$\mathbf{u}_i = h^2\nabla\Pi_i \times \mathbf{1}_z + 3\Pi_i\nabla G \times \mathbf{1}_z - z\nabla\Pi_i \times \nabla G, \tag{6}$$

with $\nabla G = h\nabla h = -x\mathbf{1}_x - y\mathbf{1}_y$.

2.3 Magnetic Field Basis

In this section we present a set of basis vectors for the 3-D magnetic field, satisfying insulating boundary conditions at the CMB. Unlike in classical geodynamo simulations, where the boundary condition is enforced at each time step of the forward iteration, the boundary condition is included in the basis elements (Zhang & Fearn, 1995; Li et al., 2010; Chen et al., 2018). The detailed derivation of such a basis is given in Appendix A.

We write the magnetic field $\mathbf{B}$ in the toroidal-poloidal expansion, so that

$$\mathbf{B} = \mathbf{B}_t + \mathbf{B}_p = \boldsymbol{\nabla} \times T\mathbf{r} + \boldsymbol{\nabla} \times \boldsymbol{\nabla} \times P\mathbf{r}. \tag{7}$$

The toroidal and poloidal scalars are written for each spherical harmonic degree l, order m and radial degree n, so that

$$T_{lmn} = (1-r^2)r^{2n}R_l^m, \tag{8}$$

$$P_{lmn} = -r^{2(n+1)}\frac{R_l^m}{2(n+1)(2(l+n)+3)}. \tag{9}$$

with $R_l^m = r^l Y_l^m(\theta,\phi)$ the solid spherical harmonics. We have $|m| \leq l$ and $l \in [1, N]$, $n \in [0, (N-l)/2\rfloor$ for the toroidal basis and $l \in [0, N-1]$, $n \in [0, (N+1-l)/2-1\rfloor$ for the poloidal basis, resulting in a total of $N_3 = \frac{1}{6}N(N+1)(2N+7)$ basis vectors. The toroidal part of $\mathbf{B}$ is given by

$$\mathbf{B}_{t,lmn} = \boldsymbol{\nabla} \times T_{lmn}\mathbf{r}. \tag{10}$$

The poloidal magnetic field has to satisfy the continuity at the core-mantle boundary $\partial\mathcal{V}$, so that $\nabla\Phi^i + \mathbf{B}_p = \nabla\Phi^e$, with Φ^i and Φ^e the interior and exterior potential field, respectively. The exterior potential field must vanish at infinity, if the source of the magnetic field lies within the interior. The poloidal basis vectors are thus given by

$$\mathbf{B}_{p,lmn} = \boldsymbol{\nabla} \times \boldsymbol{\nabla} \times P_{lmn}\mathbf{r} + \nabla\Phi^i_{lmn}, \tag{11}$$

with $\Phi^i_{lmn} = -\frac{(l+1)}{(2l+1)(2n+2)} r^l Y_l^m$.

Together with the toroidal component (10), this basis can be transformed to Cartesian coordinates by representing the spherical harmonics in terms of unit Cartesian coordinates, as presented in Appendix B. We choose the Schmidt-semi normalization for the spherical harmonics, but any other may be chosen, as we normalize the basis vectors afterwards, so that $\int_\mathcal{V} \mathbf{B}_i \cdot \mathbf{B}_i \,\mathrm{d}V = 1$.

2.4 Projection Method

We introduce a hybrid quasi-geostrophic (QG) model with QG velocities and 3-D magnetic field , following Gerick et al. (2020). The linearized momentum equation (3a) and induction equation (3b) are projected onto a QG basis $\mathbf{u}'$ of the form of (4) and a 3-D magnetic field basis $\mathbf{B}'$ of the form (10) and (11), respectively. This method is essentially a variational approach, which consists in finding solutions $[\tilde{\mathbf{u}}, \tilde{\mathbf{B}}]$ satisfying

$$\begin{aligned}\int_\mathcal{V} \mathbf{u}' \cdot \frac{\partial \tilde{\mathbf{u}}}{\partial t} \,\mathrm{d}V = &-\int_\mathcal{V} \mathbf{u}' \cdot \left(\frac{2}{\mathrm{Le}}\mathbf{1}_z \times \tilde{\mathbf{u}} + \nabla p\right) \mathrm{d}V \\ &+ \int_\mathcal{V} \mathbf{u}' \cdot \Big((\boldsymbol{\nabla} \times \mathbf{B}_0) \times \tilde{\mathbf{B}} + (\boldsymbol{\nabla} \times \tilde{\mathbf{B}}) \times \mathbf{B}_0\Big) \,\mathrm{d}V \end{aligned} \qquad \forall\, \mathbf{u}' \tag{12a}$$

$$\int_\mathcal{V} \mathbf{B}' \cdot \frac{\partial \mathbf{B}}{\partial t} \,\mathrm{d}V = \int_\mathcal{V} \mathbf{B}' \cdot \boldsymbol{\nabla} \times (\tilde{\mathbf{u}} \times \mathbf{B}_0) \,\mathrm{d}V \quad \forall\, \mathbf{B}' \tag{12b}$$

This set of equations may be reduced to a scalar evolution equation for the stream function ψ accompanied by the 3-D induction equation, as shown in equation (48) of Gerick et al. (2020). This hybrid model has been verified against a fully 3-D model at moderate polynomial truncation (see also Gerick et al., 2020).

When replacing the test functions $\mathbf{u}'$ in (12a) by the subset of purely geostrophic velocities $\mathbf{u}_G = u_G(s)\mathbf{1}_\phi$ we obtain the equation for the diffusion-less torsional Alfvén modes (TM) initially discovered by Braginsky (1970). The one-dimensional (1-D) TM equation is written

$$s^3 h \frac{\partial^2 \xi}{\partial t^2} = \frac{\partial}{\partial s}\left(s^3 h v_A^2 \frac{\partial \xi}{\partial s}\right) \tag{13}$$

with $\xi = u_G(s)/s$ and the mean squared cylindrical Alfvén velocity

$$v_A^2(s) = \frac{1}{4\pi s h} \oint \int (\mathbf{B}_0 \cdot \mathbf{1}_s)^2 s \,\mathrm{d}z\mathrm{d}\phi. \tag{14}$$

For more details on the derivation we refer the reader to Jault (2003). Equation (13) diverges near the equator as $s \to 1$, but solutions exist, if $v_A^2(1) \neq 0$ (Maffei & Jackson, 2016). Since we can compute solutions to the 1-D equation for a given background magnetic field satisfying these conditions, TM suit well as a benchmark of our hybrid QG model capable of capturing TM.

2.5 Quasi-geostrophic Inertial and Magneto-Coriolis Modes

Lehnert (1954) introduced two distinct families of MHD modes as solutions to the linearized MHD equations (3), namely slow MCM and fast, slightly modified RM.

The phase velocity is prograde for slightly modified RM and retrograde for MCM. Malkus (1967) has shown that for an idealized magnetic field $\mathbf{B}_{0,M} = s\mathbf{1}_\phi$ of uniform current density analytical solutions exists for these two mode families. The dispersion relations are given by (Labbé et al., 2015)

$$\omega^{\pm}_{n,m} = \frac{1}{2\mathrm{Le}}\lambda_{n,m}\left(1 \pm \left(1 + \frac{4\mathrm{Le}^2 m(m-\lambda_{n,m})}{\lambda^2_{n,m}}\right)^{1/2}\right), \tag{15}$$

with $\omega^{+}_{n,m}$, $\omega^{-}_{n,m}$ and $\lambda_{n,m}$ the frequencies of the slightly modified RM, MCM and hydrodynamic (HD) inertial modes of azimuthal wave number m and radial scale n, respectively. The dispersion relation shows that the difference between $\omega^{+}_{n,m}$ and $\lambda_{n,m}/\mathrm{Le}$ is small, if $\mathrm{Le} \ll 1$. The frequencies $\lambda_{n,m}$ are scaled by the rotation frequency and can be obtained as solutions to a univariate polynomial in the sphere (Zhang et al., 2001). An approximate value for the equatorially symmetric inertial modes is given by (Zhang et al., 2001)

$$\lambda_{n,m} \approx -\frac{2}{m+2}\left(\left(1 + \frac{m(m+2)}{n(2n+2m+1)}\right)^{1/2} - 1\right). \tag{16}$$

As the magnetic field perturbations in the Malkus field satisfy the perfectly conducting boundary condition, with $\mathbf{B}\cdot\mathbf{n} = 0$ at $\partial\mathcal{V}$, the solutions cannot be associated with the SV at the CMB and a more suitable background magnetic field needs to be introduced.

2.6 Numerical Calculation of the Modes

The velocity and magnetic field perturbations are assumed to be periodic in time, i.e.

$$\tilde{\mathbf{u}}(\mathbf{r}, t) = \tilde{\mathbf{u}}(\mathbf{r})\exp(i\omega t), \tag{17a}$$

$$\tilde{\mathbf{B}}(\mathbf{r}, t) = \tilde{\mathbf{B}}(\mathbf{r})\exp(i\omega t). \tag{17b}$$

Enumerating the QG velocity basis $\tilde{\mathbf{u}}_i$, with $i = 1, ..., N_2$ and magnetic field basis $\tilde{\mathbf{B}}_i$, with $i = 1, ..., N_3$, the projections (12) discretize to

$$\mathrm{i}\omega\mathbf{M}\mathbf{x} = \mathbf{D}\mathbf{x}, \tag{18}$$

with $\mathbf{x} = (\hat{\alpha}_j, \zeta_j) \in \mathbb{C}^{N_2+N_3}$, and $\mathbf{M}, \mathbf{D} \in \mathbb{R}^{N_2+N_3\times N_2+N_3}$ of the form

$$\mathbf{M} = \begin{pmatrix} U_{ij} & 0 \\ 0 & B_{ij} \end{pmatrix}, \qquad \mathbf{D} = \begin{pmatrix} C_{ij} & L_{ij} \\ V_{ij} & 0 \end{pmatrix}. \tag{19}$$

Here, the coefficient matrices $U_{ij}, C_{ij} \in \mathbb{R}^{N_2\times N_2}$, $L_{ij} \in \mathbb{R}^{N_2\times N_3}$, $B_{ij} \in \mathbb{R}^{N_3\times N_3}$ and $V_{ij} \in \mathbb{R}^{N_3\times N_2}$ correspond to the inertial acceleration, Coriolis force, Lorentz force, time change of magnetic field and magnetic induction respectively. This form is referred to as a generalized eigen problem solvable for eigen pairs $(\omega_k, \mathbf{x}_k)$. A large part of $\mathbf{M}$ and $\mathbf{D}$ is zero, which allows us to use large polynomial degrees whilst keeping computational efforts small. To avoid numerical inaccuracies we use quadruple precision numbers (see supplementary material for more details). Our model extends the code available at `https://github.com/fgerick/Mire.jl` by the magnetic field basis introduced in 2.3.

3 Results

We choose a poloidal magnetic field of low polynomial degree, given by

$$\begin{aligned}\mathbf{B}_0 =& \boldsymbol{\nabla}\times\boldsymbol{\nabla}\times(P_{100}+P_{110})\mathbf{r} + \nabla\left(\alpha_{100}\Phi^i_{100} + \alpha_{110}\Phi^i_{110}\right)\\ =& \frac{1}{c}\begin{pmatrix} x^2 + xz + 2y^2 + 2z^2 - 5/3 \\ -xy + yz \\ -2x^2 - xz - 2y^2 - z^2 + 5/3 \end{pmatrix},\end{aligned} \tag{20}$$

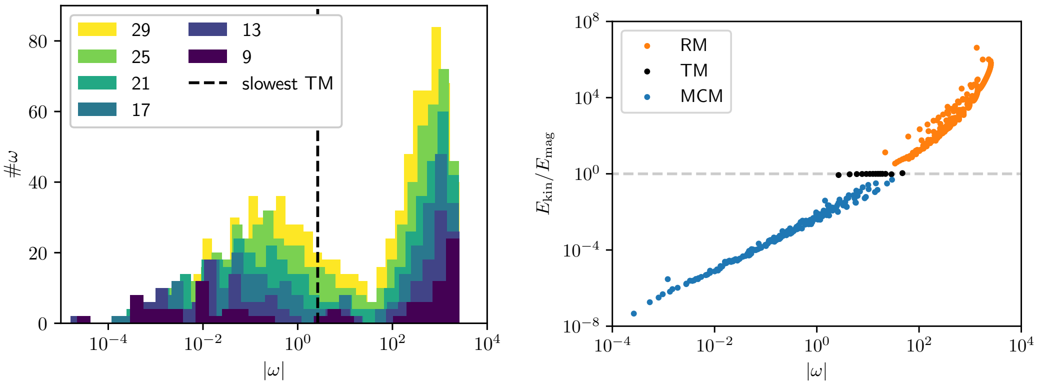

Figure 1. An overlap of the density of eigen solution spectrums at different truncation $9 \leq N \leq 29$ and $\mathrm{Le} = 10^{-4}$ (left). Ratio of kinetic to magnetic energy at $N = 29$ (right).

with the constant $c = 5\sqrt{\frac{368}{4725}}$, so that $\int_{\mathcal{V}} \mathbf{B}_0 \cdot \mathbf{B}_0 \, \mathrm{d}V = 1$. This field has a non-zero mean radial magnetic field at the equator. Its mean squared radial Alfvén velocity profile is given by

$$v_A^2(s) = -\frac{189}{1840}s^4 - \frac{42}{115}s^2 + \frac{1281}{1840}, \tag{21}$$

which decays slowly enough to ensure that TM are captured with low polynomial degrees. The Lehnert number is chosen to be $\mathrm{Le} = 10^{-4}$, corresponding to a mean magnetic field strength of about 3 mT within Earth's core (Gillet et al., 2010).

3.1 Properties of the Mode Spectrum

The density of the eigen solution spectrum is shown in Figure 1 (left) for different degrees of truncation up to $N = 29$. The band limitation of the spectrum is easily seen on the fast end of the spectrum with a similar upper end of frequencies for all truncation degrees. The fastest mode in the spectrum approximately corresponds to $|\omega^{+}_{1,5}| \approx 0.26\mathrm{Le}^{-1}$ (or 0.26Ω) instead of $|\omega| < 2\Omega$ for inertial modes (Greenspan, 1968). For MCM the slowest frequency is affected by the truncation. This is due to the fact that the convergence of magnetic modes depends on the truncation, as the Lorentz force alters the polynomial degree of the modes, unlike the Coriolis operator (Ivers et al., 2015). For a truncation $N \leq 13$ TM are separated from the MCM and the fast modes. At larger N some MCM are present also in the frequency range of TM. At low truncation the classification of MCM, RM and TM is straightforward by the difference in frequencies. At higher truncation we classify the modes by their kinetic and magnetic energies.

The kinetic and magnetic energies are respectively given by

$$E_{\mathrm{kin}} = \frac{1}{2}\int_{\mathcal{V}} \mathbf{u} \cdot \mathbf{u} \, \mathrm{d}V, \tag{22}$$

$$E_{\mathrm{mag}} = \frac{1}{2}\int_{\mathcal{V}} \mathbf{B} \cdot \mathbf{B} \, \mathrm{d}V. \tag{23}$$

At the degree of $N = 29$ both RM and MCM reach frequencies around the TM frequency range, but their energy ratio $E_{\mathrm{kin}}/E_{\mathrm{mag}}$ is still different from unity (see Figure 1, right). At the considered polynomial degrees more MCM have periods comparable to those of TM than RM. This bias can be explained by the periods of Malkus modes as a function of n and m (compare middle Figure 2 in Labbé et al.,

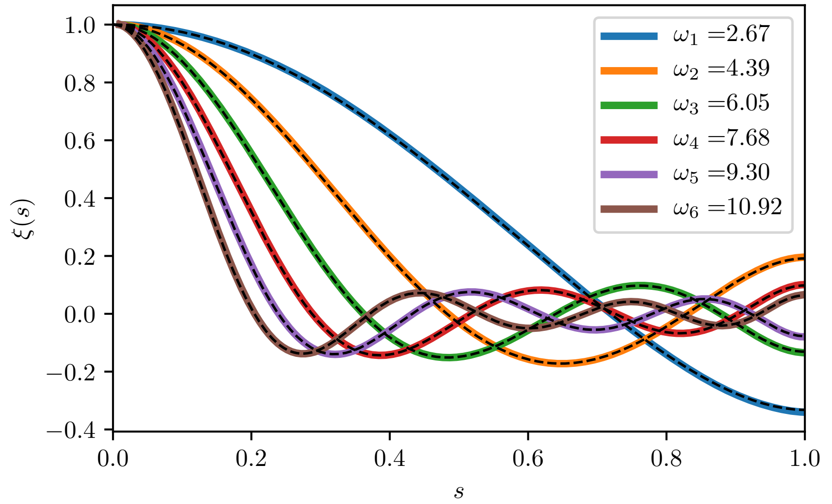

Figure 2. The six largest scale TM of the hybrid model at $N = 29$ and $\mathrm{Le} = 10^{-4}$ (solid colors) and of the 1-D equation (dashed black).

2015). For RM the periods only decrease towards unity as a function of n, not of m (unless $m \gg 1$). For MCM both an increase in m and n leads to an increase of the mode period towards unity. This explains why at a certain truncation level the fastest MCM is closer to the periods of TM than the slowest RM. Compared to the Malkus field, MCM (RM) spread out to higher (lower) frequencies and higher (lower) energy ratio.

3.2 Torsional Modes

Given the profile of $v_A^2(s)$ we compute the TM by integrating (13) using finite differencing. The 1-D equation implies that $\partial\xi/\partial s = 0$ at $s = 1$ and it is automatically satisfied in our solver, if $v_A^2(1) \neq 0$. The selection of TM in the spectrum of modes of the hybrid solution is done by considering the frequency range indicated by the 1-D solutions and by a unit ratio of kinetic to magnetic energy of the eigen solutions. The comparison between the 1-D solutions (dashed black) and the hybrid model (solid colors) is shown in Figure 2. The six largest scale TM calculated by the hybrid model are in excellent agreement with the 1-D solutions. The frequencies obtained from the two models have a relative difference of $\mathcal{O}(10^{-3})$. We see that for both models $\partial\xi/\partial s = 0$ at $s = 1$, as expected. For the hybrid model the resolution of this boundary condition depends on the radial wave number of the TM in s, the spatial heterogeneity of $\mathbf{B}_0$ and the polynomial truncation. At a polynomial truncation of $N = 29$ at least the six largest scale TM are well resolved by the basis. The spatial structure of the magnetic field component of the TM depends only on the structure of $\mathbf{B}_0$ and the complexity of the TM in s (not presented here, see e.g. Cox et al., 2016).

3.3 Slightly Modified Rossby Modes

For the range of polynomial degrees studied here, RM are only slightly influenced by the presence of the magnetic field. Their spatial structure and frequency remain comparable to that of the RM in the purely HD case. We compared the frequencies of some of the largest scale RM to the frequencies of the RM when including magnetic forces with the Malkus field $\mathbf{B}_{0,M} = s\mathbf{1}_\phi$ and (20). The relative differences between

Table 1. Non-dimensional frequency ω, dimensionalized period T in years (for $|\mathbf{B}_0| = 3$ mT), and ratio of kinematic to magnetic energy $E_{\mathrm{kin}}/E_{\mathrm{mag}}$ of the six slowest TM (displayed in Figure 2), the three fastest RM and MCM (displayed in Figure 3).

Type	ω	T[yr]	$E_{\mathrm{kin}}/E_{\mathrm{mag}}$
TM	2.67	10.3	0.86
TM	4.39	6.2	0.94
TM	6.05	4.5	0.97
TM	7.68	3.6	0.98
TM	9.30	2.9	0.99
TM	10.92	2.5	0.99
MCM1	1.72	15.91	0.02
MCM2	2.66	10.28	0.03
MCM3	5.95	4.60	0.13
RM1	112.25	0.24	49.57
RM2	118.09	0.23	12.26
RM3	136.79	0.20	23.03

the frequencies of the three models are below 10^{-5} for all modes up to a truncation of $N = 29$. This difference can increase at $N > 29$, as may be anticipated by the dispersion relation (15). The spatial structure also remains mostly unchanged and their phase velocity is prograde, as observed in the HD case. We show the velocity and the radial magnetic field at the surface of three RM in Figure 3a. The slowest modes are associated with $m = 1$ and increasingly large N (see the top mode). This can be seen also by a careful analysis of the approximated dispersion relation (16). We found even slower RM in our model, but we display three modes that are well converged from degree $N = 29$ to $N = 35$ (see details in supplementary material). In both the HD and MHD case an increase of the velocity amplitudes near the equator is observed (compare with RM in Kloss & Finlay, 2019). Their ratio of kinetic to magnetic energy is $\mathcal{O}(10)$, suggesting that their surface magnetic field perturbation might be observable in the future.

3.4 Magneto-Coriolis Modes

MCM are strongly influenced by the background magnetic field. They are not easily compared between different magnetic fields, e.g. between the idealized Malkus field and the magnetic field $\mathbf{B}_0$. Instead we focus on the MCM of relatively high frequency, that are of particular interest here. From Figure 1 we see that some MCM evolve on time scales similar to those of TM. We select three MCM (MCM1–3) with dimensionalized periods of a few years (see exact figures in Table 1), that show a polynomial complexity below that of the truncation degree and a converged structure (see supplementary material). The spatial structure of these selected MCM is presented in Figure 3b, showing that they have a large complexity along the cylindrical radius and a relatively small azimuthal wave number. The short length scale in cylindrical radius is even more evident in the radial profile of the azimuthal velocity in the equatorial plane, shown in Figure 3c. Similarly to the slow RM, the fast MCM concentrate their kinetic and magnetic energy near the equator. All MCM observed here travel retrograde, compared to the prograde direction of RM, as predicted by Hide (1966). For an azimuthal wave number $m = 2$ in the equatorial band, the magnetic field perturbations of the three displayed MCM have a phase velocity of $\omega m^{-1} u_A \approx 680 - 2400$ km/yr. However, we highlight that other wave numbers contribute to each mode with different phase velocities.

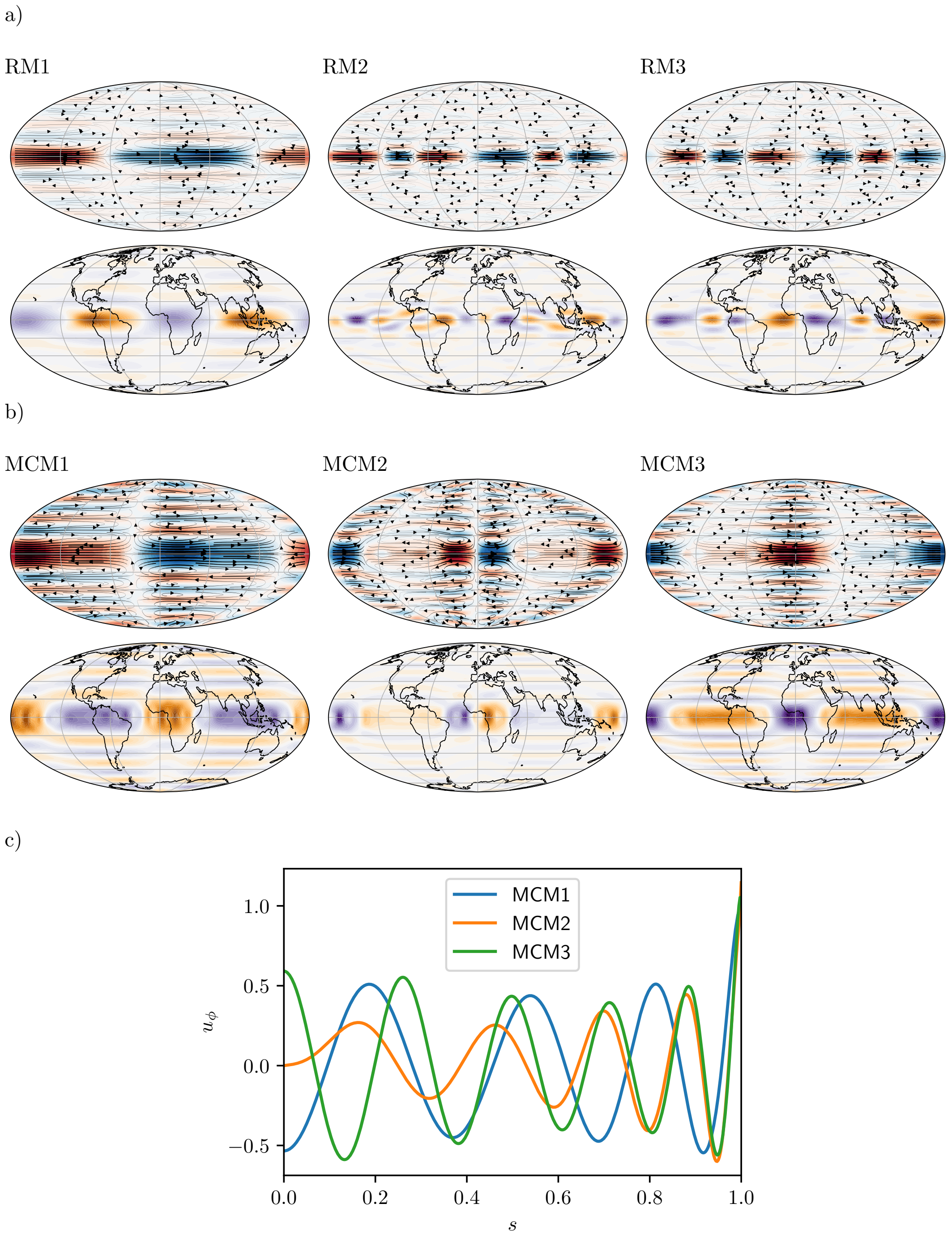

Figure 3. a) Core surface flows (top row) and associated radial magnetic field perturbation at the surface (bottom row) of the three fastest, converged, RM (RM1–3). b) Core surface flows (top row) and associated radial magnetic field perturbation at the surface (bottom row) of three selected MCM (MCM1–3) in the TM frequency range. Colors indicate the azimuthal velocity magnitude with blue being prograde and red being retrograde and inward (blue) and outward (orange) magnetic flux. The arrows indicate tracers of the surface velocity. c) Cylindrical-radial profile of the azimuthal velocity in the equatorial plane at $\phi = 0$ of MCM1–3. The modes are computed for a maximum polynomial degree $N = 35$. The frequencies and periods of the modes are given in Table 1.

4 Discussion

We have shown, for Le $= 10^{-4}$ and a mean magnetic field strength in the core interior of about 3 mT, that changes of the magnetic field on periods as short as a few years could be explained by MCM. Since the periods of these fast MCM are only a few years they may be associated with the periodic secular acceleration impulses inferred from recent satellite observations (Chulliat et al., 2015; Kloss & Finlay, 2019; Chi-Durán et al., 2020). These observations have been interpreted as the signature of MCM in the presence of a strong azimuthal magnetic field (Hori et al., 2015) or of MAC waves in a stratified layer at the top of the core (Knezek & Buffett, 2018; Buffett & Matsui, 2019). We find there is no need to introduce a magnetic field stronger than inferred from TM or a stratified layer to account for fast wave propagation in the equatorial region of the core. A key result of our study is the presence of large horizontal scales of B_r at the core surface next to the equator associated with MCM, while the mode structure itself remains small scale in the cylindrical radial direction. Such large magnetic features near the equator should be captured by satellite observations. Meanwhile, Aubert and Finlay (2019) have linked the secular variation impulses to so-called QG Alfvén waves arising near strongly heterogeneous magnetic fields of buoyant plumes in their numerical simulations. Whether or not our fast MCM are in agreement with their explanation remains to be investigated. Our model could be used to invert geomagnetic observations for such a possible excitation mechanism, as described by Buffett et al. (2009) for TM.

Fast MCM show a concentration of energy near the equator, similar to the slowest RM. Equatorially trapped waves have been much discussed either from observations (Chulliat et al., 2015) or from physical models (Bergman, 1993). The surface core flow calculations of Gillet et al. (2019) also show the largest core flow acceleration pattern in an equatorial belt below 10° of latitude. Concentration of energy of the modes could be favored by the weaker intensity of $\mathbf{B}_0$ in the equatorial region, which Knezek and Buffett (2018); Buffett and Matsui (2019) also found to be important for the focusing of MAC waves in the equatorial region of a stratified layer. A systematic study over a wider range of magnetic field geometries would be needed to make this statement quantitative.

Bergman (1993) and Buffett and Matsui (2019) have shown that equatorially trapped MAC modes are strongly affected by damping. We haven't included diffusion in our study and an investigation into how a diffusive layer at the top of the core may influence the observed fast MCM is necessary, even though they are of large spatial scale at the equator. The new basis presented here potentially allows us to include magnetic diffusion, at a substantial computational cost.

Previously, dynamics in the bulk of the core have been linked to inverted surface flows, but not directly to the observed changes in the magnetic field. Being able to associate at once MCM, as well as TM, to magnetic field changes occurring with periods of 10 years or less and yet with large horizontal scale in an equatorial band at the CMB opens new perspectives for data assimilation and analyses of the dynamics occurring in the Earth's outer core.

References

Amit, H., & Olson, P. (2004). Helical core flow from geomagnetic secular variation. *Physics of the Earth and Planetary Interiors*, *147*(1), 1–25. doi: 10.1016/j.pepi.2004.02.006

Aubert, J., & Finlay, C. C. (2019). Geomagnetic jerks and rapid hydromagnetic waves focusing at Earth's core surface. *Nature Geoscience*, *12*(5), 393–398. doi: 10.1038/s41561-019-0355-1

Backus, G., Parker, R., & Constable, C. (1996). *Foundations of Geomagnetism.* Cambridge, UK: Cambridge University Press.

Bardsley, O. P. (2018). Could hydrodynamic Rossby waves explain the westward drift? *Proceedings of the Royal Society A: Mathematical, Physical and Engineering Science*, *474*(2213). doi: 10.1098/rspa.2018.0119

Bardsley, O. P., & Davidson, P. A. (2016). Inertial–Alfvén waves as columnar helices in planetary cores. *Journal of Fluid Mechanics*, *805*. doi: 10.1017/jfm.2016.577

Bärenzung, J., Holschneider, M., Wicht, J., Sanchez, S., & Lesur, V. (2018). Modeling and Predicting the Short-Term Evolution of the Geomagnetic Field. *Journal of Geophysical Research: Solid Earth*, *123*(6), 4539–4560. doi: 10.1029/2017JB015115

Bergman, M. I. (1993). Magnetic Rossby waves in a stably stratified layer near the surface of the Earth's outer core. *Geophysical & Astrophysical Fluid Dynamics*, *68*(1-4), 151–176. doi: 10.1080/03091929308203566

Braginsky, S. I. (1970). Torsional magnetohydrodynamics vibrations in the Earth's core and variations in day length. *Geomagnetism and Aeronomy*, *10*, 3–12.

Buffett, B. (2014). Geomagnetic fluctuations reveal stable stratification at the top of the Earth's core. *Nature*, *507*(7493), 484–487. doi: 10.1038/nature13122

Buffett, B., & Matsui, H. (2019). Equatorially trapped waves in Earth's core. *Geophysical Journal International*, *218*(2), 1210–1225. doi: 10.1093/gji/ggz233

Buffett, B., Mound, J., & Jackson, A. (2009). Inversion of torsional oscillations for the structure and dynamics of Earth's core. *Geophysical Journal International*, *177*(3), 878–890. doi: 10.1111/j.1365-246X.2009.04129.x

Busse, F. H. (1976). Generation of planetary magnetism by convection. *Physics of the Earth and Planetary Interiors*, *12*(4), 350–358. doi: 10.1016/0031-9201(76)90030-3

Canet, E., Finlay, C. C., & Fournier, A. (2014). Hydromagnetic quasi-geostrophic modes in rapidly rotating planetary cores. *Physics of the Earth and Planetary Interiors*, *229*(Supplement C), 1–15. doi: 10.1016/j.pepi.2013.12.006

Canet, E., Fournier, A., & Jault, D. (2009). Forward and adjoint quasi-geostrophic models of the geomagnetic secular variation. *Journal of Geophysical Research: Solid Earth*, *114*(B11). doi: 10.1029/2008JB006189

Chen, L., Herreman, W., Li, K., Livermore, P. W., Luo, J. W., & Jackson, A. (2018). The optimal kinematic dynamo driven by steady flows in a sphere. *Journal of Fluid Mechanics*, *839*, 1–32. doi: 10.1017/jfm.2017.924

Chi-Durán, R., Avery, M. S., Knezek, N., & Buffett, B. A. (2020). Decomposition of geomagnetic secular acceleration into traveling waves using complex empirical orthogonal functions. *Geophysical Research Letters*, *47*(17), e2020GL087940. doi: 10.1029/2020GL087940

Chulliat, A., Alken, P., & Maus, S. (2015). Fast equatorial waves propagating at the top of the Earth's core. *Geophysical Research Letters*, *42*(9), 3321–3329. doi: 10.1002/2015GL064067

Chulliat, A., & Hulot, G. (2000). Local computation of the geostrophic pressure at the top of the core. *Physics of the Earth and Planetary Interiors*, *117*(1), 309–328. doi: 10.1016/S0031-9201(99)00104-1

Cox, G. A., Livermore, P. W., & Mound, J. E. (2016). The observational signature of modelled torsional waves and comparison to geomagnetic jerks. *Physics of the Earth and Planetary Interiors*, *255*, 50–65. doi: 10.1016/j.pepi.2016.03.012

Gerick, F., Jault, D., Noir, J., & Vidal, J. (2020). Pressure torque of torsional Alfvén modes acting on an ellipsoidal mantle. *Geophysical Journal International*, *222*(1), 338–351. doi: 10.1093/gji/ggaa166

Gillet, N., Huder, L., & Aubert, J. (2019). A reduced stochastic model of core surface dynamics based on geodynamo simulations. *Geophysical Journal Interna-*

tional, *219*(1), 522–539. doi: 10.1093/gji/ggz313

Gillet, N., Jault, D., Canet, E., & Fournier, A. (2010). Fast torsional waves and strong magnetic field within the Earth's core. *Nature*, *465*(7294), 74–77. doi: 10.1038/nature09010

Gillet, N., Jault, D., & Finlay, C. C. (2015). Planetary gyre, time-dependent eddies, torsional waves, and equatorial jets at the Earth's core surface. *Journal of Geophysical Research: Solid Earth*, *120*(6), 3991–4013. doi: 10.1002/2014JB011786

Gillet, N., Pais, M. A., & Jault, D. (2009). Ensemble inversion of time-dependent core flow models. *Geochemistry, Geophysics, Geosystems*, *10*(6). doi: 10.1029/2008GC002290

Gillet, N., Schaeffer, N., & Jault, D. (2011). Rationale and geophysical evidence for quasi-geostrophic rapid dynamics within the Earth's outer core. *Physics of the Earth and Planetary Interiors*, *187*(3), 380–390. doi: 10.1016/j.pepi.2011.01.005

Greenspan, H. P. (1968). *The theory of rotating fluids*. Cambridge, UK: Cambridge University Press.

Hide, R. (1966). Free hydromagnetic oscillations of the earth's core and the theory of the geomagnetic secular variation. *Philosophical Transactions of the Royal Society of London. Series A, Mathematical and Physical Sciences*, *259*(1107), 615–647. doi: 10.1098/rsta.1966.0026

Hide, R., & Stewartson, K. (1972). Hydromagnetic oscillations of the Earth's core. *Reviews of Geophysics*, *10*(2), 579–598. doi: 10.1029/RG010i002p00579

Holme, R. (2015). 8.04 - Large-Scale Flow in the Core. In G. Schubert (Ed.), *Treatise on Geophysics (Second Edition)* (pp. 91–113). Oxford: Elsevier. doi: 10.1016/B978-0-444-53802-4.00138-X

Hori, K., Jones, C. A., & Teed, R. J. (2015). Slow magnetic Rossby waves in the Earth's core. *Geophysical Research Letters*, *42*(16), 6622–6629. doi: 10.1002/2015GL064733

Ivers, D. J., Jackson, A., & Winch, D. (2015). Enumeration, orthogonality and completeness of the incompressible Coriolis modes in a sphere. *Journal of Fluid Mechanics*, *766*, 468–498. doi: 10.1017/jfm.2015.27

Jault, D. (2003). Electromagnetic and topographic coupling, and LOD variations. In C. A. Jones, A. M. Soward, K. Zhang, A. M. Soward, & K. Zhang (Eds.), *Earth's Core and Lower Mantle* (pp. 55–76). CRC Press.

Jault, D., & Finlay, C. C. (2015). 8.09 - Waves in the Core and Mechanical Core–Mantle Interactions. In G. Schubert (Ed.), *Treatise on Geophysics (Second Edition)* (pp. 225–244). Oxford: Elsevier. doi: 10.1016/B978-0-444-53802-4.00150-0

Kloss, C., & Finlay, C. C. (2019). Time-dependent low-latitude core flow and geomagnetic field acceleration pulses. *Geophysical Journal International*, *217*(1), 140–168. doi: 10.1093/gji/ggy545

Knezek, N., & Buffett, B. (2018). Influence of magnetic field configuration on magnetohydrodynamic waves in Earth's core. *Physics of the Earth and Planetary Interiors*, *277*, 1–9. doi: 10.1016/j.pepi.2018.01.005

Labbé, F., Jault, D., & Gillet, N. (2015). On magnetostrophic inertia-less waves in quasi-geostrophic models of planetary cores. *Geophysical & Astrophysical Fluid Dynamics*, *109*(6), 587–610. doi: 10.1080/03091929.2015.1094569

Lebovitz, N. R. (1989). The stability equations for rotating, inviscid fluids: Galerkin methods and orthogonal bases. *Geophysical & Astrophysical Fluid Dynamics*, *46*(4), 221–243. doi: 10.1080/03091928908208913

Lehnert, B. (1954). Magnetohydrodynamic Waves Under the Action of the Coriolis Force. *The Astrophysical Journal*, *119*, 647. doi: 10.1086/145869

Le Mouël, J. L. (1984). Outer-core geostrophic flow and secular variation of Earth's geomagnetic field. *Nature*, *311*(5988), 734–735. doi: 10.1038/311734a0

Li, K., Jackson, A., & Livermore, P. W. (2018). Taylor state dynamos found by optimal control: axisymmetric examples. *Journal of Fluid Mechanics*, *853*, 647–697. doi: 10.1017/jfm.2018.569

Li, K., Livermore, P. W., & Jackson, A. (2010). An optimal Galerkin scheme to solve the kinematic dynamo eigenvalue problem in a full sphere. *Journal of Computational Physics*, *229*(23), 8666–8683. doi: 10.1016/j.jcp.2010.07.039

Maffei, S., & Jackson, A. (2016). Propagation and reflection of diffusionless torsional waves in a sphere. *Geophysical Journal International*, *204*(3), 1477–1489. doi: 10.1093/gji/ggv518

Maffei, S., & Jackson, A. (2017). Kinematic validation of a quasi-geostrophic model for the fast dynamics in the Earth's outer core. *Geophysical Journal International*, *210*(3), 1772–1786. doi: 10.1093/gji/ggx263

Malkus, W. V. R. (1967). Hydromagnetic planetary waves. *Journal of Fluid Mechanics*, *28*(4), 793–802. doi: 10.1017/S0022112067002447

Pozzo, M., Davies, C., Gubbins, D., & Alfe, D. (2014). Thermal and electrical conductivity of solid iron and iron–silicon mixtures at Earth's core conditions. *Earth and Planetary Science Letters*, *393*, 159–164. doi: 10.1016/j.epsl.2014.02.047

Schaeffer, N., & Cardin, P. (2005). Quasigeostrophic model of the instabilities of the Stewartson layer in flat and depth-varying containers. *Physics of Fluids*, *17*(10), 104111–104111. doi: 10.1063/1.2073547

Schaeffer, N., Jault, D., Nataf, H.-C., & Fournier, A. (2017). Turbulent geodynamo simulations: a leap towards Earth's core. *Geophysical Journal International*, *211*(1), 1–29. doi: 10.1093/gji/ggx265

Stewartson, K. (1957). The dispersion of a current on the surface of a highly conducting fluid. *Mathematical Proceedings of the Cambridge Philosophical Society*, *53*(3), 774–775. doi: 10.1017/S0305004100032837

Vantieghem, S. (2014). Inertial modes in a rotating triaxial ellipsoid. *Proceedings of the Royal Society A: Mathematical, Physical and Engineering Sciences*, *470*(2168), 20140093. doi: 10.1098/rspa.2014.0093

Vidal, J., & Cébron, D. (2017). Inviscid instabilities in rotating ellipsoids on eccentric Kepler orbits. *Journal of Fluid Mechanics*, *833*, 469–511. doi: 10.1017/jfm.2017.689

Vidal, J., Cébron, D., ud Doula, A., & Alecian, E. (2019). Fossil field decay due to nonlinear tides in massive binaries. *Astronomy & Astrophysics*, *629*, A142. doi: 10.1051/0004-6361/201935658

Vidal, J., Su, S., & Cébron, D. (2020). Compressible fluid modes in rigid ellipsoids: towards modal acoustic velocimetry. *Journal of Fluid Mechanics*, *885*. doi: 10.1017/jfm.2019.1004

Wijs, G. A. d., Kresse, G., Vočadlo, L., Dobson, D., Alfe, D., Gillan, M. J., & Price, G. D. (1998). The viscosity of liquid iron at the physical conditions of the Earth's core. *Nature*, *392*(6678), 805. doi: 10.1038/33905

Zatman, S., & Bloxham, J. (1997). Torsional oscillations and the magnetic field within the Earth's core. *Nature*, *388*(6644), 760–763. doi: 10.1038/41987

Zhang, K., Earnshaw, P., Liao, X., & Busse, F. H. (2001). On inertial waves in a rotating fluid sphere. *Journal of Fluid Mechanics*, *437*, 103–119. doi: 10.1017/S0022112001004049

Zhang, K., & Fearn, D. R. (1995, December). Hydromagnetic waves in rapidly rotating spherical shells generated by poloidal decay modes. *Geophysical & Astrophysical Fluid Dynamics*, *81*(3-4), 193–209. doi: 10.1080/03091929508229063

Appendix A Derivation of Magnetic Field Basis

Let us write the current density $\mathbf{j} = \boldsymbol{\nabla} \times \mathbf{B}$ in the toroidal-poloidal expansion, so that

$$\mathbf{j} = \boldsymbol{\nabla} \times Q\mathbf{r} + \boldsymbol{\nabla} \times \boldsymbol{\nabla} \times S\mathbf{r}. \tag{A1}$$

We can also write the magnetic field in the toroidal-poloidal expansion, with

$$\mathbf{B} = \boldsymbol{\nabla} \times T\mathbf{r} + \boldsymbol{\nabla} \times \boldsymbol{\nabla} \times P\mathbf{r}. \tag{A2}$$

It follows (Backus et al., 1996) that

$$S = T, \tag{A3}$$

$$\nabla^2 P = -Q. \tag{A4}$$

We construct the toroidal and poloidal scalars for the basis of $\mathbf{j}$ following the velocity basis introduced by Ivers et al. (2015), so that

$$Q_{lmn} = r^{2n} R_l^m, \tag{A5}$$

$$S_{lmn} = (1 - r^2) r^{2n} R_l^m, \tag{A6}$$

with $R_l^m = r^l Y_l^m(\theta, \phi)$ the solid spherical harmonics. We have $|m| \leq l$ and $l \in [1, N]$, $n \in [0, (N-l)/2\rfloor$ for the toroidal basis and $l \in [0, N-1]$, $n \in [0, (N+1-l)/2 - 1\rfloor$ for the poloidal basis. These $N_3 = \frac{1}{6} N(N+1)(2N+7)$ elements form a complete basis for the current density in the set of polynomial vector fields of degree N in the volume $\mathcal{V}$ (Ivers et al., 2015). Then, the toroidal part of $\mathbf{B}$ is directly given by

$$\mathbf{B}_{t,lmn} = \boldsymbol{\nabla} \times S_{lmn}\mathbf{r}. \tag{A7}$$

For the poloidal part

$$\mathbf{B}_{p,lmn} = \boldsymbol{\nabla} \times \boldsymbol{\nabla} \times P_{lmn}\mathbf{r}, \tag{A8}$$

we need to solve the Poisson equation

$$\nabla^2 P_{lmn} = -Q_{lmn}. \tag{A9}$$

We can use a slightly modified version of equation (3.1.9) in Backus et al. (1996)

$$\nabla^2 \left(r^{2(n+1)} \frac{R_l^m}{2(n+1)(2(l+n)+3)} \right) = r^{2n} R_l^m, \tag{A10}$$

to find that

$$P_{lmn} = -r^{2(n+1)} \frac{R_l^m}{2(n+1)(2(l+n)+3)}. \tag{A11}$$

It remains to ensure that the internal magnetic field can be matched to a potential field at the boundary. The poloidal component has to satisfy

$$\nabla \Phi^i + \mathbf{B}_p = \nabla \Phi^e \quad \text{at } \partial\mathcal{V}, \tag{A12}$$

with Φ^i and Φ^e the interior and exterior potential field, respectively. The exterior potential field must vanish at infinity, if the source of the magnetic field lies within the interior. We can solve for Φ^i and Φ^e by considering the radial component of (A12) and the horizontal component of (A12)

$$\partial_r \Phi^i - \partial_r \Phi^e = -B_{p,r}, \tag{A13a}$$

$$\nabla_H \Phi^i - \nabla_H \Phi^e = -\mathbf{B}_{p,H} \tag{A13b}$$

Using the properties of the spherical harmonics, we find that

$$B_{p,r} = \frac{1}{r} L^2 P, \qquad \mathbf{B}_{p,H} = \nabla_H \left(\frac{\partial}{\partial r}(rP) \right), \tag{A14}$$

with $L^2P = \partial_r(r^2\partial P/\partial r) - r^2\nabla^2 P$ and the system simplifies to

$$\partial_r\Phi^i - \partial_r\Phi^e = -L^2P, \tag{A15a}$$
$$\Phi^i - \Phi^e = -\partial_r(rP). \tag{A15b}$$

Since this is linearly independent of l, m, and n we can consider this system for each $\mathbf{B}_{p,lmn}$ individually, so that

$$\partial_r\Phi^i_{lmn} - \partial_r\Phi^e_{lmn} = -L^2P_{lmn}, \tag{A16a}$$
$$\Phi^i_{lmn} - \Phi^e_{lmn} = -\partial_r(rP_{lmn}). \tag{A16b}$$

Since $L^2Y_l^m = l(l+1)Y_m^l$ and

$$\partial_r(rP_{lmn}) = \frac{2(n+1)+l+1}{2(n+1)(2(l+n)+3)} r^{2(n+1)+l}Y_l^m, \tag{A17}$$

we need to search for potentials of the form

$$\Phi^i_{lmn} = \alpha_{lmn}r^lY_l^m, \tag{A18a}$$
$$\Phi^e_{lmn} = \beta_{lmn}r^{-(l+1)}Y_l^m. \tag{A18b}$$

The system to be solved for each l, n is then

$$\begin{pmatrix} l & l+1 \\ 1 & -1 \end{pmatrix}\begin{pmatrix} \alpha_{lmn} \\ \beta_{lmn} \end{pmatrix} = -\frac{1}{\alpha}\begin{pmatrix} l(l+1) \\ 2n+l+3 \end{pmatrix}, \tag{A19}$$

with $\alpha = 2(n+1)(2(l+n)+3)$, for each l, n. The solutions to (A19) are

$$\alpha_{lmn} = -\frac{(l+1)}{(2l+1)(2n+2)}, \tag{A20a}$$
$$\beta_{lmn} = \frac{l}{(2l+1)(2l+2n+3)}, \tag{A20b}$$

so that the poloidal basis vectors are given by

$$\mathbf{B}_{p,lmn} = \boldsymbol{\nabla}\times\boldsymbol{\nabla}\times P_{lmn}\mathbf{r} + \nabla\Phi^i_{lmn}. \tag{A21}$$

Li et al. (2010) presented a similar basis to express the magnetic field for an insulating mantle, which involves slightly more complicated expressions for the poloidal and toroidal scalars with Jacobi polynomials. We have not proven any weighted orthogonal inner products of the poloidal and toroidal scalars, but our basis vectors show the same orthogonality for the unweighted inner product between vectors of different harmonic order and degree as does the basis of Li et al. (2010). Orthogonal bases, based on Jacobi polynomials and spherical harmonics, have been presented in Chen et al. (2018); Li et al. (2018). These bases are desirable for reducing computational efforts, but without an orthogonal QG basis, no such computational advantage is given for the hybrid model presented here.

Appendix B Spherical Harmonics in Cartesian Coordinates

The unnormalized spherical harmonics are defined as

$$\tilde{Y}_l^m(\theta,\phi) = e^{im\phi}P_l^m(\cos\theta), \tag{B1}$$

with the so-called associated Legendre functions

$$P_l^m(x) = \frac{1}{2^l l!}\left(1-x^2\right)^{m/2}\frac{\partial^m}{\partial x^m}P_l(x) \tag{B2}$$

with

$$P_l(x) = \frac{\partial^l}{\partial x^l}\left(x^2-1\right)^l. \tag{B3}$$

The unit Cartesian coordinates are given by

$$\hat{x} = x/r = \cos\phi\sin\theta, \tag{B4}$$
$$\hat{y} = y/r = \sin\phi\sin\theta, \tag{B5}$$
$$\hat{z} = z/r = \cos\theta. \tag{B6}$$

We can rewrite (B2), so that

$$P_l^m(\cos\theta) = P_l^m(\hat{z}) = \frac{1}{2^l l!}(\sin\theta)^m \frac{\partial^m}{\partial\hat{z}^m}P_l(\hat{z}). \tag{B7}$$

Using the trigonometric identities

$$\sin(m\phi) = \sum_{k \text{ odd}} (-1)^{\frac{k-1}{2}}\binom{m}{k}(\cos\phi)^{m-k}(\sin\phi)^k, \tag{B8}$$
$$\cos(m\phi) = \sum_{k \text{ even}} (-1)^{\frac{k}{2}}\binom{m}{k}(\cos\phi)^{m-k}(\sin\phi)^k, \tag{B9}$$

we are able to rewrite the spherical harmonics in terms of the unit Cartesian coordinates, so that

$$\begin{aligned}\tilde{Y}_l^m(\theta,\phi) =& \tilde{Y}_l^m(\hat{x},\hat{y},\hat{z})\\ =& \frac{1}{2^l l!}\left(\sum_{k \text{ odd}}(-1)^{\frac{k-1}{2}}\binom{m}{k}\hat{x}^{m-k}\hat{y}^k\right.\\ &\left.+i\sum_{k \text{ even}}(-1)^{\frac{k}{2}}\binom{m}{k}\hat{x}^{m-k}\hat{y}^k\right)\frac{\partial^m}{\partial\hat{z}^m}P_l(\hat{z}).\end{aligned} \tag{B10}$$

The solid spherical harmonics are

$$\tilde{R}_l^m(x,y,z) = r^l\tilde{Y}_l^m(\hat{x},\hat{y},\hat{z}), \tag{B11}$$

which is polynomial in x, y and z.

Acknowledgments

The authors like to thank Henri-Claude Nataf and two anonymous reviewers for their help in improving this work. FG was partly funded by Labex OSUG@2020 (ANR10 LABX56). Support is acknowledged from the European Space Agency through contract 4000127193/19/NL/IA. This work has been carried out with financial support from CNES (Centre National d'Études Spatiales, France). JN was partly funded by SNF Grant #200021_185088. Computations were performed on ETH Zurich's Euler cluster. The data and the code to calculate it can be found at `https://dx.doi.org/10.5281/zenodo.4008396`.

Supporting Information for ”Fast Quasi-Geostrophic Magneto-Coriolis Modes in the Earth’s core”

F. Gerick[1,2], D. Jault[1], J. Noir[2]

[1]CNRS, ISTerre, University of Grenoble Alpes, Grenoble, France

[2]Institute of Geophysics, ETH Zurich, Zurich, Switzerland

arXiv:2101.01493v2 [physics.geo-ph] 23 Feb 2021

Solving the Generalized Eigen Problem

The generalized eigen problem

$$\mathrm{i}\omega \mathbf{M}\mathbf{x} = \mathbf{D}\mathbf{x}, \tag{1}$$

is transformed to a standard eigenvalue problem by inverting $\mathbf{M}$, so that

$$\lambda \mathbf{x} = \mathbf{A}\mathbf{x}, \tag{2}$$

where $\lambda = \mathrm{i}\omega$ and $\mathbf{A} = \mathbf{M}^{-1}\mathbf{D}$. In practice this inverse is not calculated explicitly, as $\mathbf{M}^{-1}$ is not necessarily sparse and its calculation costly. Instead we factorize $\mathbf{M}$ to be able to solve the linear problem $\mathbf{A}\mathbf{x} = \mathbf{b}$ for $\mathbf{x}$. The standard eigenvalue problem (2) can then be solved iteratively for the largest eigen pairs $(\lambda_k, \mathbf{x}_k)$ using the Krylov-Schur method implemented in the Julia programming language. The advantage of this implementation is an easy adaptation to higher accuracy floating point numbers. In our model we observe

---

an increase in the real part of the numerical eigen solutions for increasing polynomial degree due to numerical inaccuracies, demonstrated in Figure S1 for the Malkus field. We compensate this by using quadruple precision (128bit) floating point numbers throughout all of our computations, which are able to ensure stable enough solutions. Due to the hybrid model a large portion of the eigen solutions are degenerate modes of zero frequency so that we choose to calculate only the non-zero modes.

Another difficulty, present for magnetic fields that are not linear in x,y and z, is the convergence of the modes. In this case spurious modes are always possible and they can perturb the physically relevant modes significantly. We have thus to make sure that the calculated modes are converged. To do so, first, the frequency shouldn't change significantly between different truncation degrees. Further, the velocity and magnetic field must also not change more than a given threshold. We impose that the mode calculated at a degree N, $\mathbf{u}_N$, must be able to be matched to a mode calculated at a higher degree $N+2$, $\mathbf{u}_{N+2}$, with a correlation

$$\frac{\int_{\mathcal{V}} \mathbf{u}_N \cdot \mathbf{u}_{N+2} \, \mathrm{d}V}{\int_{\mathcal{V}} \mathbf{u}_N \cdot \mathbf{u}_N \, \mathrm{d}V} > 1 - \epsilon, \tag{3}$$

with ϵ the allowed error.

For the RM we choose $\epsilon = 0.01$ and from a degree $N = 29$ to $N = 35$ the three modes presented in Figure 3a and S2a are the fastest modes that satisfy this constraint. For the MCM the threshold is lowered to $\epsilon = 0.05$. This way we ensure that for $N = 29, 31, 33, 35$ the modes keep their spatial structure approximately. We reproduce Figure 3 of the article in Figure S2 to illustrate the difference. Especially the equatorial region of the MCM is prone to the influence of spurious modes. Nevertheless the broad structure, e.g.

dominant wave number and equatorial focusing, are preserved throughout different degrees of truncation, making us confident that these modes are indeed sufficiently converged.

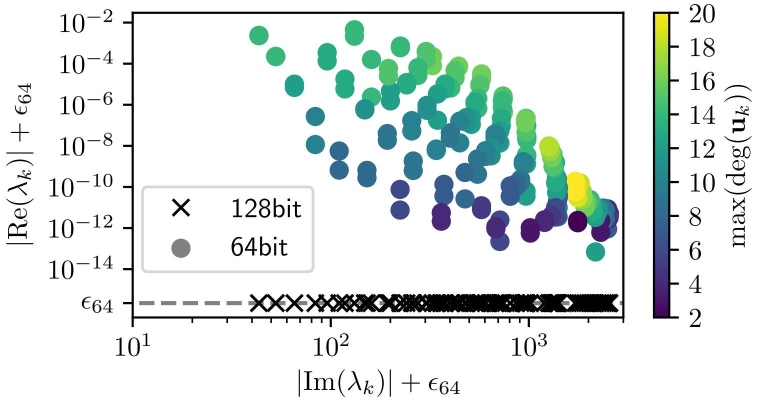

Figure S1. Comparison of eigen values to the Malkus problem using a 64bit accurate solver and a 128bit accurate solver for a truncation of $N = 20$. We focus here on the frequency regime of the fast RM. The solutions of the 64bit solver are colored by the polynomial degree of their peak amplitude basis vector. The solutions to the 128bit solver are shown as orange crosses and lie on the line of $\mathrm{Re}(\lambda_k) + \epsilon_{64} \approx \epsilon_{64} \approx 2.2 \times 10^{-16}$, the 64bit floating point error.

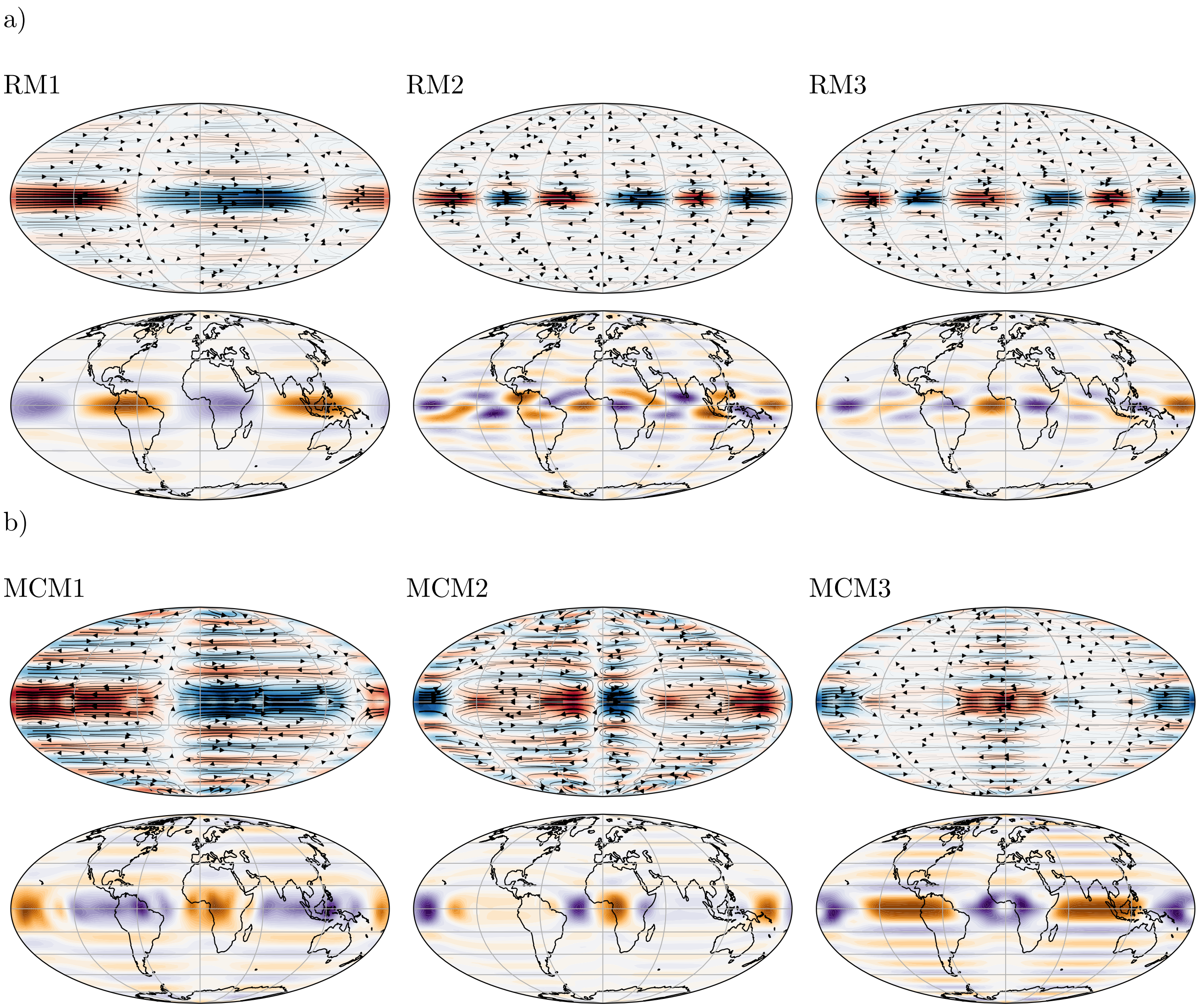

Figure S2. Same as Figure 3 of the article with truncation degree $N = 29$.

5.2 Diffusive Magneto-Coriolis modes

In our study we have neglected magnetic diffusion. When considering MCM of higher wave numbers, the spatial scale l decreases and the effect of diffusion may become important. This is seen by the ratio of the advective term and the magnetic diffusion term, also known as the magnetic Reynolds number $\mathrm{Rm} = Ul\eta^{-1}$. For small spatial scales Rm is not necessarily very large. The dependency on diffusion of the MCM in the idealized Malkus field with a perfectly conducting mantle has been studied by Zhang and Busse (1995). In their study the stability of the Malkus modes was found to be weakly affected by diffusion and instabilities are only found within a Hartmann boundary layer. Schmitt (2010) showed MCM of the Malkus field as a function of diffusion at very large values of $\mathrm{Le} \approx 0.6$, and concluded that a more thorough study on the influence of diffusion is needed. In the context of MAC waves within a stratified layer it has been suggested that diffusion plays a crucial role (Bergman, 1993; Buffett and Matsui, 2019). The propagation of these modes would be prohibited by their strong damping. When diffusion is strong, quasi-free-decay (QFD) modes are possible (Schmitt, 2012). They are characterized by decaying much faster than their period when the Lundquist number is $\mathcal{O}(1)$. In principle these modes should exist in a global study as the one presented here, when diffusion is included. Schmitt (2012) had difficulties following the QFD modes (potentially also undergoing avoided crossing, as he describes a *jumping* of modes) from a small Lundquist number to a more geophysically relevant regime, noting that the modes are clustered in a region of similar frequencies and damping rates.

As the basis for the magnetic field does not need to be modified when including magnetic diffusion, an extension is straightforward. To include magnetic diffusion term $\mathrm{Lu}^{-1}\boldsymbol{\nabla}^2\mathbf{B}$ in our Galerkin approach we need to calculate

$$K_{ij} = \frac{1}{\mathrm{Lu}} \int_{\mathcal{V}} \mathbf{B}_i' \cdot \boldsymbol{\nabla}^2 \mathbf{B}_j \,\mathrm{d}V, \tag{5.1}$$

with $K_{ij} \in \mathbb{R}^{N_3 \times N_3}$. The right hand side matrix (2.103), or (35) in Section 5.1, is then given as

$$\mathbf{D} = \begin{pmatrix} C_{ij} & L_{ij} \\ V_{ij} & K_{ij} \end{pmatrix}. \tag{5.2}$$

Although straightforward to implement, significant computational effort is added to the problem, as the large square matrix K_{ij} has to be assembled and solved for all non-zero frequency modes.

In the diffusive case the time dependence of velocity and magnetic field is complemented by the damping factor σ, so that

$$\mathbf{u}(\mathbf{r}, t) = \mathbf{u}(\mathbf{r}) \exp((\sigma + \mathrm{i}\omega)t), \tag{5.3}$$

and also for $\mathbf{B}$. To quantify the damping we calculate the quality factor $Q = |\omega/\sigma|$. When $Q \gg 1$ the mode is only weakly influenced by the damping and oscillates

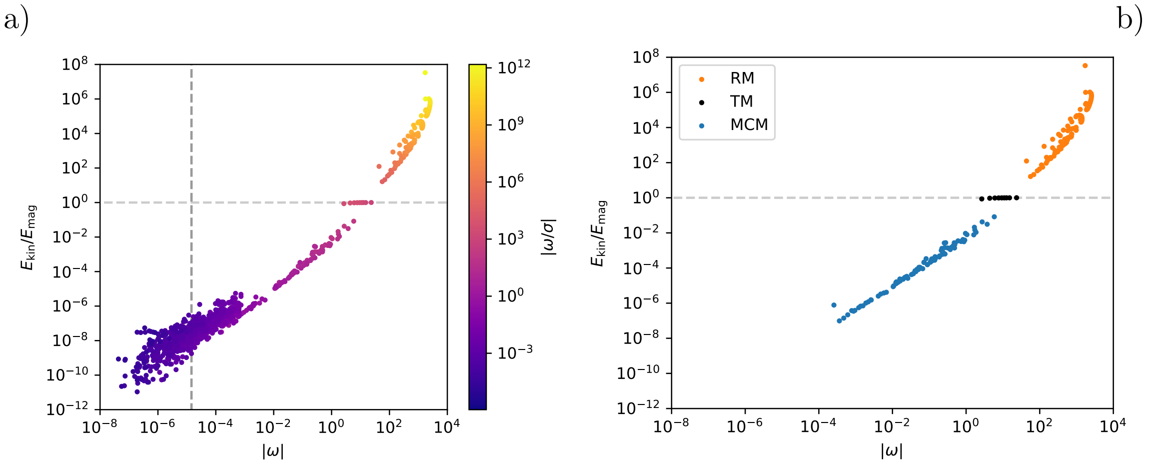

Figure 5.1: Mode spectrum including diffusion in the model (left) at $\mathrm{Le} = 10^{-4}$, $\mathrm{Lu} = 10^{5}$, $N = 19$. The modes kinetic to magnetic energy ratio is shown as a function of frequency with the quality factor $|\omega/\sigma|$ as a color code. The vertical dashed line shows the diffusion time $T_\eta = \mathrm{Lu} T_A$. Diffusion-less case for the same truncation (right).

multiple times before being damped/diffused. Conversely, when $Q \ll 1$ the oscillation is damped before propagation is observable.

We have calculated eigen solutions using the same magnetic field as in our study of diffusion-less modes at a truncation of $N = 19$ and a Lundquist number $\mathrm{Lu} = 10^5$. We did not compute the full spectrum at higher truncation levels, as the number of non-zero frequency modes is increased and eigen solutions of small frequency can still have a large damping. Then, calculating eigenvalues in the order of their amplitude requires also the computation of most geostrophic modes. For $N = 19$ we can still use standard floating point numbers and calculate the full spectrum of the dense matrices by using *LAPACK*. At higher degrees this quickly becomes unfeasible and numerical inaccuracies can occur (see supplementary material of Gerick et al., 2021). The calculation of these dense spectra, even at $N = 19$, making a detailed investigation expensive and is therefore out of the scope of this thesis.

The ratio $E_{\mathrm{kin}}/E_{\mathrm{mag}}$ as a function of the frequencies of the modes including diffusion is presented in Figure 5.1a together with the associated quality factor as a color code. As a comparison we show the diffusion-less spectrum at $N = 19$ in Figure 5.1b. It is seen that the frequencies of the RM, TM and the fastest MCM are not strongly affected by the diffusion. This is also evident when we compare the histograms of the diffusive and diffusion-less case (Figure 5.2, right). In the histograms, we see also that the low frequency modes in the diffusive case are actually modes that have a zero frequency in the diffusion-less case. These zero frequency modes are not shown for the diffusion-less case, as they are of limited relevance. They are of very small scale and mostly have no physical meaning, as the eigen vectors can be chosen almost arbitrarily for the zero frequency.

The small effect on the non-zero frequency modes is illustrated by the slowest MCM

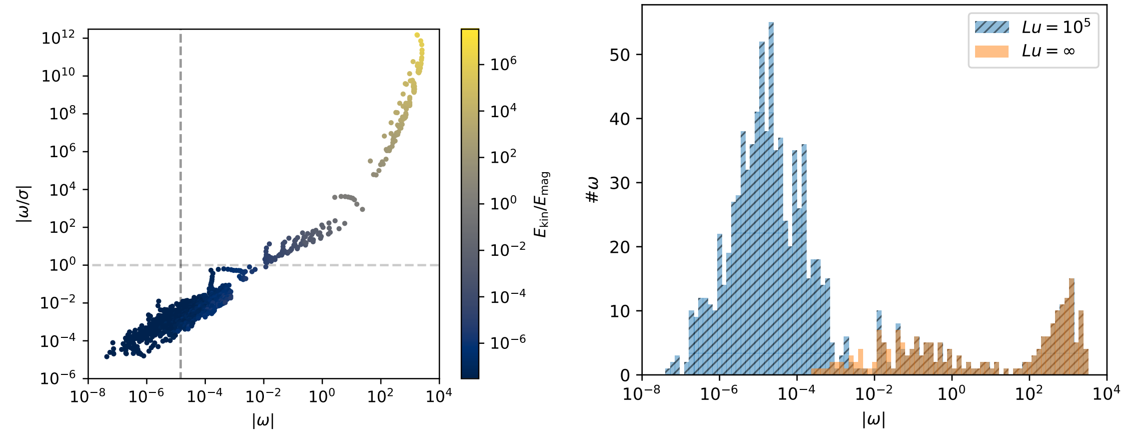

Figure 5.2: Left: Another presentation of the mode spectrum with the quality factor on the y-axis, making it easier to read the values of it, and color coded by $E_{\mathrm{kin}}/E_{\mathrm{mag}}$. The vertical dashed line shows the magnetic diffusion time $T_\eta = \mathrm{Lu}\, T_A$. Right: Histograms of the non-diffusive case ($\mathrm{Lu} = \infty$) and for $\mathrm{Lu} = 10^5$.

displayed in Gerick et al. (2021). It is found at almost the same frequency in the diffusive case, with $\lambda = -0.01 + 1.68\mathrm{i}$. This corresponds to a quality factor of $Q = 168$ and this modes has a damping period of $(2\pi/0.01)T_A \approx 2700$ yr. The surface velocity and radial magnetic field perturbations are displayed in Figure 5.3 (top). No significant difference to the diffusion-less case is seen in the spatial structure. To quantify the influence of diffusion on the magnetic field perturbation the absolute values of the advection term and the diffusion term of the mode are shown in the bottom of Figure 5.3. Temporal changes by diffusion are about 10–20 times smaller than those caused by advection.

We do not expect any significant differences to the other modes at even larger frequencies, as can be anticipated from the spectrum in Figure 5.2 (left). The quality factor increases for the MCM that approach the Alfvén wave frequency.

We find that many MCM with frequencies $\omega > 10^{-2}$ and a quality factor $Q = \mathcal{O}\left(10^0 - 10^2\right)$ exist for Earth-like parameters ($\mathrm{Le} = 10^{-4}$, $\mathrm{Lu} = 10^5$). These MCM could play an important role also for geomagnetic secular variations on periods of a few hundreds of years. Two MCM with periods of 45 yr and 380 yr are shown in Figures 5.4 and 5.5, respectively. Although the spatial scales are larger, the quality factor decreases as the frequency is decreased. Also, the strength of the magnetic diffusion term relative to the advection of the magnetic field increases. As expected, for the mode with $\omega = 0.6$ and a quality factor of $Q = 69$ (Figure 5.4) diffusion is less important than for the mode at $\omega = 0.07$ and a quality factor of $Q = 26$ (Figure 5.5), where diffusion and advection are on the same order of magnitude.

A big difference between the diffusion-less and diffusive mode spectra are the very slow modes of periods on the order of the diffusion time scale $T_\eta = \mathrm{Lu}\, T_A$ (shown as a dashed vertical line in Figure 5.1a). Whether these modes are of physical relevance

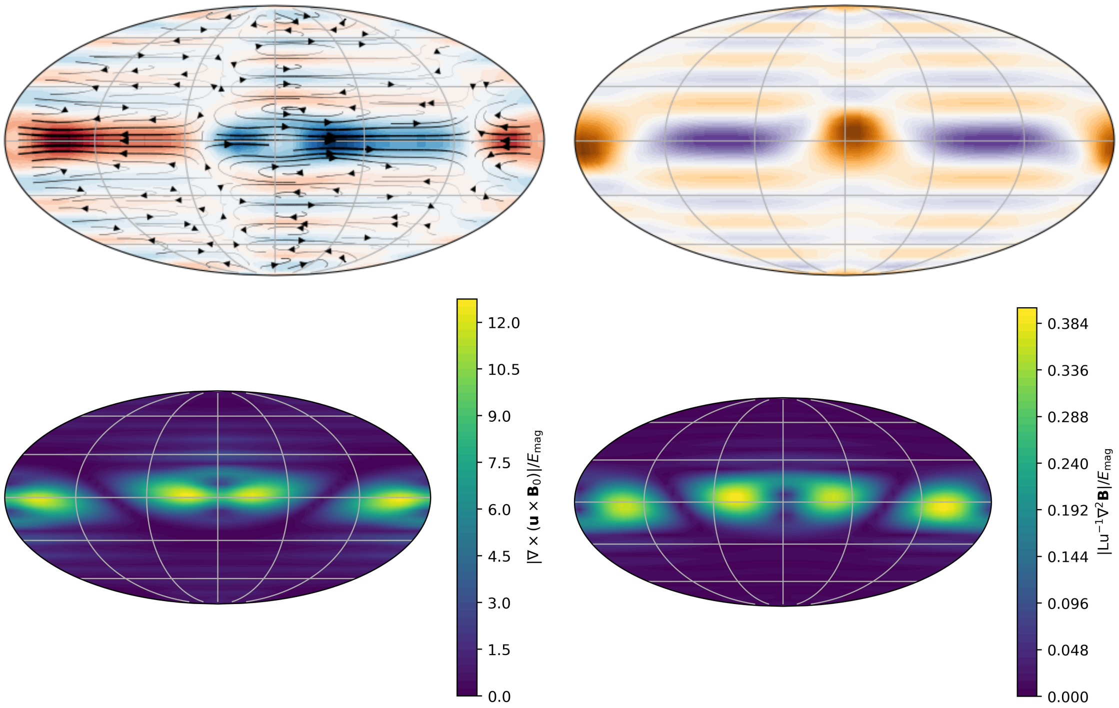

Figure 5.3: Surface fields of the fast MCM with $\omega \approx 1.7$ as shown in Gerick et al. (2021) for the diffusion-less case. Top: Surface velocity (left) and radial magnetic field perturbation (right). Bottom: Strength of magnetic advection (left) and of diffusion (right) on the surface, normalized by the total magnetic energy.

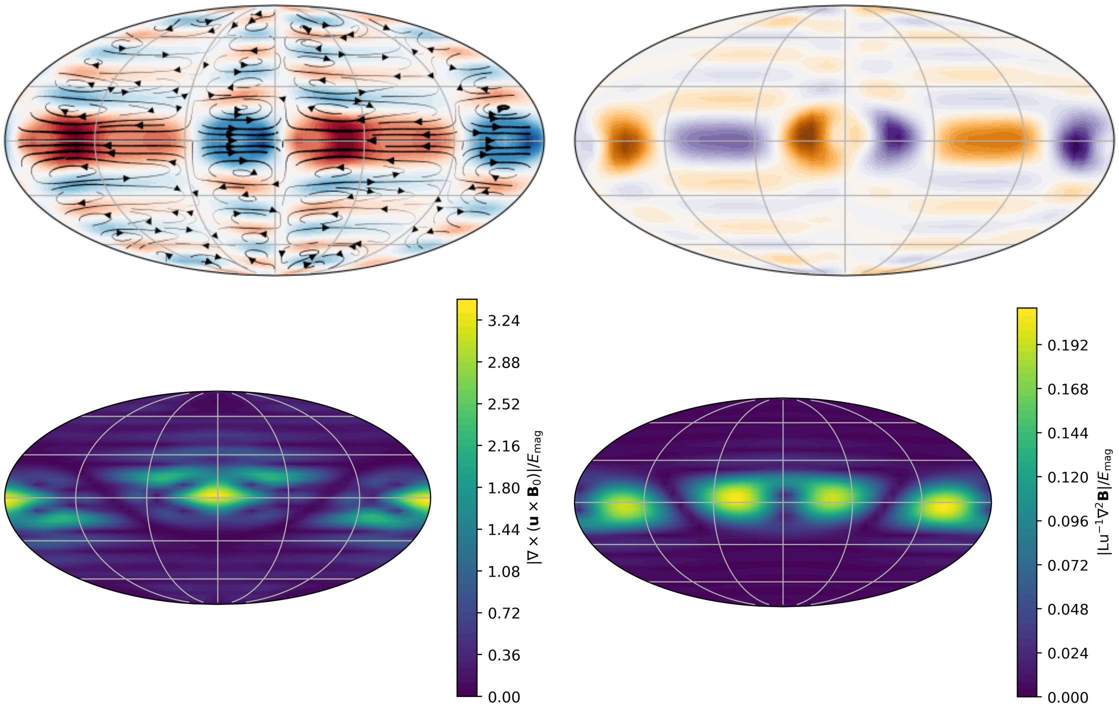

Figure 5.4: Analogous to Figure 5.3 for mode with $\omega = 0.6$, $Q = 69$, $T\,[\mathrm{yr}] = 45$.

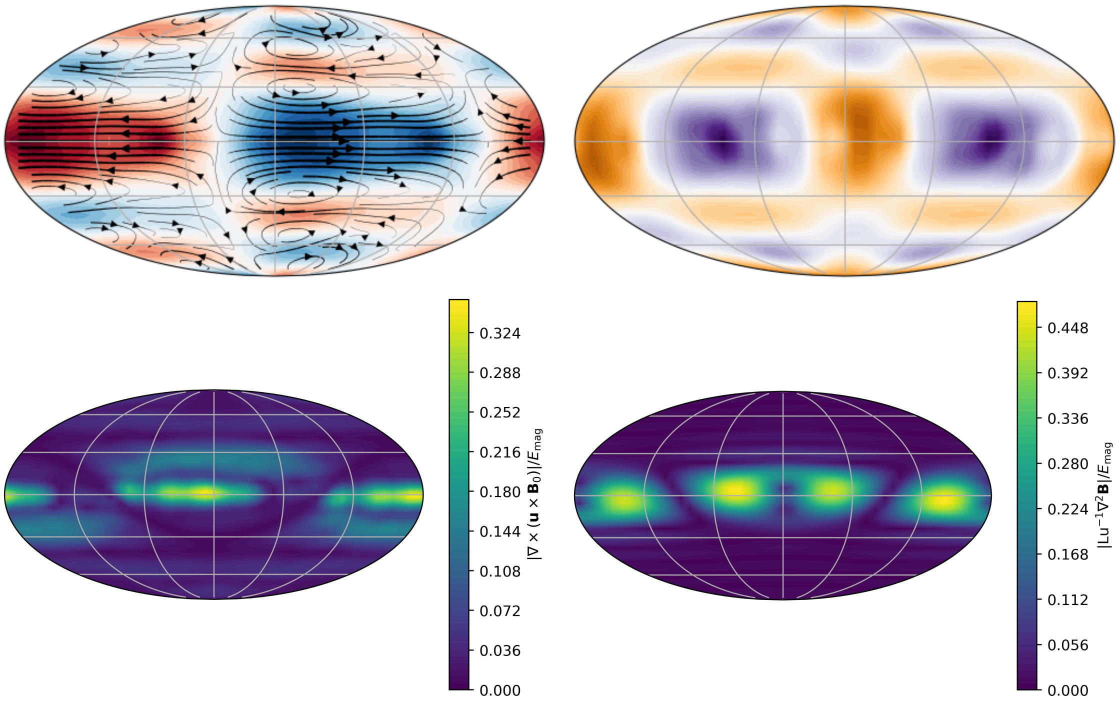

Figure 5.5: Analogous to Figure 5.3 for mode with $\omega = 0.07$, $Q = 26$, $T\,[\mathrm{yr}] = 380$.

is unclear, as they degenerate into the geostrophic mode for Lu → ∞. If they are physically relevant, they could possibly correspond to the QFD modes introduced by Schmitt (2012). As pointed out by Schmitt (2012) QFD modes accumulate in a region of similar frequencies and damping rates, as the damping is decreased (starting from a very large damping in his study). This could be supported by the cluster of modes in our spectrum. However, if the modes observed here correspond to QFD modes is unclear and needs to be investigated. Should it be the case, our results suggest that such modes can coexist with MCM in a diffusive core model, as initially pointed out by Schmitt (2012).

Whether or not these results are specific for the background magnetic field considered here, or are valid more generally, remains to be investigated. Strong toroidal magnetic fields near the boundary might influence modes more strongly. Also, a thorough study of the dependency of the modes as a function of Lu is needed.

Another interesting question are mode interaction in the presence of diffusion. If magnetic diffusion separates modes more strongly in the eigen solution space, mode interactions could be lowered. It is not clear that there is any influence on these interactions, as for example in the viscous diffusion case these interactions are also present (Triana et al., 2019) and maybe have been also observed in the presence of magnetic diffusion (Schmitt, 2012).

5.3 Towards an insulating magnetic field basis in the ellipsoid

The study of the radial magnetic field perturbations of QG MCM in the previous sections was initially motivated by a change in boundary conditions for the magnetic field for the investigation of torques. The net magnetic pressure torque is eliminated for an insulating magnetic field. The study of torques, however, requires a non-axisymmetric (or ellipsoidal in our context) volume. A magnetic field basis in a Cartesian expression that satisfies this condition in the ellipsoid was sought, but the dependency of the boundary condition on the spherical harmonic properties could not be lifted. Here, an attempt at transforming an insulating magnetic field basis in the sphere to the ellipsoid is presented.

We follow Ivers (2017) notation, namely $\mathbf{L} = a^{-1}\mathbf{1}_x\mathbf{1}_x + b^{-1}\mathbf{1}_y\mathbf{1}_y + c^{-1}\mathbf{1}_z\mathbf{1}_z$, $\mathring{\mathbf{r}} = \mathbf{L}\cdot\mathbf{r}$. Let us define the current density as a toroidal poloidal expansion

$$\mathbf{j} = \mathbf{L}^{-1}\cdot\mathring{\boldsymbol{\nabla}}\times\mathring{Q}\mathring{\mathbf{r}} + \mathbf{L}^{-1}\cdot\mathring{\boldsymbol{\nabla}}\times\mathring{\boldsymbol{\nabla}}\times\mathring{S}\mathring{\mathbf{r}}, \tag{5.4}$$

with $\mathring{Q} = \mathcal{P}(Q)$ and $\mathring{S} = \mathcal{P}(S)$ the Poincaré transformed toroidal and poloidal scalars from the sphere with $\mathcal{P}(f(x,y,z)) = f(x/a, y/b, z/c)$. This current density fulfills the boundary condition $\mathbf{j}\cdot\mathbf{n} = \mathbf{j}\cdot(\mathbf{L}\cdot\mathring{\mathbf{r}}) = 0$ on the ellipsoidal surface. We can define

$$\hat{\mathbf{B}} = \hat{\mathbf{L}}\cdot\mathring{\boldsymbol{\nabla}}\times\mathring{T}\mathring{\mathbf{r}} + \hat{\mathbf{L}}\cdot\mathring{\boldsymbol{\nabla}}\times\mathring{\boldsymbol{\nabla}}\times\mathring{P}\mathring{\mathbf{r}} + \hat{\mathbf{L}}\cdot\mathring{\nabla}\mathring{\Phi}_i, \tag{5.5}$$

with $\hat{\mathbf{L}} = abc\mathbf{L}$. Using $\boldsymbol{\nabla} \times \hat{\mathbf{L}} \cdot \mathbf{u} = \mathbf{L}^{-1}\mathring{\boldsymbol{\nabla}} \times \mathbf{u}$, we see that

$$\boldsymbol{\nabla} \times \hat{\mathbf{B}} = \mathbf{j}. \tag{5.6}$$

However, this field is not divergence free, $\boldsymbol{\nabla} \cdot \hat{\mathbf{B}} \neq 0$. We must therefore include a scalar potential, so that

$$\boldsymbol{\nabla} \cdot (\hat{\mathbf{L}} \cdot \mathring{\nabla}\phi_{p,t}) = -\boldsymbol{\nabla} \cdot \hat{\mathbf{B}}_{p,t}, \tag{5.7}$$

for both the poloidal part $\hat{\mathbf{B}}_p$ and the toroidal part $\hat{\mathbf{B}}_t$. There are some challenges that arise here, one being the fact that the integration over the surface of the ellipsoid can no longer be done analytically. So far, attempts to solve this have not been fruitful and most likely one has to make use of an ellipsoidal harmonic basis for $\phi_{p,t}$.

Chapter 6

Conclusions & Perspectives

In this thesis the pressure torque associated with torsional Alfvén modes (TM), as well as the geomagnetic field changes accompanied by Magneto-Coriolis modes (MCM) have been investigated. The main findings are summarized and a discussion on open questions is given.

Pressure torques on Earth's core-mantle boundary

The pressure torque linked to TM is found to be two orders of magnitudes below the value needed to explain the observed variations in LOD on Earth at the 6 yr period. Our study of TM in a full ellipsoid has revealed that previous estimates of the pressure have been too large. The pressure has been suggested to scale as $p \sim \rho\Omega u_0 R_0$ (Hide, 1969; Jault and Mouël, 1989). This dependence on Ω is lifted for TM, that only depend on the strength of the magnetic field, when the core volume does not have non-closed geostrophic contours. We have concluded that the pressure linked to TM should scale as $p \sim \rho u_0 u_A$, independent of the rotation rate Ω. This estimate is supported by the numerical values of the pressure torque obtained in our study.

TM observed in a strongly deformed ellipsoid remain pseudo-geostrophic as in the sphere, so that their motions follow the elliptical geostrophic contours (see Figure 5 in Section 4.1, Gerick et al., 2020). It has been shown by Ivers (2017), that in the inviscid and incompressible limit and in the case of the ellipsoid, the only flow component that can have a net angular momentum is the uniform vorticity component. We have confirmed this in our model, where the angular momentum of the modes is fully accounted for by exactly that component. This property once again highlights, that the pressure of pseudo-geostrophic motions, which includes the component of axial uniform vorticity, is not equal to the geostrophic pressure.

From the torque balance it is seen that the change in axial angular momentum must be balanced by the hydrodynamic or magnetic pressure torque in the inviscid limit. The magnetic pressure torque can be eliminated only when considering an insulating mantle. This is a very difficult task, as the boundary condition is applied globally not locally, as for example the non-penetration condition. In general, the insulating boundary condition has only been implemented to the spherical case, where the properties of spherical harmonics can be exploited. Being able to impose the insulating boundary condition in the ellipsoid remains a major challenge that most likely involves the use of ellipsoidal harmonics, for which no explicit expression exists (Niven, 1891).

The fact that the change in angular momentum is directly linked to a pressure torque raises the obvious question what the actual pressure field associated with the (in our case) QG flows is. This question is not easy to answer, as the pressure is eliminated from the equations that govern the QG flows. However, as discussed in Section 4.2, approaches that consider the energy equation or Lagrangian of the MHD system could lead to 2-D equations that carry a Lagrange multiplier akin a 2-D pressure term (see also Section 2.5). The relationship to the 3-D pressure is not obvious and needs to be investigated. Similarly, a comparison of the QG flow pressure to the pressure accompanied by tangentially geostrophic flows would be interesting, as this approximation has been used widely in the literature (e.g. Jault and Mouël, 1990; Fang et al., 1996; Buffett et al., 2009; Gillet et al., 2021). If one has access to the actual pressure linked to a QG flow, one could project the surface expression of the flow (Holdenried-Chernoff et al., 2020) on the tangential geostrophic basis to test how a tangential geostrophic pressure, that is easily obtained (Jault and Mouël, 1989), compares to a QG flow pressure.

The ellipsoid is the first step in introducing non-axisymmetry. It is unclear if a more complex geometry could increase the pressure torque associated with TM and an investigation is needed in the future, using the QG model in non-orthogonal coordinate systems. Due to the explicit dependency of the volume element in a more complex geometry, TM might have a stronger pressure torque, despite having closed geostrophic contours. Through non-closed geostrophic contours the dependency of the pressure on the rotation rate can be reintroduced. In this case, the geostrophic mode is replaced by an infinite number of Rossby waves, that now possess a mean circulation (Greenspan, 1968). These Rossby waves are not independent of the rotation rate and we can expect the same for the scaling of the pressure associated with them. Scenarios, where such non-closed geostrophic contours occur are simple to imagine. First, a spherical inner core within the non-spherical outer core creates non-closed contours at the tangent cylinder. This region is important for TM, that emerge exactly at this point (Gillet et al., 2017; Teed et al., 2019). Another possibility for non-closed geostrophic contours are troughs near the equatorial region. To investigate such volumes with non-closed contours is challenging and the approaches presented here are not able to rigorously introduce such domains. A new approach is needed to investigate this.

We have not considered the presence of a mean flow $\mathbf{u}_0$, that could be crucial for the pressure on the CMB (Jault, 2020). To impose such a mean flow consistently, one has to find an appropriate Taylor state for a given background magnetic field in the ellipsoid. So far, Taylor states have only been constructed for the spherical case (e.g. Livermore et al., 2008; Li et al., 2018; Hardy et al., 2018). An extension of the methods that were used to create these Taylor states to the ellipsoid is not obvious and requires some investigations.

In case the topographic coupling remains inefficient, even in the case of a present Taylor state, an insulating boundary or in the presence of non-closed geostrophic contours, another coupling mechanism is needed to transfer angular momentum from Earth's core to its mantle. Gravitational and electromagnetic coupling then remain the possible efficient couplings. For the latter a lowermost mantle that is more conducting than inferred from a simple extrapolation from above is needed (e.g. Gillet et al., 2010). Assuming that gravitational coupling is inefficient, changes in LOD on Earth could be related directly to the conductivity of the mantle, a quantity that is poorly constrained to date.

In our study we encountered so-called avoided crossings, where eigen frequencies approach each other, but never cross, when following them as a function of Lehnert number. Before and after these avoided crossings the eigen solutions exchange their properties. These numerical investigations as a function of Lehnert number are difficult to transfer to the actual physical system. One could imagine, e.g that locally the magnetic field strength of the core increases and changes the relevant Lehnert number accordingly. Then, two modes of similar frequency could exchange their properties. This phenomenon has been observed in other configurations of fluid modes (Rogister and Valette, 2009; Triana et al., 2019), but it remains unclear when these avoided crossings occur and what their physical significance is. The role of viscous or magnetic diffusion for such interactions is also uncertain. A proper investigation of the topic is necessary.

Fast Magneto-Coriolis modes and their geomagnetic field changes

In a spherical setup we investigated MCM and their radial magnetic field perturbation at the insulating CMB. To do so we used the same model as the one that has been introduced for the ellipsoidal problem, based on Cartesian polynomials, and introduced a 3-D magnetic field basis that satisfies the insulating boundary condition. It is found that MCM with frequencies on the order of the Alfvén wave frequency exist. They are characterized by a focusing of kinetic and magnetic energy in the equatorial region and have a westward phase velocity. These fast changes of periods of a few years could explain some of the inter-annual geomagnetic field changes observed on Earth (Gillet et al., 2019; Kloss and Finlay, 2019; Chi-Durán et al., 2020). Similar to the modes we calculate, these geomagnetic field observations have a strong amplitude near the equatorial and polar region, with the inferred core surface flows showing a focusing near the equatorial region as well.

Our results show that strong stratification near the core surface, previously suggested to be a requirement for non-zonal modes of frequencies of a few years (Knezek and Buffett, 2018; Buffett and Matsui, 2019), is not needed for MCM to exist at these fast frequencies.

Not all observed secular variations are explained by retrograde phase velocities, that all MCM in our model possess. Spatially steady secular variations could be explained by a superposition of multiple modes, but this needs to be tested. If there are background magnetic fields for which MCM show prograde phase velocities is an open question. Slow, slightly modified QG inertial modes could account for some of the eastward motions, but the slowest RM investigated here are evolving on periods of only a few month, much faster than the observed geomagnetic field changes. Also, the magnetic field perturbation associated with them is weak compared to their kinetic energy. At even larger polynomial degrees they could possess periods of a few years, but at small spatial scales an effect of viscous damping is possible. To include viscosity is a large effort, as the boundary conditions on the velocity have to be modified and the resolution of the boundary layer for Earth like parameters is computationally very expensive.

Previously, it has been assumed that MCM of spatial scales large enough so as not to be affected by diffusion, are on periods much larger than the Alfvén time (Braginsky, 1967; Bergman, 1993). Therefore, we have investigated the influence of diffusion on the MCM by calculating modes at a Lundquist number $\mathrm{Lu} = 10^5$, relevant for Earth's core. Diffusion was found to be insignificant for the fastest MCM, but a more thorough study on the dependency on the strength of the diffusion is needed. First results, introduced in Section 5.2, suggest that the quality factor of these modes is $\mathcal{O}(10^2)$, i.e. they can propagate for a few thousand years before being diffused (for $\mathrm{Le} = 10^4$). Other slow MCM of frequencies $\omega \gtrsim 10^{-2}$ have a quality factor $Q > 1$, making them also significant for secular variations on time scales of a few centuries. At even longer periods, approaching the diffusion time scale, modes with a very small quality factor are found. They could be quasi-free-decay modes (Schmitt, 2012), but further validation of this hypothesis is needed.

Whether or not the observed modes are in agreement with so-called QG Alfvén waves, observed in geodynamo simulations (Aubert et al., 2017), needs to be checked. These waves travel along strongly heterogeneous magnetic fields and are spawned by an uprising buoyant plume. Their small scale perturbation leads to a large scale magnetic field perturbation at the core surface, that has been linked to a fast change in geomagnetic secular acceleration (Aubert and Finlay, 2019).

The new model, with a QG velocity and a 3-D magnetic field of non-zero radial magnetic field at the CMB potentially allows to invert geomagnetic field observations to core flows and the magnetic field within the core. Core flow inversions based on geostrophic motions tangential to the CMB are only kinematically constrained, i.e. the core flow field does not depend on the magnetic field amplitude. Inversions that assimilate data from 3-D dynamo simulations are inverting for a prior that operates on parameters different to Earth's core conditions. Another inversion approach could be the assimilation of MHD modes within the core, at rotational and magnetic parameters expected for Earth's core conditions. The periods of TM and MCM depend on the mean magnetic field strength as B_0 and B_0^2, respectively. Then, admissible flow fields are constrained by the periods and magnetic field imprints of these modes. The implementation of this inversion approach is currently being conceptualized within the 4D-Earth-SWARM ESA project[1].

As in the case of the investigation of torques, a mean velocity field has been neglected. Considering a basic state that satisfies Taylor's constraint is possible and could be implemented in the future.

A more technical improvement could be the consideration of an orthonormal basis for the QG model and the magnetic field. Such bases for the magnetic field have been proposed in the literature (Chen et al., 2018; Li et al., 2018). For the QG velocities this has to be developed, but analytical expressions of the orthogonal QG inertial modes already exist in polar coordinates (Maffei et al., 2017) and an extension should be possible. Then, the generalized eigen problem transforms into a standard eigen problem, significantly simplifying the calculation of modes.

---

[1] `https://4d-earth-swarm.univ-grenoble-alpes.fr/`

Appendix A

Tensor calculus

We mostly follow the standard conventions also followed by Aris (1989), e.g. index summation. One difference to Aris (1989) is the notation of the Christoffel symbols, here Γ^i_{jk}.
We express the Cartesian coordinates

$$\mathbf{r} = (x, y, z) = (x(\mathbf{q}), y(\mathbf{q}), z(\mathbf{q})), \tag{A.1}$$

in terms of new coordinates $\mathbf{q} = (q^1, q^2, q^3)$. The covariant base vectors for the new system are given by

$$\mathbf{g}_i = \frac{\partial \mathbf{r}}{\partial q^i}, \tag{A.2}$$

which, in general, are not orthogonal. The metric tensor is given as

$$\mathbf{G} = g_{ij} = \mathbf{g}_i \cdot \mathbf{g}_j, \tag{A.3}$$

which is diagonal in the orthogonal case. The covariant base vectors define the volume element

$$\gamma = \mathbf{g}_1 \cdot (\mathbf{g}_2 \times \mathbf{g}_3), \tag{A.4}$$

with $\gamma^2 = \det \mathbf{G} = g$.
The contravariant base vectors, being normal vectors to the surfaces of constant coordinate q_i, are

$$\mathbf{g}^i = \frac{1}{\gamma} \mathbf{g}_j \times \mathbf{g}_k, \tag{A.5}$$

with ijk being even permutations of 123. It is also called reciprocal basis, with the property $\mathbf{g}^i \cdot \mathbf{g}_j = \delta_{ij}$. Similar to the covariant basis the contravariant base vectors define the conjugate metric tensor

$$\mathbf{G}^{-1} = g^{ij} = \mathbf{g}^i \cdot \mathbf{g}^j. \tag{A.6}$$

A vector $\mathbf{u}$ can be expressed in both the covariant and the contravariant basis by

$$\mathbf{u} = u^i \mathbf{g}_i = u_i \mathbf{g}^i, \tag{A.7}$$

where u^i and u_i are called the contravariant and covariant components of a vector, respectively.
The dot product is given by

$$\mathbf{u} \cdot \mathbf{v} = g_{ij} u^i v^j = g^{ij} u_i v_j, \tag{A.8}$$

and the cross product by

$$\mathbf{u} \times \mathbf{v} = g^{-1/2} \epsilon^{ijk} u_j v_k = g^{1/2} \epsilon_{ijk} u^j v^k, \tag{A.9}$$

where $\epsilon_{ijk} = \epsilon^{ijk}$ is the well known Levi-Cevita symbol, which is 0 when any two of ijk equal each other, 1 for even permutations of $ijk = 123$ and -1 for odd permutations.
The gradient of a scalar $\psi = \psi(\mathbf{q})$ is simply

$$\nabla \psi = \frac{\partial \psi}{\partial q^i} \mathbf{g}^i, \tag{A.10}$$

and the Laplacian is given by

$$\nabla^2 \psi = \frac{1}{\gamma} \frac{\partial}{\partial q^j} \left(\gamma g^{ij} \frac{\partial \psi}{\partial q^i} \right). \tag{A.11}$$

The divergence of a vector $\mathbf{u}$ is given by

$$\nabla \cdot \mathbf{u} = \frac{1}{\gamma} \frac{\partial}{\partial q^i} \left(\gamma u^i \right) = \frac{1}{\gamma} \frac{\partial}{\partial q^i} \left(\gamma g^{ij} u_i \right), \tag{A.12}$$

and its curl is

$$\nabla \times \mathbf{u} = g^{-1/2} \epsilon^{ijk} u_{k,j} = g^{-1/2} \epsilon_{ijk} g_{kp} u^p_{,j}, \tag{A.13}$$

where we use the differentiation of the covariant vector components

$$u_{k,j} = \frac{\partial u_k}{\partial q^j} - \Gamma^i_{kj} u_i, \tag{A.14}$$

or the differentiation of the contravariant vector components

$$u^p_{,j} = \frac{\partial u^p}{\partial q^j} + \Gamma^p_{ij} u^i, \tag{A.15}$$

with the Christoffel symbols

$$\Gamma^i_{jk} = \frac{g^{ip}}{2} \left(\frac{\partial g_{pj}}{\partial q^k} + \frac{\partial g_{pk}}{\partial q^j} - \frac{\partial g_{jk}}{\partial q^p} \right). \tag{A.16}$$

Bibliography

Abarca del Rio, R., Gambis, D., and Salstein, D. A. Interannual signals in length of day and atmospheric angular momentum. *Annales Geophysicae*, 18(3):347–364, 2000, doi: 10.1007/s00585-000-0347-9. 13

Acheson, D. J. On the hydromagnetic stability of a rotating fluid annulus. *Journal of Fluid Mechanics*, 52(3):529–541, 1972, doi: 10.1017/S0022112072001570. 59

Acheson, D. J. and Hide, R. Hydromagnetics of rotating fluids. *Reports on Progress in Physics*, 36(2):159–221, 1973, doi: 10.1088/0034-4885/36/2/002. 52

Alfvén, H. Existence of Electromagnetic-Hydrodynamic Waves. *Nature*, 150(3805):405–406, 1942, doi: 10.1038/150405d0. 10

Amit, H. and Christensen, U. R. Accounting for magnetic diffusion in core flow inversions from geomagnetic secular variation. *Geophysical Journal International*, 175(3):913–924, 2008, doi: 10.1111/j.1365-246X.2008.03948.x. 19

Anderson, E., Bai, Z., Bischof, C., Blackford, S., Demmel, J., Dongarra, J., Du Croz, J., Greenbaum, A., Hammarling, S., McKenney, A., and Sorensen, D. *LAPACK Users' Guide*. Society for Industrial and Applied Mathematics, third edition, 1999, doi: 10.1137/1.9780898719604. 60

Aris, R. *Vectors, tensors and the basis equations of fluids mechanics*. Dover, 1989. 118

Aubert, J. Flow throughout the Earth's core inverted from geomagnetic observations and numerical dynamo models. *Geophysical Journal International*, 192(2):537–556, 2013, doi: 10.1093/gji/ggs051. 19

Aubert, J. Earth's core internal dynamics 1840–2010 imaged by inverse geodynamo modelling. *Geophysical Journal International*, 197(3):1321–1334, 2014, doi: 10.1093/gji/ggu064. 19

Aubert, J. and Finlay, C. C. Geomagnetic jerks and rapid hydromagnetic waves focusing at Earth's core surface. *Nature Geoscience*, page 1, 2019, doi: 10.1038/s41561-019-0355-1. 2, 11, 116

Aubert, J., Gillet, N., and Cardin, P. Quasigeostrophic models of convection in rotating spherical shells. *Geochemistry, Geophysics, Geosystems*, 4(7), 2003, doi: 10.1029/2002GC000456. 20, 25

Aubert, J., Gastine, T., and Fournier, A. Spherical convective dynamos in the rapidly rotating asymptotic regime. *Journal of Fluid Mechanics*, 813:558–593, 2017, doi: 10.1017/jfm.2016.789. 11, 116

Backus, G. Kinematics of geomagnetic secular variation in a perfectly conducting core. *Philosophical Transactions of the Royal Society of London. Series A, Mathematical and Physical Sciences*, 263(1141):239–266, 1968, doi: 10.1098/rsta.1968.0014. 1, 19

Backus, G. and Rieutord, M. Completeness of inertial modes of an incompressible inviscid fluid in a corotating ellipsoid. *Physical Review E*, 95(5):053116, 2017, doi: 10.1103/PhysRevE.95.053116. 38, 48

Backus, G., Parker, R., and Constable, C. *Foundations of Geomagnetism*. Cambridge University Press, 1996. 6

Backus, G. E. Application of mantle filter theory to the magnetic jerk of 1969. *Geophysical Journal International*, 74(3):713–746, 1983, doi: 10.1111/j.1365-246X.1983.tb01901.x. 18

Backus, G. E. and Le Mouël, J.-L. The region on the core—mantle boundary where a geostrophic velocity field can be determined from frozen-flux magnetic data. *Geophysical Journal International*, 85(3):617–628, 1986, doi: 10.1111/j.1365-246X.1986.tb04536.x. 19

Badro, J., Aubert, J., Hirose, K., Nomura, R., Blanchard, I., Borensztajn, S., and Siebert, J. Magnesium Partitioning Between Earth's Mantle and Core and its Potential to Drive an Early Exsolution Geodynamo. *Geophysical Research Letters*, 45(24):13,240–13,248, 2018, doi: 10.1029/2018GL080405. 5

Bardsley, O. P. Could hydrodynamic Rossby waves explain the westward drift? *Proceedings of the Royal Society A: Mathematical, Physical and Engineering Science*, 474(2213), 2018, doi: 10.1098/rspa.2018.0119. 18, 24, 50

Barrois, O., Gillet, N., and Aubert, J. Contributions to the geomagnetic secular variation from a reanalysis of core surface dynamics. *Geophysical Journal International*, 211(1): 50–68, 2017, doi: 10.1093/gji/ggx280. 19

Barrois, O., Hammer, M. D., Finlay, C. C., Martin, Y., and Gillet, N. Assimilation of ground and satellite magnetic measurements: inference of core surface magnetic and velocity field changes. *Geophysical Journal International*, 215(1):695–712, 2018, doi: 10.1093/gji/ggy297. 19

Baumjohann, W. and Nakamura, R. 5.03 - Magnetospheric Contributions to the Terrestrial Magnetic Field. In Schubert, G., editor, *Treatise on Geophysics (Second Edition)*, pages 79–90. Elsevier, 2007, doi: 10.1016/B978-0-444-53802-4.00097-X. 18

Bell, P. I. and Soward, A. M. The influence of surface topography on rotating convection. *Journal of Fluid Mechanics*, 313:147–180, 1996, doi: 10.1017/S0022112096002169. 36

Bercovici, D. 7.01 - Mantle Dynamics: An Introduction and Overview. In Schubert, G., editor, *Treatise on Geophysics (Second Edition)*, pages 1–22. Elsevier, 2015, doi: 10.1016/B978-0-444-53802-4.00125-1. 6

Bergman, M. I. Magnetic Rossby waves in a stably stratified layer near the surface of the Earth's outer core. *Geophysical & Astrophysical Fluid Dynamics*, 68(1-4):151–176, 1993, doi: 10.1080/03091929308203566. 106, 116

Bezanson, J., Edelman, A., Karpinski, S., and Shah, V. B. Julia: A Fresh Approach to Numerical Computing. *SIAM Review*, 59(1):65–98, 2017, doi: 10.1137/141000671. 62

Biggin, A. J., Piispa, E. J., Pesonen, L. J., Holme, R., Paterson, G. A., Veikkolainen, T., and Tauxe, L. Palaeomagnetic field intensity variations suggest Mesoproterozoic inner-core nucleation. *Nature*, 526(7572):245–248, 2015, doi: 10.1038/nature15523. 5

Braginsky, S. I. Magnetohydrodynamics of the Earth's core. *Geomagnetism and Aeronomy*, 4:698–712, 1964. 55

Braginsky, S. I. Magnetic waves in the Earth's core. *Geomagnetism and Aeronomy*, 7: 851–859, 1967. 55, 116

Braginsky, S. I. Torsional magnetohydrodynamics vibrations in the Earth's core and variations in day length. *Geomagnetism and Aeronomy*, 10:3–12, 1970. 2, 46, 56, 57, 59

Braginsky, S. I. MAC-Oscillations of the Hidden Ocean of the Core. *Journal of geomagnetism and geoelectricity*, 45(11-12):1517–1538, 1993, doi: 10.5636/jgg.45.1517. 5

Braginsky, S. I. Magnetic Rossby waves in the stratified ocean of the core, and topographic core-mantle coupling. *Earth, Planets and Space*, 50(8):641–649, 1998, doi: 10.1186/BF03352159. 17

Brons, J. A., Thomas, P. J., and Pothérat, A. Transition between advection and inertial wave propagation in rotating turbulence. *Journal of Fluid Mechanics*, 886, 2020, doi: 10.1017/jfm.2019.1051. 48

Bryan, G. H. and Darwin, G. H. VI. The waves on a rotating liquid spheroid of finite ellipticity. *Philosophical Transactions of the Royal Society of London. Series A, Mathematical and Physical Sciences*, 180:187–219, 1889, doi: 10.1098/rsta.1889.0006. 46, 47

Buffett, B. Geomagnetic fluctuations reveal stable stratification at the top of the Earth's core. *Nature*, 507(7493):484–487, 2014, doi: 10.1038/nature13122. 2, 59

Buffett, B. and Matsui, H. Equatorially trapped waves in Earth's core. *Geophysical Journal International*, 218(2):1210–1225, 2019, doi: 10.1093/gji/ggz233. 2, 106, 116

Buffett, B. A. Constraints on magnetic energy and mantle conductivity from the forced nutations of the Earth. *Journal of Geophysical Research: Solid Earth*, 97(B13):19581–19597, 1992, doi: 10.1029/92JB00977. 17

Buffett, B. A. Gravitational oscillations in the length of day. *Geophysical Research Letters*, 23(17):2279–2282, 1996a, doi: 10.1029/96GL02083. 16

Buffett, B. A. A mechanism for decade fluctuations in the length of day. *Geophysical Research Letters*, 23(25):3803–3806, 1996b, doi: 10.1029/96GL03571. 16

Buffett, B. A. and Christensen, U. R. Magnetic and viscous coupling at the core—mantle boundary: inferences from observations of the Earth's nutations. *Geophysical Journal International*, 171(1):145–152, 2007, doi: 10.1111/j.1365-246X.2007.03543.x. 17

Buffett, B. A., Mound, J., and Jackson, A. Inversion of torsional oscillations for the structure and dynamics of Earth's core. *Geophysical Journal International*, 177(3):878–890, 2009, doi: 10.1111/j.1365-246X.2009.04129.x. 59, 114

Bullard, E. C., Freedman, C., Gellman, H., and Nixon, J. The westward drift of the Earth's magnetic field. *Philosophical Transactions of the Royal Society of London. Series A, Mathematical and Physical Sciences*, 243(859):67–92, 1950, doi: 10.1098/rsta.1950.0014. 3, 16, 18

Burmann, F. and Noir, J. Effects of bottom topography on the spin-up in a cylinder. *Physics of Fluids*, 30(10):106601, 2018, doi: 10.1063/1.5051111. 48

Busse, F. H. Thermal instabilities in rapidly rotating systems. *Journal of Fluid Mechanics*, 44(3):441–460, 1970, doi: 10.1017/S0022112070001921. 11, 20, 21

Busse, F. H. A Model of the Geodynamo. *Geophysical Journal International*, 42(2):437–459, 1975, doi: 10.1111/j.1365-246X.1975.tb05871.x. 21

Calkins, M. A. Quasi-geostrophic dynamo theory. *Physics of the Earth and Planetary Interiors*, 276:182–189, 2018, doi: 10.1016/j.pepi.2017.05.001. 11

Calkins, M. A., Noir, J., Eldredge, J. D., and Aurnou, J. M. The effects of boundary topography on convection in Earth's core. *Geophysical Journal International*, 189(2): 799–814, 2012, doi: 10.1111/j.1365-246X.2012.05415.x. 36

Calkins, M. A., Julien, K., Tobias, S. M., and Aurnou, J. M. A multiscale dynamo model driven by quasi-geostrophic convection. *Journal of Fluid Mechanics*, 780:143–166, 2015, doi: 10.1017/jfm.2015.464. 11

Canet, E., Fournier, A., and Jault, D. Forward and adjoint quasi-geostrophic models of the geomagnetic secular variation. *Journal of Geophysical Research: Solid Earth*, 114(B11), 2009, doi: 10.1029/2008JB006189. 20, 35

Canet, E., Finlay, C. C., and Fournier, A. Hydromagnetic quasi-geostrophic modes in rapidly rotating planetary cores. *Physics of the Earth and Planetary Interiors*, 229:1–15, 2014, doi: 10.1016/j.pepi.2013.12.006. 11, 20, 25, 35, 50

Charney, J. G. On the Scale of Atmospheric Motions. *Geofysiske Publikasjoner*, 17(2), 1948, doi: 10.1007/978-1-944970-35-2_14. 11, 20

Chen, L., Herreman, W., Li, K., Livermore, P. W., Luo, J. W., and Jackson, A. The optimal kinematic dynamo driven by steady flows in a sphere. *Journal of Fluid Mechanics*, 839: 1–32, 2018, doi: 10.1017/jfm.2017.924. 117

Cheng, J. S. and Aurnou, J. M. Tests of diffusion-free scaling behaviors in numerical dynamo datasets. *Earth and Planetary Science Letters*, 436:121–129, 2016, doi: 10.1016/j.epsl.2015.12.004. 11

Chi-Durán, R., Avery, M. S., Knezek, N., and Buffett, B. A. Decomposition of Geomagnetic Secular Acceleration Into Traveling Waves Using Complex Empirical Orthogonal Functions. *Geophysical Research Letters*, 47(17):e2020GL087940, 2020, doi: 10.1029/2020GL087940. 18, 115

Christensen, U. R., Aubert, J., and Hulot, G. Conditions for Earth-like geodynamo models. *Earth and Planetary Science Letters*, 296(3):487–496, 2010, doi: 10.1016/j.epsl.2010.06.009. 11

Chulliat, A., Alken, P., and Maus, S. Fast equatorial waves propagating at the top of the Earth's core. *Geophysical Research Letters*, 42(9):3321–3329, 2015, doi: 10.1002/2015GL064067. 18, 60

Courtillot, V., Ducruix, J., and Le Mouël, J. L. Inverse methods applied to continuation problems in geophysics. In Sabatier, P. C., editor, *Applied Inverse Problems*, Lecture Notes in Physics, pages 48–82. Springer, 1978, doi: 10.1007/3-540-09094-0_72. 1, 18

Cui, Z., Zhang, K., and Liao, X. On the completeness of inertial wave modes in rotating annular channels. *Geophysical & Astrophysical Fluid Dynamics*, 108(1):44–59, 2014, doi: 10.1080/03091929.2013.821117. 48

Davidson, P. A. *Turbulence in Rotating, Stratified and Electrically Conducting Fluids*. Cambridge University Press, 2013, doi: 10.1017/CBO9781139208673. 4

Davidson, P. A. *Introduction to Magnetohydrodynamics*. Cambridge University Press, 2016, doi: 10.1017/9781316672853. 15

Davis, T. A. Algorithm 832: UMFPACK V4.3—an unsymmetric-pattern multifrontal method. *ACM Transactions on Mathematical Software*, 30(2):196–199, 2004, doi: 10.1145/992200.992206. 61

Deguen, R. Structure and dynamics of Earth's inner core. *Earth and Planetary Science Letters*, 333-334:211–225, 2012, doi: 10.1016/j.epsl.2012.04.038. 16

Dehant, V. and Mathews, P. M. Information About the Core from Earth Nutation. In *Earth's Core: Dynamics, Structure, Rotation*, pages 263–277. American Geophysical Union (AGU), 2013, doi: 10.1029/GD031p0263. 6

Dehant, V., Laguerre, R., Rekier, J., Rivoldini, A., Triana, S. A., Trinh, A., Van Hoolst, T., and Zhu, P. Understanding the effects of the core on the nutation of the Earth. *Geodesy and Geodynamics*, 8(6):389–395, 2017, doi: 10.1016/j.geog.2017.04.005. 2

Dellar, P. J. Dispersive shallow water magnetohydrodynamics. *Physics of Plasmas*, 10(3): 581–590, 2003, doi: 10.1063/1.1537690. 30

Dellar, P. J. Quasi-two-dimensional liquid-metal magnetohydrodynamics and the anticipated vorticity method. *Journal of Fluid Mechanics*, 515:197–232, 2004, doi: 10.1017/S0022112004000217. 30

Dellar, P. J. Variations on a beta-plane: derivation of non-traditional beta-plane equations from Hamilton's principle on a sphere. *Journal of Fluid Mechanics*, 674:174–195, 2011, doi: 10.1017/S0022112010006464. 31

Dellar, P. J. and Salmon, R. Shallow water equations with a complete Coriolis force and topography. *Physics of Fluids*, 17(10):106601, 2005, doi: 10.1063/1.2116747. 31

Ding, H. and Chao, B. F. A 6-year westward rotary motion in the Earth: Detection and possible MICG coupling mechanism. *Earth and Planetary Science Letters*, 495:50–55, 2018, doi: 10.1016/J.EPSL.2018.05.009. 16

Duan, P. and Huang, C. Intradecadal variations in length of day and their correspondence with geomagnetic jerks. *Nature Communications*, 11(1):2273, 2020a, doi: 10.1038/s41467-020-16109-8. 13

Duan, P. and Huang, C. On the Mantle-Inner Core Gravitational Oscillation Under the Action of the Electromagnetic Coupling Effects. *Journal of Geophysical Research: Solid Earth*, 125(2):e2019JB018863, 2020b, doi: 10.1029/2019JB018863. 16

Dumberry, M. and Bloxham, J. Azimuthal flows in the Earth's core and changes in length of day at millennial timescales. *Geophysical Journal International*, 165(1):32–46, 2006, doi: 10.1111/j.1365-246X.2006.02903.x. 12

Dumberry, M. and More, C. Weak magnetic field changes over the Pacific due to high conductance in lowermost mantle. *Nature Geoscience*, 13(7):516–520, 2020, doi: 10.1038/s41561-020-0589-y. 17

Dumberry, M. and Mound, J. E. Constraints on core-mantle electromagnetic coupling from torsional oscillation normal modes. *Journal of Geophysical Research: Solid Earth*, 113 (B3), 2008, doi: 10.1029/2007JB005135. 17

Durran, D. R. *Numerical Methods for Wave Equations in Geophysical Fluid Dynamics*. Number 32 in Texts in Applied Mathematics. Springer Science & Business Media, 2013, doi: 10.1007/978-1-4757-3081-4. 37, 43, 60

Dziewonski, A. M. and Anderson, D. L. Preliminary reference Earth model. *Physics of the Earth and Planetary Interiors*, 25(4):297–356, 1981, doi: 10.1016/0031-9201(81)90046-7. 4

Ekman, V. W. On the influence of the earth's rotation on ocean-currents. *Arkiv för matematik, astronomi och fysik*, 2(11), 1905. 10

Elsasser, W. M. Induction Effects in Terrestrial Magnetism Part I. Theory. *Physical Review*, 69(3-4):106–116, 1946, doi: 10.1103/PhysRev.69.106. 5

Fang, M., Hager, B. H., and Herring, T. A. Surface deformation caused by pressure changes in the fluid core. *Geophysical Research Letters*, 23(12):1493–1496, 1996, doi: 10.1029/96GL00743. 114

Fearn, D. R. and Loper, D. E. Compositional convection and stratification of Earth's core. *Nature*, 289(5796):393–394, 1981, doi: 10.1038/289393a0. 5

Finlay, C. Magnetohydrodynamic Waves. In Gubbins, D. and Herrero-Bervera, E., editors, *Encyclopedia of Geomagnetism and Paleomagnetism*, pages 632–639. Springer Netherlands, 2007, doi: 10.1007/978-1-4020-4423-6_202. 55

Finlay, C. C. Course 8 Waves in the presence of magnetic fields, rotation and convection. In Cardin, P. and Cugliandolo, L. F., editors, *Les Houches*, volume 88 of *Dynamos*, pages 403–450. Elsevier, 2008, doi: 10.1016/S0924-8099(08)80012-1. 46

Finlay, C. C. and Jackson, A. Equatorially Dominated Magnetic Field Change at the Surface of Earth's Core. *Science*, 300(5628):2084–2086, 2003, doi: 10.1126/science.1083324. 2, 60

Finlay, C. C., Dumberry, M., Chulliat, A., and Pais, M. A. Short Timescale Core Dynamics: Theory and Observations. *Space Science Reviews*, 155(1):177–218, 2010, doi: 10.1007/s11214-010-9691-6. 59

Finlay, C. C., Kloss, C., Olsen, N., Hammer, M. D., Tøffner-Clausen, L., Grayver, A., and Kuvshinov, A. The CHAOS-7 geomagnetic field model and observed changes in the South Atlantic Anomaly. *Earth, Planets and Space*, 72(1):156, 2020, doi: 10.1186/s40623-020-01252-9. 1

Fornberg, B. Generation of finite difference formulas on arbitrarily spaced grids. *Mathematics of Computation*, 51(184):699–706, 1988, doi: 10.1090/S0025-5718-1988-0935077-0. 42

Forte, A. M. and Peltier, W. R. Core-mantle boundary topography and whole-mantle convection. *Geophysical Research Letters*, 16(7):621–624, 1989, doi: 10.1029/GL016i007p00621. 6

Forte, A. M., Mitrovica, J. X., and Woodward, R. L. Seismic-geodynamic determination of the origin of excess ellipticity of the core-mantle boundary. *Geophysical Research Letters*, 22(9):1013–1016, 1995, doi: 10.1029/95GL01065. 6

Fourier, J.-B.-J. *Théorie analytique de la chaleur.* F. Didot, 1822. 43

Fournier, A., Hulot, G., Jault, D., Kuang, W., Tangborn, A., Gillet, N., Canet, E., Aubert, J., and Lhuillier, F. An Introduction to Data Assimilation and Predictability in Geomagnetism. *Space Science Reviews*, 155(1):247–291, 2010, doi: 10.1007/s11214-010-9669-4. 19

Frigo, M. and Johnson, S. The Design and Implementation of FFTW3. *Proceedings of the IEEE*, 93(2):216–231, 2005, doi: 10.1109/JPROC.2004.840301. 43

Fultz, D. A note on overstability and the elastoid–inertia oscillations of Kelvin, Solberg and Bjerknes. *Journal of Meteorology*, 16(2):199–208, 1959, doi: 10.1175/1520-0469(1959)016<0199:ANOOAT>2.0.CO;2. 46

Galtier, S. Weak inertial-wave turbulence theory. *Physical Review E*, 68(1):015301, 2003, doi: 10.1103/PhysRevE.68.015301. 48

Gans, R. F. On hydromagnetic oscillations in a rotating cavity. *Journal of Fluid Mechanics*, 50(3):449–467, 1971, doi: 10.1017/S0022112071002696. 56

Gastine, T. pizza: an open-source pseudo-spectral code for spherical quasi-geostrophic convection. *Geophysical Journal International*, 217(3):1558–1576, 2019, doi: 10.1093/gji/ggz103. 2, 20, 30

Gerick, F., Jault, D., Noir, J., and Vidal, J. Pressure torque of torsional Alfvén modes acting on an ellipsoidal mantle. *Geophysical Journal International*, 222(1):338–351, 2020, doi: 10.1093/gji/ggaa166. 28, 35, 38, 40, 41, 58, 61, 65, 80, 113

Gerick, F., Jault, D., and Noir, J. Fast Quasi-Geostrophic Magneto-Coriolis Modes in the Earth's Core. *Geophysical Research Letters*, 48(4):e2020GL090803, 2021, doi: 10.1029/2020GL090803. 38, 83, 107, 108, 109

Gillet, N., Jault, D., Canet, E., and Fournier, A. Fast torsional waves and strong magnetic field within the Earth's core. *Nature*, 465(7294):74–77, 2010, doi: 10.1038/nature09010. 3, 10, 13, 17, 59, 115

Gillet, N., Schaeffer, N., and Jault, D. Rationale and geophysical evidence for quasi-geostrophic rapid dynamics within the Earth's outer core. *Physics of the Earth and Planetary Interiors*, 187(3):380–390, 2011, doi: 10.1016/j.pepi.2011.01.005. 2, 20

Gillet, N., Jault, D., Finlay, C. C., and Olsen, N. Stochastic modeling of the Earth's magnetic field: Inversion for covariances over the observatory era. *Geochemistry, Geophysics, Geosystems*, 14(4):766–786, 2013, doi: 10.1002/ggge.20041. 18

Gillet, N., Jault, D., and Finlay, C. C. Planetary gyre, time-dependent eddies, torsional waves, and equatorial jets at the Earth's core surface. *Journal of Geophysical Research: Solid Earth*, 120(6):3991–4013, 2015, doi: 10.1002/2014JB011786. 13, 16

Gillet, N., Jault, D., and Canet, E. Excitation of travelling torsional normal modes in an Earth's core model. *Geophysical Journal International*, 210(3):1503–1516, 2017, doi: 10.1093/gji/ggx237. 59, 114

Gillet, N., Huder, L., and Aubert, J. A reduced stochastic model of core surface dynamics based on geodynamo simulations. *Geophysical Journal International*, 219(1):522–539, 2019, doi: 10.1093/gji/ggz313. 18, 115

Gillet, N., Dumberry, M., and Rosat, S. The limited contribution from outer core dynamics to global deformations at the Earth's surface. *Geophysical Journal International*, 224(1): 216–229, 2021, doi: 10.1093/gji/ggaa448. 114

Gire, C. and Le Mouël, J.-L. Tangentially geostrophic flow at the core-mantle boundary compatible with the observed geomagnetic secular variation: the large-scale component of the flow. *Physics of the Earth and Planetary Interiors*, 59(4):259–287, 1990, doi: 10.1016/0031-9201(90)90234-O. 1, 19

Glane, S. and Buffett, B. Enhanced Core-Mantle Coupling Due to Stratification at the Top of the Core. *Frontiers in Earth Science*, 6:171, 2018, doi: 10.3389/feart.2018.00171. 17

Glatzmaier, G. A. and Coe, R. S. 8.11 - Magnetic Polarity Reversals in the Core. In Schubert, G., editor, *Treatise on Geophysics (Second Edition)*, pages 279–295. Elsevier, 2015, doi: 10.1016/B978-0-444-53802-4.00146-9. 18

Glatzmaiers, G. A. and Roberts, P. H. A three-dimensional self-consistent computer simulation of a geomagnetic field reversal. *Nature*, 377(6546):203–209, 1995, doi: 10.1038/377203a0. 5

Green, A. E. and Naghdi, P. M. A derivation of equations for wave propagation in water of variable depth. *Journal of Fluid Mechanics*, 78(2):237–246, 1976, doi: 10.1017/S0022112076002425. 27

Greenspan, H. P. *The theory of rotating fluids.* Cambridge University Press, 1968. 2, 6, 47, 48, 114

Gross, R. S. 3.09 - Earth Rotation Variations – Long Period. In Schubert, G., editor, *Treatise on Geophysics (Second Edition)*, pages 215–261. Elsevier, 2015, doi: 10.1016/B978-0-444-53802-4.00059-2. 4, 12

Gross, R. S., Fukumori, I., and Menemenlis, D. Atmospheric and oceanic excitation of the Earth's wobbles during 1980–2000. *Journal of Geophysical Research: Solid Earth*, 108 (B8), 2003, doi: 10.1029/2002JB002143. 13

Guervilly, C., Cardin, P., and Schaeffer, N. Turbulent convective length scale in planetary cores. *Nature*, 570(7761):368–371, 2019, doi: 10.1038/s41586-019-1301-5. 2

Hager, B. H., Clayton, R. W., Richards, M. A., Comer, R. P., and Dziewonski, A. M. Lower mantle heterogeneity, dynamic topography and the geoid. *Nature*, 313(6003):541–545, 1985, doi: 10.1038/313541a0. 6

Halley, E. An account of the cause of the change of the variation of the magnetical needle. with an hypothesis of the structure of the internal parts of the earth: as it was proposed to the Royal Society in one of their late meetings. *Philosophical Transactions of the Royal Society of London*, 17(195):563–578, 1692, doi: 10.1098/rstl.1686.0107. 18

Hardy, C. M. and Wong, J. Stably stratified layers within Earth's core. *Astronomy & Geophysics*, 60(3):3.30–3.35, 2019, doi: 10.1093/astrogeo/atz148. 5

Hardy, C. M., Livermore, P. W., Niesen, J., Luo, J., and Li, K. Determination of the instantaneous geostrophic flow within the three-dimensional magnetostrophic regime. *Proceedings of the Royal Society A: Mathematical, Physical and Engineering Sciences*, 474(2218):20180412, 2018, doi: 10.1098/rspa.2018.0412. 56, 115

Hernandez, V., Roman, J. E., and Vidal, V. SLEPc: A scalable and flexible toolkit for the solution of eigenvalue problems. *ACM Transactions on Mathematical Software*, 31(3): 351–362, 2005, doi: 10.1145/1089014.1089019. 61

Hernandez, V., Román, J., Tomas, A., and Vidal, V. Krylov-Schur Methods in SLEPc, 2015. URL `https://slepc.upv.es/documentation/reports/str7.pdf`. 61

Hernández, V., Román, J., Tomas, A., and Vidal, V. Arnoldi Methods in SLEPc, 2007. URL `https://slepc.upv.es/documentation/reports/str4.pdf`. 61

Herrmann, J. and Busse, F. H. Stationary and time dependent convection in the rotating cylindrical annulus with modulated height. *Physics of Fluids*, 10(7):1611–1620, 1998, doi: 10.1063/1.869680. 36

Heyn, B. H., Conrad, C. P., and Trønnes, R. G. Core-mantle boundary topography and its relation to the viscosity structure of the lowermost mantle. *Earth and Planetary Science Letters*, 543:116358, 2020, doi: 10.1016/j.epsl.2020.116358. 6

Hide, R. Free hydromagnetic oscillations of the Earth's core and the theory of the geomagnetic secular variation. *Philosophical Transactions of the Royal Society of London. Series A, Mathematical, Physical and Engineering Sciences*, 259(1107):615–647, 1966, doi: 10.1098/rsta.1966.0026. 2, 20, 46, 52, 59

Hide, R. Interaction between the Earth's Liquid Core and Solid Mantle. *Nature*, 222(5198): 1055–1056, 1969, doi: 10.1038/2221055a0. 3, 17, 113

Hide, R. Fluctuations in the Earth's rotation and the topography of the core-mantle interface. *Philosophical Transactions of the Royal Society of London. Series A, Mathematical and Physical Sciences*, 328(1599):351–363, 1989, doi: 10.1098/rsta.1989.0040. 15

Hide, R. and Roberts, P. H. The origin of the main geomagnetic field. *Physics and Chemistry of the Earth*, 4:27–98, 1961, doi: 10.1016/0079-1946(61)90003-9. 59

Hide, R. and Weightman, J. A. Towards a theory of irregular variations in the length of the day and core-mantle coupling. *Philosophical Transactions of the Royal Society of London. Series A, Mathematical and Physical Sciences*, 284(1326):547–554, 1977, doi: 10.1098/rsta.1977.0030. 3, 17

Hills, R. G. *Convection in the Earth's mantle due to viscous shear at the core-mantle interface and due to large scale buoyancy*, PhD thesis, New Mexico State University, 1979. 19

Holdenried-Chernoff, D., Maffei, S., and Jackson, A. The Surface Expression of Deep Columnar Flows. *Geochemistry, Geophysics, Geosystems*, 21(6):e2020GC009039, 2020, doi: 10.1029/2020GC009039. 114

Holme, R. Electromagnetic core—mantle coupling—I. Explaining decadal changes in the length of day. *Geophysical Journal International*, 132(1):167–180, 1998, doi: 10.1046/j.1365-246x.1998.00424.x. 17

Holme, R. and de Viron, O. Geomagnetic jerks and a high-resolution length-of-day profile for core studies. *Geophysical Journal International*, 160(2):435–439, 2005, doi: 10.1111/j.1365-246X.2004.02510.x. 13

Holme, R. and de Viron, O. Characterization and implications of intradecadal variations in length of day. *Nature*, 499(7457):202–204, 2013, doi: 10.1038/nature12282. 13

Hori, K., Jones, C. A., and Teed, R. J. Slow magnetic Rossby waves in the Earth's core. *Geophysical Research Letters*, 42(16):6622–6629, 2015, doi: 10.1002/2015GL064733. 2, 55

Hulot, G., Sabaka, T. J., Olsen, N., and Fournier, A. 5.02 - The Present and Future Geomagnetic Field. In Schubert, G., editor, *Treatise on Geophysics (Second Edition)*, pages 33–78. Elsevier, 2015, doi: 10.1016/B978-0-444-53802-4.00096-8. 18

Ivers, D. Enumeration, orthogonality and completeness of the incompressible Coriolis modes in a tri-axial ellipsoid. *Geophysical & Astrophysical Fluid Dynamics*, 111(5):333–354, 2017, doi: 10.1080/03091929.2017.1330412. 38, 47, 48, 49, 80, 111, 113

Ivers, D. J., Jackson, A., and Winch, D. Enumeration, orthogonality and completeness of the incompressible Coriolis modes in a sphere. *Journal of Fluid Mechanics*, 766:468–498, 2015, doi: 10.1017/jfm.2015.27. 47, 48

Jackson, A. and Finlay, C. 5.05 - Geomagnetic Secular Variation and Its Applications to the Core. In Schubert, G., editor, *Treatise on Geophysics (Second Edition)*, pages 137–184. Elsevier, 2015, doi: 10.1016/B978-0-444-53802-4.00099-3. 19

Jackson, A. and Maffei, S. Plesio-geostrophy for Earth's core: I. Basic equations, inertial modes and induction. *Proceedings of the Royal Society A: Mathematical, Physical and Engineering Sciences*, 476(2243):20200513, 2020, doi: 10.1098/rspa.2020.0513. 35

Jackson, A., Jonkers, A. R. T., and Walker, M. R. Four centuries of geomagnetic secular variation from historical records. *Philosophical Transactions of the Royal Society of London. Series A: Mathematical, Physical and Engineering Sciences*, 358(1768):957–990, 2000, doi: 10.1098/rsta.2000.0569. 18

Jault, D. Model Z by computation and Taylor's condition. *Geophysical & Astrophysical Fluid Dynamics*, 79(1-4):99–124, 1995, doi: 10.1080/03091929508228993. 16

Jault, D. Electromagnetic and topographic coupling, and LOD variations. In Jones, C. A., Soward, A. M., Zhang, K., Soward, A. M., and Zhang, K., editors, *Earth's Core and Lower Mantle*, pages 55–76. CRC Press, 2003, doi: 10.1201/9780203207611. 17, 57

Jault, D. Axial invariance of rapidly varying diffusionless motions in the Earth's core interior. *Physics of the Earth and Planetary Interiors*, 166(1):67–76, 2008, doi: 10.1016/j.pepi.2007.11.001. 10

Jault, D. Illuminating the electrical conductivity of the lowermost mantle from below. *Geophysical Journal International*, 202(1):482–496, 2015, doi: 10.1093/gji/ggv152. 17, 18

Jault, D. Tangential stress at the core–mantle interface. *Geophysical Journal International*, 221(2):951–967, 2020, doi: 10.1093/gji/ggaa048. 17, 18, 114

Jault, D. and Finlay, C. C. 8.09 - Waves in the Core and Mechanical Core–Mantle Interactions. In Schubert, G., editor, *Treatise on Geophysics (Second Edition)*, pages 225–244. Elsevier, 2015, doi: 10.1016/B978-0-444-53802-4.00150-0. 21, 56

Jault, D. and Le Mouël, J. L. Physical properties at the top of the core and core surface motions. *Physics of the Earth and Planetary Interiors*, 68(1):76–84, 1991, doi: 10.1016/0031-9201(91)90009-7. 19

Jault, D. and Mouël, J.-L. The topographic torque associated with a tangentially geostrophic motion at the core surface and inferences on the flow inside the core. *Geophysical & Astrophysical Fluid Dynamics*, 48(4):273–295, 1989, doi: 10.1080/03091928908218533. 17, 113, 114

Jault, D. and Mouël, J.-L. Exchange of Angular Momentum between the Core and the Mantle. *Journal of geomagnetism and geoelectricity*, 43(2):111–129, 1991, doi: 10.5636/jgg.43.111. 3, 49

Jault, D. and Mouël, J.-L. L. Core-mantle boundary shape: constraints inferred from the pressure torque acting between the core and the mantle. *Geophysical Journal International*, 101(1):233–241, 1990, doi: 10.1111/j.1365-246X.1990.tb00770.x. 17, 114

Jault, D., Gire, C., and Le Mouel, J. L. Westward drift, core motions and exchanges of angular momentum between core and mantle. *Nature*, 333:353–353, 1988, doi: 10.1038/333353a0. 2, 18

Jones, C. A. Convection–driven geodynamo models. *Philosophical Transactions of the Royal Society of London. Series A: Mathematical, Physical and Engineering Sciences*, 358(1768):873–897, 2000, doi: 10.1098/rsta.2000.0565. 5

Jones, C. A. Course 2 Dynamo theory. In Cardin, P. and Cugliandolo, L. F., editors, *Les Houches*, volume 88 of *Dynamos*, pages 45–135. Elsevier, 2008, doi: 10.1016/S0924-8099(08)80006-6. 9

Jones, C. A. 8.05 - Thermal and Compositional Convection in the Outer Core. In Schubert, G., editor, *Treatise on Geophysics (Second Edition)*, pages 115–159. Elsevier, 2015, doi: 10.1016/B978-0-444-53802-4.00141-X. 5, 7, 10

Kerswell, R. R. Tidal excitation of hydromagnetic waves and their damping in the Earth. *Journal of Fluid Mechanics*, 274:219–241, 1994, doi: 10.1017/S0022112094002107. 59

Kerswell, R. R. Upper bounds on the energy dissipation in turbulent precession. *Journal of Fluid Mechanics*, 321:335–370, 1996, doi: 10.1017/S0022112096007756. 5

Kloss, C. and Finlay, C. C. Time-dependent low-latitude core flow and geomagnetic field acceleration pulses. *Geophysical Journal International*, 217(1):140–168, 2019, doi: 10.1093/gji/ggy545. 18, 115

Knezek, N. and Buffett, B. Influence of magnetic field configuration on magnetohydrodynamic waves in Earth's core. *Physics of the Earth and Planetary Interiors*, 277:1–9, 2018, doi: 10.1016/j.pepi.2018.01.005. 116

Koper, K. D., Pyle, M. L., and Franks, J. M. Constraints on aspherical core structure from PKiKP-PcP differential travel times. *Journal of Geophysical Research: Solid Earth*, 108 (B3), 2003, doi: 10.1029/2002JB001995. 6

Kuang, W., Chao, B. F., and Chen, J. Reassessment of electromagnetic core-mantle coupling and its implications to the Earth's decadal polar motion. *Geodesy and Geodynamics*, 10(5):356–362, 2019, doi: 10.1016/j.geog.2019.06.003. 17

Labbé, F., Jault, D., and Gillet, N. On magnetostrophic inertia-less waves in quasi-geostrophic models of planetary cores. *Geophysical & Astrophysical Fluid Dynamics*, 109(6):587–610, 2015, doi: 10.1080/03091929.2015.1094569. 2, 24, 27, 29, 35, 36, 44, 52

Labrosse, S. Thermal evolution of the core with a high thermal conductivity. *Physics of the Earth and Planetary Interiors*, 247:36–55, 2015, doi: 10.1016/j.pepi.2015.02.002. 5

Lanczos, C. *The variational principles of mechanics*. Mathematical expositions. Dover, 4th ed edition, 1986. 30, 35

Larmor, J. How could a rotating body such as the Sun become a magnet. *Report of the British Association for the Advancement of Science*, pages 159–160, 1919. 5

Le Bars, M., Cébron, D., and Le Gal, P. Flows Driven by Libration, Precession, and Tides. *Annual Review of Fluid Mechanics*, 47(1):163–193, 2015, doi: 10.1146/annurev-fluid-010814-014556. 59

Le Mouël, J. L. Outer-core geostrophic flow and secular variation of Earth's geomagnetic field. *Nature*, 311(5988):734–735, 1984, doi: 10.1038/311734a0. 19

Le Mouël, J. L., Gire, C., and Madden, T. Motions at core surface in the geostrophic approximation. *Physics of the Earth and Planetary Interiors*, 39(4):270–287, 1985, doi: 10.1016/0031-9201(85)90140-2. 1, 17, 19

Le Reun, T., Favier, B., Barker, A. J., and Le Bars, M. Inertial Wave Turbulence Driven by Elliptical Instability. *Physical Review Letters*, 119(3):034502, 2017, doi: 10.1103/PhysRevLett.119.034502. 48

Le Reun, T., Favier, B., and Bars, M. L. Experimental study of the nonlinear saturation of the elliptical instability: inertial wave turbulence versus geostrophic turbulence. *Journal of Fluid Mechanics*, 879:296–326, 2019, doi: 10.1017/jfm.2019.646. 48

Lebovitz, N. R. The stability equations for rotating, inviscid fluids: Galerkin methods and orthogonal bases. *Geophysical & Astrophysical Fluid Dynamics*, 46(4):221–243, 1989, doi: 10.1080/03091928908208913. 27, 37, 38, 39

Lehmann, I. P'. *Publications du Bureau Central Séismologique International*, 14:87–115, 1936. 3

Lehnert, B. Magnetohydrodynamic Waves Under the Action of the Coriolis Force. *The Astrophysical Journal*, 119:647–647, 1954, doi: 10.1086/145869. 2, 10, 46, 52

Lehoucq, R., Sorensen, D., and Yang, C. *ARPACK Users' Guide*. Software, Environments and Tools. Society for Industrial and Applied Mathematics, 1998, doi: 10.1137/1.9780898719628. 61

Li, K., Livermore, P. W., and Jackson, A. An optimal Galerkin scheme to solve the kinematic dynamo eigenvalue problem in a full sphere. *Journal of Computational Physics*, 229(23):8666–8683, 2010, doi: 10.1016/j.jcp.2010.07.039. 27

Li, K., Jackson, A., and Livermore, P. W. Taylor state dynamos found by optimal control: axisymmetric examples. *Journal of Fluid Mechanics*, 853:647–697, 2018, doi: 10.1017/jfm.2018.569. 115, 117

Liao, X. and Zhang, K. A new Legendre-type polynomial and its application to geostrophic flow in rotating fluid spheres. *Proceedings of the Royal Society A: Mathematical, Physical and Engineering Sciences*, 466(2120):2203–2217, 2010, doi: 10.1098/rspa.2009.0582. 47

Lighthill, J. *Waves in fluids*. Cambridge University Press, 1978. 46

Livermore, P. W., Ierley, G., and Jackson, A. The structure of Taylor's constraint in three dimensions. *Proceedings of the Royal Society A: Mathematical, Physical and Engineering Sciences*, 464(2100):3149–3174, 2008, doi: 10.1098/rspa.2008.0091. 56, 115

Lloyd, D. and Gubbins, D. Toroidal fluid motion at the top of the Earth's core. *Geophysical Journal International*, 100(3):455–467, 1990, doi: 10.1111/j.1365-246X.1990.tb00698.x. 19

Lundquist, S. Experimental Investigations of Magneto-Hydrodynamic Waves. *Physical Review*, 76(12):1805–1809, 1949, doi: 10.1103/PhysRev.76.1805. 10

Maffei, S. and Jackson, A. Propagation and reflection of diffusionless torsional waves in a sphere. *Geophysical Journal International*, 204(3):1477–1489, 2016, doi: 10.1093/gji/ggv518. 58

Maffei, S. and Jackson, A. Kinematic validation of a quasi-geostrophic model for the fast dynamics in the Earth's outer core. *Geophysical Journal International*, 210(3):1772–1786, 2017, doi: 10.1093/gji/ggx263. 35

Maffei, S., Jackson, A., and Livermore, P. W. Characterization of columnar inertial modes in rapidly rotating spheres and spheroids. *Proceedings of the Royal Society A: Mathematical, Physical and Engineering Sciences*, 473(2204), 2017, doi: 10.1098/rspa.2017.0181. 2, 29, 37, 38, 43, 44, 50, 51, 82, 117

Malkus, W. V. R. Hydromagnetic planetary waves. *Journal of Fluid Mechanics*, 28(4): 793–802, 1967, doi: 10.1017/S0022112067002447. 2, 46, 52

Malkus, W. V. R. Precession of the Earth as the Cause of Geomagnetism: Experiments lend support to the proposal that precessional torques drive the earth's dynamo. *Science*, 160(3825):259–264, 1968, doi: 10.1126/science.160.3825.259. 5

Mancinelli, N. and Shearer, P. Scattered energy from a rough core-mantle boundary modeled by a Monte Carlo seismic particle method: Application to PKKP precursors. *Geophysical Research Letters*, 43(15):7963–7972, 2016, doi: 10.1002/2016GL070286. 6

Mathews, P. M., Herring, T. A., and Buffett, B. A. Modeling of nutation and precession: New nutation series for nonrigid Earth and insights into the Earth's interior. *Journal of Geophysical Research: Solid Earth*, 107(B4):ETG 3–1–ETG 3–26, 2002, doi: 10.1029/2001JB000390. 6

McDonough, W. F. 2.15 - Compositional Model for the Earth's Core. In Holland, H. D. and Turekian, K. K., editors, *Treatise on Geochemistry*, pages 547–568. Pergamon, 2003, doi: 10.1016/B0-08-043751-6/02015-6. 4

Meurer, A., Smith, C. P., Paprocki, M., Čertík, O., Kirpichev, S. B., Rocklin, M., Kumar, A., Ivanov, S., Moore, J. K., Singh, S., Rathnayake, T., Vig, S., Granger, B. E., Muller, R. P., Bonazzi, F., Gupta, H., Vats, S., Johansson, F., Pedregosa, F., Curry, M. J., Terrel, A. R., Roučka, v., Saboo, A., Fernando, I., Kulal, S., Cimrman, R., and Scopatz, A. Sympy: symbolic computing in python. *PeerJ Computer Science*, 3:e103, 2017, doi: 10.7717/peerj-cs.103. 42

Miles, J. and Salmon, R. Weakly dispersive nonlinear gravity waves. *Journal of Fluid Mechanics*, 157:519–531, 1985, doi: 10.1017/S0022112085002488. 31

Moffatt, H. K. *Magnetic field generation in electrically conducting fluids.* Cambridge University Press, 1978. 5

Moffatt, K. and Dormy, E. *Self-Exciting Fluid Dynamos.* Cambridge University Press, 2019, doi: 10.1017/9781107588691. 5

Mound, J. E. and Buffett, B. A. Interannual oscillations in length of day: Implications for the structure of the mantle and core. *Journal of Geophysical Research: Solid Earth*, 108 (B7), 2003, doi: 10.1029/2002JB002054. 16

Mound, J. E. and Buffett, B. A. Detection of a gravitational oscillation in length-of-day. *Earth and Planetary Science Letters*, 243(3):383–389, 2006, doi: 10.1016/j.epsl.2006.01.043. 16

Munk, W. H. and MacDonald, G. J. F. *The rotation of the earth; a geophysical discussion.* Cambridge University Press, 1960. 2, 17

Nataf, H. C. and Schaeffer, N. 8.06 - Turbulence in the Core. In Schubert, G., editor, *Treatise on Geophysics (Second Edition)*, pages 161–181. Elsevier, 2015, doi: 10.1016/B978-0-444-53802-4.00142-1. 11

Nataf, H. C., Alboussière, T., Brito, D., Cardin, P., Gagnière, N., Jault, D., and Schmitt, D. Rapidly rotating spherical Couette flow in a dipolar magnetic field: An experimental study of the mean axisymmetric flow. *Physics of the Earth and Planetary Interiors*, 170 (1):60–72, 2008, doi: 10.1016/j.pepi.2008.07.034. 2

Niven, W. D. VI. On ellipsoidal harmonics. *Philosophical Transactions of the Royal Society of London. (A.)*, 182:231–278, 1891, doi: 10.1098/rsta.1891.0006. 114

Nornberg, M. D., Ji, H., Schartman, E., Roach, A., and Goodman, J. Observation of Magnetocoriolis Waves in a Liquid Metal Taylor-Couette Experiment. *Physical Review Letters*, 104(7):074501, 2010, doi: 10.1103/PhysRevLett.104.074501. 46

Ohta, K., Hirose, K., Ichiki, M., Shimizu, K., Sata, N., and Ohishi, Y. Electrical conductivities of pyrolitic mantle and MORB materials up to the lowermost mantle conditions. *Earth and Planetary Science Letters*, 289(3):497–502, 2010, doi: 10.1016/j.epsl.2009.11.042. 17

Oldham, R. D. The Constitution of the Interior of the Earth, as Revealed by Earthquakes. *Quarterly Journal of the Geological Society*, 62(1-4):456–475, 1906, doi: 10.1144/GSL.JGS.1906.062.01-04.21. 3

Olsen, N. and Stolle, C. Satellite Geomagnetism. *Annual Review of Earth and Planetary Sciences*, 40(1):441–465, 2012, doi: 10.1146/annurev-earth-042711-105540. 1, 18

Olson, P. Core Dynamics: An Introduction and Overview. In Schubert, G., editor, *Treatise on Geophysics (Second Edition)*, pages 1–25. Elsevier, 2015, doi: 10.1016/B978-0-444-53802-4.00137-8. 4

Orman, J. A. V. On the viscosity and creep mechanism of Earth's inner core. *Geophysical Research Letters*, 31(20), 2004, doi: 10.1029/2004GL021209. 16

Oser, H. Experimentelle Untersuchung über harmonische Schwingungen in rotierenden Flüssigkeiten. *ZAMM - Journal of Applied Mathematics and Mechanics / Zeitschrift für Angewandte Mathematik und Mechanik*, 38(9-10):386–391, 1958, doi: 10.1002/zamm.19580380909. 46

Otsuka, K. and Karato, S.-i. Deep penetration of molten iron into the mantle caused by a morphological instability. *Nature*, 492(7428):243–246, 2012, doi: 10.1038/nature11663. 16

Ozawa, H., Hirose, K., Mitome, M., Bando, Y., Sata, N., and Ohishi, Y. Experimental study of reaction between perovskite and molten iron to 146 GPa and implications for chemically distinct buoyant layer at the top of the core. *Physics and Chemistry of Minerals*, 36(6):355–363, 2009, doi: 10.1007/s00269-008-0283-x. 16

O'Rourke, J. G. and Stevenson, D. J. Powering Earth's dynamo with magnesium precipitation from the core. *Nature*, 529(7586):387–389, 2016, doi: 10.1038/nature16495. 5

Pais, M. A. and Jault, D. Quasi-geostrophic flows responsible for the secular variation of the Earth's magnetic field. *Geophysical Journal International*, 173(2):421–443, 2008, doi: 10.1111/j.1365-246X.2008.03741.x. 11, 23, 25

Plumley, M., Calkins, M. A., Julien, K., and Tobias, S. M. Self-consistent single mode investigations of the quasi-geostrophic convection-driven dynamo model. *Journal of Plasma Physics*, 84(4), 2018, doi: 10.1017/S0022377818000831. 11

Poincaré, H. Sur l'équilibre d'une masse fluide animée d'un mouvement de rotation. *Acta Mathematica*, 7:259–380, 1885, doi: 10.1007/BF02402204. 37

Poincaré, H. Sur la précession des corps déformables. *Bulletin Astronomique, Serie I*, 27: 321, 1910. 17

Pozzo, M., Davies, C., Gubbins, D., and Alfè, D. Thermal and electrical conductivity of iron at Earth's core conditions. *Nature*, 485(7398):355–358, 2012, doi: 10.1038/nature11031. 5

Pozzo, M., Davies, C., Gubbins, D., and Alfè, D. Thermal and electrical conductivity of solid iron and iron–silicon mixtures at Earth's core conditions. *Earth and Planetary Science Letters*, 393:159–164, 2014, doi: 10.1016/j.epsl.2014.02.047. 5

Proudman, J. On the motion of solids in a liquid possessing vorticity. *Proceedings of the Royal Society of London. Series A, Containing Papers of a Mathematical and Physical Character*, 92(642):408–424, 1916, doi: 10.1098/rspa.1916.0026. 1, 7

Reddy, K. S., Favier, B., and Bars, M. L. Turbulent Kinematic Dynamos in Ellipsoids Driven by Mechanical Forcing. *Geophysical Research Letters*, 45(4):1741–1750, 2018, doi: 10.1002/2017GL076542. 5

Rieutord, M. and Valdettaro, L. Inertial waves in a rotating spherical shell. *Journal of Fluid Mechanics*, 341:77–99, 1997, doi: 10.1017/S0022112097005491. 48, 61

Roberts, P. H. *An Introduction to Magnetohydrodynamics*. Longmans, Green and Co ltd, London, 1967. 6

Roberts, P. H. 8.03 - Theory of the Geodynamo. In Schubert, G., editor, *Treatise on Geophysics (Second Edition)*, pages 57–90. Elsevier, 2015, doi: 10.1016/B978-0-444-53802-4.00144-5. 5

Roberts, P. H. and Aurnou, J. M. On the theory of core-mantle coupling. *Geophysical & Astrophysical Fluid Dynamics*, 106(2):157–230, 2012, doi: 10.1080/03091929.2011.589028. 3, 15, 16, 57

Roberts, P. H. and Scott, S. On Analysis of the Secular Variation. *Journal of geomagnetism and geoelectricity*, 17(2):137–151, 1965, doi: 10.5636/jgg.17.137. 19

Roberts, P. H. and Soward, A. M. Magnetohydrodynamics of the Earth's Core. *Annual Review of Fluid Mechanics*, 4(1):117–154, 1972, doi: 10.1146/annurev.fl.04.010172.001001. 46

Rochester, M. G. and Bullard, E. C. Geomagnetic westward drift and irregularities in the Earth's rotation. *Philosophical Transactions of the Royal Society of London. Series A, Mathematical and Physical Sciences*, 252(1018):531–555, 1960, doi: 10.1098/rsta.1960.0014. 16

Rochester, M. G., Hide, R., Wilkins, G. A., McCrea, W. H., Message, P. J., and Runcorn, S. K. Causes of fluctuations in the rotation of the Earth. *Philosophical Transactions of the Royal Society of London. Series A, Mathematical and Physical Sciences*, 313(1524): 95–105, 1984, doi: 10.1098/rsta.1984.0086. 16

Rogister, Y. and Valette, B. Influence of liquid core dynamics on rotational modes. *Geophysical Journal International*, 176(2):368–388, 2009, doi: 10.1111/j.1365-246X.2008.03996.x. 115

Rossby, C.-G. Relation between variations in the intensity of the zonal circulation of the atmosphere and the displacements of the semi-permanent centers of action. *Journal of Marine Research*, 2:38–55, 1939, doi: 10.1357/002224039806649023. 20, 50, 52

Runcorn, S. K. The electrical conductivity of the Earth's mantle. *Eos, Transactions American Geophysical Union*, 36(2):191–198, 1955, doi: 10.1029/TR036i002p00191. 18

Salmon, R. Practical use of Hamilton's principle. *Journal of Fluid Mechanics*, 132:431–444, 1983, doi: 10.1017/S0022112083001706. 30, 31, 33

Sasao, T., Okubo, S., and Saito, M. A Simple Theory on Dynamical Effects of Stratified Fluid Core upon Nutational Motion of the Earth. *Symposium - International Astronomical Union*, 78:165, 1980, doi: 10.1017/S0074180900032009. 35

Schaeffer, N. and Cardin, P. Quasigeostrophic model of the instabilities of the Stewartson layer in flat and depth-varying containers. *Physics of Fluids*, 17(10):104111–104111, 2005, doi: 10.1063/1.2073547. 20, 23, 24, 25, 26, 30

Schaeffer, N., Jault, D., Nataf, H.-C., and Fournier, A. Turbulent geodynamo simulations: a leap towards Earth's core. *Geophysical Journal International*, 211(1):1–29, 2017, doi: 10.1093/gji/ggx265. 2, 5, 20, 59

Schmitt, D. Magneto-inertial waves in a rotating sphere. *Geophysical & Astrophysical Fluid Dynamics*, 104(2-3):135–151, 2010, doi: 10.1080/03091920903439746. 106

Schmitt, D. Quasi-free-decay magnetic modes in planetary cores. *Geophysical & Astrophysical Fluid Dynamics*, 106(6):660–680, 2012, doi: 10.1080/03091929.2012.681306. 106, 111, 116

Schmitt, D., Alboussière, T., Brito, D., Cardin, P., Gagnière, N., Jault, D., and Nataf, H.-C. Rotating spherical Couette flow in a dipolar magnetic field: experimental study of magneto-inertial waves. *Journal of Fluid Mechanics*, 604:175–197, 2008, doi: 10.1017/S0022112008001298. 46

Schmitt, D., Cardin, P., La Rizza, P., and Nataf, H. C. Magneto–Coriolis waves in a spherical Couette flow experiment. *European Journal of Mechanics - B/Fluids*, 37:10–22, 2013, doi: 10.1016/j.euromechflu.2012.09.001. 46

Schubert, G., Turcotte, D. L., and Olson, P. *Mantle Convection in the Earth and Planets.* Cambridge University Press, 2001. 5

Spiegel, E. A. and Veronis, G. On the Boussinesq Approximation for a Compressible Fluid. *The Astrophysical Journal*, 131:442, 1960, doi: 10.1086/146849. 7

Stephenson, F. R., Morrison, L. V., and Smith, F. T. Long-term fluctuations in the Earth's rotation: 700 BC to AD 1990. *Philosophical Transactions of the Royal Society of London. Series A: Physical and Engineering Sciences*, 351(1695):165–202, 1995, doi: 10.1098/rsta.1995.0028. 12

Stephenson, F. R., Morrison, L. V., and Hohenkerk, C. Y. Measurement of the Earth's rotation: 720 BC to AD 2015. *Proceedings of the Royal Society A: Mathematical, Physical and Engineering Sciences*, 472(2196):20160404, 2016, doi: 10.1098/rspa.2016.0404. 12

Stewart, G. W. A Krylov–Schur Algorithm for Large Eigenproblems. *SIAM Journal on Matrix Analysis and Applications*, 23(3):601–614, 2001, doi: 10.1137/S0895479800371529. 61

Stix, M. and Roberts, P. H. Time-dependent electromagnetic core-mantle coupling. *Physics of the Earth and Planetary Interiors*, 36(1):49–60, 1984, doi: 10.1016/0031-9201(84)90098-0. 16

Sutcliffe, R. C. Cyclonic and anticyclonic development. *Quarterly Journal of the Royal Meteorological Society*, 65(282):518–524, 1939, doi: 10.1002/qj.49706528208. 20

Sze, E. K. M. and van der Hilst, R. D. Core mantle boundary topography from short period PcP, PKP, and PKKP data. *Physics of the Earth and Planetary Interiors*, 135(1):27–46, 2003, doi: 10.1016/S0031-9201(02)00204-2. 6

Tarduno, J. A., Cottrell, R. D., Watkeys, M. K., Hofmann, A., Doubrovine, P. V., Mamajek, E. E., Liu, D., Sibeck, D. G., Neukirch, L. P., and Usui, Y. Geodynamo, Solar Wind, and Magnetopause 3.4 to 3.45 Billion Years Ago. *Science*, 327(5970):1238–1240, 2010, doi: 10.1126/science.1183445. 5

Tarduno, J. A., Cottrell, R. D., Bono, R. K., Oda, H., Davis, W. J., Fayek, M., van t'Erve, O., Nimmo, F., Huang, W., Thern, E. R., Fearn, S., Mitra, G., Smirnov, A. V., and Blackman, E. G. Paleomagnetism indicates that primary magnetite in zircon records a strong Hadean geodynamo. *Proceedings of the National Academy of Sciences*, 2020, doi: 10.1073/pnas.1916553117. 5

Taylor, G. I. Motion of solids in fluids when the flow is not irrotational. *Proceedings of the Royal Society of London A: Containing Papers of a Mathematical and Physical Character*, 93(648):99–113, 1917, doi: 10.1098/rspa.1917.0007. 1, 7

Taylor, J. B. The magneto-hydrodynamics of a rotating fluid and the earth's dynamo problem. *Proceedings of the Royal Society A: Mathematical, Physical and Engineering Sciences*, 274(1357):274–283, 1963, doi: 10.1098/rspa.1963.0130. 56

Teed, R. J., Jones, C. A., and Tobias, S. M. The transition to Earth-like torsional oscillations in magnetoconvection simulations. *Earth and Planetary Science Letters*, 419:22–31, 2015, doi: 10.1016/j.epsl.2015.02.045. 59

Teed, R. J., Jones, C. A., and Tobias, S. M. Torsional waves driven by convection and jets in Earth's liquid core. *Geophysical Journal International*, 216(1):123–129, 2019, doi: 10.1093/gji/ggy416. 59, 114

Thomson, W. XXIV. Vibrations of a columnar vortex. *The London, Edinburgh, and Dublin Philosophical Magazine and Journal of Science*, 10(61):155–168, 1880, doi: 10.1080/14786448008626912. 46, 47

Tort, M. and Dubos, T. Dynamically consistent shallow-atmosphere equations with a complete Coriolis force. *Quarterly Journal of the Royal Meteorological Society*, 140(684): 2388–2392, 2014, doi: 10.1002/qj.2274. 30

Triana, S. A., Rekier, J., Trinh, A., and Dehant, V. The coupling between inertial and rotational eigenmodes in planets with liquid cores. *Geophysical Journal International*, 218(2):1071–1086, 2019, doi: 10.1093/gji/ggz212. 111, 115

Turner, G. M., Rasson, J., and Reeves, C. 5.04 - Observation and Measurement Techniques. In Schubert, G., editor, *Treatise on Geophysics (Second Edition)*, pages 91–135. Elsevier, 2015, doi: 10.1016/B978-0-444-53802-4.00098-1. 18

Vantieghem, S. Inertial modes in a rotating triaxial ellipsoid. *Proceedings of the Royal Society A: Mathematical, Physical and Engineering Sciences*, 470(2168):20140093, 2014, doi: 10.1098/rspa.2014.0093. 48, 60

Verhoogen, J. Heat Balance of the Earth's Core. *Geophysical Journal International*, 4 (Supplement_1):276–281, 1961, doi: 10.1111/j.1365-246X.1961.tb06819.x. 5

Vidal, J. and Cébron, D. Inviscid instabilities in rotating ellipsoids on eccentric Kepler orbits. *Journal of Fluid Mechanics*, 833:469–511, 2017, doi: 10.1017/jfm.2017.689. 38

Vidal, J. and Schaeffer, N. Quasi-geostrophic modes in the Earth's fluid core with an outer stably stratified layer. *Geophysical Journal International*, 202(3):2182–2193, 2015, doi: 10.1093/gji/ggv282. 49, 61

Vidal, J., Cébron, D., and Schaeffer, N. Diffusionless hydromagnetic modes in rotating ellipsoids: a road to weakly nonlinear models? *Comptes-Rendus de la 19e Rencontre du Non-Linéaire*, pages 121–121, 2016. 3, 38, 59

Vidal, J., Cébron, D., ud Doula, A., and Alecian, E. Fossil field decay due to nonlinear tides in massive binaries. *Astronomy & Astrophysics*, 629:A142, 2019, doi: 10.1051/0004-6361/201935658. 38, 58

Vondrak, J. The rotation of the earth between 1955.5 and 1976.5. *Studia Geophysica et Geodaetica*, 21:107–117, 1977, doi: 10.1007/BF01634821. 13

Watkins, A., Fu, Y., and Gross, R. Earth's Subdecadal Angular Momentum Balance from Deformation and Rotation Data. *Scientific Reports*, 8(1):13761, 2018, doi: 10.1038/s41598-018-32043-8. 16

Whaler, K. A. and Gubbins, D. Spherical harmonic analysis of the geomagnetic field: an example of a linear inverse problem. *Geophysical Journal International*, 65(3):645–693, 1981, doi: 10.1111/j.1365-246X.1981.tb04877.x. 1, 18

Wicks, J. K., Jackson, J. M., and Sturhahn, W. Very low sound velocities in iron-rich (Mg,Fe)O: Implications for the core-mantle boundary region. *Geophysical Research Letters*, 37(15), 2010, doi: 10.1029/2010GL043689. 16

Wiechert, E. Über die Massenverteilung im Inneren der Erde. *Nachrichten von der Gesellschaft der Wissenschaften zu Göttingen, Mathematisch-Physikalische Klasse*, 1897: 221–243, 1897. 3

Wijs, G. A. d., Kresse, G., Vočadlo, L., Dobson, D., Alfè, D., Gillan, M. J., and Price, G. D. The viscosity of liquid iron at the physical conditions of the Earth's core. *Nature*, 392(6678):805, 1998, doi: 10.1038/33905. 4, 16

Wu, C.-C. and Roberts, P. H. On magnetostrophic mean-field solutions of the geodynamo equations. *Geophysical & Astrophysical Fluid Dynamics*, 109(1):84–110, 2015, doi: 10.1080/03091929.2014.988711. 56

Yoder, C. F., Williams, J. G., and Parke, M. E. Tidal variations of earth rotation. *Journal of Geophysical Research*, 86(B2):881, 1981, doi: 10.1029/JB086iB02p00881. 35

Yu, N., Chen, G., Ray, J., Chen, W., and Chao, N. Semi-decadal and decadal signals in atmospheric excitation of length-of-day. *Earth and Space Science*, 7(2):e2019EA000976, 2020, doi: 10.1029/2019EA000976. 13

Yukutake, T. A stratified core motion inferred from geomagnetic secular variations. *Physics of the Earth and Planetary Interiors*, 24(4):253–258, 1981, doi: 10.1016/0031-9201(81)90112-6. 18

Zatman, S. and Bloxham, J. Torsional oscillations and the magnetic field within the Earth's core. *Nature*, 388(6644):760–763, 1997, doi: 10.1038/41987. 59

Zhang, K. On equatorially trapped boundary inertial waves. *Journal of Fluid Mechanics*, 248:203–217, 1993, doi: 10.1017/S0022112093000746. 50

Zhang, K. and Busse, F. H. On hydromagnetic instabilities driven by the Hartmann boundary layer in a rapidly rotating sphere. *Journal of Fluid Mechanics*, 304:263–283, 1995, doi: 10.1017/S0022112095004423. 106

Zhang, K. and Liao, X. *Theory and Modeling of Rotating Fluids*. Cambridge Monographs on Mechanics. Cambridge University Press, 2017, doi: 10.1017/9781139024853. 6, 48

Zhang, K., Earnshaw, P., Liao, X., and Busse, F. H. On inertial waves in a rotating fluid sphere. *Journal of Fluid Mechanics*, 437:103–119, 2001, doi: 10.1017/S0022112001004049. 48, 49, 51

Zhang, K., Liao, X., and Earnshaw, P. On inertial waves and oscillations in a rapidly rotating spheroid. *Journal of Fluid Mechanics*, 504:1–40, 2004, doi: 10.1017/S0022112003007456. 48